

University of Southampton Research Repository ePrints Soton

Copyright © and Moral Rights for this thesis are retained by the author and/or other copyright owners. A copy can be downloaded for personal non-commercial research or study, without prior permission or charge. This thesis cannot be reproduced or quoted extensively from without first obtaining permission in writing from the copyright holder/s. The content must not be changed in any way or sold commercially in any format or medium without the formal permission of the copyright holders.

When referring to this work, full bibliographic details including the author, title, awarding institution and date of the thesis must be given e.g.

AUTHOR (year of submission) "Full thesis title", University of Southampton, name of the University School or Department, PhD Thesis, pagination



Faculty of Engineering and the Environment
Computational Engineering and Design Research Group

Cost Optimization Tools for Advanced Gas Turbine Technologies

by **Stephan Langmaak**

Thesis submitted in partial satisfaction
of the requirements for the degree of

DOCTOR OF ENGINEERING

Academic Supervisors: Prof. James Scanlan, Dr András Sóbester

Industrial Supervisors: Dr Stephen Wiseall (†), Martin Rhodes

August 2015

UNIVERSITY OF SOUTHAMPTON

ABSTRACT

FACULTY OF ENGINEERING AND THE ENVIRONMENT
COMPUTATIONAL ENGINEERING AND DESIGN RESEARCH GROUP

Doctor of Engineering

COST OPTIMIZATION TOOLS FOR ADVANCED GAS TURBINE TECHNOLOGIES

by Stephan Langmaak

This thesis presents two studies that illustrate how cost modelling can be integrated into the various design process stages, ranging from strategic gas turbine and airframe system design to preliminary and detailed component design and production planning.

The first study investigates which cruise speed the next generation of short-haul aircraft with 150 seats should fly at and whether a conventional two- or three-shaft turbofan, a geared turbofan, a turboprop or an open rotor should be employed in order to make the aircraft's direct operating cost robust to uncertain fuel and carbon (CO_2) prices in the Year 2030, taking the aircraft productivity, the passenger value of time and the modal shift into account. To answer this question, an optimization loop was set up in MATLAB consisting of nine modules covering gas turbine and airframe design and performance, flight and aircraft fleet simulation, operating cost and optimization. If the passenger value of time is included, the most robust aircraft design is powered by geared turbofan engines and cruises at Mach 0.80. If the value of time is ignored, however, then a turboprop aircraft flying at Mach 0.70 is the optimum solution. This demonstrates that the most *fuel-efficient* option, the open rotor, is not automatically the most *cost-efficient* solution because of the relatively high engine and airframe costs.

The second study shows how a factory cost model can be combined with a parametric component production time model, to not only calculate costs at the manufacturing operation level for production planning, but also the total unit costs of future integrally bladed disc (blisk) designs for component trade-off studies. As future process times can only be estimated and the correlation between operation times and blisk design parameters, including the number of blades, the disc diameter and other design variables, is never perfect, all operation times have uncertainty distributions. These are cascaded through the model to generate a probability distribution of the unit cost.

Contents

1	Cost Optimization	1
1.1	Background	1
1.1.1	Costing within the Aerospace Industry	1
1.1.2	Design Optimization	2
1.2	Research Motivation	3
1.2.1	System Study	4
1.2.2	Component Study	7
1.3	System Costing	8
1.3.1	Fuel and Carbon Prices	8
1.3.2	Multi-Disciplinary Optimization	12
1.4	Component Costing	22
1.4.1	Activity-Based Costing	22
1.4.2	Parametric Costing	24
2	Advanced Gas Turbine Technology	27
2.1	Gas Turbine and Airframe System Options	27
2.1.1	System Option 1: Two-Shaft Turbofan	28
2.1.2	System Option 2: Three-Shaft Turbofan	29
2.1.3	System Option 3: Geared Turbofan	31
2.1.4	System Option 4: Turboprop	32
2.1.5	System Option 5: Open Rotor	33
2.2	Gas Turbine Component Options	36
2.2.1	Blinks	36

3	System Study	41
3.1	Methodology and Assumptions	41
3.1.1	Module 1: Engine Design	43
3.1.2	Module 2: Airframe Design	51
3.1.3	Module 3: Engine Performance	55
3.1.4	Module 4: Airframe Performance	56
3.1.5	Module 5: Performance Requirement	57
3.1.6	Module 6: Flight Simulation	64
3.1.7	Module 7: Aircraft Fleet Simulation	73
3.1.8	Module 8: Direct Operating Cost	75
3.1.9	Module 9: Optimizer	81
3.2	Results and Discussion	83
3.2.1	Optimum Design	83
3.2.2	Mission Performance	89
3.2.3	Optimum Cruise Speed	100
3.2.4	Verification	107
4	Component Study	111
4.1	Factory Cost Model	111
4.1.1	Model Schematics	111
4.2	Scalable Blisk Cost Model	114
4.2.1	Blisk Design Variability	115
4.2.2	Model Structure	115
4.2.3	Regression Analysis	118
4.2.4	Uncertainty	119
4.3	Results and Discussion	123
4.3.1	Unit Cost Prediction	123
4.3.2	Blisk Design Space	126
5	Conclusion and Recommendations	129
5.1	System Study	129
5.1.1	Contribution and Limitations	129
5.1.2	Future Work	130

5.2	Component Study	132
5.2.1	Factory Cost Model	132
5.2.2	Scalable Blisk Cost Model	133
A	Design Optimization Data	135
B	Performance Diagrams	147
C	Cruise Speed Optimization Data	155
D	Cost Diagrams	167

List of Figures

1.1	Design Phases within the Product Life-Cycle	3
1.2	Correlation Between Oil Price and Direct Operating Cost from 1971 to 2009	9
1.3	Direct Operating Cost Elements from 1971 to 2009	10
1.4	Total Flight Journey Time Vs. Direct Distance	17
1.5	Aircraft, High-Speed Train and Car Market Share Vs. Direct Distance	18
1.6	Aircraft Market Share Vs. Average Door-to-Door Speed	19
1.7	Impact of Cruise Speed on Aircraft Market Share	19
1.8	Single-Aisle Aircraft Flight Distance Distribution	20
1.9	Effect of Cruise Speed on 150-Seater RPK	21
1.10	Conventional Vs. Activity-Based Costing	23
2.1	Two-Shaft Turbofan Aircraft (Cruise Speed: Mach 0.78)	29
2.2	Three-Shaft Turbofan Aircraft (Cruise Speed: Mach 0.78)	30
2.3	Geared Turbofan Aircraft (Cruise Speed: Mach 0.78)	31
2.4	Turboprop Aircraft (Cruise Speed: Mach 0.70)	33
2.5	Open Rotor Aircraft (Cruise Speed: Mach 0.70)	35
2.6	Open Rotor Aircraft (Cruise Speed: Mach 0.76)	36
2.7	Blisk Weight Saving	37
2.8	Axial-Flow Gas Turbine Compressor with LFW, MFS and ECM Blisks	37
2.9	Linear Friction Welding	38
3.1	System Design Methodology	42
3.2	Engine Design Framework	44
3.3	Blade, Disc and Drum Schematic	50
3.4	Airframe Design Framework	52
3.5	Engine Performance Framework	55

3.6	Airframe Performance Framework	56
3.7	Takeoff Field Length Simulation Framework	60
3.8	Balanced Field Length Simulation Framework	61
3.9	Climb Requirement Simulation Framework	62
3.10	Cruise Requirement Simulation Framework	63
3.11	Landing Requirement Simulation Framework	64
3.12	Flight Profile	65
3.13	Flight Taxi Simulation Framework	67
3.14	Flight Landing Simulation Framework	68
3.15	Flight Deceleration Simulation Framework	69
3.16	Flight Descent Simulation Framework	70
3.17	Flight Cruise Simulation Framework	70
3.18	Flight Ascent Simulation Framework	71
3.19	Flight Acceleration Simulation Framework	71
3.20	Flight Takeoff Simulation Framework	72
3.21	Aircraft Fleet Simulation Framework	74
3.22	Fleet Size, Annual Flight Cycles and Flight Hours Vs. Cruise Speed	74
3.23	Direct Operating Cost Elements	76
3.24	Correlation between Crude Oil and Jet Fuel Prices	80
3.25	Optimization Framework	82
3.26	Two-Shaft Turbofan Mission True Airspeed, Thrust and Fuel and Core Mass Flow Rates (Cruise Speed: Mach 0.78)	90
3.27	Two-Shaft Turbofan Mission Turbine Entry Temperature and Rotational Speeds (Cruise Speed: Mach 0.78)	92
3.28	Two-Shaft Turbofan Mission Bypass Ratio and Pressure Ratios (Cruise Speed: Mach 0.78)	93
3.29	Turboprop Mission True Airspeed, Thrust and Fuel and Core Mass Flow Rates (Cruise Speed: Mach 0.70)	96
3.30	Turboprop Mission Turbine Entry Temperature and Rotational Speeds (Cruise Speed: Mach 0.70)	97
3.31	Turboprop Mission Propeller Efficiency and Overall Pressure Ratio (Cruise Speed: Mach 0.70)	98
3.32	Direct Operating Cost Breakdown Vs. Cruise Speed	102

3.33	System Options MSD of Direct Operating Cost (incl. Value of Time) Vs. Cruise Speed	103
3.34	Optimum System Options (incl. Value of Time) Vs. Actual U.S. Passenger Airlines Direct Operating Cost Breakdown	104
3.35	System Options MSD of Direct Operating Cost (excl. Value of Time) Vs. Cruise Speed	105
3.36	Optimum System Options (excl. Value of Time) Vs. Actual U.S. Passenger Airlines Direct Operating Cost Breakdown	106
4.1	Factory Cost Model Structure	112
4.2	Factory Cost Model Inputs	113
4.3	Factory Cost Model Hierarchy	113
4.4	Scalable Blisk and Factory Cost Model Interaction	114
4.5	Scaling Rules for the Generic LFW Method of Manufacture	116
4.6	Scalable Blisk Cost Model User Interface	117
4.7	A Scaling Rule with a Good Fit	119
4.8	A Scaling Rule with a Bad Fit	119
4.9	Triangular Uncertainty Distribution	120
4.10	Unit Cost Uncertainty Distribution of the Complex Blisk	124
4.11	Unit Cost Uncertainty Distribution of the Simple Blisk	124
4.12	Operation and Feature Unit Costs of the Complex Blisk	125
4.13	Operation and Feature Unit Costs of the Simple Blisk	125
4.14	Unit Cost Sensitivity of the Complex Blisk	127
4.15	Unit Cost Sensitivity of the Simple Blisk	127
B.1	Three-Shaft Turbofan Mission True Airspeed, Thrust and Fuel and Core Mass Flow Rates (Cruise Speed: Mach 0.78)	147
B.2	Three-Shaft Turbofan Mission Turbine Entry Temperature and Rotational Speeds (Cruise Speed: Mach 0.78)	148
B.3	Three-Shaft Turbofan Mission Bypass Ratio and Pressure Ratios (Cruise Speed: Mach 0.78)	148
B.4	Geared Turbofan Mission True Airspeed, Thrust and Fuel and Core Mass Flow Rates (Cruise Speed: Mach 0.78)	149

B.5	Geared Turbofan Mission Turbine Entry Temperature and Rotational Speeds (Cruise Speed: Mach 0.78)	149
B.6	Geared Turbofan Mission Bypass Ratio and Pressure Ratios (Cruise Speed: Mach 0.78)	150
B.7	Open Rotor Mission True Airspeed, Thrust and Fuel and Core Mass Flow Rates (Cruise Speed: Mach 0.70)	150
B.8	Open Rotor Mission Turbine Entry Temperature and Rotational Speeds (Cruise Speed: Mach 0.70)	151
B.9	Open Rotor Mission Propeller Efficiency and Overall Pressure Ratio (Cruise Speed: Mach 0.70)	151
B.10	Open Rotor Mission True Airspeed, Thrust and Fuel and Core Mass Flow Rates (Cruise Speed: Mach 0.76)	152
B.11	Open Rotor Mission Turbine Entry Temperature and Rotational Speeds (Cruise Speed: Mach 0.76)	152
B.12	Open Rotor Mission Propeller Efficiency and Overall Pressure Ratio (Cruise Speed: Mach 0.76)	153
D.1	Three-Shaft Turbofan Direct Operating Cost Breakdown Vs. Cruise Speed .	167
D.2	Geared Turbofan Direct Operating Cost Breakdown Vs. Cruise Speed . . .	168
D.3	Open Rotor Direct Operating Cost Breakdown Vs. Cruise Speed	168

List of Tables

1.1	System Study Literature Review	5
1.2	Direct and Indirect Operating Cost	15
1.3	Comparison of NPV _P and DOC Parameters	16
3.1	System Study Input Parameter Constraints	43
3.2	Fixed Engine Design Performance Values	45
3.3	Fixed Engine Annulus Design Values	45
3.4	Engine Materials	49
3.5	Fixed Airframe Design Values	53
3.6	Airframe Weight Formulas and Values	54
3.7	Performance Requirements	58
3.8	Optimization Method Requirements	81
3.9	Optimization Step Lengths	83
3.10	Optimized System Design Parameters	84
3.11	Performance Data of System Options 1–3	94
3.12	Performance Data of System Options 4–5	99
3.13	Direct Operating Cost Range	101
3.14	Comparison of $\sqrt{\text{MSD}}$ and Mean DOC	107
3.15	Verification of Cruise Speed and Fuel Consumption Results	108
3.16	Verification of Aircraft Wing Span, Operating Weight Empty and Acquisition Cost Results	108
A.1	Two-Shaft Turbofan Design Space	136
A.2	Two-Shaft Turbofan Design Cost Space	137
A.3	Three-Shaft Turbofan Design Space	138
A.4	Three-Shaft Turbofan Design Cost Space	139

A.5	Geared Turbofan Design Space	140
A.6	Geared Turbofan Design Cost Space	141
A.7	Turboprop Design Space	142
A.8	Turboprop Design Cost Space	143
A.9	Open Rotor Design Space	144
A.10	Open Rotor Design Cost Space	145
C.1	Two-Shaft Turbofan Cruise Speed Space	156
C.2	Two-Shaft Turbofan Cruise Speed Cost Space	157
C.3	Three-Shaft Turbofan Cruise Speed Space	158
C.4	Three-Shaft Turbofan Cruise Speed Cost Space	159
C.5	Geared Turbofan Cruise Speed Space	160
C.6	Geared Turbofan Cruise Speed Cost Space	161
C.7	Turboprop Cruise Speed Space	162
C.8	Turboprop Cruise Speed Cost Space	163
C.9	Open Rotor Cruise Speed Space	164
C.10	Open Rotor Cruise Speed Cost Space	165

Declaration of Authorship

I, Stephan Langmaak, declare that this thesis titled “Cost Optimization Tools for Advanced Gas Turbine Technologies” and the work presented in it is my own and has been generated by me as the result of my own original research. I confirm that:

- This work was done wholly or mainly while in candidature for a research degree at this university.
- Where any part of this thesis has previously been submitted for a degree or any other qualification at this university or any other institution, this has been clearly stated.
- Where I have consulted the published work of others, this is always clearly attributed.
- Where I have quoted from the work of others, the source is always given. With the exception of such quotations, this thesis is entirely my own work.
- I have acknowledged all main sources of help.
- Where the thesis is based on work done by myself jointly with others, I have made clear exactly what was done by others and what I have contributed myself.
- Parts of this work have been published as:
 - Langmaak, S., Wiseall, S., Bru, C., Adkins, R., Scanlan, J., Sóbester, A., “An Activity-Based Parametric Hybrid Cost Model to Estimate the Unit Cost of a Novel Gas Turbine Component,” *International Journal of Production Economics*, Vol. 142, No. 1, 2013, pp. 74–88. Available from: <http://www.sciencedirect.com/science/article/pii/S0925527312004161>.
 - Langmaak, S., Scanlan, J., Sóbester, A., Wiseall, S., “Strategic Jet Engine System Design in Light of Uncertain Fuel and Carbon Prices,” *11th AIAA Aviation*

Technology, Integration, and Operations (ATIO) Conference, Virginia Beach, Virginia, USA, 2011. Available from: <http://arc.aiaa.org/doi/abs/10.2514/6.2011-6928>.

- Langmaak, S., Scanlan, J., Wiseall, S., “Strategic Jet Engine System Design in Light of Uncertain Fuel and Carbon Prices,” *2nd International Air Transport and Operations Symposium (ATOS)*, Delft University of Technology, Delft, The Netherlands, 2011. Available from: <http://ebooks.iospress.nl/publication/31860>.

Signed:.....

Date:

Acknowledgements

I particularly want to express my gratitude towards my main supervisors, Prof. James Scanlan at the University of Southampton and the late Dr Stephen Wiseall at Rolls-Royce plc, especially for giving me the freedom to pursue the research theme that interested me most and for providing the generous funding of my studentship. I would also like to thank my second academic supervisor, Dr András Sóbester, for brainstorming the idea of investigating the effect of uncertain oil prices on gas turbine design and conscientiously reviewing my written work. Furthermore, my gratefulness also applies to the support provided by many other colleagues at Rolls-Royce, especially Russell Adkins, Dr Christoph Becker, Dr Christophe Bru, Dr Phani Chinchapatnam, Martin Rhodes, Dr Sree Tammineni and John Whurr. I could also not have completed my work without my parents, Dr Andreas Knittel and Dr Klaus Heinig, who not only encouraged and advised me, but also proofread this thesis.

Abbreviations

ABC	Activity-Based Costing
ACARE	The Advisory Council for Aeronautics Research in Europe
Al	Aluminium
Blisk	Integrally Bladed Disc
CDF	Cumulative Distribution Function
CER	Cost Estimating Relationship
DOC	Direct Operating Cost
DoE	Design of Experiments
DREAM	validAtion of Radical Engine Architecture systeMs
EAS	Equivalent Airspeed
ECM	Electro-Chemical Machining
EU	European Union
FPR	Fan Pressure Ratio
HPC	High-Pressure Compressor
HPT	High-Pressure Turbine
ICAO	International Civil Aviation Organization
IOC	Indirect Operating Cost
IPC	Intermediate-Pressure Compressor
IPT	Intermediate-Pressure Turbine
ISA	International Standard Atmosphere
LCD	Lognormal Cumulative Distribution
LFW	Linear Friction Welding
LPC	Low-Pressure Compressor
LPT	Low-Pressure Turbine

MFS	Machining From Solid
MLW	Maximum Landing Weight
MoM	Method of Manufacture
MSD	Mean-Square Deviation
MTOW	Maximum Takeoff Weight
Ni	Nickel
NPV	Net Present Value
OPEC	Organization of Petroleum Exporting Countries
OPR	Overall Pressure Ratio
OWE	Operating Weight Empty
PDF	Probability Density Function
PI	Prediction Interval
R-R	Rolls-Royce plc
RPK	Revenue-Passenger-Kilometre
SBCE	Set-Based Concurrent Engineering
SL	Sea Level
SO	System Option
TET	Turbine Entry Temperature
Ti	Titanium
TOC	Total Operating Cost
UK	United Kingdom
VoT	Value of Time
ZFW	Zero Fuel Weight

kn	knots (i.e. nautical miles per hour)
l	litre
nm	nautical mile
rpm	revolutions per minute

Chapter 1

Cost Optimization

1.1 Background

1.1.1 Costing within the Aerospace Industry

Cost estimating is the process of predicting the cost of a work activity or output by interpreting historical data or knowledge, which is usually done by creating a cost model [1]. Cost modelling, as practised in industry, is nevertheless largely based on experience rather than science, because it lacks a consolidating theory [1, 2]. Cost estimation is also information intensive, as it requires knowledge capture from various disciplines and it is affected by unpredictable factors outside design, such as inflation and market conditions [1, 2]. Unfortunately, the aerospace industry is a typical example of high-tech but low-volume manufacturing, where it is very challenging to obtain well documented and comprehensible costing information [1]. Often sparse and inaccurate data increases the challenge of creating objective cost estimates and validating these [3, 4].

Parametric tools use historical data to unravel patterns and probabilistic relationships between product features and cost without having to understand the details of fabrication processes, materials and their interactions [4]. Activity-Based Costing (ABC), on the other hand, is based on the laws of physics and fundamental manufacturing knowledge, such as production operations [5]. Few quantitative cost models exist between the two ends of this spectrum because no suitable method has been found that can deal with multi-fidelity data from multiple levels of product definition [5]. The cost model presented in Chapter 4 aims to bridge the gap by making use of the synergy effects from using an ABC and a parametric model in conjunction.

In the past, aerospace product prices were simply based on cost plus profit plus contingency, as the market was not very competitive [6]. The aerospace industry was therefore not forced to fully understand and reduce its cost base. Consequently, only a few cost experts dealt with cost estimation for high-level bidding processes or detailed process-time-based models [6].

Within the last 15 years, however, market pressure from low cost airlines and reduced government defence budgets have forced aerospace companies to adapt to the conventional rule of profit, which is price minus total cost [6]. This, and the emergence of long-term ‘power-by-the-hour’ service contracts provided by companies such as Rolls-Royce (R-R), has increased the interest of gas turbine manufacturers in reducing and controlling their manufacturing costs [5].

1.1.2 Design Optimization

The design phase contributes less than 10 % to the total product cost [1]. It is nevertheless extremely important to be able to have accurate cost predictions as early as possible in the design process, because 70–80 % of the manufacturing cost is controlled during this phase [1, 7, 8].

Consequently, the ultimate goal for aircraft design is that it is driven by a balanced trade-off between cost and performance, leading to affordability and sustainability for operators over the life cycle of the aircraft [1]. The design optimization process within the aerospace industry has tended to focus on aerodynamics, weight and structural performance and over time highly reliable computational stress and fluid dynamics analysis packages have been developed [5].

Unfortunately, unit cost has rarely been included in the iterative optimization loop because it is difficult to find the true relationship between design variables and manufacturing cost [1, 3, 7]. The fact that cost predictions can only be made for a relatively well defined product means that cost estimates are typically highly inaccurate during the early stages of design. Such crude cost evaluations could lead to false results during design optimization, which is why cost models tend to only be used for a limited number of design studies [2].

The cost estimating paradox is therefore that when accurate cost information is needed during the conceptual design phase, it is not readily available. Once the design is fixed,

however, cost predictions become more reliable, leading to costly re-engineering and modification work [1, 9]. It can be concluded that the cost models that are available today are not adequate for designing aerospace systems. Industries that deal with similarly complex systems face comparable challenges, however, including civil engineering [10].

In order to generate a similar level of accuracy for cost predictions as for performance estimates, more information is required [2]. The challenge for the aerospace industry is therefore to control all aspects of cost and link these into the design decision making process during the conceptual design phase [1]. This can only be achieved by developing appropriate costing tools and integrating them into the optimization framework.

1.2 Research Motivation

This thesis presents two projects, the *System Study* and the *Component Study*, that show how cost modelling can be integrated into the various design process stages as illustrated in Fig. 1.1. While the System Study focuses on strategic gas turbine and airframe system design at the ‘Innovation & Opportunity Selection Stage’, the Component Study deals with preliminary and detailed component design and manufacturing planning during ‘Stage 1’ and ‘Stage 2’. The costing and technology aspects of the two studies are jointly covered in Chapters 1 and 2, before the methodology and results of each study are discussed separately in Chapters 3 and 4. Finally, Chapter 5 draws conclusions from the two projects and makes recommendations for future work.

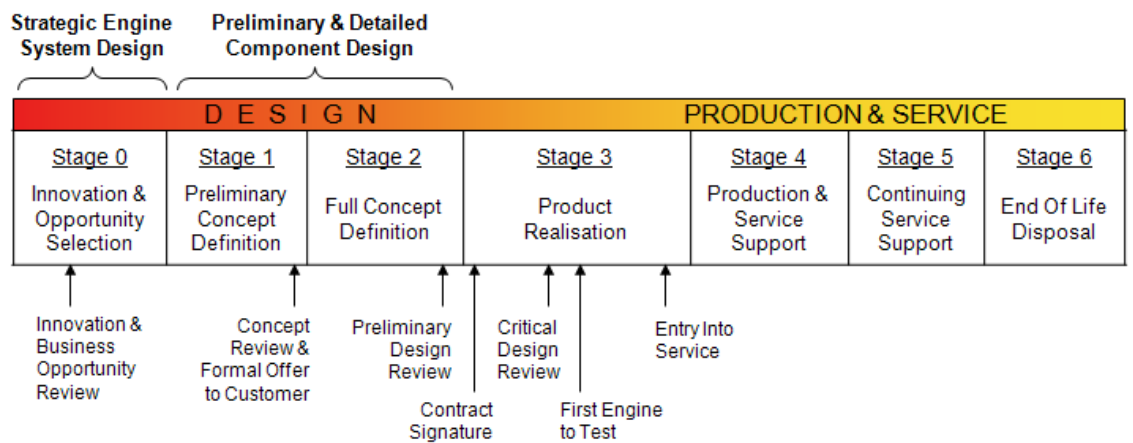


Figure 1.1: Design Phases within the Product Life-Cycle (adapted from Ref. [11]).

1.2.1 System Study

It takes around 5 years to develop a gas turbine engine, which then typically remains in production for more than two decades [11, 12]. Similar to the rest of the aerospace industry, gas turbine makers therefore have to make multi-billion investments into these large and long-term projects and it normally takes at least 15 years until the costs are recuperated [12]. Consequently, the strategic design team must make a sound prediction 30 years into the future and optimize the product in such a way that it remains competitive throughout that period.

The Advisory Council for Aeronautics Research in Europe (ACARE) [12] states: “The future is uncertain, except that changes will be rapid and marked, especially in the price of resources, and this scenario will become a normal phenomenon.” Such uncertainties led to the development of the principle known as ‘robust design’, which involves a departure from the classic search for the global optimum. Instead, objective function plateaus are sought that balance nominal performance against performance variability [13]. Thus:

*The System Study uses a ‘robust design’ methodology
to find the optimum cruise speed, gas turbine and airframe
to minimize the direct operating cost
of the next generation of short-range 150-seat aircraft
in light of uncertain oil and carbon (CO₂) prices in the Year 2030.*

Although 2030 is less than two decades away, this timeframe was chosen because 2025 to 2030 is the likely service entry window for the next generation of short-range aircraft [14]. In the 2020s, the engine system options described in Section 2.1 on page 27 will also be mature enough to potentially be used on such an airframe. No prognosis beyond the Year 2030 is made because of the unpredictability of many factors thereafter, not just oil and carbon prices, but also technological capabilities and aircraft rollout dates [15].

The significance of the System Study is reflected in the richness of the literature on the subject, some of which is captured in Table 1.1. Although as a whole the 11 references listed in Table 1.1 cover most of the work carried out in the System Study, each reference primarily focuses on one of the four sub-headings given in Table 1.1, which are discussed accordingly in the following sub-sections. Even though the System Study does not vary the aircraft capacity, the flight distance, nor the passenger number (i.e. the demand for

air travel), the uniqueness of the methodology used lies in its all-encompassing approach to attempt to truly optimize the different engine and airframe system options to allow a fair quantitative comparison. For this reason, the model created to carry out the System Study was written entirely in MATLAB without using existing commercial or open source code.

Table 1.1: System Study Literature Review.

Project Objectives	System Study	Cost			Environment			Uncertainty		Performance		
		Ref. [16]	Ref. [17]	Ref. [18]	Ref. [19]	Ref. [20]	Ref. [21]	Ref. [22]	Ref. [23]	Ref. [24]	Ref. [25]	Ref. [26]
comparison of different gas turbine systems	✓	✗	✗	✗	✗	✗	✓	✗	✓	✓	✓	✓
uncertain future fuel and CO ₂ prices	✓	✗	✗	✗	✗	✗	✗	✓	✓	✗	✗	✗
optimization based on operating cost	✓	✗	✗	✗	✓	✓	✗	✓	✗	✗	✗	✗
trade-off between various engine and airframe design parameters	✓	✓	✓	✗	✓	✓	✓	✓	✗	✗	✗	✗
variable aircraft capacity	✗	✗	✗	✗	✗	✓	✗	✗	✗	✗	✗	✗
various flight distances	✗	✗	✗	✗	✗	✓	✗	✓	✓	✗	✗	✗
impact of cruise speed on aircraft utilization	✓	✓	✓	✗	✗	✓	✗	✗	✗	✗	✗	✗
influence of cruise speed on the modal shift	✓	✗	✓	✗	✗	✗	✗	✗	✗	✗	✗	✗
passenger value of time	✓	✗	✓	✗	✗	✗	✗	✗	✓	✗	✗	✗
variable passenger numbers	✗	✗	✗	✗	✗	✗	✗	✓	✓	✗	✗	✗

Cost

In 1940, Mentzer and Nourse [16] analytically investigated the trade-off between the fixed and variable cost of civil aircraft, i.e. the balance between aircraft acquisition and fuel cost, by improving aerodynamic efficiency and specific fuel consumption. Their paper also discusses the effect of the passenger value of time and the cruise speed on the aircraft's utilization and operating cost.

This discussion is taken further in the paper by Morrison [17] from 1984 that defines aircraft design optimization as a compromise between the cost of fuel and the cost of time of the aircraft, crew and passengers. It argues in the historical context of the higher fuel prices in the 1970s than in the 1960s, that engineers would subsequently trade the cost of

time for the cost of fuel by designing aircraft that are optimized for lower cruise speeds. As induced drag becomes more critical than parasite drag at lower cruise speeds, these aircraft would have larger wing spans.

The review paper by Lee et al. [18] analyses historical aircraft performance, cost and emissions data and discusses future trends. Just like Mentzer and Nourse [16] and Morrison [17], Lee et al. [18] does not provide practical gas turbine and airframe system design solutions for the future, as indicated in Table 1.1.

Environment

The next three papers listed in Table 1.1 investigate the trade-off between aircraft emissions and cost. While Antoine et al. [19] and Bower and Kroo [20] both use a genetic algorithm to create a Pareto Front that highlights the conflict between noise, NO_x and operating cost, Kernstine et al. [21] investigates which new aircraft technologies reduce the environmental impact most effectively in terms of cost-benefit ratios. Unfortunately, the three papers do not state what the optimum compromise between these conflicting targets would look like, nor what the practical incentive is to implement it.

Uncertainty

In contrast to the other papers, Mavris et al. [22] and Ryerson and Hansen [23] examine how uncertainty affects the optimum engine system. Mavris et al. [22] applies this to a turbofan aircraft using probability distributions, to not only model uncertain fuel prices, but also aircraft production quantities, aircraft utilization and other economic factors. By subsequently varying several aircraft design parameters, Mavris et al. [22] creates an operating cost distribution for the various designs and effectively selects robust solutions by only choosing designs which have a 70 % chance of meeting various design and cost constraints. As Table 1.1 shows, Mavris et al. [22] does not explore different engine options and the value of time.

Instead of using probability distributions to model uncertainty, Ryerson and Hansen [23] plots the operating cost of a narrow body jet, a regional jet and a turboprop aircraft against a range of fuel prices and flight distances and explores the effect of the fuel price on the passenger numbers. It concludes that as fuel prices increase, the turboprop aircraft offers lower operating costs over a wider range of distances than the two jet aircraft. Although

the value of time is included in the analysis, the paper does not provide an insight into the system design trade-offs involved nor optimizes them. Just like Mavris et al. [22], it also ignores the modal shift and aircraft utilization.

Performance

Guynn et al. [24], Peters [25] and Hendricks and Tong [26] compare direct drive and geared open rotors to geared and conventional turbofan designs in terms of thrust, specific fuel consumption, noise and weight. Unlike the System Study, the three papers only present one design point for each system.

1.2.2 Component Study

There is limited literature on models that estimate the manufacturing cost of a design, also known as unit cost, using parametric process time estimation in combination with a bottom-up calculation of the resources consumed by every manufacturing process:

*While the Component Study's bottom-up Factory Cost Model
determines the £-per-hour cost rate of every manufacturing operation,
the parametric Scalable Blisk Cost Model
uses the correlation between historical operation times
and integrally bladed disc (blisk)¹ design data
to estimate the operation times of a future blisk based on its design parameters.
The unit cost of the new blisk design is then predicted
by multiplying the regressed operation times by the respective cost rates
and adding up the resulting costs.*

A similar hybrid cost model that combines bottom-up and parametric costing is described by Qian and Ben-Arieh [27]. It estimates the machining times by multiplying the volume of material removed by the machine's material removal rate. Unfortunately, this approach is restricted to simple cylindrical parts as it depends on volumetric equations to calculate the amount of material removed. These equations would have to be changed manually in order to predict the cost of other geometries.

¹Blisks are used by the aerospace industry in gas turbine compressors and are described in more detail in Section 2.2.1 on page 36.

Although the Scalable Blisk Cost Model is also confined to a limited range of integrally bladed disc designs, the model accounts for uncertainty and is based on a more complex method of manufacture where more than half of the operations are only carried out under certain design conditions. Furthermore, the number of extra features, such as holes and seals, is not restricted. The Factory Cost Model itself has the flexibility to determine the costs of any factory or manufacturing cell.

1.3 System Costing

1.3.1 Fuel and Carbon Prices

Fuel Price Variability

Between 1971 and 2009, the 12-month average oil price fluctuated between \$17 and \$99 per barrel in 2012 prices, which in turn caused the fuel cost fraction to vary between 14 % and 42 % of the Direct Operating Cost (DOC)² of U.S. passenger airlines [28, 29], as Fig. 1.2 shows. In July 2008, for example, jet fuel prices peaked at \$4.33 per U.S. gallon, but plummeted to \$1.28 by late December that year [30]. Similarly, between June 2014 and January 2015 the oil price dropped from around \$110 to below \$50 per barrel [31].

This short-term volatility is caused by market inelasticity both on the supply and the demand side, which means that small changes on either side of the economic equation have a large effect on price [32]. Figure 1.2 indicates that the first oil price peak between 1980 and 1981 was mainly due to political events, including the Organization of Petroleum Exporting Countries (OPEC) Oil Embargo of 1973, the Iranian Revolution in 1979 and the Iraq-Iran War in 1980 [33]. Although several more wars in the Middle East contributed to the second peak in 2008, financial speculation and an increasing demand from China and India had a significant impact on the oil price as well [33]. Figure 1.2 also illustrates that, unlike the high-bypass turbofan, the open rotor concept designs were developed as oil prices were dropping which is why they never went into full production [34]. The turbofan and the open rotor, also known as the unducted fan or propfan, are covered in more detail in Section 2.1 on page 27.

²As implied by the name and defined in Table 1.2 on page 15, Direct Operating Cost is the cost directly incurred by operating an aircraft, i.e.: (1) the cost of fuel; (2) engine and airframe depreciation and maintenance costs; (3) landing, navigation, crew and ground charges.

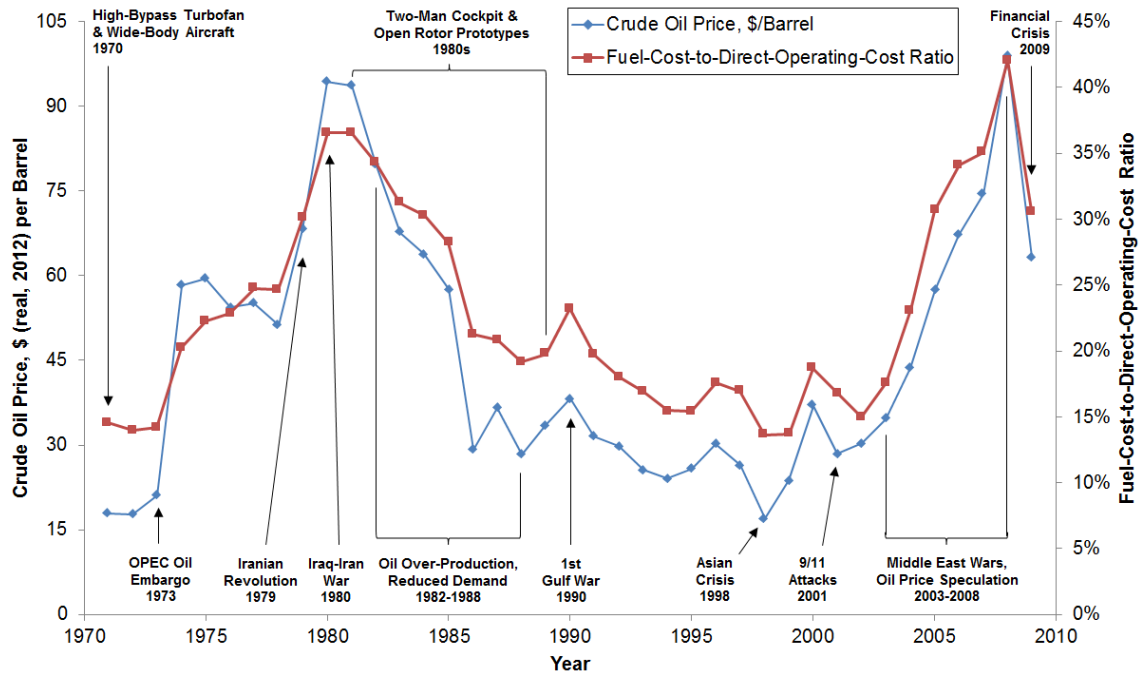


Figure 1.2: Correlation Between Oil Price and Direct Operating Cost from 1971 to 2009 (based on data from Refs. [28, 29, 33]).

Figure 1.3 displays the Direct Operating Cost of U.S. airlines per Revenue-Passenger-Kilometre (RPK) in 2012 prices, as well as the DOC's three constituent cost elements [28, 29]. While the engine and airframe depreciation and maintenance costs and the landing, navigation, crew and ground charges were the bigger cost factors in the past, they have been declining steadily since 1971. Although the fuel cost has, on average, also decreased over the last 30 years, it has varied significantly because of the volatility of the oil price. While the standard deviation of the yearly engine and airframe depreciation and maintenance costs is 0.62 U.S. cents (¢) per RPK with respect to the linear trend, the standard deviation of the fuel cost of 1.27 ¢ /RPK is twice as high.

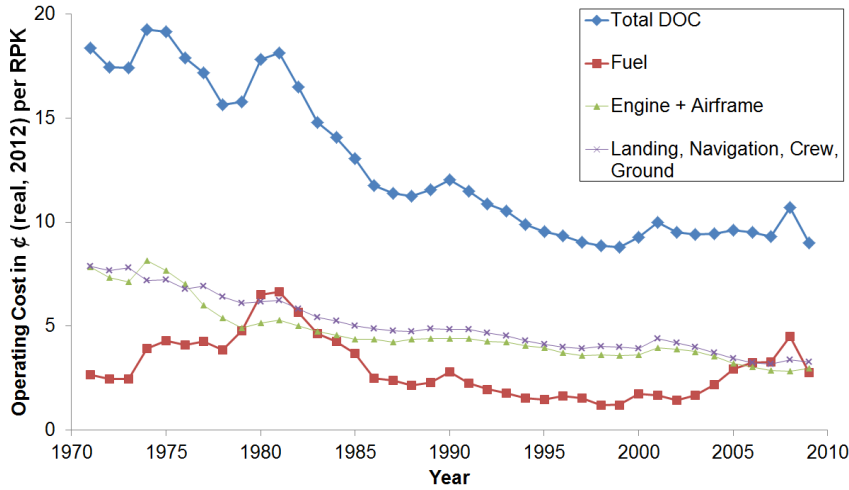


Figure 1.3: Direct Operating Cost Elements from 1971 to 2009 (based on data from Refs. [28, 29]).

Although the oil price in 2008 was six times higher than in 1971, Figure 1.3 highlights that the Direct Operating Cost per RPK halved during that period because of significant efficiency improvements, including:

- The average utilization of U.S. aircraft, for example, increased from 50 % in 1971 to 80 % in 2009 [28].
- Continuously improving engine efficiencies, including the service entry of the high-bypass turbofan in 1970, lighter and more aerodynamic airframes and other technologies reduced the total energy intensity of airliners by more than 60 % between 1970 and 2000 [15].
- The rollout of the first twin-aisle aircraft, the Boeing 747, in 1970 enabled the average capacity of planes with more than 90 seats to increase by 21 % in North America, for example, from 122 seats in 1972 to 148 in 2008 [30].
- The introduction of the two-man cockpit in the 1980s and the increasing market share of low-cost airlines since the 1970s have contributed to reduced operating costs [35, 36, 37].

According to various forecasts, oil prices will continue to increase and exhibit increasing volatility [12, 32]. The uncertainty of future oil prices is reflected by the U.S. Energy Information Administration's (EIA) large price disparity between the best and worst case

scenarios for 2030 of around 73 and 196 \$/barrel in 2012 prices, respectively [29, 38]. The United Kingdom (UK) Department of Energy & Climate Change concurs with that prediction [39]. As in the past, the impact of increasing fuel prices can be minimized by efficiency gains, which, as the System Study shows, is partly made possible by advanced gas turbine technology in combination with an airframe optimized for the most cost-efficient cruise speed.

Aircraft Emissions

Since the Wright brothers took to the skies over 100 years ago, aviation has been powered by fossil fuels, just like 94 % of the rest of the transport industry [40]. According to ACARE³ [12], global CO₂ equivalent emissions have to drop by 50–85 % by 2050 relative to the Year 2000 to ensure that pre-industrial temperatures are not exceeded by more than 2.0 to 2.4 °C on average. In order to meet this target “all industry sectors, including aviation, need to contribute their share of emissions reduction” [12].

In 1992, aviation accounted for 2 % [12, 20] of global CO₂ emissions and 3.5 % [20, 41] of the global anthropogenic radiative forcing⁴. While air traffic is expected to grow approximately 5 % per year [12, 20, 30], specific fuel consumption is projected to decrease by only 0.7–1.5 % per annum [12, 15]. As this results in a net increase in aircraft emissions, aviation’s share in global man-made radiative forcing is predicted to increase to 5 % by 2050 [12, 20, 41]. Considering that the aviation industry has agreed to pay its full external costs [41], the only way to legitimize and secure the aviation business in the long-run is through a “clean approach” [12] where growth and ecological damage are uncoupled.

Carbon Trading

In 2009, the UK’s House of Commons Transport Committee [14] stated that the cost of jet fuel does not provide enough incentive to achieve significant emission reductions and encourage airlines to operate the latest generation of aircraft. An additional charge is

³The Advisory Council for Aeronautics Research in Europe

⁴According to Refs. [15] and [42], radiative forcing is measured in W/m² and is a surrogate for the global mean surface temperature. It is used to compare the contribution of changes in individual atmospheric constituents (forcing agents) to the energy imbalance of the earth-atmosphere system since 1750, i.e. pre-industrial times.

therefore required whereby 1 metric-ton of CO₂ emissions⁵ would have to cost between €100 and €300 [14], i.e. around \$131 to \$392 in 2012 prices [29, 43].

As economic instruments are more cost-efficient and flexible in comparison to fixed regulation [44], the British government, the aviation industry as well as environmental groups believe that for the international airline industry, international emission trading across all industrial sectors is the best solution [41, 45]. Since 2012, all flights within the European Union (EU) with a maximum take-off weight above 5,700 kg are therefore obliged to participate in the EU's Emission Trading Scheme [44, 46].

Considering that CO₂ was traded at approximately €6 (\approx \$8) per metric-ton in 2014 [43, 47] shows that currently the EU Emission Trading Scheme has a relatively small impact on ticket prices in comparison to the fuel cost. However, the UK's Committee on Climate Change published low- and high-price scenarios for 2030 of £35 and £105 (around \$62 to \$186) per metric-ton of CO₂ in 2012 prices [15, 29, 43].

1.3.2 Multi-Disciplinary Optimization

In theory, engineering design simply involves finding and analysing all conceivable designs and then selecting the best one [48]. In order to find the best solution objectively, however, all significant design consequences have to be compared on an equal basis [49, 50]. Most real design problems have more than one objective that has to be addressed, for example minimizing cost while meeting a particular quality standard. These goals and constraints often conflict, which means that the objective functions have to be traded off in some way [50].

There are several multi-disciplinary optimization methods available, including:

1. *Surrogate Objective* [20]: Instead of taking many different objective functions into account, a surrogate is chosen that best mimics the objectives. For gas turbine design, for example, this is often the specific fuel consumption.
2. *Objective Aggregation* [51]: All objectives are weighted and combined into one formula.
3. *Pareto Optimization* [13, 51]: This technique is based on Objective Aggregation but optimizes the design for a range of different objective function weightings. The

⁵Based on U.S. passenger airlines data [28], in 2009 an aircraft had to fly approximately 5,400 mi on an 11-hour flight from Seattle to Beijing, for example, in order to emit 1 metric-ton of CO₂ per passenger.

line that connects the various optimum solutions on a multivariate plot, where one objective is plotted against the other, is known as the Pareto Front. Each point on the front is said to be ‘non-dominated’, that is, an objective can only be improved at the expense of another. As the Pareto Front provides no guidance as to which of the points on the line is the ‘best’, the designer has to choose an objective function weighting in order to select his optimum solution.

Although monetary value is a form of objective aggregation, there are many ways of measuring and optimizing it, as the following sub-sections show.

Profit

Airlines try to increase their profit by maximizing their revenue and reducing their operating costs. They consequently purchase aircraft (i.e. airframes and propulsion systems) that promise a greater profit than investing the money in other assets, i.e. competing aircraft designs or even different business ventures or financial products [52]. The profitability of the aircraft in comparison to other investments can be calculated using the Net Present Value (NPV) formula presented in Eq. 1.1, which is derived from Refs. [49] and [52]. It is the sum of the present values of the yearly operating profits (i.e. the yearly revenues minus the total operating costs) generated during the service life of the aircraft [52]. The depreciation of the aircraft is not included in the operating costs, because it is accounted for in the aircraft acquisition cost which is subtracted separately. While the airline revenue is primarily the sum of the passenger and freight tickets sold, the discount rate is the annual interest other investments would generate [52]. Operating cost is covered in more detail in the next sub-section.

$$NPV_P = \sum_{t=1}^L \left[\frac{R_t - TOC_t}{(1 + i_{dis})^t} \right] - AAC \quad \text{where} \quad \begin{array}{ll} NPV_P &= \text{net present value of profits} \\ L &= \text{aircraft service life in years} \\ t &= t^{\text{th}} \text{ year of service} \\ R_t &= \text{revenue for year } t \\ TOC_t &= \text{total operating cost for year } t \\ &\quad (\text{excl. aircraft depreciation}) \\ i_{dis} &= \text{discount rate} \\ AAC &= \text{aircraft acquisition cost} \end{array} \quad (1.1)$$

The gas turbine and airframe manufacturers are more likely to maximize their sales and hence their profits if they design an aircraft that maximizes the profit of the airlines. The best aircraft design can therefore be found by maximizing Eq. 1.1. Net Present Value consequently enables multi-disciplinary optimization by expressing the aircraft’s

specification in terms of monetary value. Rather than applying subjective weightings to incompatible design requirements, like specific fuel consumption and manufacturing cost where the optimum trade-off is not immediately apparent, the invisible hand of the market conducts the trade-off. This means that when specific fuel consumption is converted into fuel cost, the fuel price is used as the weighting parameter.

Operating Cost

The author believes that the all-encompassing nature of Eq. 1.1 is its strength but also its weakness, because a large dataset is required in order to model the entire service life of the aircraft. In addition, it is particularly difficult to estimate the airline revenue because ticket prices, passenger numbers and freight volume are controlled by many variables outside the engineering realm, including economic, geographic, political and time factors [37]. Although fuel and carbon prices in 2030 are similarly unpredictable as airline revenues, the fuel and carbon costs of an airline are also influenced by the design of the aircraft through its fuel efficiency. Assuming that aircraft safety, noise and passenger appeal are not significantly altered, the only aircraft performance metric that has an impact on the revenue is the cruise speed. It affects the ticket prices and the number of tickets sold through the value of time and the modal shift, respectively. The value of time and the modal shift are discussed in more detail in the next two sub-sections.

Rather than modelling Eq. 1.1 in its entirety and obscuring the results by factors that are not related to the design of the aircraft, the focus was laid on the total operating cost. According to Doganis [53], total operating cost can be divided into direct and indirect operating costs, as shown in Table 1.2.

Table 1.2: Direct and Indirect Operating Cost (adapted from Ref. [53]).

Direct Operating Cost	Indirect Operating Cost
<ul style="list-style-type: none"> • aircraft depreciation (represented by AAC in Eq. 1.1) • interest on aircraft • aircraft insurance • aircraft maintenance • fuel and oil • flight crew • cabin crew • airport charges • en-route charges 	<ul style="list-style-type: none"> • ground buildings, equipment and transport • ground staff • ticketing, sales and promotion • administration

The Indirect Operating Cost (IOC) is primarily dependent on how the airline is run and is therefore difficult to estimate [52, 54]. For these reasons, IOC is usually ignored by the aircraft designer [54] and consequently it was also not included in the System Study.

The Direct Operating Cost (DOC), on the other hand, is significantly affected by the design of the aircraft [54]. As a figure of merit in economic analysis, aircraft comparison and design trade-off studies, DOC is usually expressed in \$ per seat-mile or \$ per revenue-passenger-kilometre flown [52]. This accounts for the effect the load factor and the cruise speed have on the productivity of the aircraft. As DOC is effectively the value of time (aircraft and crew) and resources consumed (fuel and oil), it could also include the passengers' value of time [17]. Table 1.2 indicates that DOC includes aircraft depreciation, which is equivalent to dividing Eq. 1.1's aircraft acquisition cost by the aircraft service life, assuming that a simple linear depreciation method is used over the operating life of the aircraft. Eq. 1.2 shows that the NPV of the Direct Operating Costs could be calculated in a similar way as for the profits in Eq. 1.1. The DOC for only one year of operation was calculated, however, because the author believes that the work involved in predicting uncertain cost data for every year of service would not improve the accuracy of the result. The futility of fully modelling both Eq. 1.1 and Eq. 1.2 is aggravated by the discount factor, which has the effect that costs incurred at the end of the service life have a diminishing effect on the NPV. A further reason why Eq. 1.2 was not used in the System Study is that the discount factor is another variable that is independent of the aircraft design.

$$NPV_{DOC} = \sum_{t=1}^L \left[\frac{DOC_t}{(1 + i_{dis})^t} \right] \quad (1.2)$$

Based on the arguments presented above, which are summarized in Table 1.3, the author believes that DOC covers all the aircraft-design related aspects of Eq. 1.1 and is therefore a good substitute for the net present value of profits.

Table 1.3: Comparison of NPV_P and DOC Parameters.

Parameter	NPV _P	DOC
aircraft service life	t, L	aircraft depreciation
ticket price	R	value of time (the only ticket price factor directly affected by the aircraft design, assuming that aircraft safety, noise and passenger appeal are not altered)
number of tickets sold	R	seat miles or RPK
Direct Operating Cost	TOC	included
Indirect Operating Cost	TOC	not included (not affected by the aircraft design)
discount factor	i_{dis}	not included (not affected by the aircraft design)
aircraft acquisition cost	AAC	aircraft depreciation

Cost of Time

Value of Time (VoT) is a concept often found in cost-benefit analyses of transport services and infrastructure [55]. In transport, it reflects how much travellers are willing to pay to save time during a journey and, conversely, how much monetary compensation they would expect for slow or delayed transport [17, 55]. As with ticket prices, the value of time depends on many factors, including the length, time, location and itinerary of the journey, the mode of transport, the fare class, the purpose of the trip and other socio-economic characteristics of the passenger [55, 56]. As the value of time is an opportunity cost, it only applies if the passenger has the *opportunity* to choose a faster mode of transport, i.e. in this case a competing aircraft with a higher cruise speed [17, 55, 56].

For business passengers, the value of time is equivalent to their rate of pay minus the value of the work done during the journey [55]. The value of non-working time can be found by analysing the transport choices leisure travellers make, based on journey time and cost [55]. Business passengers generally value time higher than leisure travellers [57], which is reflected by ITA's [56] and EUROCONTROL's [58] estimates for air travel: while business passengers' average value of time is around €67 (\approx \$82) per hour in 2012 prices,

it is only €26 (\approx \$32) per hour for tourists. Taking the passenger distribution [56, 58] into account, this gives an average value of time of €48 (\approx \$58) per hour.

Modal Shift

In order to determine how the market share of the aircraft is affected by its cruise speed, official travel time data from airline websites was collected that offered transport services between 40 European city pairs. To account for actual door-to-door times, three hours were added to the flight times, assuming that it takes one hour to get to the airport, one hour to check in and board the aircraft and one hour to travel to the final destination [59]. Figure 1.4 shows these 40 door-to-door times plotted against the direct distance between the city pairs. These data points were then used to generate the linear regression line that is also displayed in Fig. 1.4. While the inverse of the regression line's gradient reflects today's average cruise speed of 812 km/h (\approx 500 mph), the intercept of 3 hours and 40 minutes is the sum of the regressed idle time of the flights (40 minutes) and the three hours added by the author. The regression line forms the basis of the second graph in Fig. 1.4, which shows how the average door-to-door speed increases with distance.

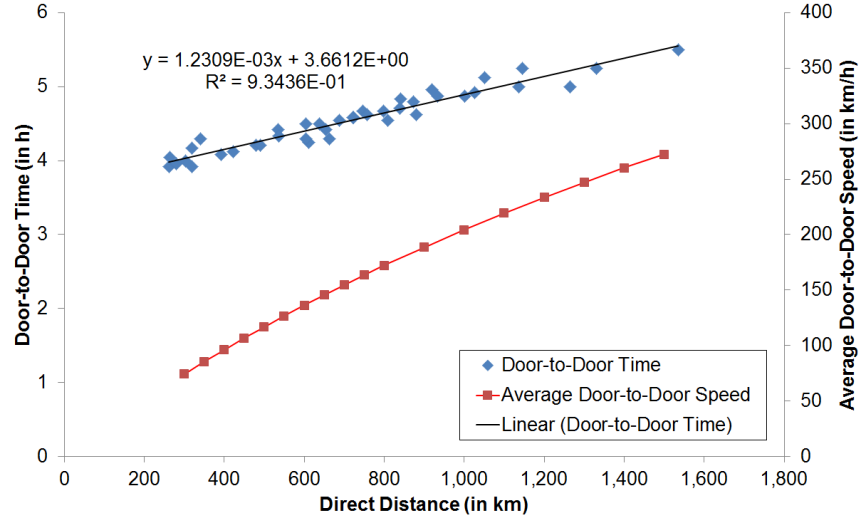


Figure 1.4: Total Flight Journey Time Vs. Direct Distance.

Figure 1.5 illustrates how the market share of the aircraft, the high-speed train and the car changes with distance, based on a diagram presented by Jenkinson et al. [54]. While the market share graphs of the aircraft and the car were constructed using the Lognormal Cumulative Distribution (LCD), the train curve simply represents the remaining market

share. The distributions would probably look very different for city pairs without a high-speed train connection. By including high-speed rail rather than other slower modes of transport that compete less with air travel, however, a conservative estimate about the market share of the aircraft is being made.

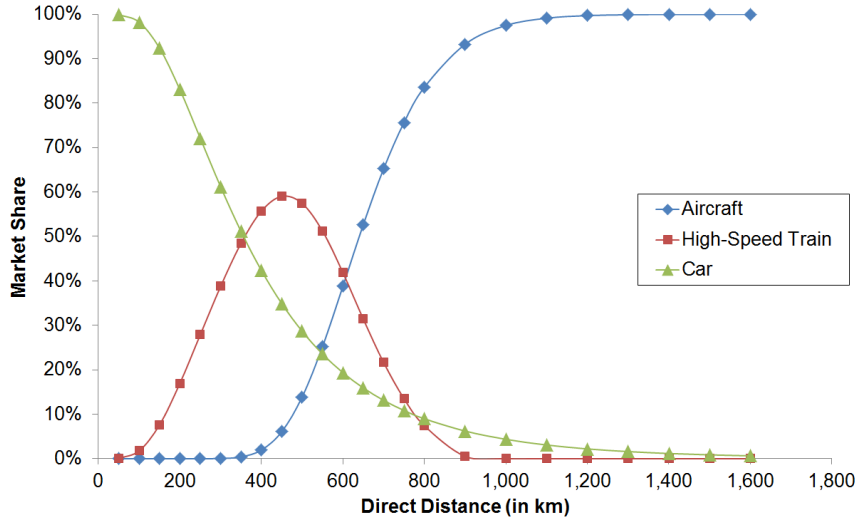


Figure 1.5: Aircraft, High-Speed Train and Car Market Share Vs. Direct Distance (data based on Ref. [54]).

The market share data shown in Fig. 1.5 was used in conjunction with the speed-distance relationship in Fig. 1.4 to derive how the aircraft's market share is related to its average door-to-door speed. Rather than using Fig. 1.5's LCD based on distance, the aircraft's market share can also be described by a LCD as a function of the average door-to-door speed, as Fig. 1.6 indicates that the two distributions overlap almost perfectly.

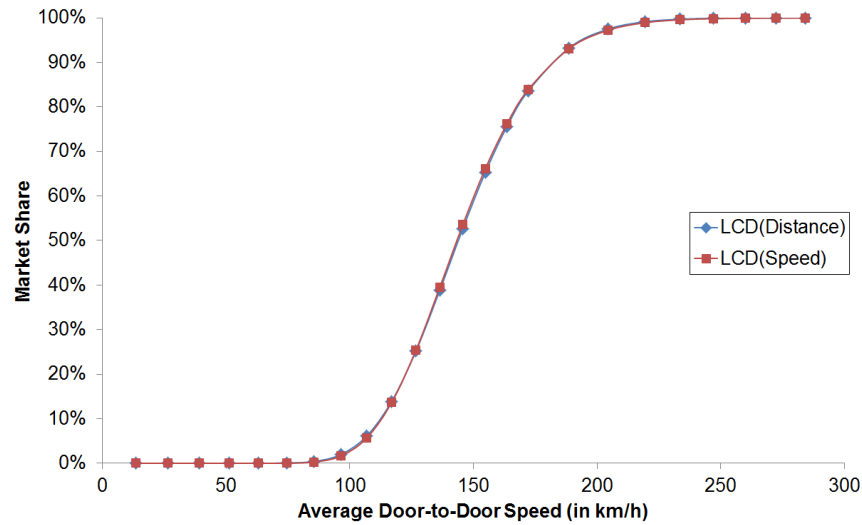


Figure 1.6: Aircraft Market Share Vs. Average Door-to-Door Speed.

Assuming that the market share of the aircraft is dependent on the average door-to-door speed, the four graphs in Fig. 1.7 were created by first calculating the average door-to-door times for the various cruise speeds and direct distances, and then using these in conjunction with Fig. 1.6's speed-based LCD to obtain the respective market shares. For cruise speeds above 600 km/h (≈ 370 mph), Fig. 1.7 clearly shows that the aircraft becomes competitive at a direct travel distance of around 400 km (≈ 250 mi) and reaches a market share above 90 % at 1,000 km (≈ 620 mi) almost regardless of the cruise speed. Between 400 and 1,000 km, where the aircraft competes most with the other forms of transport, however, the cruise speed does affect the market share.

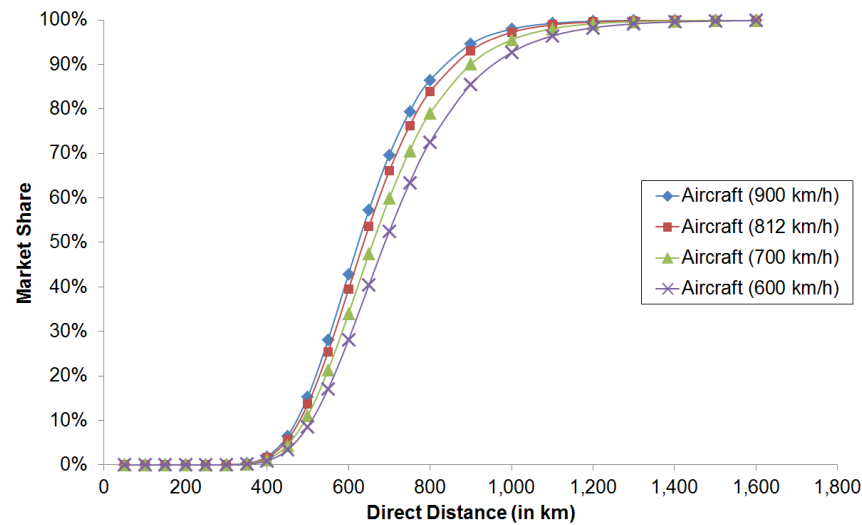


Figure 1.7: Impact of Cruise Speed on Aircraft Market Share.

According to Airbus [30], 70 % of single-aisle aircraft will fly 1,850 km (\approx 1,150 mi) or less in 2028. This information, together with the assumption that no 150-seater flight will be less than 250 km (\approx 150 mi) but 5 % will be less than 500 km, produced the LCD shown in Fig. 1.8. The LCD was capped at a flight distance of 3,000 nautical miles (\approx 5,550 km / 3,450 mi) because that is the likely design range for the next-generation 150-seater [60]. Based on 10,000 stochastic samples of this distribution, the mean flight distance is 1,546 km with a standard error⁶ of 10.2 km. To save computing time, only the average flight distance was used to find the optimum engine and airframe design.

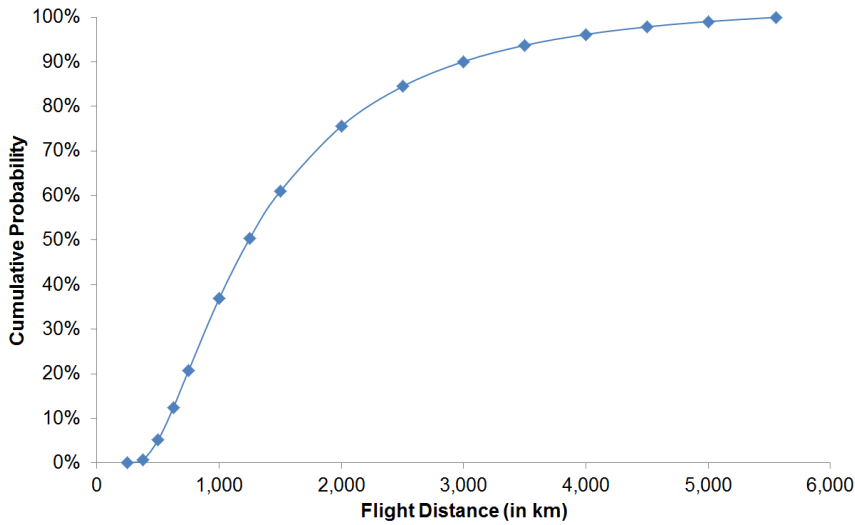


Figure 1.8: Single-Aisle Aircraft Flight Distance Distribution.

As Fig. 1.8 indicates that less than 40 % of the single-aisle flights are less than 1,000 km, Fig. 1.9 illustrates that the reduced market share in the 400–1,000 km segment only starts to affect the cumulative market share of the aircraft significantly if the cruise speed falls below 400 km/h. Here the cumulative market share is expressed in relative passenger-kilometres, i.e. the RPKs flown at the various speeds are divided by the RPKs flown at today’s cruise speed of 812 km/h.

⁶The standard error is a measure of the precision of the estimate and is defined as the standard deviation of the distribution divided by the square root of the sample number [61].

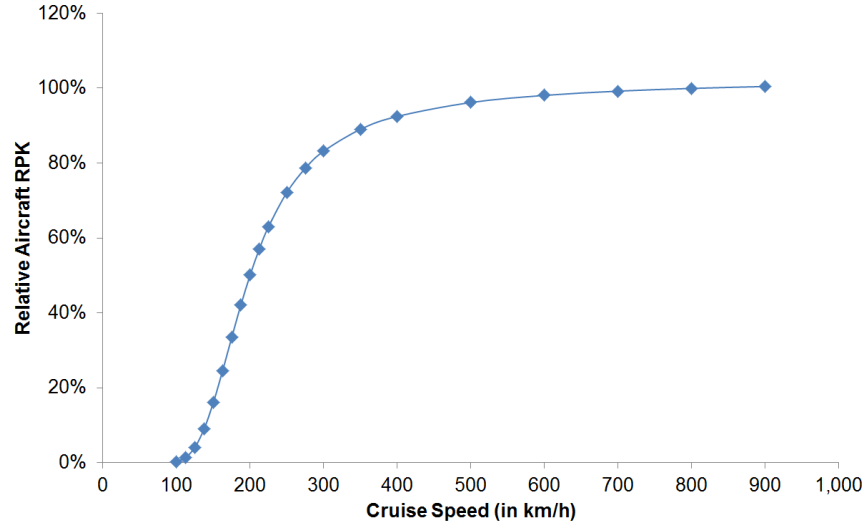


Figure 1.9: Effect of Cruise Speed on 150-Seater RPK.

Robust Design

There are several metrics for measuring robustness in which the trade-off between the mean and the variability of the objective function is weighted differently. While ‘minimax’ optimization involves minimizing the maximum value and is therefore a conservative approach because it optimizes the worst-case scenario, Bayes Principle focuses on the average-case scenario by simply minimizing the mean [13]. In this study, the Mean-Square Deviation (MSD), defined in Eq. 1.3, was minimized because it takes both the mean and the variability into account and is therefore a compromise between the other two approaches. Eq. 1.3 is adapted from Keane and Nair [13] where M represents the sample number and y_j is the j^{th} sample of the objective function.

$$MSD = \frac{1}{M} \sum_{j=1}^M y_j^2 \quad (1.3)$$

Although the reader might expect a slower but more fuel-efficient turboprop to produce the most robust design, the optimum solution is not that straightforward because of the following design trade-offs:

- As the cruise speed affects aircraft utilization, the optimization loop has to trade productivity against fuel and carbon costs [17].
- Expensive gas turbine and airframe technology tends to reduce fuel consumption. Fuel and carbon costs therefore have to be balanced against acquisition cost [17].

- A small wing area reduces parasite drag which tends to improve cruise performance but it leads to higher takeoff and landing speeds which requires more powerful engines [17].

The Airbus A380 has a much larger fan that increases fuel burn by 1–2% in order to meet night-time noise restrictions at London Heathrow airport [41]. This shows that there is also a complex trade-off between emissions and noise [62]. Noise is not included in the optimization loop, however, because of the complexity of predicting it as well as estimating its impact on the operating costs in 2030. Considering that even the open rotor is likely to meet the International Civil Aviation Organization (ICAO) Chapter 14 standard, that will take effect in 2020, shows that noise is unlikely to be a critical design factor [63].

1.4 Component Costing

1.4.1 Activity-Based Costing

Before the automation of production lines, the direct costs, including labour and material, dominated the expenses of running a factory [1, 64]. Many factory cost models therefore allocated machine depreciation and other indirect costs to a product according to the labour hours spent on the item [1, 64].

Since the introduction of industrial robots in the 1960s, however, machine depreciation costs have increased dramatically, while labour time has decreased in relation to the total production hours [1]. This means that the indirect costs, also known as factory overheads, now constitute the major part of the total production costs [1, 64, 65]. As overheads are almost independent of factory utilisation and therefore labour time, many companies are discovering that traditional accounting methods are too aggregated and distorted to support decision making in costing [27, 65, 66]. If production volume is used to allocate overheads for example, then high-volume products are likely to receive an excessively high fraction of the overheads and will therefore subsidise the low-volume products [65].

Kaplan and Cooper consequently introduced Activity-Based Costing (ABC), also known as bottom-up costing, in the 1980s as an alternative to the classic costing techniques [66]. ABC can account for indirect costs more realistically by costing the time and resources spent on each activity in the manufacture of a product [27, 66]. This means that the depreciation cost of a machine is converted into a £-per-hour cost rate that is allocated

to the individual products the machine processes, while the setup costs of a production batch will be distributed across the batch [65].

Figure 1.10 is a simple example of how much the unit costs of two parts, derived from an average factory cost rate for the depreciation of two machines, can diverge from the true unit costs calculated using ABC. The advantages of ABC therefore are:

- ABC provides more logical, detailed and hence more comprehensive and accurate estimates of cost, especially when overhead costs are significant or when the product range is very diverse [27, 64, 67].
- The cause and effect of every activity is understood, which allows the identification of value and non-value added manufacturing operations and how resources are consumed [1, 27, 64, 66, 67, 68].

The drawbacks of such an in-depth breakdown of cost are:

- A significant amount of very specific and accurate data is required [1, 2, 27]. This means that a detailed design definition is needed that is usually not available during the conceptual design phase [2].
- Developing and implementing such an accounting system is time consuming and requires expert knowledge [1].

Description	LFW Machine	Polishing Machine
Investment Cost (in £)	10,000,000	100,000
Depreciation Period (in yr)	10	10
Part 1 Operation Time (in hr)	5	10
Part 1 Annual Production Rate	400	
Part 2 Operation Time (in hr)	2	1
Part 2 Annual Production Rate	800	
Machine Cost Rate (in £/hr)	$\frac{10,000,000}{10 \times (5 \times 400 + 2 \times 800)} = 277.78$	$\frac{100,000}{10 \times (10 \times 400 + 1 \times 800)} = 2.08$
Factory Cost Rate (in £/hr)	$\frac{10,000,000 + 100,000}{10 \times ((5 + 10) \times 400 + (2 + 1) \times 800)} = 120.24$	
Description	Part 1	Part 2
Unit Cost (in £) based on Factory Cost Rate	$120.24 \times (5 + 10) = \mathbf{1803.57}$	$120.24 \times (2 + 1) = \mathbf{360.71}$
Unit Cost (in £) based on Machine Cost Rate, i.e. ABC	$277.78 \times 5 + 2.08 \times 10 = \mathbf{1409.72}$	$277.78 \times 2 + 2.08 \times 1 = \mathbf{557.64}$
Unit Cost Error based on Factory Cost Rate with respect to ABC	$\frac{1803.57 - 1409.72}{1409.72} = \mathbf{27.9\%}$	$\frac{360.71 - 557.64}{557.64} = \mathbf{-35.3\%}$

Figure 1.10: Conventional Vs. Activity-Based Costing.

1.4.2 Parametric Costing

A parametric Cost Estimating Relationship (CER) establishes a relationship between cost and one or more input parameters that affect cost, often defined using a regression model based on historical data [1, 27, 67, 69]. The following criteria are important in selecting the right cost drivers:

- They have to be statistically independent of one another and logically related to cost [1, 70].
- The parameters have to be known with a reasonable level of confidence at whatever stage of the product's life-cycle a cost estimate is needed [1, 70].
- Only those variables that best explain cost should be selected to minimize correlation effects and reduce the impact of the cumulative ambiguity of these parameters on the uncertainty of the cost prediction [67, 70].

Parametric models are generally better suited to estimate recurring costs, i.e. unit costs, than non-recurring research and development costs because the former are less sensitive to programme peculiarities [71].

Advantages

Parametric cost estimation was first used by the U.S. government during the Second World War to quickly agree on unit prices for military aircraft based on their weight [5, 72]. Since then, associative cost models have become very common within aerospace because they require few inputs to achieve reasonable accuracy [70]. The advent of statistical methods, such as regression, have contributed to the popularity of the CER because regression analysis also allows the statistical accuracy of the correlation between cost and the cost-driving parameters to be determined [1]. Regression therefore enables the cost model to be used as both an analytical and a predictive tool [10], and can also highlight data outliers which is ideal for validating scaling rules and the underlying data [73].

While the ABC approach requires detailed knowledge of the manufacturing processes involved, this is not the case for parametric cost models [70]. The latter treats historical costs as facts and the manufacturing detail that generates the costs does not have to be considered [2, 3]. Other advantages are that CERs are quick and easy to implement and that non-technical experts can apply the method, even during the early stages of design

when resources are limited [1, 27, 67, 70]. In addition, parametric cost models allow the inclusion of cost as a variable in system design tools and also enable the uncertainty of the predictions to be quantified [1, 67, 74, 75].

Resolving the Disadvantages

A major drawback of the CER is that historical cost data has to be carefully normalised to eliminate the effects of inflation, exchange rates, technology levels, market forces, production volumes and varying manufacturing performance [1, 2, 67, 69]. As the Scalable Blisk Cost Model discussed in Section 4.2 on page 114 is based on the data from a single generation of one component family where only the design of each blisk differs, the data did not have to be normalised. The cost of a new blisk design can be predicted without having to alter the scaling rules as long as it belongs to the same generation, i.e. is made of the same material and does not require different manufacturing processes. Any changes in the machine cost rates due to inflation, capacity adjustments in existing production lines or the creation of a new factory can be accounted for by modifying the Factory Cost Model accordingly.

If a CER is required for design optimization, then one has to ensure that the design parameters are causally related to cost and not just correlated [9, 67]. As there is no need to model individual manufacturing activities and justify cost variability, there is a significantly higher risk that parametric methods do not identify the true cause-and-effect relationships of cost, unlike ABC [1, 27, 67]. The Scalable Blisk Cost Model is therefore an activity-based-parametric hybrid that combines the simplicity of the CER with the accuracy of estimating costs at the activity level.

Several sources [2, 4, 73] state that regression models normally require a relatively large dataset in order to identify statistically meaningful relationships. Other parametric techniques, such as artificial neural networks, also require a significant amount of data, however [1]. As the Component Study suffered from a lack of data to validate the scaling rules, the inherent uncertainty is built into the model which is discussed in more detail in Section 4.2.4 on page 119. Although Kim et al. [10] state that regression analysis cannot be applied to non-linear relationships and multiple outputs, Section 4.2.3 on page 118 explains why the Component Study was not affected by these restrictions.

Chapter 2

Advanced Gas Turbine Technology

2.1 Gas Turbine and Airframe System Options

For the next-generation 150-seater, the gas turbine and airframe manufacturers are exploring five aircraft system options: the two- and three-shaft turbofan, the geared turbofan, the turboprop and the open rotor [62, 76, 77]. Thus, the System Study modelled these five system options in conjunction with a fuselage, gear, flaps, slats and spoilers based on the current Airbus A320 [78], as shown in Figs. 2.1–2.6, because it is unlikely that a radically new design, like the flying wing, will be introduced by 2030 [15, 41]. While the three turbofan options all use the conventional low-wing airframe layout where the engines are mounted under the wing as illustrated in Figs. 2.1–2.3, the turboprop-powered aircraft displayed in Fig. 2.4 requires four engines installed on a high wing to provide enough ground clearance for the propeller tips. Both the wing and gear fairing in Fig. 2.4 are based on the BAe Avro RJ [78]. As the open rotor has two propellers mounted in tandem, Figs. 2.5 and 2.6 show that only two engines are mounted at the rear of a low-wing fuselage. The difference between the aircraft in Fig. 2.5 and Fig. 2.6 is that the former is designed for a cruise speed of Mach 0.70, while the latter is optimized for Mach 0.76 which therefore has greater wing and tail sweep angles.

Each of the five system options is explained in more detail in the following sub-sections. In order to keep a clear distinction between the engine and the rest of the aircraft, the word ‘airframe’ is used where the term ‘aircraft’ might be more appropriate. Similarly, the open rotor blades are referred to as ‘propellers’ to avoid confusion with the rest of the engine.

2.1.1 System Option 1: Two-Shaft Turbofan

The simplest gas turbine consists of a single compressor and a single turbine that are connected by a single shaft, a design first run by Frank Whittle in 1937 [11]. As the power absorbed or produced by each compressor or turbine stage is proportional to its rotational speed, ideally, each stage should rotate at a maximum speed that is only limited by the centrifugal stress acting on the blades in order to minimize the total number of stages required. In a single-shaft engine, the larger compressor and turbine blades towards the front and the rear end of the engine restrict the rotational speed of the smaller blades towards the centre of the engine. Thus, the number of stages can be reduced by splitting both the compressor and the turbine into low-pressure and high-pressure systems and introducing a second shaft that runs outside the first. First tested on the Rolls-Royce Olympus engine in 1950 [79], the inner shaft connects the slower turning fan, the low-pressure compressor (LPC) and low-pressure turbine (LPT), while the outer shaft links the high-speed high-pressure compressor (HPC) and high-pressure turbine (HPT). The two-shaft turbofan shown schematically in Fig. 2.1a consists of one fan, three LPC, nine HPC, two HPT and six LPT stages. For simplicity, the shafts are not shown in Fig. 2.1a nor in any other engine schematic in this thesis.

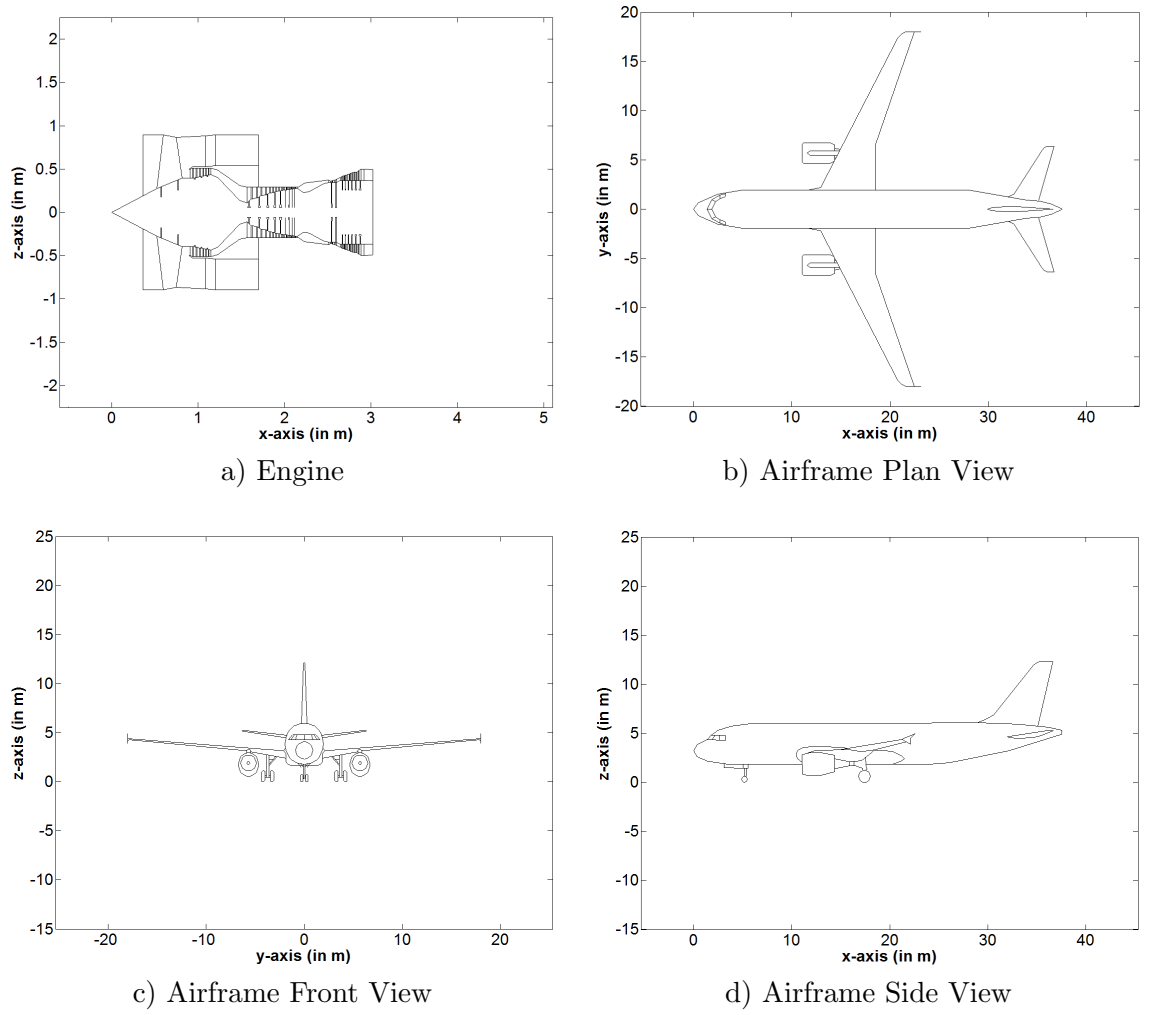


Figure 2.1: Two-Shaft Turbofan Aircraft (Cruise Speed: Mach 0.78).

2.1.2 System Option 2: Three-Shaft Turbofan

A turbofan's fuel consumption can be reduced by using a larger fan so that the bypass ratio and hence the propulsive efficiency of the engine are increased. As the size of the fan increases, however, the more the rotational speed of the LPC and the LPT is restricted. The front stages of the HPC constrain the rear HPC stages in a similar way, albeit to a lesser extent. By running the LPC, the front stages of the HPC and the second HPT stage in Fig. 2.1a on a third shaft, the rotational velocities of each stage match the optimum operating conditions more closely. First certified on the RB211 engine in 1972 [80], this additional intermediate-pressure system increases efficiency and reduces engine length and weight, but leads to higher complexity and cost [11]. Rolls-Royce [11] consequently believes that, currently, it is only the optimum architecture for engines with

more than 25,000–35,000 lb (≈ 111 –156 kN) of thrust, i.e. more powerful engines than the ones investigated in this study. The three-shaft engine in Fig. 2.2 has one fan, seven intermediate-pressure compressor (IPC), six HPC, one HPT, one intermediate-pressure turbine (IPT) and six LPT stages.

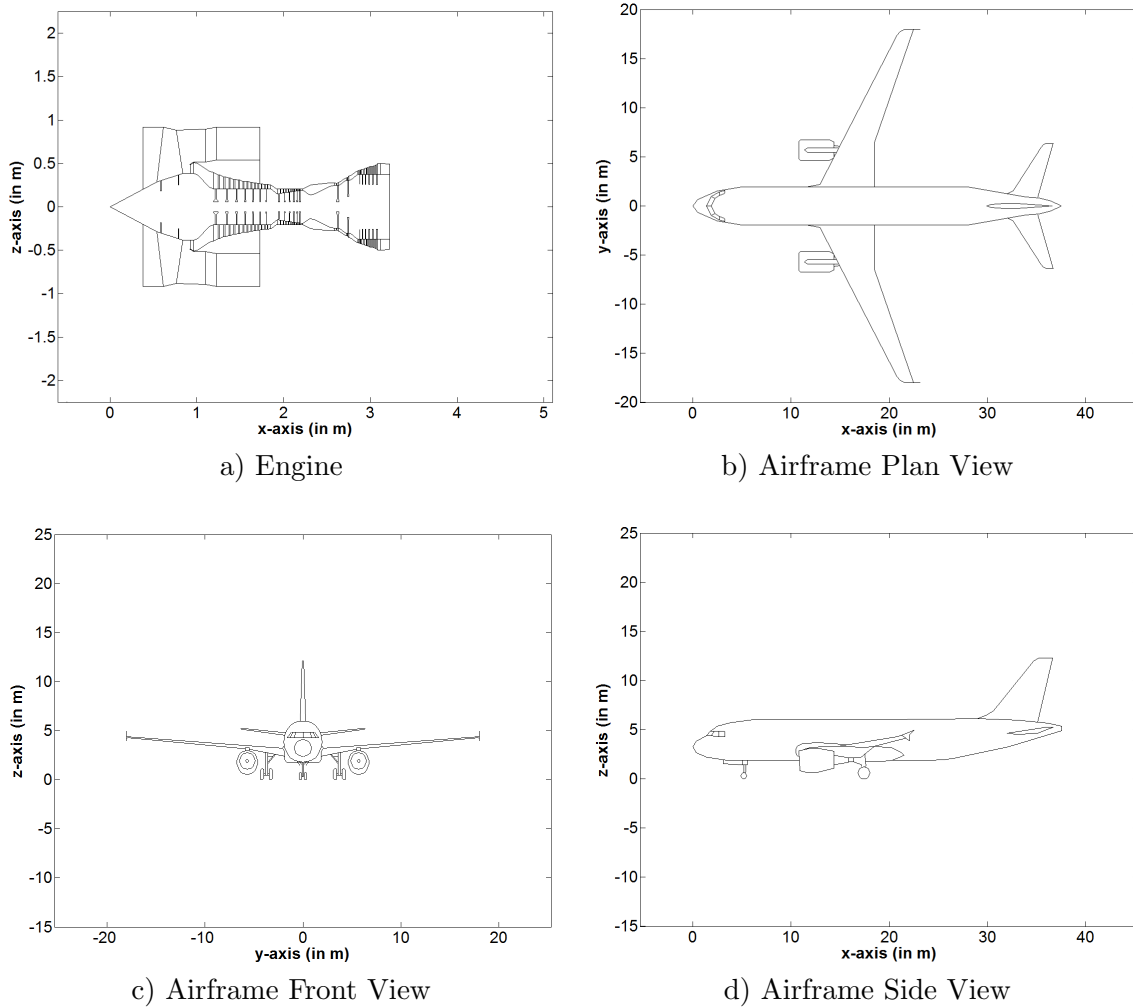


Figure 2.2: Three-Shaft Turbofan Aircraft (Cruise Speed: Mach 0.78).

2.1.3 System Option 3: Geared Turbofan

Instead of using a third shaft, the rotational speed of the fan can also be uncoupled from the low-pressure system by installing a planetary gear system between the fan and the LPC, as was first flight demonstrated on the Pratt & Whitney PW1000G in 2008 [81]. The effect of the planetary gear system, represented by the rectangular box between the fan and the LPC in Fig. 2.3a, on the engine design can clearly be seen by comparing Fig. 2.3a to Fig. 2.1a which have similar performance characteristics. Due to the increased rotational speed of the LP system, Fig. 2.3a only has three LPT stages while Fig. 2.1a has six.

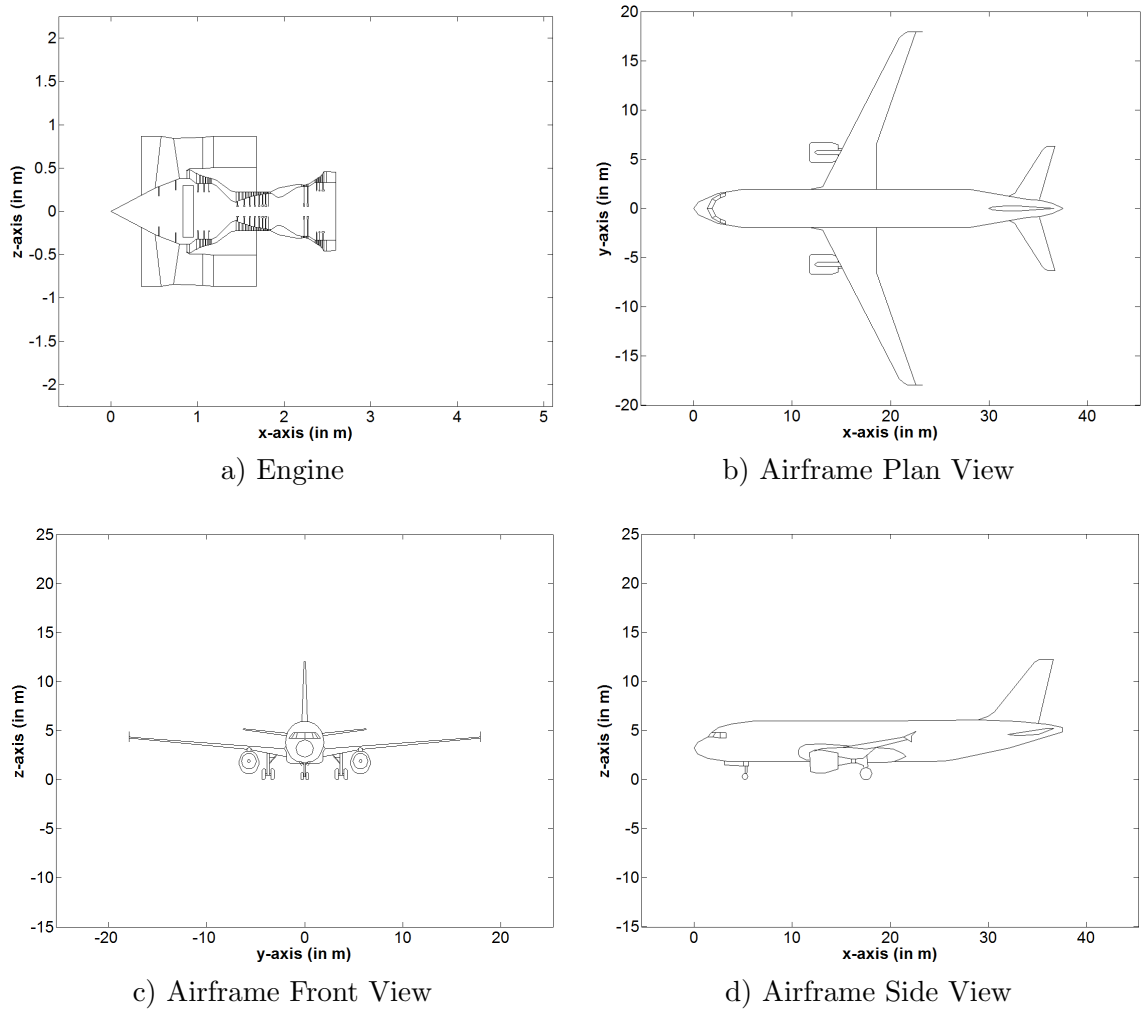


Figure 2.3: Geared Turbofan Aircraft (Cruise Speed: Mach 0.78).

2.1.4 System Option 4: Turboprop

As the weight and the drag of the nacelle limit the bypass ratio of the turbofan, the only way to further increase efficiency is by removing the fan duct and using a propeller instead of a fan, as was first flight tested on the experimental Meteor 1 with two Rolls-Royce Trent engines in 1945 [82]. The disadvantage of removing the protective fan duct is, however, that the axial speed of the air entering the propeller is primarily determined by the flight speed, rather than by the design of the fan duct, which limits the turboprop's maximum cruise speed [11]. Similar to the geared turbofan, the propeller is driven by the LPT through a reduction gearbox in order to limit the rotational speed of the propeller and minimize the number of LPT stages. Despite the gearbox, the maximum cruise speed is also restricted to prevent the airflow velocity relative to the blade tips of the propeller from exceeding the speed of sound, which would lead to a significant rise in noise and drag [83]. At present, the turboprop is consequently only used for shorter flights where the reduced cruise speed does not have a significant effect on the trip time [59].

The turboprop shown in Fig. 2.4 is based on the Europrop International TP400-D6 engine [84] which powers the Airbus A400M. Despite the higher mechanical complexity, the TP400-D6 is a three-shaft configuration because it allows the propeller to be independently powered by the LPT, while the engine core has the operational flexibility of a two-shaft engine [83, 85]. The eight-bladed propeller has a variable-pitch mechanism which means that a constant rotational speed can be maintained independently of the thrust setting by adjusting the blade pitch angle [85, 86]. The rotational speed is reduced as the cruise velocity is approached, however, to prevent the maximum flow velocity relative to the blade tips from exceeding Mach 0.95 [85]. Apart from the propeller, the engine in Fig. 2.4a consists of four IPC, six HPC, one HPT, one IPT and three LPT stages.

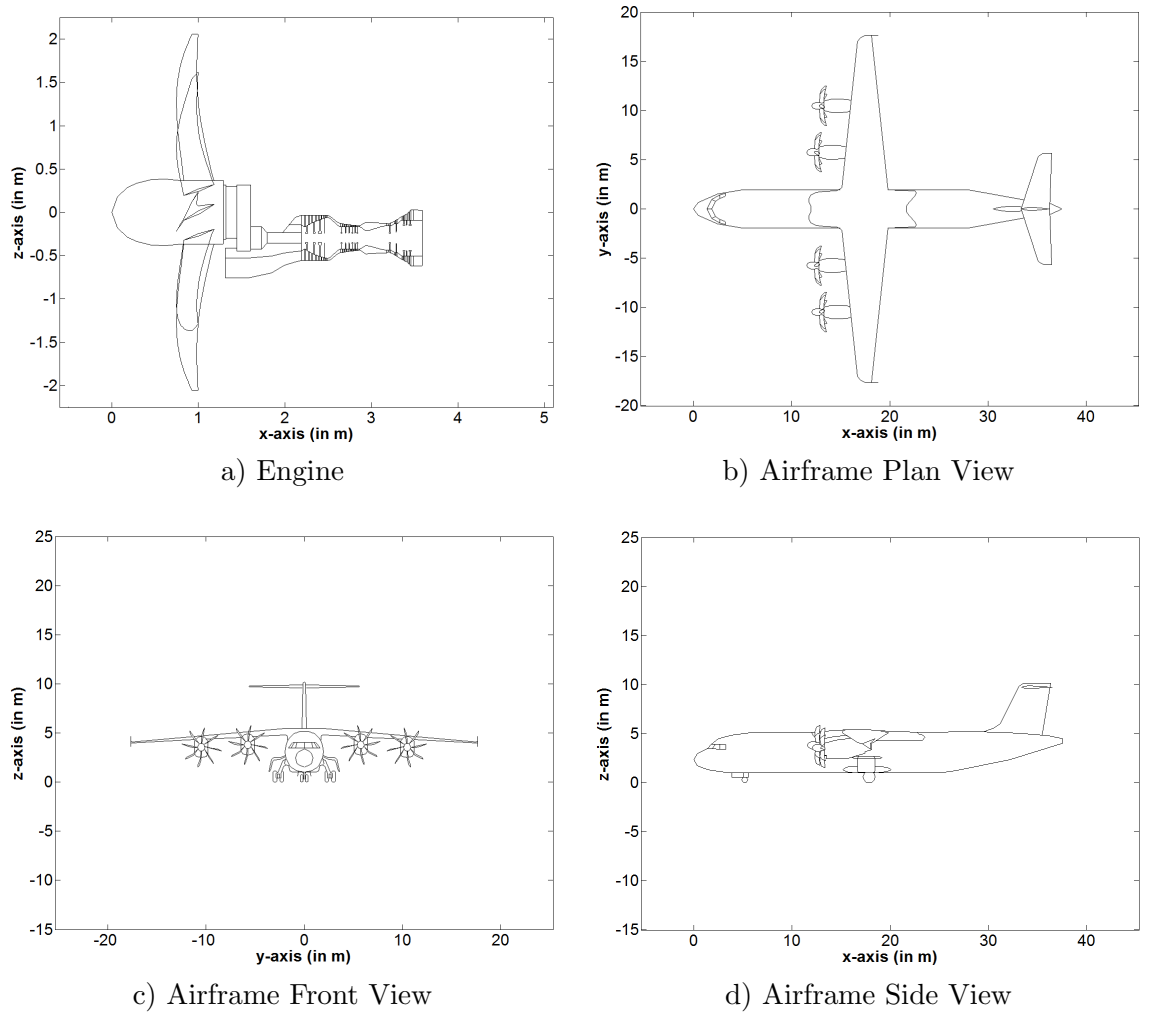


Figure 2.4: Turboprop Aircraft (Cruise Speed: Mach 0.70).

2.1.5 System Option 5: Open Rotor

Unlike the turboprop, the open rotor has two counter-rotating ‘propellers’ that are arranged in tandem. The second propeller not only increases the thrust produced, but it also recovers the air swirl leaving the first propeller, which increases engine efficiency and allows the open rotor to operate at a higher cruise speed than the turboprop [62, 83], as Fig. 2.6 shows. Figure 1.2 on page 9 indicates that the open rotor concept designs were developed and tested in the 1980s as a consequence of the OPEC oil embargo of 1973 but were cancelled by the end of the decade because of the reducing oil prices [34]. Since the oil price peak in 2008, however, there has been a renewed interest in the open rotor [87].

Of the five system options, the open rotor presents the most technological and operational challenges, however, including open rotor blade integration, control and reliability,

engine installation and noise [76, 88, 89]. The two propeller rows can either be installed at the front or the rear of the engine, respectively known as the tractor and the pusher configuration [62]. A further option is whether the propellers are driven directly by a counter-rotating turbine or through a reduction gearbox which requires cooling and increases mechanical complexity [89].

While the design of the ten upstream and eight downstream propeller blades in Figs. 2.5a and 2.6a is based on the EU's validation of Radical Engine Architecture systems (DREAM) project [90], the engine core is derived from Fig. 2.4a's turboprop but has six instead of four IPC and seven instead of six HPC stages — the reason is explained in Section 3.2.1 on page 88. The turboprop also forms the basis of the open rotor's propeller rotational speed and blade pitch control mechanism. The geared pusher configuration was selected because of its superior performance and the lower cabin noise levels when installed at the rear of the aircraft [24, 83]. Figures 2.5a and 2.6a clearly show that the open rotor's two propellers have slightly different diameters and blade numbers to avoid blade tip vortex interference [83]. While the open rotor with the lower cruise speed is referred to as System Option (SO) 5.1, the faster one is System Option 5.2.

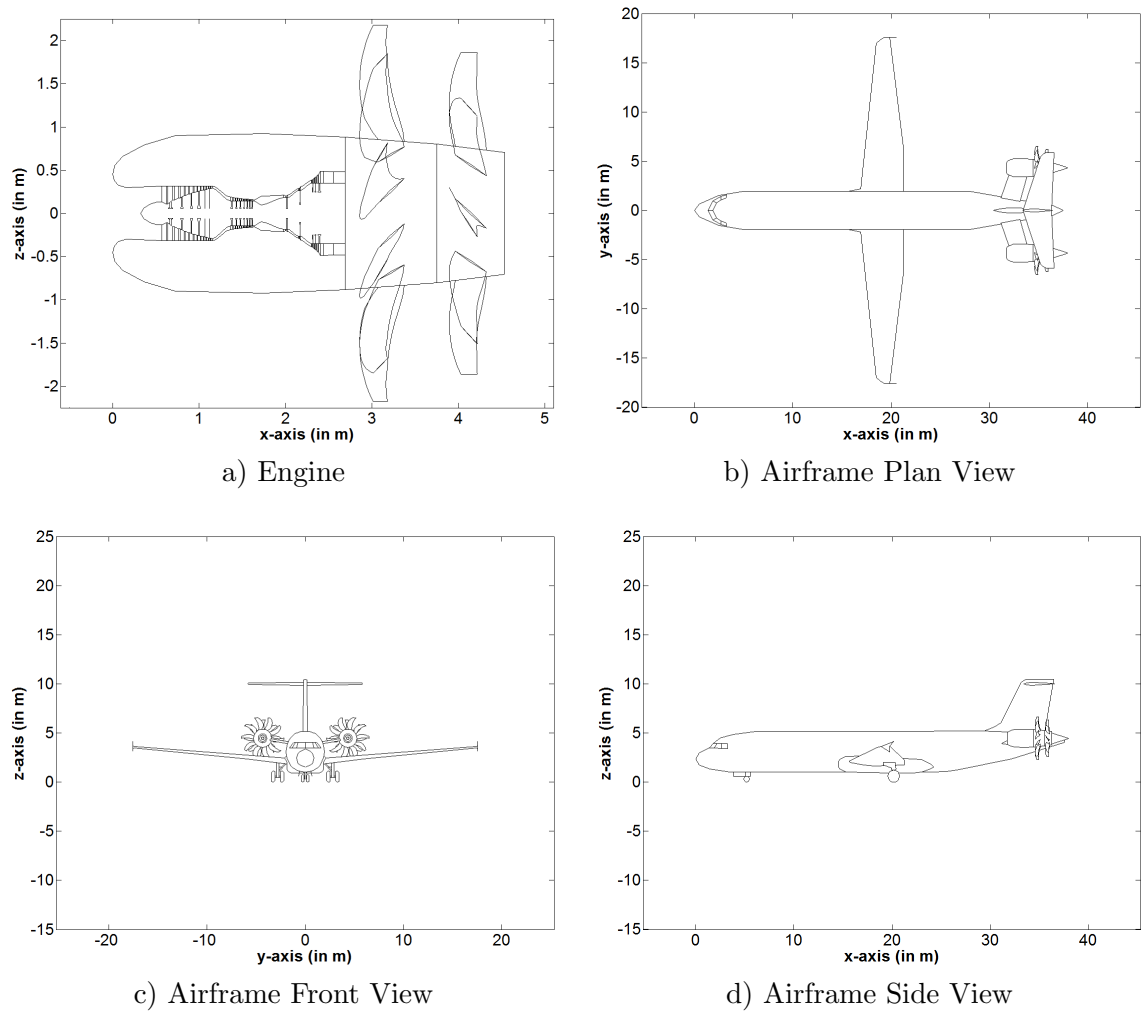


Figure 2.5: Open Rotor Aircraft (Cruise Speed: Mach 0.70).

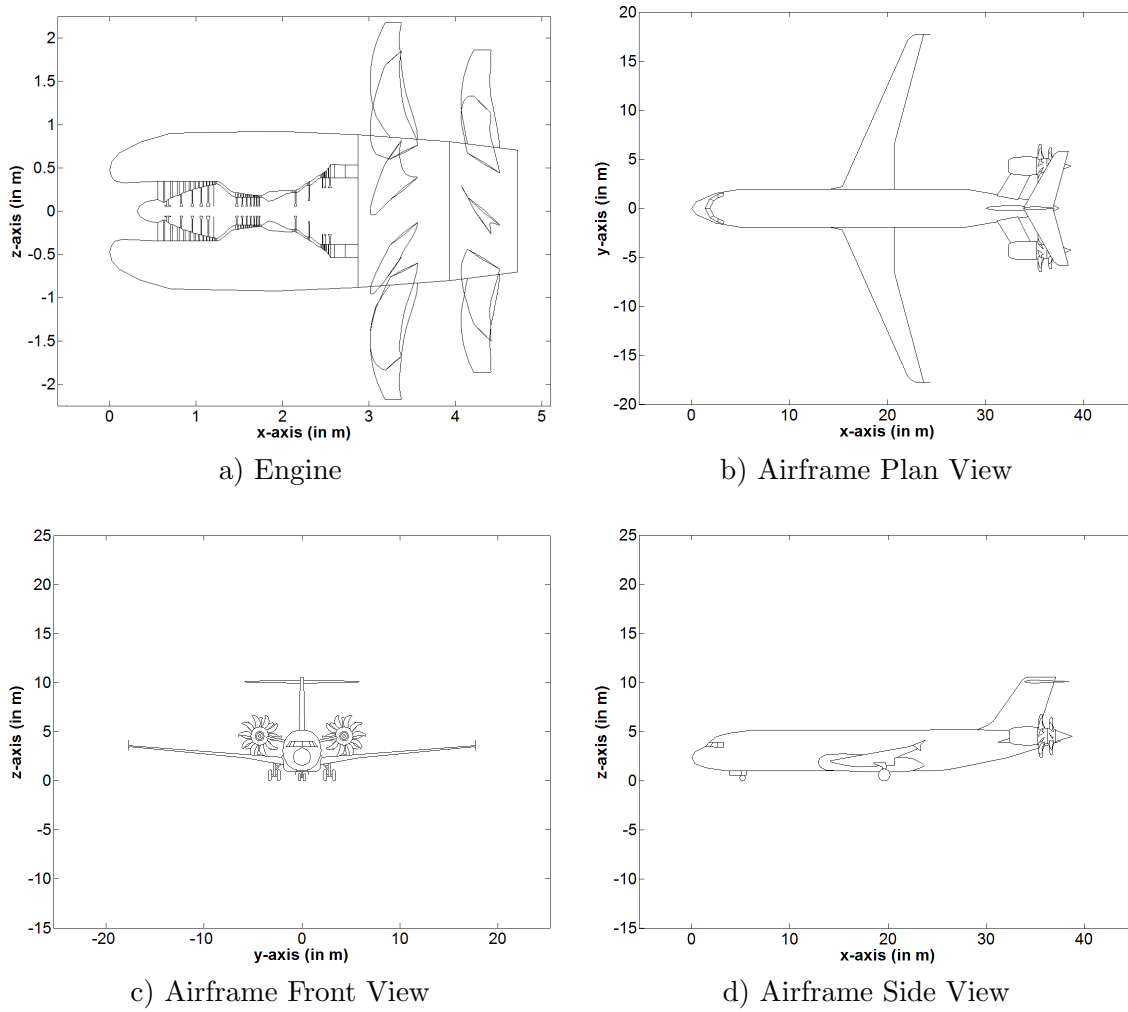


Figure 2.6: Open Rotor Aircraft (Cruise Speed: Mach 0.76).

2.2 Gas Turbine Component Options

2.2.1 Blisks

Integrally bladed discs, commonly known as blisks, are currently found in axial-flow compressors of gas turbine engines. Figure 2.7 shows that blisks require significantly less material because the dead weight from the blade roots, disc lugs and the disc structure required to support these features is no longer required. This leads to a weight saving of up to 30% [11], permitting higher blade speeds and consequently higher pressure ratios per stage [91]. A blisk compressor therefore requires one third fewer rotor stages to achieve the same total pressure ratio as a conventional design [91].

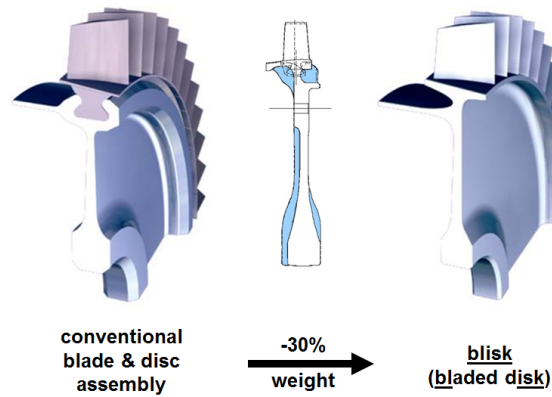


Figure 2.7: Blisk Weight Saving.

Blisks first appeared in the 1960s in small helicopter engines and gradually grew in size and production volume [92, 93, 94]. They are now common in military gas turbines and are starting to be included in commercial aircraft engines [92, 94]. Currently, turbine blisks are still in development because the high temperatures caused by the combusted gas can only be withstood by materials that are difficult to machine and weld [95].

The three techniques currently used for manufacturing blisks are: Electro-Chemical Machining (ECM) for blisks with small blades, Machining From Solid (MFS) for medium sized blades and Linear Friction Welding (LFW) for large blades [92]. Figure 2.8 demonstrates where each blisk type is typically found in the compressor of a gas turbine. As the author only modelled LFW blisks, only linear friction welding is described in more detail in the following sub-section.

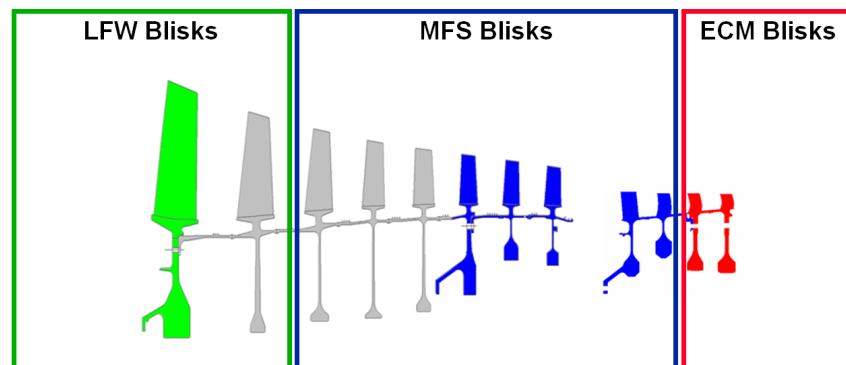


Figure 2.8: Axial-Flow Gas Turbine Compressor with LFW, MFS and ECM Blisks.

Linear Friction Welding

During the LFW process, the blade is held against the disc with an equivalent force of many tonnes while oscillating the blade on a linear path. The resulting friction causes the metal in the surrounding area to heat up until it becomes viscoplastic and is gradually squeezed out of the interface area as flash. Once the oscillation of the blade is stopped in the right location, the disc and blade material in the friction welded zone cools down to form a very high quality bond. Figure 2.9c illustrates the adaptive milling operation that follows the welding process to remove the flash and create the final blade foot geometry.



Figure 2.9: Linear Friction Welding. a) Disc and Blade Before LFW, b) LFW Process, and c) Adaptive Milling

Linear friction welding is primarily used to manufacture titanium blisks with a low blade count for the low-pressure compressor [92]. While ECM and MFS blisks can only have solid blades, LFW also permits the use of lighter hollow blades that could be made of a different alloy to the disc [11, 92, 96]. Smaller blisks are usually not linear friction welded because MFS and ECM tend to be more cost-effective. The blades on smaller blisks are also more closely stacked which can make LFW impractical due to tooling access problems.

Pros and Cons

In addition to weight reduction, blisks have the following advantages:

- They require less space which reduces the weight of the supporting engine structure, thus maximising the engine's power density and power-to-weight ratio [11, 92].
- The elimination of the blade-disc joint reduces leakage flows and fatigue, the former increasing aerodynamic efficiency and stability, the latter permitting a longer service life [92, 97].

Blisks also have several drawbacks, however, which currently preclude their use throughout the entire compressor:

- Blisks are more expensive to manufacture because the advanced technology requires more expensive machinery, increased machining time and more elaborate quality assurance measures [92].
- If a blade on a blisk is badly damaged, it is likely that the entire blisk will have to be scrapped because individual blades cannot be substituted at the moment, although a blade replacement process is currently being developed [96]. Standard repairs such as blade tip blending and patching are already carried out, however [96]. The latter process involves cutting off the damaged blade area, welding on a replacement section and restoring the original contour using adaptive milling [98].

Consequently, every compressor stage in a new gas turbine requires an in-depth trade-off study between the cheaper disc and blade assembly and the lighter, more compact and more efficient blisk. This requires performance analysis tools as well as cost and weight models.

Chapter 3

System Study

3.1 Methodology and Assumptions

Figure 3.1 shows the optimization framework set up in MATLAB to find the most robust engine and airframe specifications for the five gas turbine options. As the exact thrust requirement for each new aircraft configuration is not known in advance, Fig. 3.1 indicates that Modules 1 and 2 first create provisional engine and airframe designs based on a takeoff thrust estimate of 124kN per turbofan engine, and a turboprop and open rotor LPT power output of 5.9 MW and 18.0 MW, respectively. These thrust and power estimates are multiplied by a growth factor of 1.25 based on the thrust ratio between the growth and the baseline version of the V2500 engine [99].

These designs are then ‘tested’ in Module 5, which calculates how much more or less thrust is needed to meet the various performance requirements by calling Modules 3 and 4 for each scenario. The test condition with the highest relative thrust requirement defines the final engine and airframe design. This means that Modules 1 and 2 have to be rerun before Fig. 1.8’s average flight distance (see page 20) can be simulated in Module 6. This module calculates the total fuel consumption of the flight by running Modules 3 and 4 many times to cover the various flight stages. In Module 7, the cruise speed determines how many aircraft are needed to fly the RPKs predicted for 2030 and how much they are utilized. This information is then fed into Module 8, together with the fuel consumption and block time calculated by Module 6, to calculate the MSD of the Direct Operating Cost. Module 9’s optimizer then adjusts the design parameters and reruns the optimization loop until the MSD has been minimized. Although Module 9 could also optimize the cruise

speed, it was varied manually outside the optimization loop to see how the robustness of the optimized designs changes with cruise velocity.

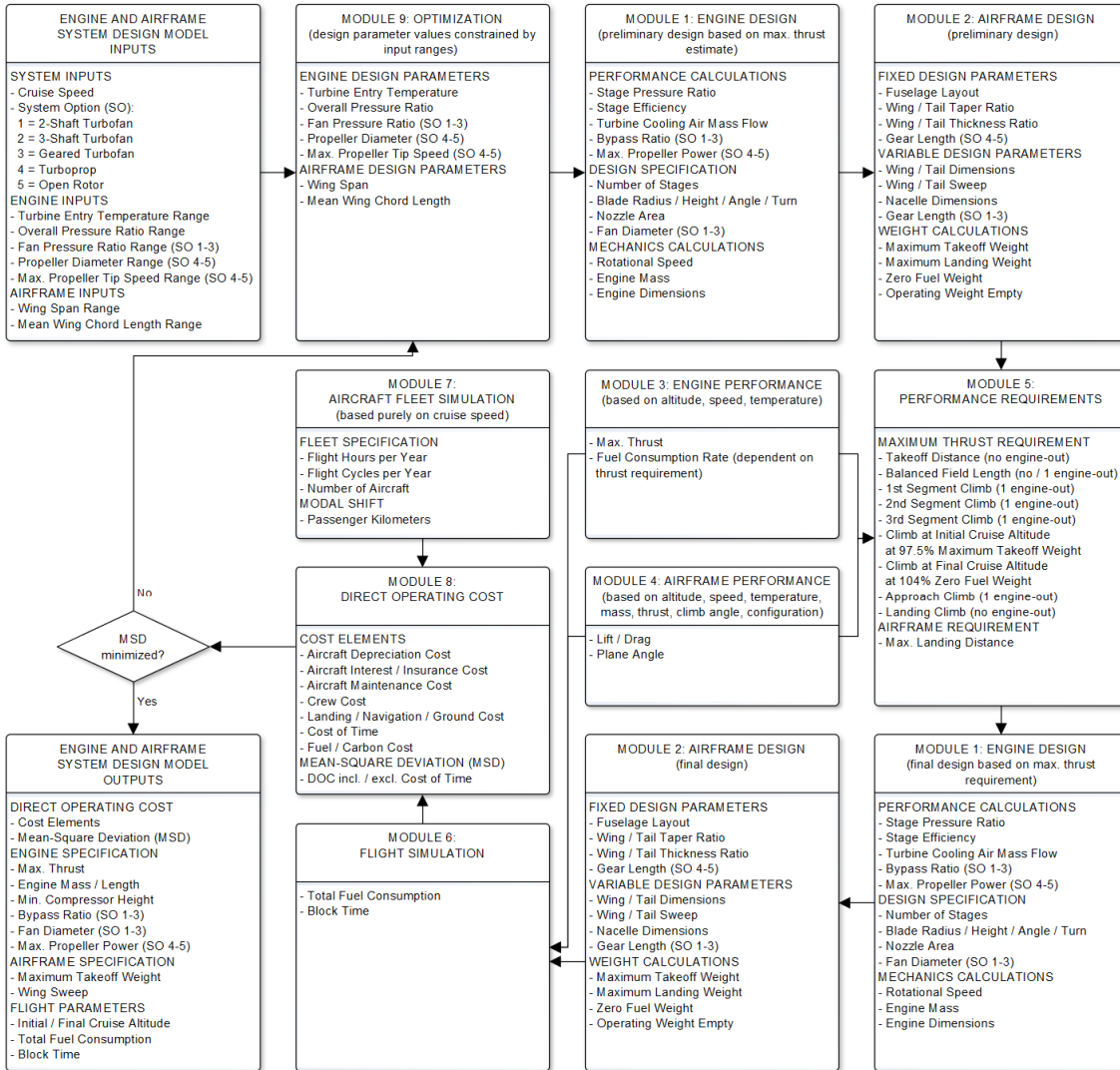


Figure 3.1: System Design Methodology.

Before each module is described in detail in the following sub-sections, Table 3.1 lists the upper and lower limits that the optimizer has to adhere to. While the soft constraints could be adjusted if the optimizer approached them, the hard constraints are fixed because of the physical limitations specified in Table 3.1. Although centrifugal compressors could alleviate the overall pressure ratio limit imposed by the minimum blade height of the axial compressor [100], these were not considered in this study.

Table 3.1: System Study Input Parameter Constraints.

Input Parameter	Minimum	Maximum
<i>Engine</i>		
Turbine Entry Temperature	1,500 K (soft constraint)	2,000 K (hard constraint imposed by turbine material technology [62])
Overall Pressure Ratio	20 (soft constraint)	50 (soft constraint) but limited by minimum axial compressor blade height of 13 mm (hard constraint due to aerodynamic losses incurred by small compressor blades [100])
Fan Pressure Ratio	1.3 (soft constraint)	2.0 (soft constraint)
Propeller Diameter	3 m (soft constraint)	5 m (soft constraint)
Maximum Propeller Rotational Tip Speed	150 m/s (soft constraint)	350 m/s (soft constraint) but maximum relative flow velocity of Mach 0.95 (hard constraint based on TP400-D6 engine [85])
<i>Airframe</i>		
Wing Span	function of minimum wing aspect ratio of 5 (hard constraint for short-range aircraft [101]) and minimum wing area (hard constraint defined by maximum approach speed of 135 kn EAS at MLW, SL, ISA ^a [60])	36 m (hard constraint to operate at ICAO Code C airports [60])
Mean Wing Chord Length	function of wing span and minimum wing area (hard constraint defined by maximum approach speed of 135 kn EAS at MLW, SL, ISA ^a [60])	function of wing span and minimum aspect ratio of 5 (hard constraint for short-range aircraft [101])
^a kn = knots, EAS = Equivalent Airspeed, MLW = Maximum Landing Weight, SL = Sea Level ISA = International Standard Atmosphere		

3.1.1 Module 1: Engine Design

Figure 3.2 illustrates that the gas turbine design module consists of nine sub-modules of which the first seven are run in a loop until the design has converged and has satisfied the design constraints. Only System Options 4 and 5 call Sub-Module 1.5, however, because only the turboprop and the open rotor have propellers.

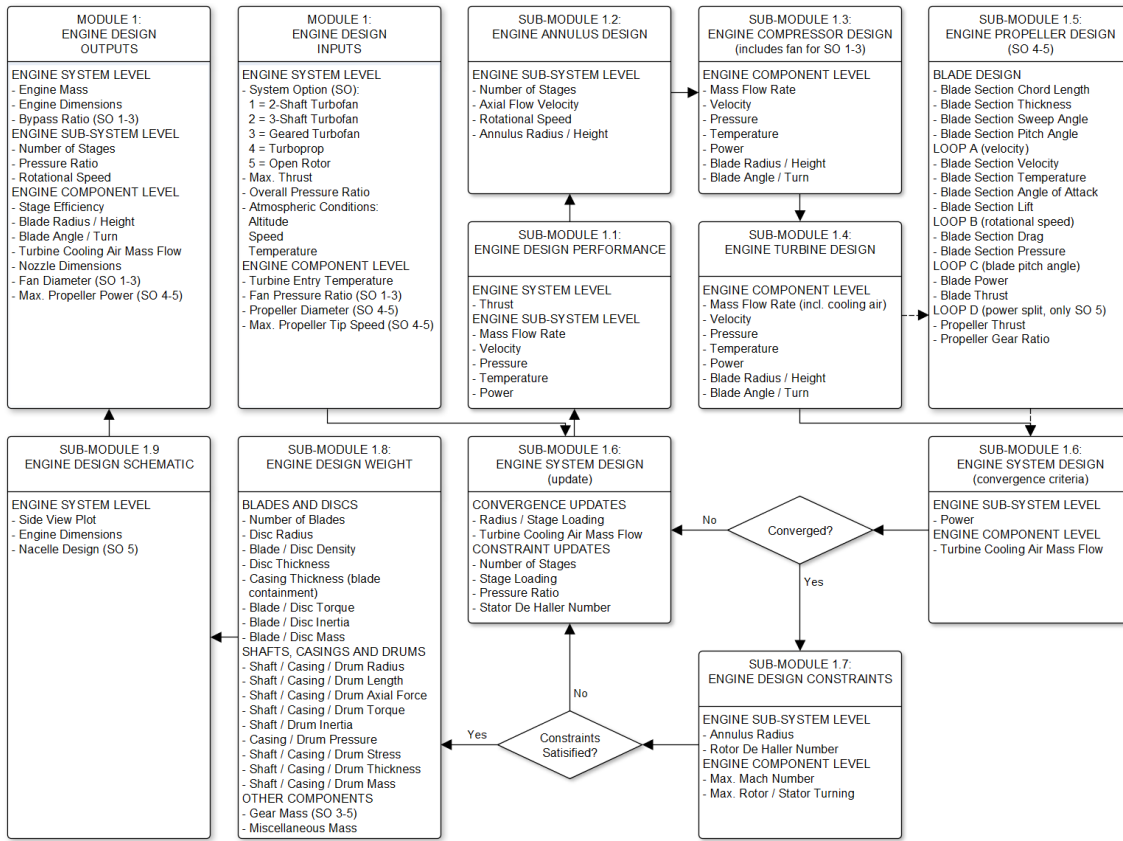


Figure 3.2: Engine Design Framework.

Sub-Module 1.1: Engine Design Performance

The design performance of the engine, including the mass flow, velocities, pressures, temperatures and power, are calculated by Sub-Module 1.1 based on the thrust requirement, the design parameters specified by the optimizer and the fixed performance values listed in Table 3.2. The inlet pressure loss is significantly higher for the turboprop than for the other system options because of the more convoluted inlet design. The power offtake is based on the assumption that all aircraft systems are driven by electrical power and that consequently no air has to be bled off the engines. As the turboprop aircraft is the only system option in this study with four engines instead of two, each turboprop engine has half the power offtake.

Table 3.2: Fixed Engine Design Performance Values.

Parameter	Value	Source
inlet pressure loss	SO 4: 3 %, others: 0.5 %	Ref. [102]
polytropic efficiency	cooled turbine stages: 90 %, rest: 92 %	extrapolated from Ref. [102]
bypass pressure loss (SO 1–3)	3 %	Ref. [100]
combustion efficiency	98 %	Ref. [103]
power offtake	SO 4: 185 kW, others: 370 kW	scaled from Refs. [100, 104]
combustion chamber pressure loss	4 %	Ref. [102]
shaft efficiency	99 %	Ref. [105]
gear efficiency	99 %	Ref. [26]
nozzle pressure loss	1.5 %	Ref. [102]

Sub-Module 1.2: Engine Annulus Design

The performance data is then passed on to Sub-Module 1.2 which defines the general arrangement of the engine, including:

- the annulus area throughout the engine, which is controlled by Table 3.3’s axial flow velocities
- the number of compressor stages, based on the total temperature rise, ΔT , per stage given in Table 3.3
- the rotational speed of the shafts, depending on the maximum turbine blade stress which is set at 25 % of the ultimate tensile strength of the blade material [100]
- the inlet and outlet radii of the sub-systems, which are influenced by Table 3.3’s stage loading, $\frac{\Delta V_{wh}}{\omega r_m}$, where ΔV_{wh} is the whirl velocity imparted on the airflow by the rotor blades, and ωr_m is the mean rotational speed of the latter components

In Table 3.3, the geared turbofan has a higher temperature rise per LPC stage than the two-shaft turbofan, because the former’s LPC rotates more quickly.

Table 3.3: Fixed Engine Annulus Design Values.

Parameter	Value	Source
axial flow velocity	fan inlet (SO 1–3): Mach 0.6, HPT inlet: Mach 0.2, LPT outlet: Mach 0.5, rest: Mach 0.4	Ref. [100]
ΔT per stage	LPC: 16 K (SO 1), LPC: 40 K (SO 3), IPC: 40 K, HPC: 56 K	Ref. [100]
stage loading	compressor: 0.4, HPT: 1.8, IPT: 2.0, LPT: 2.3	Ref. [100]

Sub-Module 1.3: Engine Compressor Design

The compressor rotors and stators, including the fan for the three turbofan system options, are designed in Sub-Module 1.3 using velocity triangles in conjunction with the boundary conditions specified by Sub-Modules 1.1 and 1.2. By calculating the mass flow, flow velocity, pressure and temperature at each stage, the power consumed by each rotor stage can be determined, as well as the height, radius and inlet and outlet angle of each blade.

Sub-Module 1.4: Engine Turbine Design

Similar computations are carried out to define the turbine in Sub-Module 1.4, except that it also calculates how much air has to be bled off the compressor outlet to cool the turbine blades, based on the following assumptions:

- the blades only require cooling if the flow temperature lies above the maximum metal operating temperature, T_{metal} , of 1350 K (extrapolated from Ref. [103])
- the turbine blades have a cooling efficiency, $\frac{T_{cool,out} - T_{cool,in}}{T_{metal} - T_{cool,in}}$, of 75 % (extrapolated from Ref. [103]) where $T_{cool,in}$ is the temperature of the cooling air as it enters the turbine blade, and $T_{cool,out}$ is its temperature as it leaves the blade
- the heat transfer coefficient of the turbine blades is 5,000 W/(m²K) according to Ref. [103]

Sub-Module 1.5: Engine Propeller Design

While the turboprop blade design is based on the TP400-D6 propeller, the open rotor blade is derived from the DREAM project, as described on page 32 and 33, respectively. Once the blades have been scaled to the diameter specified by the optimizer, the turboprop blade is discretized into 25 elements and the two open rotor blade designs into 12 each. This ensures that the discretization error is only 0.4 % for the turboprop and 0.3 % for the open rotor.

Unlike Propeller Vortex Theory, Propeller Momentum Theory and Momentum-Blade Element Theory ignore flow rotation and fail to predict no blade loading at the blade tips [86]. Propeller Vortex Theory is therefore considerably more accurate at predicting these induced effects and shows close agreement with experimental results [86]. While the turboprop needs three nested loops to determine the performance of its single propeller

based on Propeller Vortex Theory, the open rotor requires an additional fourth loop to modify the power split between the two propellers until the combined thrust is maximized.

Figure 3.2 shows that the innermost Loop A in Sub-Module 1.5 recalculates the flow velocity, temperature, angle of attack and lift of each blade section until the flow velocity's relative error has dropped below the gas turbine design module's convergence limit of 10^{-10} . The lift produced by each blade section is determined by multiplying the blade section's angle of attack by its lift slope, which is a function of the blade section's design and flow velocity [52]. Once Loop A has converged, Loop B checks whether the relative airflow velocity of each section is less than Mach 0.95. If not, the rotational speed of the propeller is reduced and Loops A and B re-run until that criterion is met. Before Loop C is initiated, the blade section pressures are determined and the induced drag, parasite drag and wave drag of each blade section computed based on equations presented in Ref. [52]. Finally, Loop C calculates the thrust produced and the power absorbed by all the blade sections and adjusts the blade pitch angle to match the power provided by the LPT.

Sub-Module 1.6: Engine System Design

At the end of each design iteration, Sub-Module 1.6 checks the convergence of the turbine cooling air mass flow and compares the power specification made by Sub-Module 1.1 against the actual power calculated by Sub-Modules 1.3, 1.4 and 1.5. For a fixed rotational speed, ω (in rad/s), and mass flow, \dot{m} (in kg/s), Eq. 3.1 [100] shows that the power, Z (in W), absorbed or produced by the compressor or turbine sub-system is controlled by its mean radius, r_m (in m), and its stage loading, $\frac{\Delta V_{wh}}{\omega r_m}$. If any of the relative errors are above the convergence limit, Sub-Module 1.6 updates the cooling air mass flow values and adjusts the radii of the sub-systems. As the mean radius of the two-shaft engine's LPC is determined by the fan, however, its stage loading is modified instead.

$$Z = \dot{m} (\omega r_m) \Delta V_{wh} = \dot{m} (\omega r_m)^2 \frac{\Delta V_{wh}}{\omega r_m} \quad (3.1)$$

Sub-Module 1.7: Engine Design Constraints

The engine design process is made more complex by the fact that it has to comply with several design constraints that are enforced by Sub-Module 1.7:

- To produce a smooth alignment of the engine's annulus, the radii of the high-pressure sub-systems cannot be greater than those of either the low- or the intermediate-pressure systems. Similarly, the outlet radius of the IPT cannot exceed the inlet radius of the LPT.
- Under no circumstance may the root radius of the blades be less than 0.1 m so that there is enough space for the discs, shafts and other miscellaneous components.
- The core's nozzle area, which controls the mass flow rate through the core, is set so that none of the velocity triangle speeds can exceed Mach 1, except for the fan whose blade tips are designed to operate at Mach 1.35 [100].
- To avoid large pressure losses or even flow separation and stall, the blade turn angle, i.e. the difference between the inlet and outlet angle of the blade, has to be less than 30° for all compressor blades, less than 65° for the first HPT stator and less than 110° for the other turbine stators and all the turbine rotors [100].
- For the same reason, the flow velocity at and relative to the trailing edge of the compressor rotor blade must not be less than 65 % of the flow velocity at and relative to the blade's leading edge [100]. This ratio is known as the DeHaller Number.
- After each turbine rotor, the exit angle of the flow relative to the engine's centre-line must not be greater than 35° to prevent excessive turning in the next turbine stator [100].

Sub-Module 1.7 tries to rectify any violation of these constraints by adjusting the stage number, the pressure ratio, the stage loading or the stator DeHaller Number of each sub-system. As resolving one constraint violation can lead to another, Sub-Module 1.7 contains a database which specifies which of the four design parameters can be used to address which violation and in what sequence in case there is a conflict with another violation and a different design parameter consequently has to be modified. The database also lists the importance of each constraint so that Sub-Module 1.7 knows which violation takes precedence in case a conflict cannot be resolved.

Sub-Module 1.8: Engine Design Weight

Once all the constraint violations have been resolved and the design has fully converged, relatively simple mechanics is used to calculate the parameters listed for Sub-Module 1.8 in Fig. 3.2 on page 44, which ultimately determine the engine weight. The engine design is based on the density, ρ (in kg/m³), Poisson's ratio, ν , and other properties of five different materials, namely composite, steel and aluminium (Al), titanium (Ti) and nickel (Ni) alloy. Table 3.4 gives an overview of which material is used for which engine component, based on Ref. [11]. Although most material selections are fixed, the compressor rotor and stator material depends on the operating temperature specified by Sub-Module 1.3.

Table 3.4: Engine Materials (adapted from Ref. [11]).

Component	Sub-System					
	Fan / Propeller	LPC	IPC	HPC	Combustion Chamber	Turbine
Rotor	composite	Ti/Ni	Ti/Ni	Ti/Ni		Ni
Stator	composite	Ti/Ni/steel	Ti/Ni/steel	Ti/Ni/steel		Ni
Disc/Drum	Ti	Ti	Ti	Ti		Ni
Shaft		steel	steel	Ti		Ni
Casing	Al	Ti	steel	steel	Ni	Ni

The blade number, n_b , is determined using Eq. 3.2 [100] where C_L is the lift coefficient (equal to 0.5 for the compressor blades and 0.8 for the turbine blades), P and p are the total pressure and the static pressure, respectively, measured relative to the leading edge of the compressor blade or relative to the trailing edge of the turbine blade, h_b is the blade height, and c_x is the axial chord length of the blade.

$$\dot{m} \Delta V_{wh} / n_b = C_L (P - p) h_b c_x \quad (3.2)$$

The blade mass is based on the assumption that the mean compressor and turbine blade thickness-to-chord (k/c) ratio is 0.05 and 0.2, respectively [100]. The fan rotors are assumed to only have a mean k/c ratio of 0.02, however, because of their thin wide-chord blade design. As multiplying the blade height by the chord length and the mean k/c ratio only gives the mass of the aerofoil, the fan and compressor rotor aerofoil mass is multiplied by 1.3, the compressor stators by 1.15, the turbine rotors by 1.5 and the turbine stators by 1.25 [100].

The thickness of the disc web, k_w (in m), and of each of the cob elements illustrated in Fig. 3.3 is based on the hoop stress formula given in Eq. 3.3 [100]. Both Fig. 3.3 and Eq. 3.3 also show that the disc not only has to contain the centrifugal stress acting on the blades, σ_b (in Pa), but also on the drum, σ_d , that links the discs within each sub-system. While σ_b depends on the number of blades, n_b , multiplied by the mass of each blade, m_b , the centrifugal load of the drum acting on each disc web is equal to the mass of the drum, m_d , divided by the number of disc webs, n_w . The number of cob pairs, n_{cp} , is only incrementally increased from zero in steps of one, if k_w is greater than 75 % of the blade's axial chord length or if the stress level exceeds the design hoop stress, σ_{hoop} , which is set at 80 % of the ultimate tensile strength of the material [100]. While the tip radius of the web, $r_{t,w}$, is dictated by the blade root radius, the root radius of the web, $r_{r,w}$, and the cobs, $r_{r,cp}$, is based on existing engine designs.

$$\begin{aligned} \sigma_{hoop} = & \left(\frac{1-\nu}{4} \right) r_{r,w}^2 \rho \omega^2 + \left(\frac{3+\nu}{4} \right) r_{t,w}^2 \rho \omega^2 + 2 n_{cp} \left[\left(\frac{1-\nu}{4} \right) r_{r,cp}^2 \rho \omega^2 \right. \\ & \left. + \left(\frac{3+\nu}{4} \right) r_{t,cp}^2 \rho \omega^2 \right] + \frac{2 (\sigma_b + \sigma_d) r_{t,w}^2}{r_{t,w}^2 - r_{r,w}^2} \end{aligned} \quad (3.3)$$

where $\sigma_b = \frac{n_b m_b r_{m,b} \omega^2}{2 \pi r_{t,w} k_w}$ and $\sigma_d = \frac{m_d r_{m,d} \omega^2 / n_w}{2 \pi r_{t,w} k_w}$

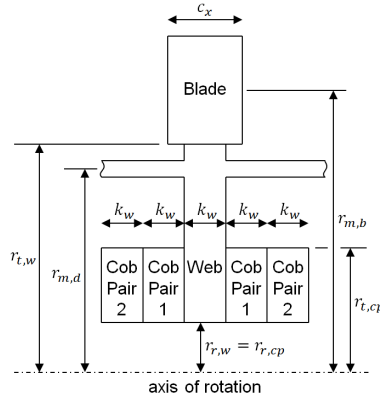


Figure 3.3: Blade, Disc and Drum Schematic.

While the pressure difference upstream and downstream of the blades creates an axial load on the rotors and stators, the turning of the flow imposes a torque on the blades. These loads have to be included in the maximum principal stress calculations to determine the thickness of the shafts, casings and drums. Additionally, the shaft and the drum thicknesses are dependent on the centrifugal load, and the casings and the drums have to contain the pressure built up inside the engine.

Irrespective of the loads, the minimum thickness of the casing is dictated by the requirement to contain a released blade, which is based on the analytical energy balance equation given in Ref. [106]. Similarly, the minimum thickness of the shafts and the drums is set by the constraint that the maximum deflection of the sub-systems due to gyroscopic torque has to be less than $1\text{ }\mu\text{m}$, assuming a maximum turn rate of 0.2 rad/s ($\approx 11\text{ deg/s}$) [107].

For the geared turbofan, the turboprop and the open rotor the mass of the planetary gear system is based on the value of 500 lb quoted in Ref. [25]. This value is multiplied by the ratio between Sub-Module 1.8's total mass estimate and the dry mass of the TP400-D6 engine of 1940 kg [84]. To account for the remaining engine components, including the oil, fuel and control systems, and the engine support structure, the engine mass prediction is multiplied by a factor of 1.15. This produces total mass estimates that deviate by less than 3 % from the dry mass of both the TP400-D6 and the V2500 engine [84, 99].

Sub-Module 1.9: Engine Design Schematic

In addition to generating the engine schematic, Fig. 3.2 on page 44 indicates that Sub-Module 1.9 calculates the engine dimensions. Except for the open rotor, the nacelles are not reproduced in the engine schematics, as Figs. 2.1–2.6 on pages 29–36 illustrate that they are already included in the airframe diagrams.

3.1.2 Module 2: Airframe Design

Figure 3.4 shows that the airframe design module re-iterates the airframe design and weight computation until the lift distribution between the wing and the horizontal tail is similar to the current Airbus A320 [78] by shifting the location of the wing and any sub-systems attached to it. This ensures that the aircraft is balanced correctly, even when the rear-fuselage mounted open rotor engines move the centre of gravity of the aircraft significantly towards the rear.

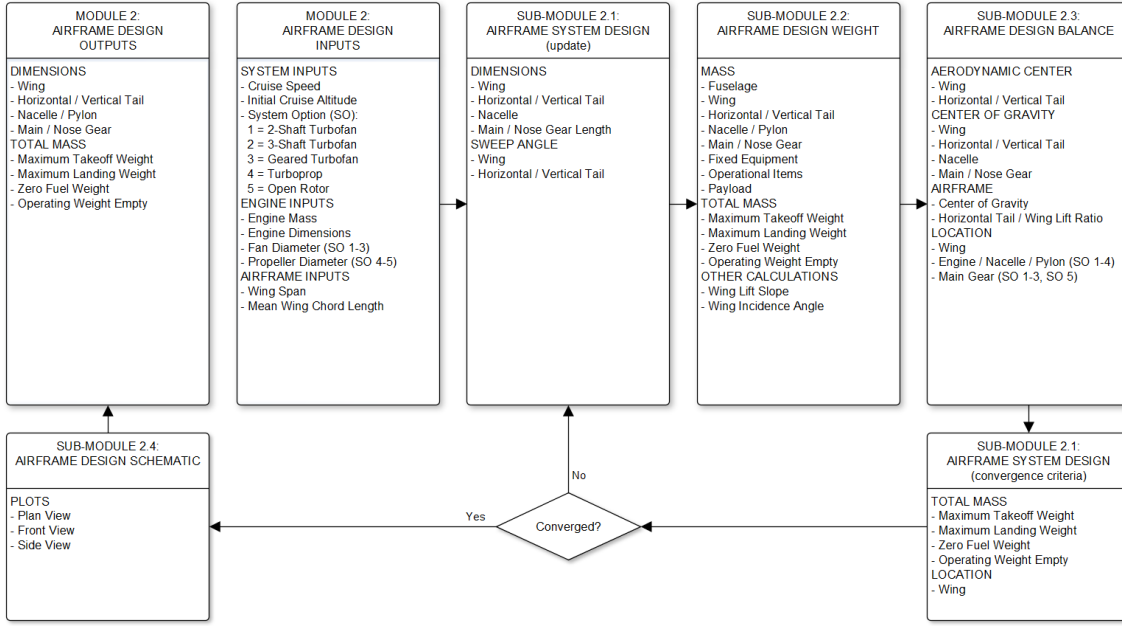


Figure 3.4: Airframe Design Framework.

Sub-Module 2.1: Airframe System Design

Only the airframe's wing span and mean chord length are varied by the optimizer, because the fuselage dimensions, as well as the taper and thickness-to-chord ratios of the wing and the tail, are based on the A320 values listed in Table 3.5. Figure 3.4 indicates that several other inputs are needed to define the airframe design, however, including:

- The system option, which specifies the wing and engine configuration.
- The dimensions of the engine and its nozzle, which are needed for the nacelle design.
- The cruise speed, which controls the sweep angles of the wing and the horizontal and vertical tail, based on the A320 [78] and other aircraft designs [54].
- While the diameter of the three turbofan system options is required to calculate the length of the landing gear, the turboprop's and the open rotor's propeller diameter determine the minimum wing span and the pylon length, respectively.

The wing span, b_W , and mean chord length, $c_{m,W}$, not only control the wing area, S_W , but also respectively influence the horizontal and vertical tail areas, S_{HT} and S_{VT} , that are calculated using Eqs. 3.4 and 3.5. These two equations are adapted from Ref. [52], where l_{HT} and l_{VT} are the distances between the aerodynamic centres of the wing and the respective tail, and C_{HT} and C_{VT} are the tail volume coefficients given in Table 3.5.

$$S_{HT} = \frac{C_{HT} \times c_{m,W} \times S_W}{l_{HT}} \quad (3.4)$$

$$S_{VT} = \frac{C_{VT} \times b_W \times S_W}{l_{VT}} \quad (3.5)$$

Unlike for the three turbofan system options, the gear lengths of the turboprop and open rotor aircraft, listed in Table 3.5, are determined by the fuselage's tail-strike angle and not the propeller diameter.

Table 3.5: Fixed Airframe Design Values.

Parameter	Value	Source
wing taper ratio	0.260	Airbus A320 [78]
wing thickness-to-chord ratio	0.101	Airbus A320 [78]
horizontal tail taper ratio	SO 1-3: 0.310, SO 4-5: 0.426	SO 1-3: Airbus A320 [78], SO 4-5: BAe Avro RJ [78]
vertical tail taper ratio	SO 1-3: 0.317, SO 4-5: 0.625	SO 1-3: Airbus A320 [78], SO 4-5: BAe Avro RJ [78]
horizontal tail volume coefficient	SO 1-3: 1.207, SO 4-5: 1.146	SO 1-3: Airbus A320 [78], SO 4-5: BAe Avro RJ [78]
vertical tail volume coefficient	SO 1-3: 0.084, SO 4-5: 0.080	SO 1-3: Airbus A320 [78], SO 4-5: BAe Avro RJ [78]
main gear length	SO 4: 1.45 m, SO 5: 1.77 m	based on BAe Avro RJ tail-strike angle [78]
nose gear length	SO 4-5: 1.01 m	based on BAe Avro RJ tail-strike angle [78]

Sub-Module 2.2: Airframe Design Weight

The various total aircraft weights listed in Fig. 3.4 for Sub-Module 2.2 are calculated using the weight formulas and fixed values given in Table 3.6. Once all the weights have been determined, they are summed up and multiplied by Table 3.6's Airbus A320 weight reference factor, which calibrates the estimated Maximum Takeoff Weight (MTOW) against that of the current A320 [78]. The fact that this factor is 0.995 shows that Sub-Module 2.2 overpredicts the MTOW of the current A320 by only 0.5 %. Finally, the weights are multiplied by the Table 3.6's composite weight factor to account for the weight reduction potential offered by composite materials.

In addition to the weight computations, Sub-Module 2.2 calculates the wing incidence angle so that the cabin floor is level during cruise. It does this by first determining

Table 3.6: Airframe Weight Formulas and Values.

Parameter	Value	Source
<i>Total Airframe Weight Formula</i>		
Airbus A320 weight reference factor	0.995	Airbus A320 [78]
composite weight factor	0.8	Ref. [54]
<i>Fuselage Weight Formula [54]</i>		
economy class seats (average)	159	Airbus A320 [78]
first class seats (average)	6	Airbus A320 [78]
cargo hold volume	37.4 m ³	Airbus A320 [78]
<i>Wing Weight Formula [101]</i>		
<i>Horizontal / Vertical Tail Weight Formula [52]</i>		
<i>Nacelle / Pylon Weight Formula [52]</i>		
propeller clearance	0.3 m	Ref. [52]
<i>Main / Nose Gear Weight Formula [52]</i>		
<i>Fixed Equipment Weight Formula [54]</i>		
<i>Operational Items Weight</i>		
supplies	2.27 kg per economy passenger, 2 × 2.27 kg per first class passenger	Ref. [54]
water	0.68 kg per passenger	Ref. [54]
safety	3.40 kg per passenger seat	Ref. [54]
flight crew weight (incl. baggage)	2 × 95 kg	Ref. [60]
cabin crew weight (incl. baggage)	5 × 85 kg	Ref. [60]
<i>Payload Weight</i>		
passenger seat utilization	80 %	Ref. [108]
passenger weight (incl. baggage)	100 kg	Ref. [60]
cargo hold utilization	40 %	assumption
cargo density	130 kg/m ³	Ref. [101]

the lift coefficient, C_L , required to fly at cruise speed at the initial cruise altitude at 97.5 % MTOW, and then dividing C_L by the wing's lift slope, which is a function of the wing design and the flight speed [52], just like for the propeller blade sections.

Sub-Module 2.3: Airframe Design Balance

Figure 3.4 shows that Sub-Module 2.3 determines the aerodynamic centres of the wing and the two tail surfaces as well as the centre of gravity of all airframe sub-systems. These locations are not only needed to calculate the two distances between the aerodynamic centres, l_{HT} and l_{VT} , in Sub-Module 2.1, but also to compute the centre of gravity of the aircraft and the lift ratio between the horizontal tail and the wing.

3.1.3 Module 3: Engine Performance

Figure 3.5 illustrates that the gas turbine performance module uses three nested loops to either calculate the engine's maximum thrust or the fuel consumption rate for a given thrust requirement. Both output options not only depend on the engine design and the performance losses specified by Module 1, but also on the atmospheric conditions listed amongst the input parameters in Fig. 3.5. The performance computations carried out by Sub-Modules 3.1 to 3.4 are identical to their counterparts in the engine design module, except that the design is fixed. Sub-Modules 3.2 and 3.3 do adjust the compressor and turbine stator angles, however, to provide a smooth flow onto and off the rotor blades.

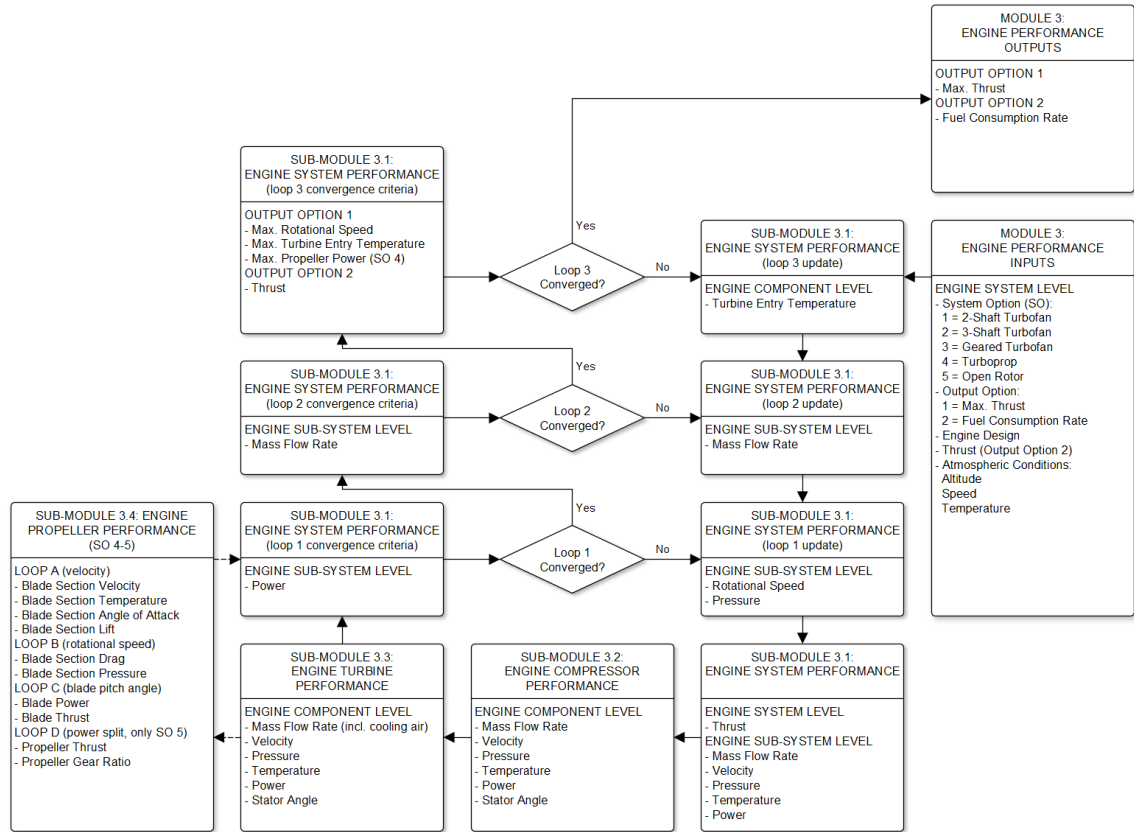


Figure 3.5: Engine Performance Framework.

Once Sub-Modules 3.1 to 3.4 have determined the engine performance for the initial turbine entry temperature, core and bypass mass flow rate, rotational speeds and pressures, Loop 1 adjusts the rotational speed of the shafts and reruns Sub-Modules 3.1 to 3.4 until the power consumed by the compressor sub-systems balances the power produced by respective turbine sub-systems. To ease convergence of the three-shaft systems, the IP and

HP rotational speeds are linked. After the relative error has dropped below Module 3's convergence limit of 10^{-3} , Loop 2 tunes the actual mass flow rate through the engine core to meet the target mass flow rate set by the core's nozzle. For the three turbofan engine options, Loop 2 simultaneously modifies the bypass mass flow rate to satisfy the separate bypass nozzle conditions. If the maximum thrust has to be determined, Loop 3 changes the turbine entry temperature until any of the design limits specified by Module 1 has been reached. These limits include the maximum rotational speed, the maximum turbine entry temperature and, in the case of the turboprop engine, the LPT power limit which is set at 85 % of the maximum power output based on the TP400 derate [85]. For the alternative output option, Loop 3 alters the turbine entry temperature until the required thrust level has been met.

3.1.4 Module 4: Airframe Performance

Before Sub-Module 4.2 can determine the aircraft's pitch angle and lift, Sub-Module 4.1 has to compute the various drag components listed in Fig. 3.6, based on Module 2's airframe design and the drag formulas given in Ref. [52]. The configuration of the gear, flaps, slats and spoilers and the engine-out condition are listed amongst the inputs in Fig. 3.6 because they affect the aircraft's parasite and induced drag. In order to determine the pitch angle of the aircraft, Sub-Module 4.2 has to calculate the wing's lift slope and the lift coefficient required to balance the thrust, weight and drag vectors. Since the pitch angle affects the thrust vector, the lift coefficient and the pitch angle are recalculated until the relative error drops below 10^{-10} .

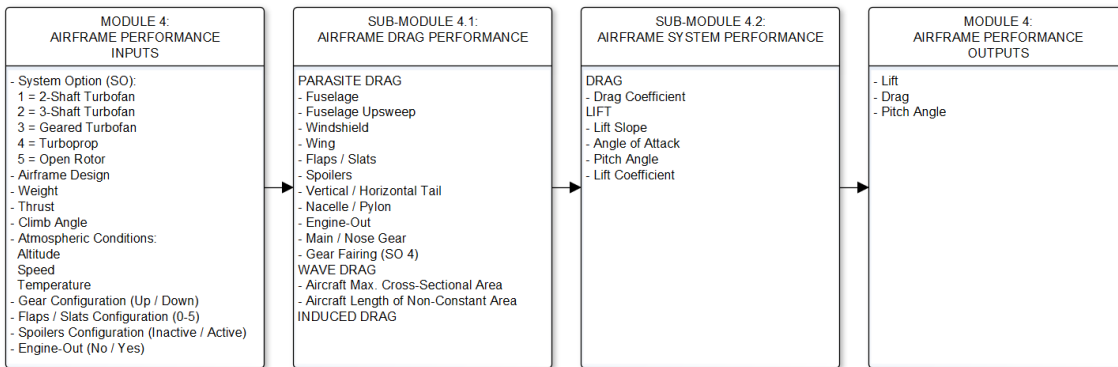


Figure 3.6: Airframe Performance Framework.

3.1.5 Module 5: Performance Requirement

The takeoff thrust or LPT power requirement for the final engine design is calculated by multiplying the respective estimate for the provisional engine design, given on page 41, by the maximum thrust ratio needed to meet the 10 performance requirements listed in Table 3.7. As a thrust ratio greater or smaller than unity affects the final engine and airframe performance, ideally, the system design should be updated until the thrust ratio converges towards 1. To save computing time, however, the convergence process is approximated by raising the thrust ratio to the power of 1.3 for the three turbofan options and 1.9 for the turboprop and the open rotor.

The initial and final cruise altitudes are the altitudes at which the true airspeed (in m/s) divided by the fuel consumption rate (in kg/s) is maximized, which depends on the aircraft design and weight. The temperatures are based on International Standard Atmosphere (ISA) conditions and the ISA temperature deviations given in Table 3.7. As the thrust changes significantly during takeoff and landing, where the Equivalent Airspeed (EAS) increases from $V_{EAS,min}$ to $V_{EAS,max}$ and vice versa, an average thrust value is used. According to Ref. [52], it is calculated at the airspeed, $V_{EAS,eng}$, specified by Eq. 3.6 for the three turbofan engines and Eq. 3.7 for the turboprop and open rotor. Each requirement is described in more detail in the following sub-sections.

$$V_{EAS,eng} = V_{EAS,min} + \frac{1}{\sqrt{2}} \times (V_{EAS,max} - V_{EAS,min}) \quad (3.6)$$

$$V_{EAS,eng} = V_{EAS,min} + 0.74 \times (V_{EAS,max} - V_{EAS,min}) \quad (3.7)$$

Table 3.7: Performance Requirements (based on Ref. [52] unless specified otherwise).

Requirement	Speed	Weight	Altitude	Gear	Flaps / Slats [78]	Spoilers	1 Engine- Out	ISA ΔT [60]	Thrust Level [54, 109]
<i>Takeoff Field Length (max. 2,000 m [60])</i>									
distance factor: 1.15 [54]	rotate at $1.1V_S$	MTOW	clear 35-ft obstacle	down	3	no	no	15	100 %
<i>Balanced Field Length (max. 2,000 m [60])</i>									
ground roll	accel. up to V_1	MTOW	0 ft	down	3	no	no	15	100 %
reaction time: 1 sec	V_1	MTOW	0 ft	down	3	no	yes	15	100 %
continued takeoff	rotate at $1.1 V_S$	MTOW	clear 35-ft obstacle	down	3	no	yes	15	100 %
rejected takeoff	brake to stop	MTOW	0 ft	down	3	yes	yes	15	7 %
<i>1st Segment Climb</i>									
climb gradient SO 4: 0.5 % others: 0.1 %	$1.25 V_S$	MTOW	35 ft	down	3	no	yes	15	100 %
<i>2nd Segment Climb</i>									
climb gradient SO 4: 3.0 % others: 2.4 %	$1.25 V_S$	MTOW	400 ft	up	3	no	yes	15	100 %
<i>3rd Segment Climb</i>									
climb gradient SO 4: 1.5 % others: 1.2 %	$1.25 V_S$	MTOW	1,500 ft	up	0	no	yes	15	87 %
<i>Initial Cruise Altitude Climb</i>									
climb rate: 300 ft/min [60]	cruise speed	0.975 MTOW	max. fuel efficiency	up	0	no	no	10	75 %
<i>Final Cruise Altitude Climb</i>									
climb rate: 300 ft/min [60]	cruise speed	1.04 ZFW ^a	max. fuel efficiency	up	0	no	no	10	75 %

^aZFW = Zero Fuel Weight

continued on next page

continued from previous page									
Require- ment	Speed	Weight	Altitude	Gear	Flaps / Slats [78]	Spoilers	1 Engine- Out	ISA ΔT [60]	Thrust Level [54, 109]
<i>Landing Distance (max. 1,600 m [60])</i>									
approach angle: -3°	$1.3 V_S$	MLW	50 ft	down	5	no	no	0	req. thrust
flare	$1.3 V_S$	MLW	50 ft	down	5	no	no	0	7 %
ground roll	brake to stop	MLW	0 ft	down	5	yes	no	0	7 %
<i>Approach Go-Around</i>									
climb gradient: SO 4: 2.7 % others: 2.1 %	$1.3 V_S$	MLW	1,500 ft	up	5	no	yes	15	100 %
<i>Landing Go-Around</i>									
climb gradient: 3.2 %	$1.3 V_S$	MLW	50 ft	down	5	no	no	15	100 %

Sub-Module 5.1: Takeoff Field Length

The average takeoff thrust reference value during the takeoff ground roll, rotation and climb transition is determined by the speed specified by either Eq. 3.6 or 3.7, where $V_{EAS,min}$ is zero and $V_{EAS,max}$ is equivalent to the takeoff velocity, which is approximately 25 % greater than the stall speed with the flaps and slats set at 3 out of a maximum setting of 5, as listed in Table 3.7.

Figure 3.7 shows that the takeoff ground roll is divided into 11 segments, each with an equal change in speed, ranging from zero to the rotation velocity, which is 1.1 times the stall velocity as indicated in Table 3.7. For each segment, the airframe performance module calculates the aircraft's lift and drag at the segment's average velocity. This data is needed so that Sub-Module 5.1 can determine the time needed to accelerate through each segment.

For the takeoff rotation, each segment now increases the total time by 0.5 seconds before the aircraft lift, drag, weight, deceleration and speed are calculated. As the aircraft rotates at a rate of $3^\circ/\text{sec}$, the pitch angle of the aircraft increases by 1.5° in each additional segment until the lift exceeds the aircraft weight. This initiates the takeoff climb transition with the only difference that the rolling friction coefficient is reduced from 0.025 [110] to zero and the aircraft rotation rate is decreased to $1.5^\circ/\text{sec}$. Additional climb transition

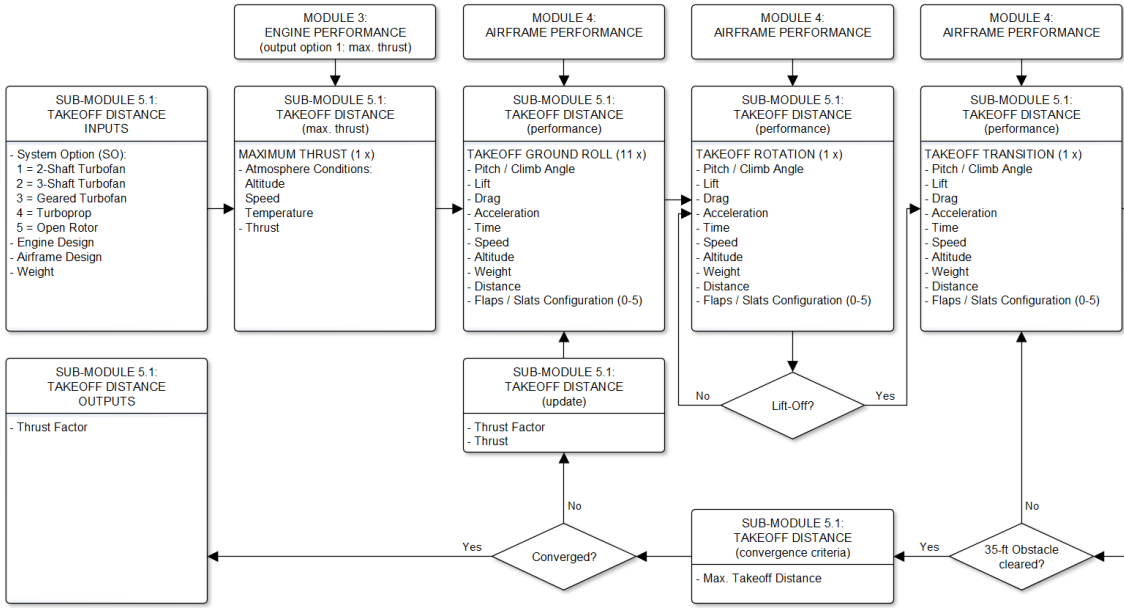


Figure 3.7: Takeoff Field Length Simulation Framework.

segments are added until the aircraft has climbed above the 35-ft obstacle height, as specified in Table 3.7.

The takeoff field length required to reach the obstacle height is then calculated by interpolation between the last two segments and the result is multiplied by Table 3.7's distance factor of 1.15 for safety reasons [54]. If the relative error between the actual takeoff field length and the maximum of 2,000 m, specified in Table 3.7, exceeds 10^{-10} , the thrust factor is adjusted and the takeoff performance reiterated until the convergence limit is reached, as illustrated in Fig. 3.7.

Sub-Module 5.2: Balanced Field Length

The balanced field length is the distance at which a continued or a rejected takeoff, after an engine failure at the speed V_1 , cover the same total distance [52]. For that reason, Fig. 3.8 shows that Sub-Module 5.2 first simulates a normal takeoff roll consisting of 11 segments up to V_1 , followed by another segment that models a 1-second reaction time. For the continued takeoff, Sub-Module 5.2 adds another 11 segments if the rotation speed has not been reached, followed by the takeoff rotation and climb transition as in Sub-Module 5.1. Apart from the braking coefficient of friction of 0.5 [52], the rejected takeoff assumes idle thrust for the operating engines and deployed spoilers and consists of 11 segments, during which the velocity reduces from the speed reached at the end of the reaction time down to

zero. As the aircraft covers similar speed ranges in Sub-Modules 5.1 and 5.2, the takeoff thrust reference value for the continued takeoff is based on the value calculated for the takeoff field length.

Before Sub-Module 5.2 can update the thrust factor required to meet the maximum balanced field length of 2,000 m given Table 3.7, Fig. 3.8 indicates that the model has to adjust V_1 and rerun the performance calculations until the relative error between the continued and rejected takeoff distances is two orders of magnitude smaller than the relative deviation from the maximum balanced field length. This convergence process is repeated until both relative errors are less than 10^{-10} .

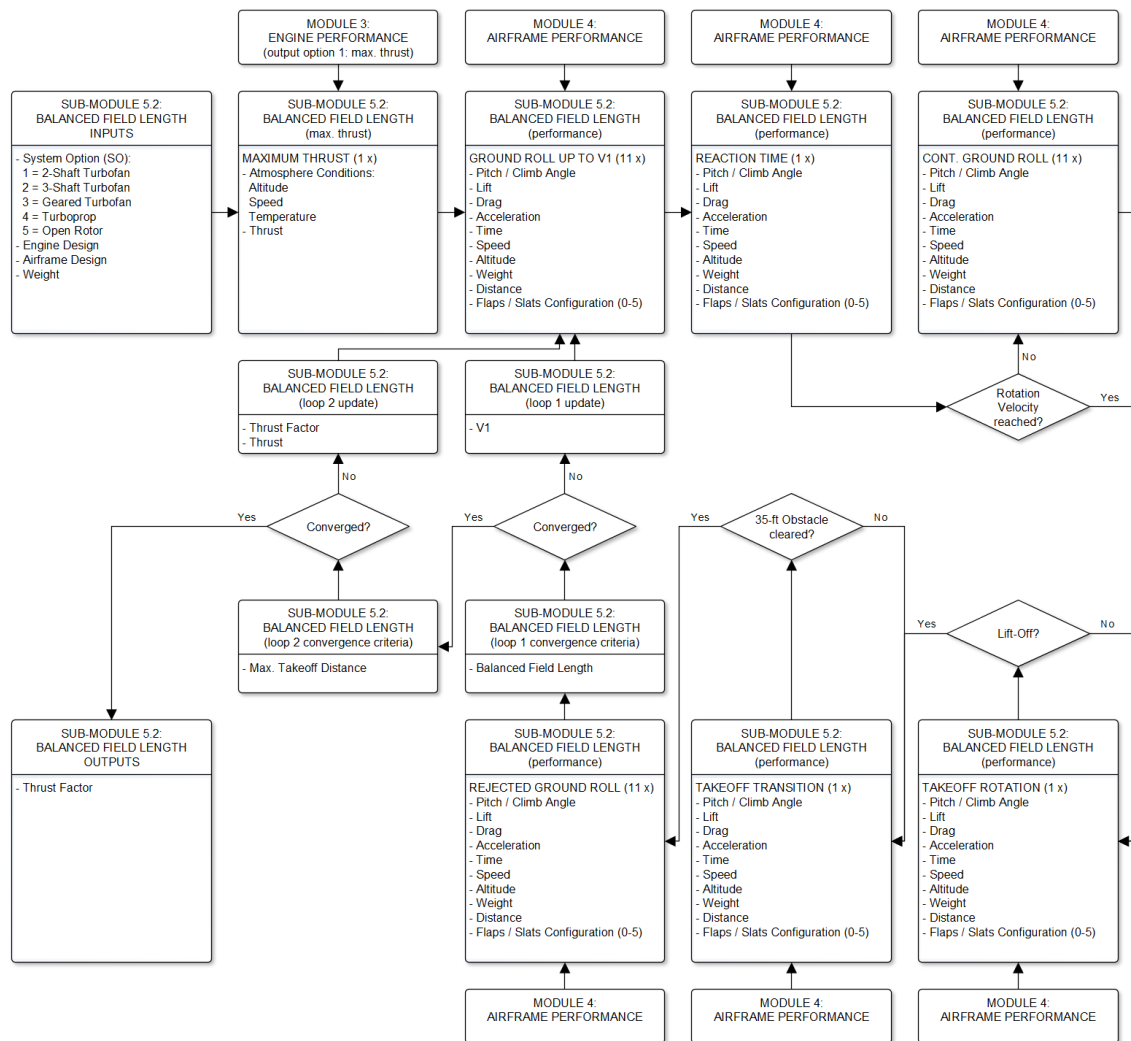


Figure 3.8: Balanced Field Length Simulation Framework.

Sub-Module 5.3: Climb Requirement

Figure 3.9 illustrates that Sub-Module 5.3 first determines the maximum thrust based on the speed, altitude and temperature specified by Module 5 and multiplies it by the specified thrust setting and the number of operating engines to obtain the reference thrust value. Sub-Module 5.3 then computes the thrust needed to meet the required climb gradient while counteracting the drag created by the specified aircraft configuration, altitude and speed. As the thrust affects the aircraft's pitch angle and hence its lift and drag, Sub-Module 5.3 has to call Module 4 and update the thrust factor until the relative error drops below 10^{-10} .

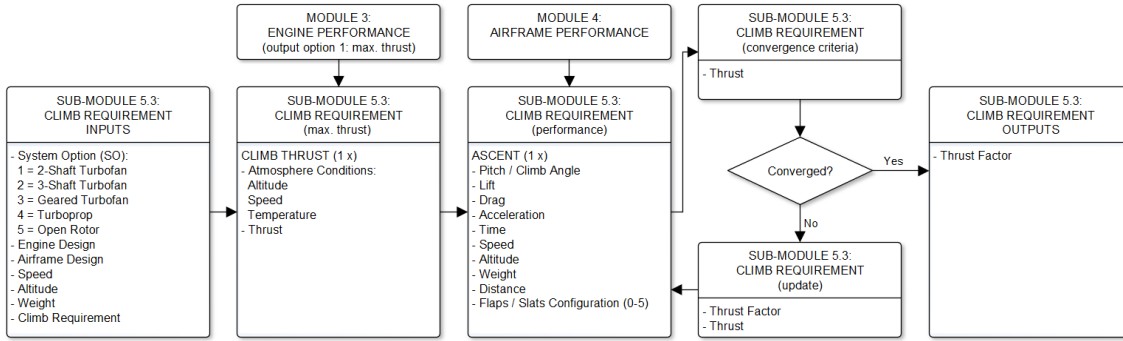


Figure 3.9: Climb Requirement Simulation Framework.

Sub-Module 5.4: Cruise Requirement

As for the climb requirement, the cruise thrust is determined iteratively in Sub-Module 5.4. Unlike in Sub-Module 5.3, however, the maximum thrust is only calculated for completeness because the main interest lies in computing the fuel consumption rate and hence the fuel efficiency, as indicated in Fig. 3.10. The effect of the thrust factor on the fuel efficiency of the final engine design is taken into account in Sub-Module 5.4 by first dividing the thrust and then multiplying the resulting fuel consumption rate by the thrust factor.

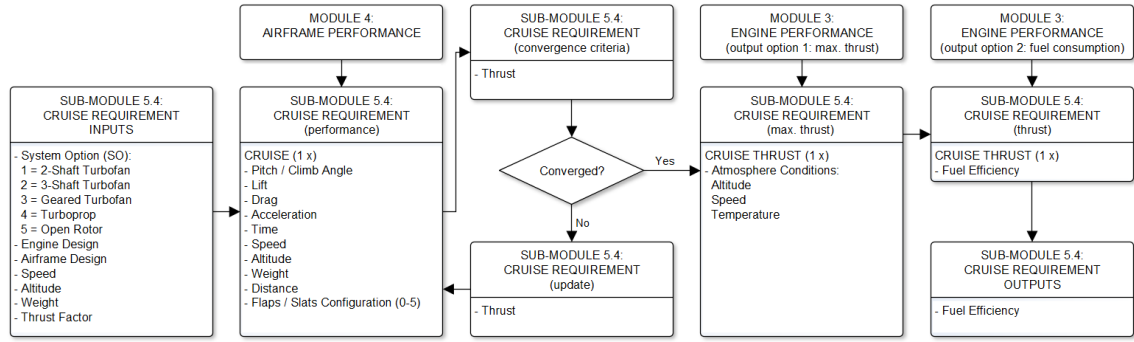


Figure 3.10: Cruise Requirement Simulation Framework.

Sub-Module 5.5: Landing Requirement

The landing distance is measured from where the aircraft is 50 ft above the runway to the stopping point, divided by a landing distance safety factor of 0.6 [52]. Table 3.7 on page 58 indicates that the aircraft descends towards the runway with an approach angle of -3° and an equivalent airspeed that is 30 % above the stall speed with the maximum flaps and slats setting of 5. From this information Sub-Module 5.5 can consequently calculate the height at which the landing flare arc has to be initiated to produce a centripetal acceleration of 0.2g. Sub-Module 5.5 models the final approach performance at mid height between the 50-ft obstacle and the landing flare initiation in order to determine the required thrust and the distance covered during the final approach, as displayed in Fig. 3.11.

The average idle thrust during the landing flare, rotation and ground roll is derived from multiplying the idle thrust setting of 7% by the thrust factor and the maximum thrust, which is determined at the speed specified by either Eq. 3.6 or 3.7 on page 57, where $V_{EAS,min}$ is zero and $V_{EAS,max}$ is equivalent to the approach velocity. Although the spoilers are deployed at touchdown, no reverse thrust is applied during the ground roll in this case. The landing flare arc is broken down into 11 segments of equal length. For each segment, Sub-Module 5.5 computes the pitch angle needed to achieve the flare angle specified by the arc. The landing rotation is also split into 11 segments with an equal change in pitch angle, a rotation rate of $3^\circ/\text{sec}$ and a rolling friction coefficient of 0.025. As for the takeoff requirements, the landing ground roll is divided into 11 segments with an identical change in speed from the nose-touchdown velocity down to zero and a braking coefficient of friction of 0.5.

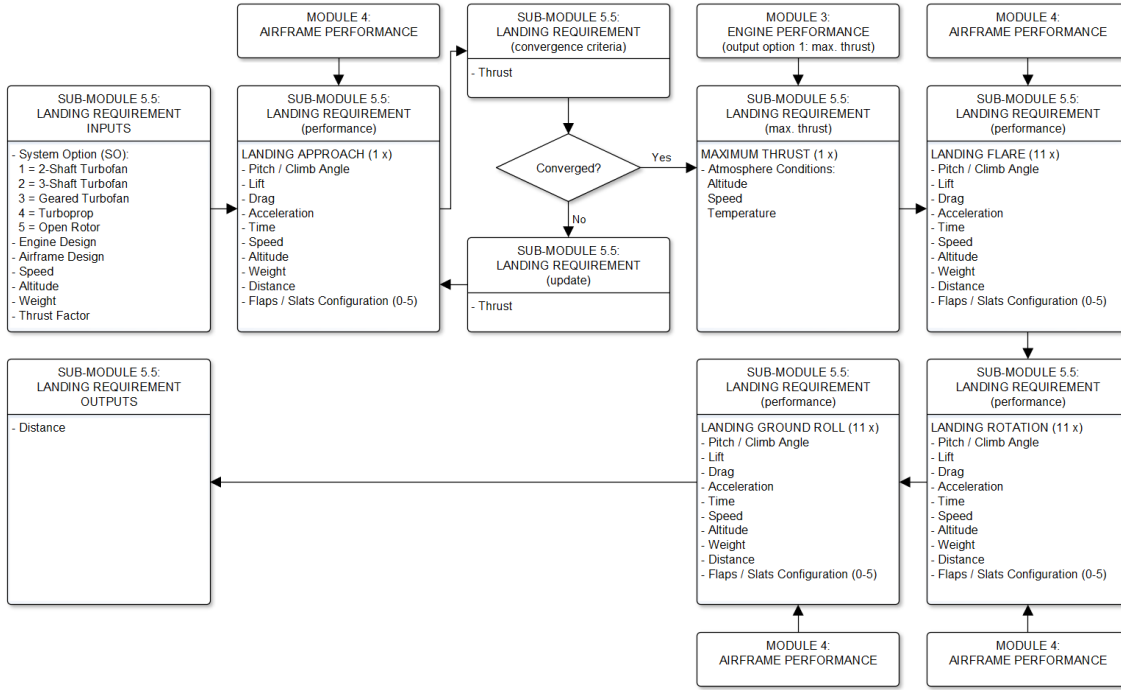


Figure 3.11: Landing Requirement Simulation Framework.

As Module 9's optimizer ensures that the wing area is large enough to allow a maximum approach speed of 135 kn EAS, the maximum landing distance specified in Table 3.7 can normally be met. In the unlikely case that it is not, the design iteration is terminated and the airframe design parameters adjusted accordingly by the optimizer.

3.1.6 Module 6: Flight Simulation

The flight profile simulated by Module 6 is adapted from Ref. [60] and is displayed in Fig. 3.12. It assumes ISA conditions with no temperature deviations and no winds and consists of three parts:

- the mission, which simulates the average flight distance of 1,546 km specified on page 20
- the continued cruise, which extends the mission's cruise by 45 minutes
- the diversion, which involves a rejected landing at the end of the mission and a 200-nautical-mile (nm) diversion to another airport

The mission climb and descent are carried out at the maximum equivalent airspeed, but is limited by the cruise Mach number. For a cruise Mach number of 0.78, the maximum

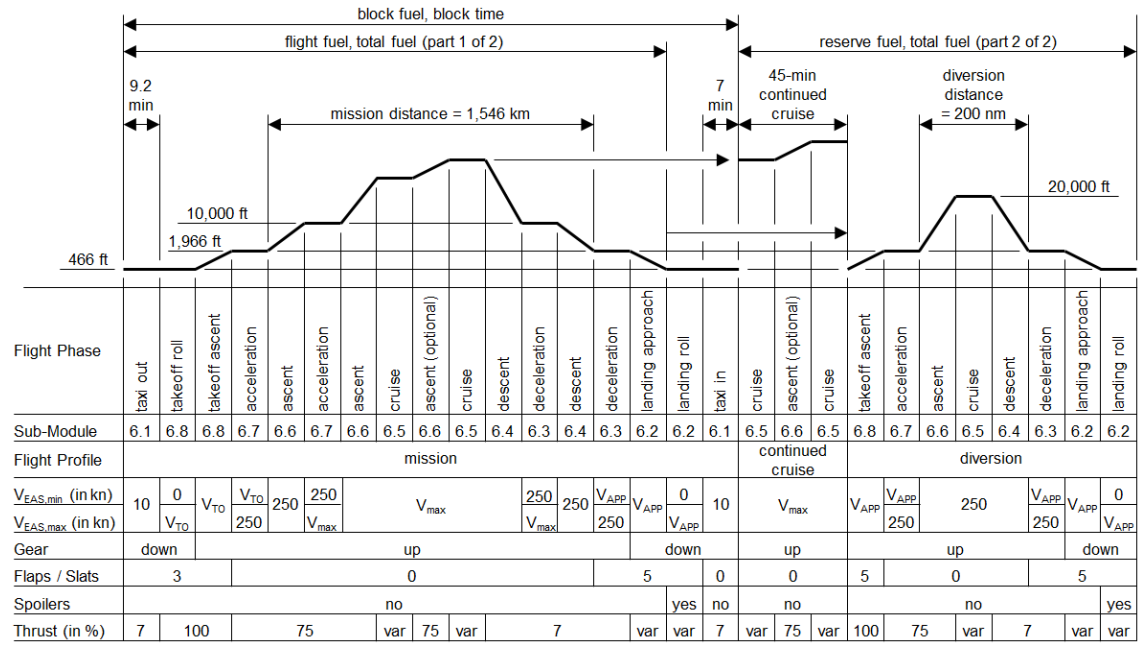


Figure 3.12: Flight Profile (partly adapted from Ref. [60]).

equivalent airspeed is 300 kn, which scales proportionately with any change in the cruise Mach number. Although only the mission's block fuel consumption and block time are used for the fuel cost and value of time analysis, the reserve fuel needed for the continued cruise and diversion is also critical because it contributes to the total fuel needed at the beginning of the mission. Although most of the block fuel is included in the total fuel, the fuel consumed during the mission's landing roll and taxi-in phases is not, because it is taken from the reserve fuel.

As the total fuel quantity is not known initially, Module 6 simulates the entire flight profile backwards, starting with the diversion landing roll where the total fuel quantity is zero. To avoid confusion, the naming convention assumes a forward flight simulation and any deviation from this convention is put in single quotation marks. Figure 3.12 indicates that the ground altitude is 466 ft above sea level because that is the average airport altitude of the 30 biggest European cities. The mission and diversion distances exclude the distance covered during takeoff, initial acceleration, final deceleration and landing, because these phases are primarily needed for air manoeuvres [60]. While each of the taxi, takeoff, acceleration, deceleration and landing phases only call their respective sub-modules once, the ascent, cruise and descent phases are divided into multiple sectors that are simulated by the sub-modules as follows:

- Between 1,966 and 10,000 ft, every ascent and descent phase is broken down into four sectors of equal height. Above 10,000 ft, the ascent and descent sectors are stacked at 2,000-ft intervals until the cruise altitude is reached. The performance of the aircraft is then determined by Sub-Modules 6.4 and 6.6 at mid-height of each sector.
- For the mission and continued cruise, Sub-Module 6.5 is called before each descent sector above 28,000 ft, so that the most fuel-efficient altitude can be selected. As before, fuel efficiency is measured by dividing the true airspeed (in m/s) by the fuel consumption rate (in kg/s).
- Sub-Module 6.5 updates the mission, continued and diversion cruise performance every 100 km to accurately simulate the effect of the ‘increasing’ fuel quantity on the aircraft weight, drag and fuel consumption rate.
- During the mission and continued cruise, the ‘increasing’ aircraft weight can make a 2,000-ft lower cruise altitude more fuel-efficient. As soon as that is the case, the aircraft ascends 2,000 ft, as illustrated in Fig. 3.12.
- Initially, Module 6 can only estimate the diversion cruise distance because the ascent profile is not known. Once the ascent has been simulated, however, Module 6 adjusts the cruise distance and recalculates the ascent profile until the diversion distance deviates by less than 0.1 km from the 200-nm target value. The same procedure and convergence limit is applied to meet the specified mission distance.

Sub-Module 6.1: Flight Taxi

Just like in Module 5, the idle thrust setting is 7 % of the maximum thrust. Figure 3.13 indicates that Sub-Module 6.1 therefore first calls Module 3 to determine the maximum thrust before calling it again to compute the fuel consumption rate for the idle thrust setting. Both thrust values are calculated at the same equivalent airspeed of 10 kn. Module 4 is only called to ensure that the idle thrust exceeds the aircraft’s drag, assuming Module 5’s rolling friction coefficient of 0.025. Since the taxi-out phase includes the engine start-up, this phase takes 2.2 minutes longer than taxiing to the terminal after landing. The taxiing time not only contributes to the block time but is also needed to determine the weight of the fuel burnt during this phase.

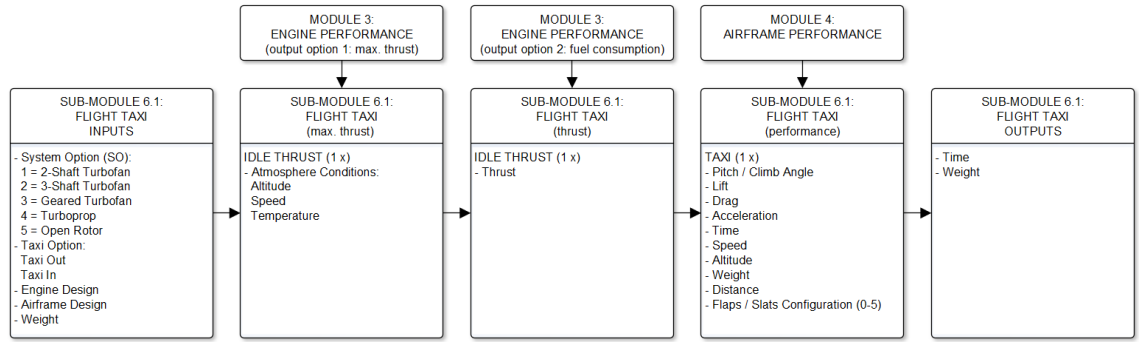


Figure 3.13: Flight Taxi Simulation Framework.

Sub-Module 6.2: Flight Landing

As in Module 5, the average idle thrust during the landing ground roll, rotation and flare is determined at the speed specified by either Eq. 3.6 or 3.7 on page 57, where $V_{EAS,min}$ is zero and $V_{EAS,max}$ is equivalent to the approach velocity, which is 30 % greater than the stall speed with the maximum flaps and slats setting of 5. For reverse thrust, $V_{EAS,max}$ is set at the nose-touchdown speed, which is approximately 1.2 times the stall velocity. For the turbofan engines $V_{EAS,min}$ is 70 kn and for the turboprop and open rotor 60 kn because reverse thrust is not applied below those speeds. While the turbofans have a reverse thrust setting of -45% , it is -60% for the turboprop and open rotor [52].

Figure 3.14 shows that the landing ground roll is once again divided into 11 segments, each with an equal change in speed, ranging from zero to the nose-touchdown velocity. As before, the airframe performance module calculates the aircraft's lift and drag at each segment's average velocity so that Sub-Module 6.2 can determine the time needed to decelerate through each segment, assuming a brake friction coefficient of 0.3 and deployed spoilers. In contrast to Module 5, however, the average idle thrust is replaced by the average reverse thrust value as soon as a segment 'exceeds' the minimum reverse thrust speed.

For the landing rotation, the idle thrust value and the rolling friction coefficient of 0.025 apply again and each segment now increases the total time by 0.5 seconds before the aircraft lift, drag, weight, deceleration and speed are calculated. As in Module 5, the aircraft rotates at a rate of $3^\circ/\text{sec}$, which means that the pitch angle of the aircraft 'increases' by 1.5° in each additional segment until the lift exceeds the aircraft weight. This 'initiates' the landing flare with the only difference that the rolling friction coefficient

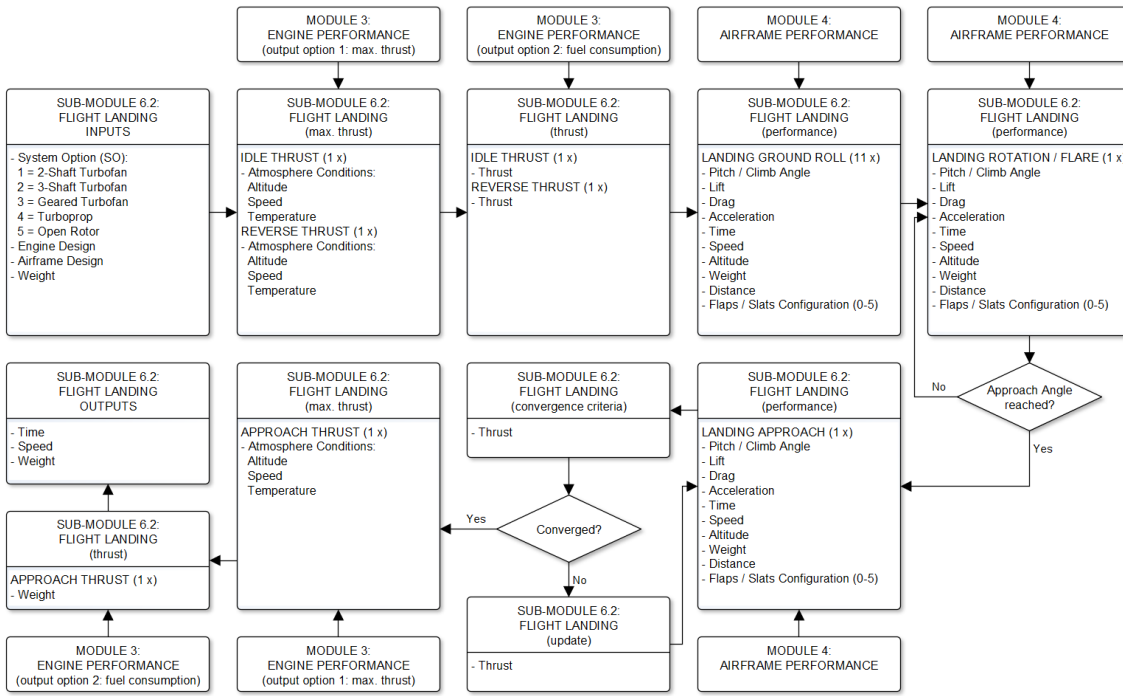


Figure 3.14: Flight Landing Simulation Framework.

is set to zero, the spoilers are ‘no longer’ deployed and with each new segment the aircraft pitch angle ‘reduces’ by the same amount as the climb angle does until the climb angle ‘reaches’ the approach angle of -3° . This rate of change in the pitch angle gives an average centripetal acceleration of 0.1 g.

As the approach angle, equivalent airspeed and initial and final altitude are specified by Fig. 3.12, the approach time and distance are fixed. Sub-Module 6.2 therefore only has to determine the thrust required to satisfy these conditions at the mid approach altitude. As the thrust affects the aircraft’s pitch angle and hence its lift and drag, Sub-Module 6.2 has to call Module 4 and re-calculate the thrust until the relative error drops below 10^{-10} . Although the maximum thrust is not needed to determine the approach thrust, the former is computed by Module 3 to ensure that the approach thrust exceeds the idle thrust setting. Finally, Module 3 is called a second time to determine the fuel consumption rate for the approach thrust setting so that the aircraft weight at the ‘end’ of the approach can be calculated. The gear is assumed to be deployed throughout the whole approach and is only ‘retracted before’ the deceleration phase.

Sub-Module 6.3: Flight Deceleration

For each flight deceleration phase, Module 6 provides the ‘initial’ aircraft weight and flaps and slats setting together with the altitude and the minimum and maximum speed. As for the landing roll, the maximum thrust is determined at the speed given by either Eq. 3.6 or 3.7 on page 57, which is then used to compute the fuel consumption rate for the idle thrust setting, as indicated in Fig. 3.15. The deceleration is divided into the standard 11 segments of equal change in speed, ranging from the minimum to the maximum velocity. For each segment, Sub-Module 6.3 adjusts the aircraft pitch angle until the lift balances the current aircraft weight. If the flaps and slats setting is greater than zero, Sub-Module 6.3 also checks whether the lift coefficient is below the minimum for the current flaps and slats setting. If it is, then the setting is ‘reduced’ by one. This process is repeated for each segment until the flaps and slats are fully ‘retracted’.

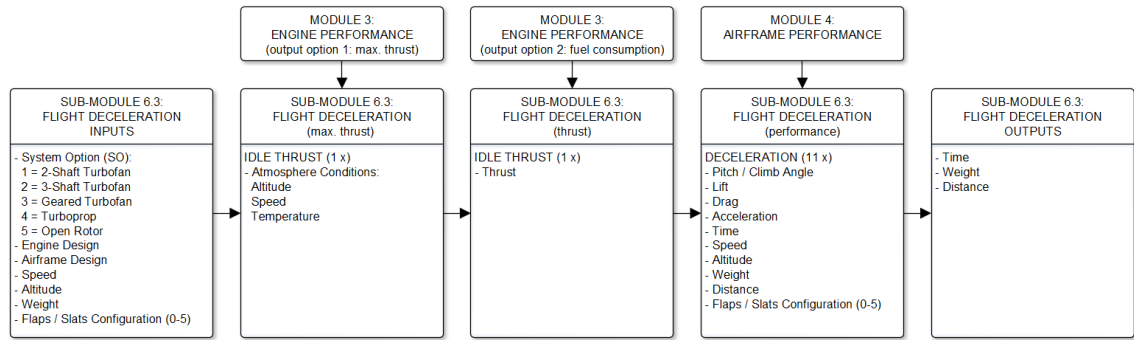


Figure 3.15: Flight Deceleration Simulation Framework.

Sub-Module 6.4: Flight Descent

Figure 3.16 shows that Sub-Module 6.4 simulates each descent sector in a similar way to the landing approach. Conversely to Sub-Module 6.2, however, here the climb angle is determined by the idle thrust while maintaining a constant equivalent airspeed but never exceeding the cruise Mach number. The climb angle not only affects the time needed to pass through each descent sector, but also the distance covered and the fuel consumed during that period.

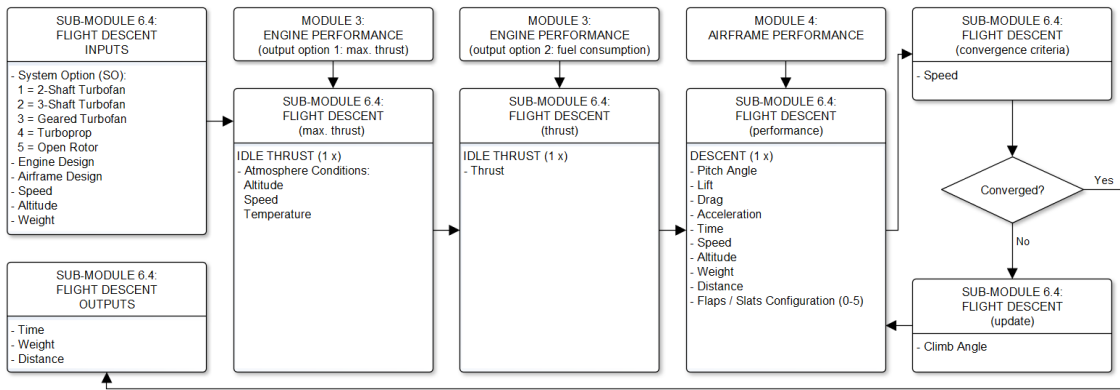


Figure 3.16: Flight Descent Simulation Framework.

Sub-Module 6.5: Flight Cruise

The flight cruise is also comparable to the landing approach as Fig. 3.17 indicates, except that the climb angle is set to zero and the speed at the cruise Mach number. As the cruise thrust setting is normally significantly greater than the idle thrust setting, the maximum thrust is only calculated for completeness.

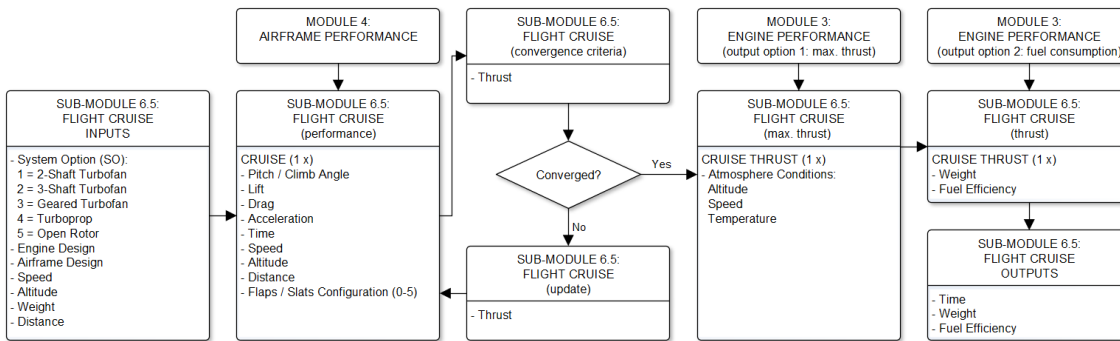


Figure 3.17: Flight Cruise Simulation Framework.

Sub-Module 6.6: Flight Ascent

Apart from the climb thrust setting of 75 % of the maximum thrust, the ascent modelling framework displayed in Fig. 3.18 is identical to the descent framework in Fig. 3.16.

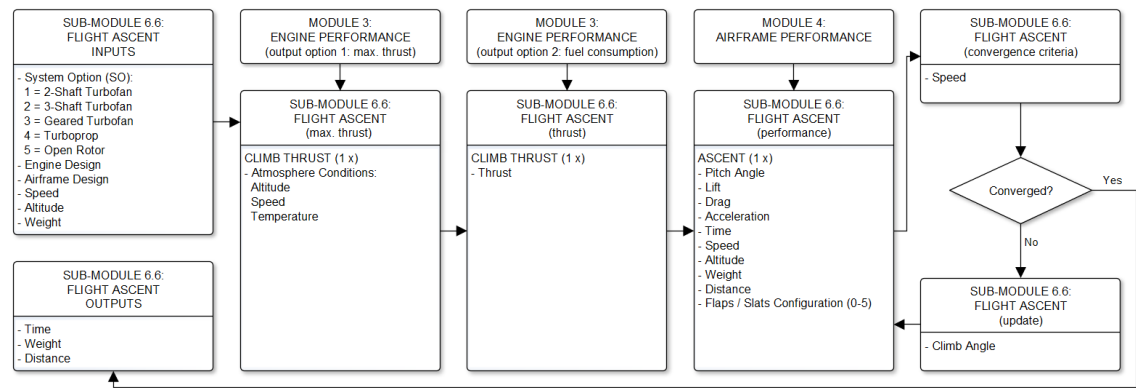


Figure 3.18: Flight Ascent Simulation Framework.

Sub-Module 6.7: Flight Acceleration

As for the ascent simulation, Fig. 3.19 indicates that Sub-Module 6.7 is a duplicate of its deceleration counterpart. The only difference is that Sub-Module 6.7 applies the climb thrust setting and uses the reverse flaps and slats setting process with different lift coefficient thresholds to model their ‘extension’. If the acceleration phase is taking place after a conventional takeoff, the flaps and slats setting is ‘limited’ to the takeoff setting of 3, whereas it is allowed to ‘increase’ to 5 for a baulked landing.

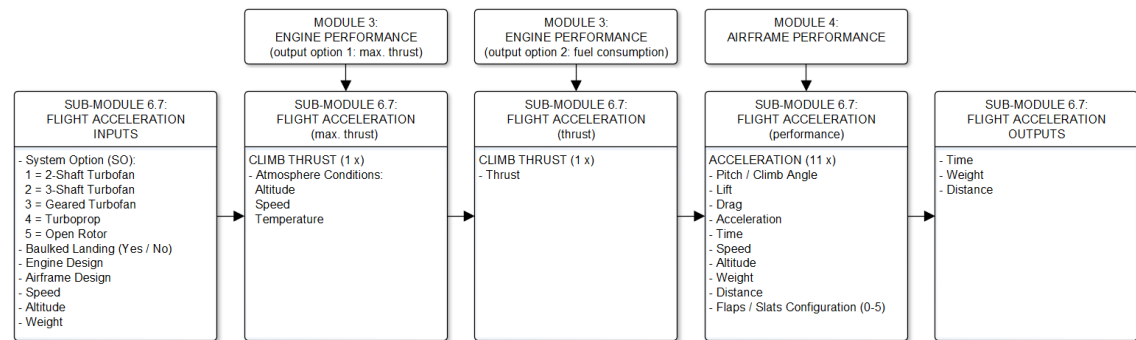


Figure 3.19: Flight Acceleration Simulation Framework.

Sub-Module 6.8: Flight Takeoff

The takeoff framework illustrated in Fig. 3.20 follows the reverse process of the landing depicted in Fig. 3.14 on page 68, but applies 100 % thrust throughout the takeoff. As for the ascent sectors, the climb angle during the takeoff climb depends on the thrust, which is calculated at mid height, just like the fuel consumption rate. During the whole takeoff climb, the gear is assumed to be retracted and the flaps and slats set at either 3 or 5,

depending on whether it is a conventional takeoff or a baulked landing.

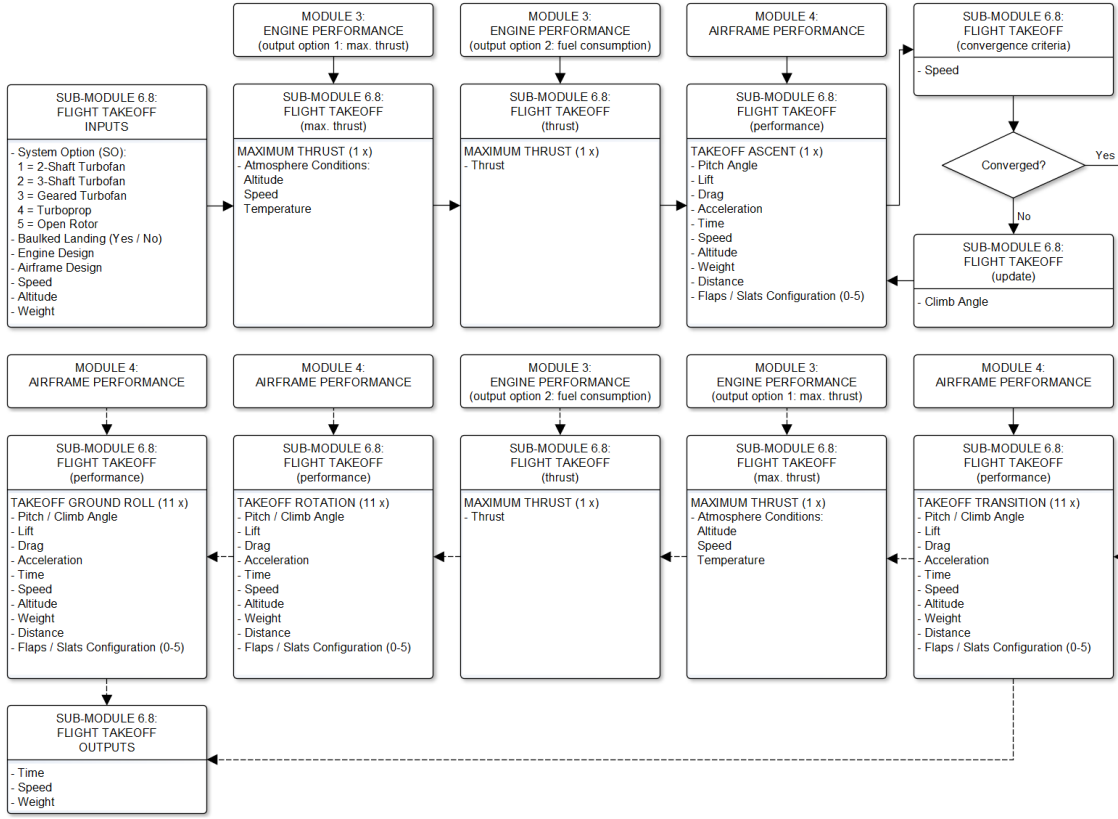


Figure 3.20: Flight Takeoff Simulation Framework.

In order to simulate a smooth takeoff transition between the takeoff climb and takeoff rotation and ground roll, the aircraft is assumed to follow a circular arc with a centripetal acceleration of $0.2g$, just like for the landing requirement in Sub-Module 5.5. This arc is broken down into 11 segments of equal length, for each of which Sub-Module 6.8 computes the pitch angle needed to achieve the climb angle specified by the arc segment. The thrust and fuel consumption rate throughout the takeoff transition is based on the values calculated for the takeoff climb.

Sub-Module 6.8 only simulates the takeoff rotation and ground roll for a conventional takeoff. While the 11 takeoff rotation segments have an equal change in pitch angle, the ground roll's 11 segments have an identical change in speed. The takeoff rotation rate is $3^\circ/\text{sec}$ and the rolling friction coefficient during both phases is 0.025 , just like for the landing rotation. Once again, either Eq. 3.6 or 3.7 is used to determine the average thrust and fuel consumption rate during these two phases as the aircraft speed 'decreases' from the takeoff velocity to zero.

3.1.7 Module 7: Aircraft Fleet Simulation

The System Study assumes that the world's single-aisle aircraft fleet, ranging from 100 to 210 seats per airliner, will fly 5.5 trillion revenue-passenger-kilometres (RPKs) in the Year 2030, based on Airbus' Global Market Forecast 2011–2030 [108]. This represents around 45 % of the total commercial RPKs predicted for 2030 and is slightly more than the total RPKs flown in 2010 [108].

In order to calculate how many single-aisle aircraft are needed to fly the 5.5 trillion RPKs and determine the annual flight hours and flight cycles per aircraft, Module 7 stochastically computes how many RPKs and flight hours and cycles one aircraft accumulates over an operating year, as illustrated in Fig. 3.21. For each flight, a random number between zero and one is sampled, which determines the number of aircraft seats, the flight distance and the turnaround time, as indicated in Fig. 3.21, assuming that the three parameters are correlated and that the aircraft is stretchable between each flight. Although this is physically not possible, only simulating one aircraft instead of the entire fleet drastically reduces the computing time with an error of less than 1 %. Based on this data, the flight's RPKs can be calculated, assuming a passenger seat utilization of 80 % [108]. The elapsed time is the sum of the turnaround time and the block time, which is based on Fig. 1.4's regression line equation on page 17, adjusted for the cruise speed specified by the optimizer. The model assumes a daily operating period of approximately 17 hours, based on the average curfew times of ten airports [111]. Figure 3.21 shows that if the total trip time for that day exceeds the operating period, the day count is increased by one. This process is repeated until the day count reaches 236. These are the number of operating days needed to fly the 5.5 trillion RPKs with Airbus' fleet size forecast of 22,975 single-aisle aircraft for the Year 2030 [108] cruising at the A320's current speed of Mach 0.78 [78].

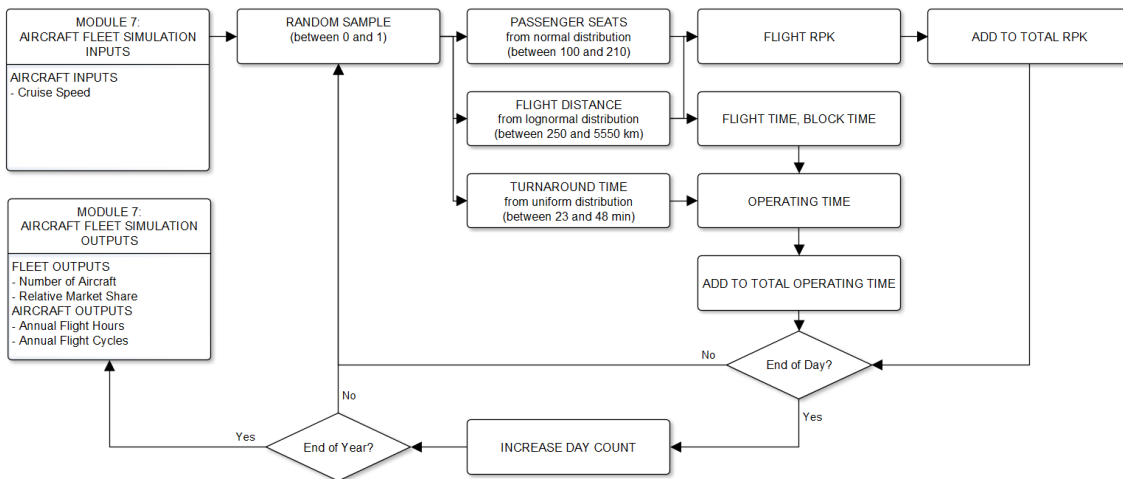


Figure 3.21: Aircraft Fleet Simulation Framework.

Figure 3.22 depicts the impact of the cruise speed on the fleet size and the annual flight cycles and flight hours per aircraft. The linear relationship between the annual flight cycles per aircraft and the cruise speed leads to an exponential increase in the number of aircraft required in order to fly the 5.5 trillion RPKs as the cruise velocity drops. The annual flight hours per aircraft do not change much, however, because the longer flight times are balanced by the reduced number of flight cycles, except when the cruise speed falls below 200 km/h where the aircraft only flies one mission a day but takes increasingly longer to do so.

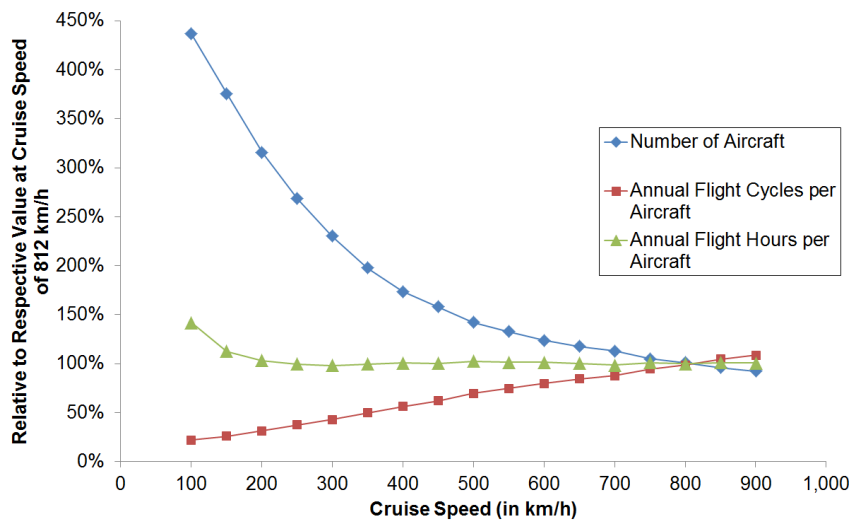


Figure 3.22: Fleet Size, Annual Flight Cycles and Flight Hours Vs. Cruise Speed.

The effect of the cruise speed on the modal shift, and thus the market share, is calculated using Fig. 1.6's Lognormal Cumulative Distribution on page 19 based on the average door-to-door speed. This market share is then divided by the market share for the A320's current cruise speed to obtain a relative value, as displayed in Fig. 1.9, which is needed for Module 8's cost calculations that are described in the next sub-section.

3.1.8 Module 8: Direct Operating Cost

The objective of Module 8 is to calculate the Mean Square Deviation (MSD) of the aircraft's direct operating cost to enable the optimizer to minimize the MSD. It is defined in Eq. 3.8, based on Eq. 1.3 on page 21, here shown to include the value of time. All costs are given in U.S. cents (¢) in 2012 prices.

$$\begin{aligned}
 MSD_{DOC} &= \frac{1}{M} \sum_{j=1}^M [(ADC_{RPK} + ATC_{RPK} + ASC_{RPK} + AMC_{RPK} \\
 &\quad + ARC_{RPK} + ALC_{RPK} + ANC_{RPK} + AGC_{RPK} + AVC_{RPK} \\
 &\quad + AFC_{RPK,j} + ACC_{RPK,j}) / f_{market}]^2
 \end{aligned}$$

MSD_{DOC} = mean square deviation of the direct operating cost
 M = number of samples (in this case 1,000)
 j = j^{th} sample
 ADC_{RPK} = aircraft depreciation cost per RPK (in ¢/km, 2012)
 ATC_{RPK} = aircraft interest cost per RPK (in ¢/km, 2012)
 ASC_{RPK} = aircraft insurance cost per RPK (in ¢/km, 2012)
 AMC_{RPK} = aircraft maintenance cost per RPK (in ¢/km, 2012)
 where ARC_{RPK} = aircraft crew cost per RPK (in ¢/km, 2012)
 ALC_{RPK} = aircraft landing cost per RPK (in ¢/km, 2012)
 ANC_{RPK} = aircraft navigation cost per RPK (in ¢/km, 2012)
 AGC_{RPK} = aircraft ground handling cost per RPK (in ¢/km, 2012)
 AVC_{RPK} = aircraft cost of time per RPK (in ¢/km, 2012)
 $AFC_{RPK,j}$ = aircraft fuel cost per RPK for sample j (in ¢/km, 2012)
 $ACC_{RPK,j}$ = aircraft carbon cost per RPK for sample j (in ¢/km, 2012)
 f_{market} = relative market share

(3.8)

Although Eq. 3.8 includes the value of time, a second MSD is calculated that excludes the opportunity cost of time to determine the effect on the optimum design and cruise speed in a monopolistic scenario where the passenger does not have the opportunity to choose a faster mode of transport. Eq. 3.8 also illustrates that the direct operating cost values are divided by Module 7's relative market share before they are squared to calculate the MSD. This means that a higher market share reduces the costs and vice versa. Although a net present value calculation of the profits generated could account for the market share more realistically, Section 3.2.3 on page 100 shows that the market share does not affect the results significantly.

Figure 3.23 gives an overview of the relationships between the input variables to Module 8 and the 10 or 11 cost elements that constitute the two direct operating cost outputs, one of which includes the value of time and the other does not. The lines in Fig. 3.23 are only coloured differently to make it easier to trace them. Each of the cost elements is discussed in more detail in the following sub-sections.

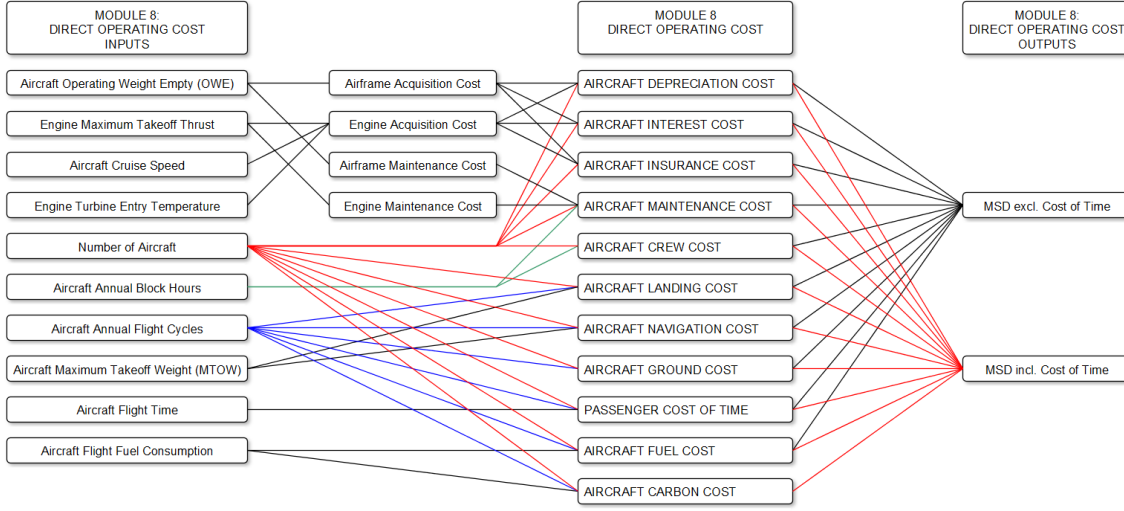


Figure 3.23: Direct Operating Cost Elements.

Aircraft Depreciation Cost

The airframe acquisition cost formula shown in Eq. 3.9, adapted from Raymer [52], is based on the aircraft's Operating Weight Empty (OWE). Since the formula is in 1995 U.S. dollars, the inflation rate between the Year 1995 and 2012 is taken into account, based on the values provided by the U.S. Department of Labor [29]. Although simplistic, this equation only overpredicts the average cost of the current Airbus A320 of \$72.6 million in 2012 prices [29, 78] by 4.3 %. To account for the increasing share of lighter but more expensive composites on future aircraft [54], the costs are increased by around 30 %. This percentage is derived from the OWE and price of the Boeing 787-9 [112].

$$FAC = (2.3 \times 10^6 + 816 \times OWE) \times (1 + i_{inf,1995}) \times f_{FAC}$$

where

FAC	=	airframe acquisition cost (in \$, 2012)	(3.9)
OWE	=	aircraft operating weight empty (in kg)	
$i_{inf,1995}$	=	inflation rate between 1995 and 2012	
f_{FAC}	=	composite airframe acquisition cost factor	

The input variables for Raymer's [52] engine acquisition cost formula are the maximum takeoff thrust, the cruise speed and the turbine entry temperature, as indicated by Eq. 3.10.

As before, the formula is adjusted for inflation and a cost increase of 10% added to the three-shaft turbofan to account for the lighter but more complex design in comparison to the two-shaft configuration.

$$\begin{aligned}
 EAC &= 2251 \times (9.66 \times F_{max} + 243.25 \times V_{Mach,max} + 1.74 \times TET - 2228) \\
 &\quad \times (1 + i_{inf,1999}) \times f_{EAC}
 \end{aligned}$$

where

$$\begin{aligned}
 EAC &= \text{engine acquisition cost (in \$, 2012)} \\
 F_{max} &= \text{maximum takeoff thrust (in kN)} \\
 V_{Mach,max} &= \text{cruise speed (in Mach)} \\
 TET &= \text{turbine entry temperature (in K)} \\
 i_{inf,1999} &= \text{inflation rate between 1999 and 2012} \\
 f_{EAC} &= \text{engine complexity acquisition cost factor}
 \end{aligned} \tag{3.10}$$

Eq. 3.11 shows how the two acquisition costs are converted into the aircraft depreciation cost in ¢ per RPK. The costs are divided by the average service life of an aircraft of 30 years [108], assuming a linear depreciation.

$$ADC_{RPK} = \frac{(FAC + n_{eng} \times EAC) \times 100 \times n_{fleet}}{L \times RPK}$$

where

$$\begin{aligned}
 n_{eng} &= \text{number of engines per aircraft} \\
 n_{fleet} &= \text{number of single-aisle aircraft worldwide in 2030} \\
 L &= \text{service life of aircraft (in years)} \\
 RPK &= \text{RPKs flown by single-aisle aircraft fleet in 2030 (in km)}
 \end{aligned} \tag{3.11}$$

Aircraft Interest Cost

The aircraft interest cost formula in Eq. 3.12 assumes an annual interest rate of approximately 9.8%, which was the mean interest rate for aircraft loans between 1985 and 2013 [113]. This rate is multiplied by 0.5 in Eq. 3.12 because this study assumes that the average aircraft is half way through its service life with a corresponding value of 50% of its acquisition cost.

$$ATC_{RPK} = \frac{i_{int} \times 0.5 \times (FAC + n_{eng} \times EAC) \times 100 \times n_{fleet}}{RPK}$$

where i_{int} = annual interest rate

$$\tag{3.12}$$

Aircraft Insurance Cost

Eq. 3.13 shows that the insurance cost is calculated the same way as the interest cost, except that the interest rate is replaced by an insurance rate of 0.2% [114].

$$ASC_{RPK} = \frac{i_{ins} \times 0.5 \times (FAC + n_{eng} \times EAC) \times 100 \times n_{fleet}}{RPK}$$

where i_{ins} = annual insurance rate

$$\tag{3.13}$$

Aircraft Maintenance Cost

Similar to the acquisition cost, Eq. 3.14 indicates that the airframe maintenance cost per block hour is based on the OWE, while the engine maintenance cost per block hour is purely derived from the maximum static thrust [54]. As these two costs are given per block hour, they are multiplied by the annual flight hours and the number of aircraft before dividing the result by the total annual RPKs to calculate the aircraft maintenance cost per RPK.

$$AMC_{RPK} = \frac{[(175 + 4.1 \times OWE/1,000) + n_{eng} \times (0.29 \times F_{max})] \times (1 + i_{inf,1994}) \times 100 \times n_{hours} \times n_{fleet}}{RPK} \quad (3.14)$$

where n_{hours} = annual block hours per aircraft

Aircraft Crew Cost

Jenkinson et al. [54] quotes cockpit crew costs of \$493 per block hour and \$90 per block hour per cabin crew member in 1989 prices, which is equivalent to \$913 and \$167, respectively, in 2012 prices. These values are multiplied by 0.5 in Eq. 3.15, as today's cockpit and cabin crew member costs are only \$534 and \$57 per block hour, respectively, assuming the cockpit is manned by two pilots, on average each pilot is paid £80,500 (\approx \$133,600) while each cabin crew member earns £17,250 (\approx \$28,600) for 1,000 flying hours per year, plus similar crew overhead costs [115, 116]. The System Study assumes that in 2030 there will still be two pilots and five cabin crew per aircraft, as specified by Ref. [60].

$$ARC_{RPK} = \frac{0.5 \times (ARC_{cockpit} + n_{cabin} \times ARC_{cabin}) \times (1 + i_{inf,1989}) \times 100 \times n_{hours} \times n_{fleet}}{RPK} \quad (3.15)$$

where $ARC_{cockpit}$ = aircraft cockpit crew cost (in \$/block hour, 1989)
 ARC_{cabin} = cost per cabin crew member (in \$/block hour, 1989)
 n_{cabin} = number of cabin crew members per aircraft

Aircraft Landing Cost

Eq. 3.16 shows that the aircraft charges per landing are proportional to the Maximum Takeoff Weight (MTOW) with a cost rate of \$6 per metric-ton in 1989 prices [54].

$$ALC_{RPK} = \frac{ALC_{MTOW} \times MTOW/1,000 \times (1 + i_{inf,1989}) \times 100 \times n_{cycles} \times n_{fleet}}{RPK} \quad (3.16)$$

where $MTOW$ = aircraft maximum takeoff weight (in kg)
 ALC_{MTOW} = aircraft landing cost per landing (in \$/metric-ton of MTOW, 1989)
 n_{cycles} = annual flight cycles per aircraft

Aircraft Navigation Cost

The air traffic control charges per flight [54] are dependent on the distance flown, in this case 1,546 km, as well as the maximum takeoff weight, as Eq. 3.17 illustrates.

$$ANC_{RPK} = \frac{d_{mission}/5 \times \sqrt{MTOW/(1,000 \times 50)} \times (1 + i_{inf,1989}) \times 100 \times n_{cycles} \times n_{fleet}}{RPK} \quad (3.17)$$

where $d_{mission}$ = flight mission distance (in km)

Aircraft Ground Cost

According to Jenkinson et al. [54], the ground handling charges are \$ 110 per metric-ton of payload in 1989 prices. As Table 3.6 on page 54 shows that the payload mass is constant, the ground handling cost per RPK, calculated using Eq. 3.18, is also constant.

$$AGC_{RPK} = \frac{AGC_m \times m_{payload} / 1,000 \times (1 + i_{inf,1989}) \times 100 \times n_{cycles} \times n_{fleet}}{RPK} \quad (3.18)$$

where $m_{payload}$ = payload mass (in kg)
 AGC_m = aircraft ground handling cost per landing (in \$/metric-ton of payload, 1989)

Passenger Cost of Time

The passenger value of time of approximately \$ 58/hour in 2012 prices, quoted on page 17, is converted into a cost per RPK using Eq. 3.19.

$$AVC_{RPK} = \frac{VOT \times t_{block} / 60 \times n_{pas} \times 100 \times n_{cycles} \times n_{fleet}}{RPK} \quad (3.19)$$

where VOT = value of time per passenger (in \$/hour, 2012)
 t_{block} = block time per flight (in min)
 n_{pas} = number of passengers per flight (see Table 3.6 on page 54)

Aircraft Fuel Cost

The best and worst case oil price scenarios of 73 and 196 \$/barrel (2012 prices), given on page 11, were modelled as a uniform uncertainty distribution using 1,000 random samples. These oil price samples were then converted into jet fuel costs using the formula given in Fig. 3.24 for the historical linear correlation between the prices per barrel of West Texas Intermediate (WTI) crude oil and jet fuel [117].

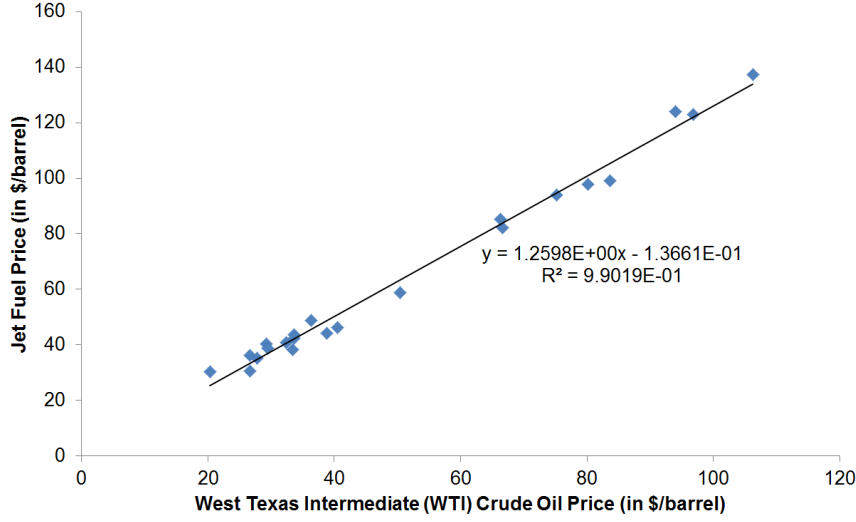


Figure 3.24: Correlation between Crude Oil and Jet Fuel Prices (based on U.S. passenger airlines data [117]).

The regression equation displayed in Fig. 3.24 is needed in Eq. 3.20 to convert the fuel consumed during the flight into a fuel cost per RPK. This calculation is carried out for each of the 1,000 oil price samples.

$$AFC_{RPK,j} = \frac{(1.2598 \times OP_j - 0.1366) / (BTL \times \rho_{fuel}) \times m_{fuel} \times 100 \times n_{cycles} \times n_{fleet}}{RPK}$$

where

OP_j	=	oil price of sample j (in \$/barrel, 2012)	(3.20)
BTL	=	U.S. barrel-to-litre conversion (1 bbl \equiv 158.99 l)	
ρ_{fuel}	=	density of jet fuel (0.8 kg/l)	
m_{fuel}	=	fuel consumption per flight (in kg)	

Aircraft Carbon Cost

As with the oil price, the carbon price is randomly sampled 1,000 times to create a uniform uncertainty distribution between 0 and 186 \$/metric-ton of CO₂ in 2012 prices and converted into a cost per RPK using Eq. 3.21. The reason for using \$0 as the lower carbon price limit, instead of the \$62 specified on page 12, is to account for countries that will not have an emission trading programme in 2030.

$$ACC_{RPK,j} = \frac{CP_j \times m_{fuel} / 1,000 \times CFR \times 100 \times n_{cycles} \times n_{fleet}}{RPK}$$

where

CP_j	=	carbon price of sample j (in \$/metric-ton of CO ₂ , 2012)	(3.21)
CFR	=	CO ₂ -fuel-weight ratio (3.16 kg CO ₂ \equiv 1 kg jet fuel)	

3.1.9 Module 9: Optimizer

Optimization is the search for a set of numerical or non-numerical inputs that either minimize or maximize the outputs of an objective function, taking inequality or equality constraints into account [13]. As with most design work [13], the System Study's objective function, the MSD of the direct operating cost, is characterized by a discontinuous relationship with the design parameter inputs listed in Table 3.1 on page 43. This is due to the fact that every gas turbine design has a discrete number of compressor and turbine stages that are subject to the numerous constraints given on page 48. These constraints are also the reason why the gas turbine design and performance modules become unstable if the design parameters are varied randomly and consequently diverge significantly from realistic solutions, as would be the case with an evolutionary search method like the genetic algorithm [13].

For this reason, an optimization method had to be found that could search locally, starting with the V2500 engine and A320 airframe specification, but deal with multiple continuous inputs and discontinuous but deterministic outputs. As indicated in Table 3.8, the non-gradient heuristic Direct Searches satisfy these requirements because, unlike gradient-based approaches, they do not calculate the local gradient which makes them insensitive to discontinuities [13]. Although there are several other Direct Searches, the approach developed by Hooke and Jeeves [118] was chosen because of its inherent simplicity and robustness [13].

Table 3.8: Optimization Method Requirements.

Optimization Method	Example	Inputs			Outputs	
		Continuous or Discrete	Single or Multiple Inputs	Local or Global Search	Linear or Non-Linear or Discontinuous	Deterministic or Time-Dependent or Stochastic
		continuous	multiple	local	discontinuous	deterministic
Direct Search	Hooke and Jeeves	✓	✓	✓	✓	✓
Gradient-Based	Conjugate Gradient	✓	✓	✓	✗	✓
Evolutionary Approaches	Genetic Algorithm	✓	✓	✗	✓	✓
Design of Experiments	Latin Hypercube	✓	✓	✗	✗	✓
Response Surface Methods	Kriging	✓	✓	✗	✗	✓

As Direct Searches cannot find the global optimum if they first have to pass poorer designs, it is critical to choose a good starting point and initial step length [13]. Starting with the V2500 engine and A320 airframe design as mentioned above, an initial step length of 4 % of the design parameter ranges listed in Table 3.1 on page 43 was chosen, which is equivalent to the values given in Table 3.9.

Table 3.9: Optimization Step Lengths.

Engine	Airframe
<ul style="list-style-type: none"> • turbine entry temperature: ± 20 K • overall pressure ratio: ± 1.2 • fan pressure ratio (SO 1–3): ± 0.028 • propeller diameter (SO 4–5): ± 0.08 m • maximum propeller rotational tip speed (SO 4–5): ± 8 m/s 	<ul style="list-style-type: none"> • wing span: $\approx \pm 1.6$ m • mean wing chord length: $\approx \pm 0.16$ m

The search was terminated as soon as the step length had to be halved for the first time due to the relatively high run time of around two hours per design iteration. Despite the unrefined search, the author believes he made a good compromise between ensuring model stability, tolerating discontinuities, acceptable convergence time and getting as close to the local optimum as possible.

As engine efficiency generally improves with a higher turbine entry temperature, higher overall engine pressure ratio, lower fan pressure ratio (i.e. higher bypass ratio), but leads to higher operating costs based on the cost formulas presented in the previous section, and similar conflicts apply to the other design parameters, it is unlikely that the design space is characterized by a multi-modal landscape where the global optimum diverges significantly from the V2500 engine. Consequently there is a good chance that the local optimum found by the optimizer is also the global optimum.

3.2 Results and Discussion

3.2.1 Optimum Design

The following sub-sections give an insight into the design and cost space surrounding the design optimum of each system option given in Table 3.10, based on the results in Tables A.1 to A.10 in Appendix A on pages 136–145. The first line in each table in Appendix A lists the optimum solution’s design and cost data. The remaining lines then

indicate how a one-design-factor-at-a-time change affects the design and cost relative to the optimum. While the three turbofan options were optimized for a cruise speed of Mach 0.78, the turboprop and open rotor were configured for Mach 0.70. Visual representations of the optimum designs are shown in Figs. 2.1 to 2.5 on pages 29–35. None of the system options have been optimized for other cruise speeds, which means that the open rotor with the higher cruise speed of Mach 0.76, referred to as System Option 5.2 and depicted in Fig. 2.6 on page 36, is based on System Option 5.1, i.e. the open rotor with the lower cruise speed of Mach 0.70 displayed in Fig. 2.5.

Table 3.10: Optimized System Design Parameters.

Design Parameters	SO 1: Two-Shaft Turbofan	SO 2: Three-Shaft Turbofan	SO 3: Geared Turbofan	SO 4: Turbo- prop	SO 5.1: Open Rotor
Cruise Speed (in Mach)	0.78	0.78	0.78	0.70	0.70
Turbine Entry Temperature (in K)	1,820	1,880	1,920	1,480	1,900
Overall Pressure Ratio	32.2	35.8	33.4	21.2	37.0
Fan Pressure Ratio ^a	1.80	1.78	1.78		
Propeller Diameter (in m) ^b				4.12	4.36
Max. Propeller Rotational Tip Speed (in m/s) ^b				227.2	283.2
Wing Span (in m)	36.0	36.0	35.8	35.3	35.2
Wing Mean Chord Length (in m)	3.31	3.31	3.26	3.24	3.17
Max. Static Thrust (in kN)	127.5 ^c	131.4 ^c	117.8 ^c	58.3 ^d	172.3 ^c
Critical Thrust Requirement ^e	1	5	1	1	5
Max. LPT Power (in MW) ^b				5.30 ^d	21.62 ^c
Fan Diameter (in m) ^a	1.79	1.83	1.74		
Bypass Ratio ^{a,f}	6.75	7.46	7.78		
Min. Blade Height (in mm)	13.1	15.4	13.0	13.1	13.3
Engine Mass (in kg)	1,868	1,871	1,449	809	2,042
Max. Takeoff Weight (in kg)	70,232	70,280	68,870	67,541	69,241
Initial Cruise Altitude (in ft)	32,000	32,000	32,000	30,000	30,000
Final Cruise Altitude (in ft)	38,000	38,000	38,000	36,000	36,000
Mission Fuel (in kg)	4,563	4,433	4,399	3,936	3,870

^aapplies to SO 1–3

^bapplies to SO 4–5

^cat $\Delta T = 15$ K, includes the thrust growth factor of 1.25

^dat $\Delta T = 15$ K, includes the thrust growth factor of 1.25 and the max. power derate factor of 0.85

^e1 = takeoff field length, 2 = balanced field length, 3 = 1st segment climb, 4 = 2nd segment climb, 5 = 3rd segment climb, 6 = initial cruise altitude, 7 = final cruise altitude

^fat max. static thrust

System Option 1: Two-Shaft Turbofan

Table A.1 illustrates that an increase in Turbine Entry Temperature (TET) would lead to a higher thrust requirement because the limiting factor for the takeoff thrust is the rotational speed which, due to the stochastic effect of the various design constraints listed on page 48 on the engine design module, is more restrictive for the higher TET. This higher thrust requirement would consequently result in a greater fan diameter and engine mass and hence a higher fuel consumption and operating cost.

As a lower TET would require a higher engine mass flow in order to generate the same thrust, this would also result in a heavier engine, greater fuel consumption and operating cost. Furthermore, the increased aircraft weight would lead to a wing span that exceeds the limit of 36 m and a breach of the minimum blade height of 13 mm due to the stochastic engine design process.

A higher Overall Pressure Ratio (OPR) would produce a favourable engine performance and mass and therefore a fuel consumption and operating cost reduction, but it would violate the minimum blade height constraint. Conversely, a lower OPR would not lead to a blade height violation but to a less cost-efficient engine.

Although a higher Fan Pressure Ratio (FPR) would reduce the bypass ratio and hence the propulsive efficiency, only the stochastic engine design process can explain the increase in engine weight and thrust. A lower FPR would consequently result in a higher bypass ratio but the propulsive efficiency gain would be outweighed by the higher fuel consumption due to the mass and drag increase from the larger fan diameter.

The increased aircraft weight due to a higher wing span would be overcompensated by the reduced drag and fuel consumption which would lead to an operating cost saving. Unfortunately, a higher wing span would exceed the limit specified earlier. It is therefore not surprising that a lower wing span would not violate the constraint but would be less cost-efficient.

Although a greater wing chord length would increase the wing area which would reduce the takeoff speed and hence the takeoff thrust requirement, the lower engine weight would be counteracted by the increased fuel consumption due to the higher cruise drag. A reduced wing chord length, on the other hand, would increase the takeoff thrust requirement by such a large amount that this would lead to a higher fuel burn and greater operating costs.

System Option 2: Three-Shaft Turbofan

In comparison to System Option 1, the optimum three-shaft turbofan has a higher TET and OPR because Table 3.10 and Fig. 2.2a on page 30 show that the three-shaft layout is not restricted by the minimum blade height. The optimum three-shaft configuration also has a slightly lower fan pressure ratio than its two-shaft counterpart because the higher bypass ratio does not lead to a significant thrust requirement increase. However, System Option 2 has a slightly higher maximum static thrust and is marginally heavier because the mass and drag of the increased fan diameter outweighs the weight saving from the more compact three-shaft design. Nevertheless, Table A.4 highlights that the higher TET and OPR and lower FPR lead to a fuel cost saving of 2.8%. This cancels out the 10% engine acquisition cost penalty imposed due to the complexity of the three-shaft layout, as explained on page 77.

Except for not violating the minimum blade height constraint, Table A.3 shows that three-shaft's design space is similar to System Option 1's displayed in Table A.1. The only difference is that Table A.3 indicates that a higher OPR would not lead to a reduced thrust requirement as in Table A.1, which, again, would be caused by the stochastic engine design process. Consequently, Table A.4 highlights that the reduced fuel consumption due to the higher OPR would be outweighed by the extra costs incurred by the higher engine weight.

System Option 3: Geared Turbofan

Table 3.10 illustrates that the optimum geared turbofan design has an even higher TET than System Option 2, the same fan pressure ratio, but a lower OPR to remain above the minimum blade height. Unlike with the two- and three-shaft turbofan, Table A.5 shows that a lower fan pressure ratio would lead to a higher fuel efficiency but this is trumped by the higher engine and airframe weight and the associated cost.

As Fig. 2.3a on page 31 displays that the geared turbofan only has eight HPC and three LPT stages in comparison to the two-shaft's nine HPC and six LPT stages depicted in Fig. 2.1a, the engine mass is reduced by over 22%, despite the additional weight of the gearbox. Although this mass saving only decreases the maximum takeoff weight by 2%, it notably reduces the maximum thrust requirement and the fan diameter, and therefore the fuel consumption by 3.6% and the operating cost (excluding the value of time) by 2.2%

in comparison to the two-shaft turbofan.

System Option 4: Turboprop

As the turboprop aircraft is the only system option with four engines, Table 3.10 indicates that the maximum static thrust requirement is approximately half of the three turbofan options. As an engine failure in this case is not as critical, it is not surprising that Table A.7 illustrates that the thrust requirement is regularly set by the initial cruise altitude and never by the initial climb segments.

In order to avoid a violation of the minimum blade height due to the drastically lower thrust requirement and its effect on the core mass flow, the optimum turboprop engine's TET is only 1480 K and its OPR only 21.2 in comparison to the three-shaft turbofan's TET of 1880 K and OPR of 35.8.

The turboprop engine only weighs 43 % of the three-shaft turbofan, despite the propeller and the gearbox, partly because of the low thrust requirement, but also because the low OPR and the gearbox significantly reduce the stage count: Fig. 2.4a on page 33 shows that the turboprop engine only has four IPC and three LPT stages in comparison to the three-shaft's seven IPC and six LPT stages displayed in Fig. 2.2a.

The optimum turboprop design agrees well with that of the TP400-D6 engine considering that the propeller's maximum rotational tip speed of 227.2 m/s and disc loading of 398 kW/m² only deviate by 3 % and 7 % respectively from the TP400's tip speed of 233.7 m/s and disc loading of 372 kW/m² [85]. The maximum takeoff weight is also lower than for the turbofan options, primarily because of the reduced aerodynamic loads acting on the airframe at Mach 0.70 instead of Mach 0.78.

Table A.7 shows that a greater propeller diameter would increase the engine mass and therefore the thrust requirement, maximum takeoff weight, fuel consumption and operating cost. Although a smaller propeller diameter would consequently reduce the engine weight, the reduced propeller efficiency due to the higher propeller disc loading would lead to a greater fuel consumption that would outweigh the weight saving.

A higher propeller tip speed would greatly increase the operating cost because it would lead to a higher initial cruise altitude and therefore a much higher thrust requirement. A reduced tip speed paradoxically leads to the same result which shows that the initial cruise altitude is highly sensitive to the tip speed.

The initial cruise altitude is similarly sensitive to an increase in either the wing span or the wing chord length, which is why a greater wing span would not reduce the operating costs, unlike for System Options 1–3. However, similar to the turbofan options, a lower wing span or wing chord length would also increase the operating costs because of the higher thrust required to meet the maximum takeoff field length.

Despite the low TET and OPR, the propeller makes the turboprop the most fuel-efficient aircraft described so far with a fuel consumption and an operating cost (excluding the value of time) that are respectively 13.7 % and 4.3 % lower than the two-shaft turbofan's.

System Option 5.1: Open Rotor

Although the open rotor is unducted, just like the turboprop, Table 3.10 reveals that the optimum open rotor design is markedly different to the optimum turboprop configuration. As with the three turbofan options, there are only two open rotor engines per aircraft. This means that the open rotor's LPT has to generate approximately three times as much power and thrust as each turboprop engine in order to satisfy the third segment climb requirement with an engine-out. Consequently, the optimum open rotor design has a similar TET and OPR as the geared turbofan. As with the geared turbofan, a higher TET and OPR is not feasible due to the minimum blade height.

Despite the similar diameter, the higher blade number means that the total surface area of the two propellers is almost 2.5 times as much as the turboprop's. In addition, the open rotor's maximum propeller tip speed is 25 % greater than the turboprop's. As lift increases with the square of the speed for a given lift coefficient, density and surface area, each propeller blade therefore generates 55 % more lift, i.e. thrust, even without increasing the angle of attack.

Table A.9 shows that a greater propeller diameter would reduce the fuel consumption. Although this would be cost-effective because the fuel saving would outweigh the increased engine weight, the blade height would again drop below the limit due to the stochastic engine design process.

Unlike all other system options, the open rotor is at the lower wing chord length limit, as an increase would raise the drag and hence the fuel consumption, which would financially outweigh the reduced power requirement and engine weight, similar to an increase in the

propeller's rotational tip speed.

Due to the high power and thrust output and the two propeller rows that are driven by a complex gear mechanism, the open rotor is 9.3% heavier than the two-shaft turbofan. Consequently, the maximum takeoff weight is 2.5% higher than the turboprop's, despite also cruising at Mach 0.7. Nevertheless, the high TET and OPR outweigh the increased weight in terms of fuel efficiency in comparison to the turboprop. The open rotor is therefore paradoxically the heaviest but also the most fuel-efficient system option investigated, with a fuel consumption that is 15.2% lower than the two-shaft turbofan's. However, the open rotor is only 2.0% cheaper to operate (excluding the value of time) than the two-shaft turbofan, and therefore not as cost-efficient as the turboprop, because the open rotor engine is 17.6% more expensive to acquire and maintain than the two-shaft turbofan.

3.2.2 Mission Performance

This section shows how the five system options perform for the mission profile outlined in Fig. 3.12 on page 65. For conciseness, this does not include the continued cruise nor the diversion performance. As the three turbofan options have a similar performance profile, they are grouped in the first sub-section, while the turboprop and the open rotor are discussed separately in the second sub-section.

System Options 1–3: Turbofans

As the three-shaft turbofan's IP and HP rotational speeds are linked, the system effectively behaves like System Option 1 and 3's two-shaft configuration. Consequently, only the two-shaft turbofan's performance diagrams are shown and discussed in detail in this sub-section, while the three-shaft and geared turbofans' profiles are displayed in Figs. B.1 to B.6 in Appendix B on pages 147–150.

As the blue line in Fig. 3.26 displays the altitude of the aircraft throughout the mission relative to the maximum of 38,000 ft, it closely reflects the profile illustrated in Fig. 3.12. The line also clearly shows that all acceleration and deceleration phases, including takeoff and landing, are relatively short in comparison to the other flight stages. As in Fig. 3.12, the flight profile in Fig. 3.26 includes one stepped climb in order to minimize fuel consumption. As the thrust drops with increasing altitude, the climb rate decreases proportionately

and vice versa for the descent. The altitude is shown in all other figures in this section to aid interpretation.

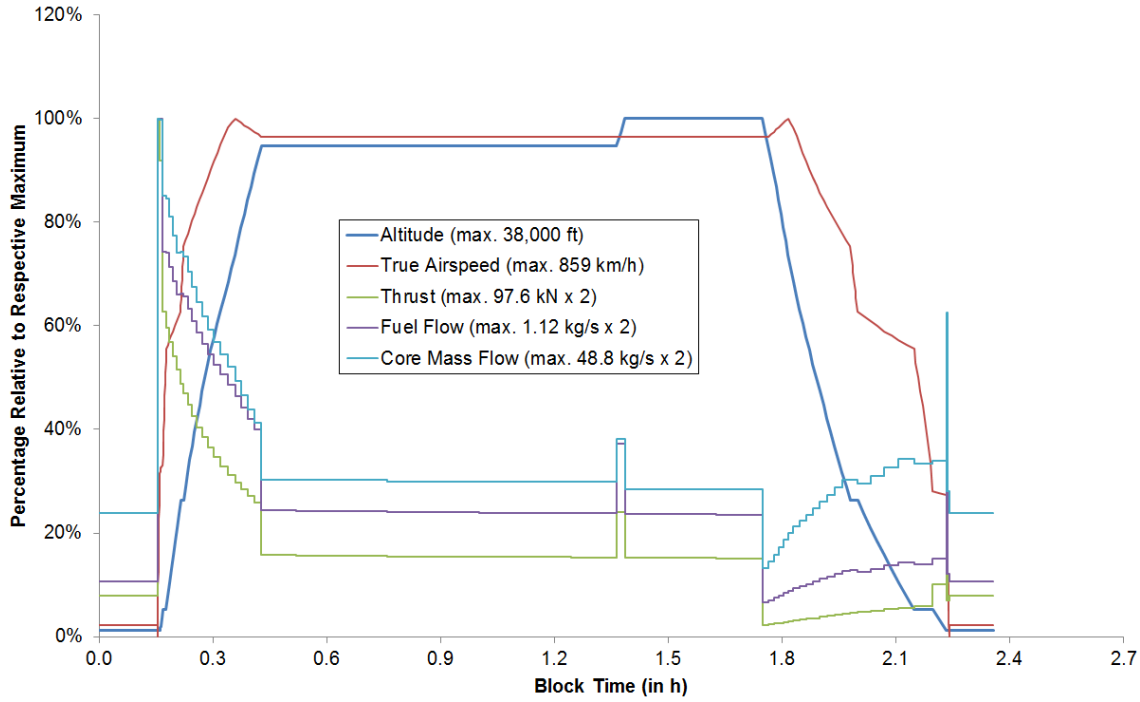


Figure 3.26: Two-Shaft Turbofan Mission True Airspeed, Thrust and Fuel and Core Mass Flow Rates (Cruise Speed: Mach 0.78).

The true airspeed also clearly illustrates the rapid acceleration and slightly longer deceleration phases, but increases and decreases more slowly as the aircraft climbs and descends at constant equivalent airspeed. As the aircraft reaches its cruise Mach number shortly before it levels off for cruise, the true airspeed starts to drop again as the temperature and hence the speed of sound decrease with increasing altitude. The true airspeed does not drop further during the stepped climb, however, because International Standard Atmosphere (ISA) specifies that the temperature is constant above 11,000 m ($\approx 36,000$ ft) [54].

A comparison of the thrust and fuel flow rate rate reveals that the two-shaft turbofan has the lowest specific fuel consumption (i.e. fuel-flow-rate-to-thrust ratio) during takeoff. As the thrust is at its maximum during takeoff, the absolute fuel flow rate is also at its highest level during that phase, however, before the engine is throttled back from 100 % to 75 % for the climb stage. The stepped change in thrust and fuel flow rate during the climb and descent reflects the discrete performance calculations at 2,000-ft intervals. There are

slight kinks in the fuel flow rate steps during the acceleration and deceleration stages because the fuel consumption rate is also proportional to the speed. The thrust and fuel flow rate also drop slightly during cruise as fuel is burnt off and the aircraft consequently becomes lighter. As the thrust increases again for approach and reverse thrust, so does the fuel flow rate. The relative air mass flow rate through the core of the engine shows close agreement with the fuel flow rate in Fig. 3.26, except at the lower thrust settings where the relative fuel flow rate drops to a lower level because the engine is working less hard.

The turbine entry temperature and rotational speeds depicted in Fig. 3.27 follow a similar pattern as the thrust and fuel flow rate in Fig. 3.26, except that they increase with altitude, albeit to a lesser extent. The rotational speed of the low-pressure system changes more than the high-pressure system because, as the name implies, the former is more sensitive to changes in either engine or atmospheric pressure. Although Fig. 3.26 shows that the fuel consumption rate does not increase after the stepped climb, Fig. 3.27 indicates that the engine has to work harder to generate the same thrust at the higher altitude. The TET and rotational speeds have similar kinks during the deceleration stages as the fuel flow rate in Fig. 3.26, but have an additional one at the beginning of the descent due to the initial rise in true airspeed.

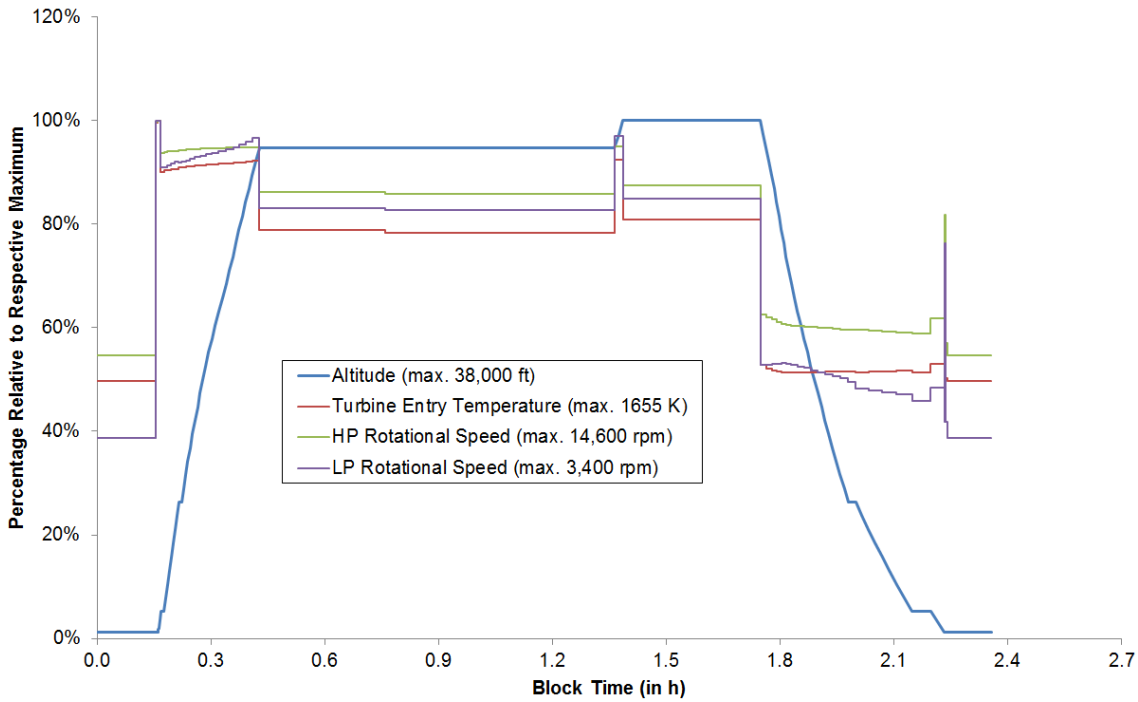


Figure 3.27: Two-Shaft Turbofan Mission Turbine Entry Temperature and Rotational Speeds (Cruise Speed: Mach 0.78).

The fan and overall pressure ratios, displayed in Fig. 3.28, are respectively correlated with the LP and HP rotational speeds in Fig. 3.27. In contrast to the rotational speeds, however, the OPR varies more extremely than the FPR, because the former is generated cumulatively by 13 compressor stages while the fan only consists of one stage.

Figure 3.28 also highlights that the bypass ratio has an inverse relationship with the fan pressure ratio and is at its maximum at the beginning of the descent where the combination of low-density but high-velocity air and idle thrust mean that the fan has to put least work into compressing the air.

Table 3.11 on page 94 indicates that the maximum thrust values recorded during the mission are significantly lower than the design values. This is due to the fact that the engines are designed for stretched versions of the Airbus A320 with 25 % more thrust, as explained on page 41. The engines used for the A320 mission simulated in this study are consequently derated, which explains why the maximum TET, rotational speeds, FPR and OPR values are also less than the design values.

In some cases there are significant performance variations between the mission and the design performance data that are not only caused by the thrust derate. These are

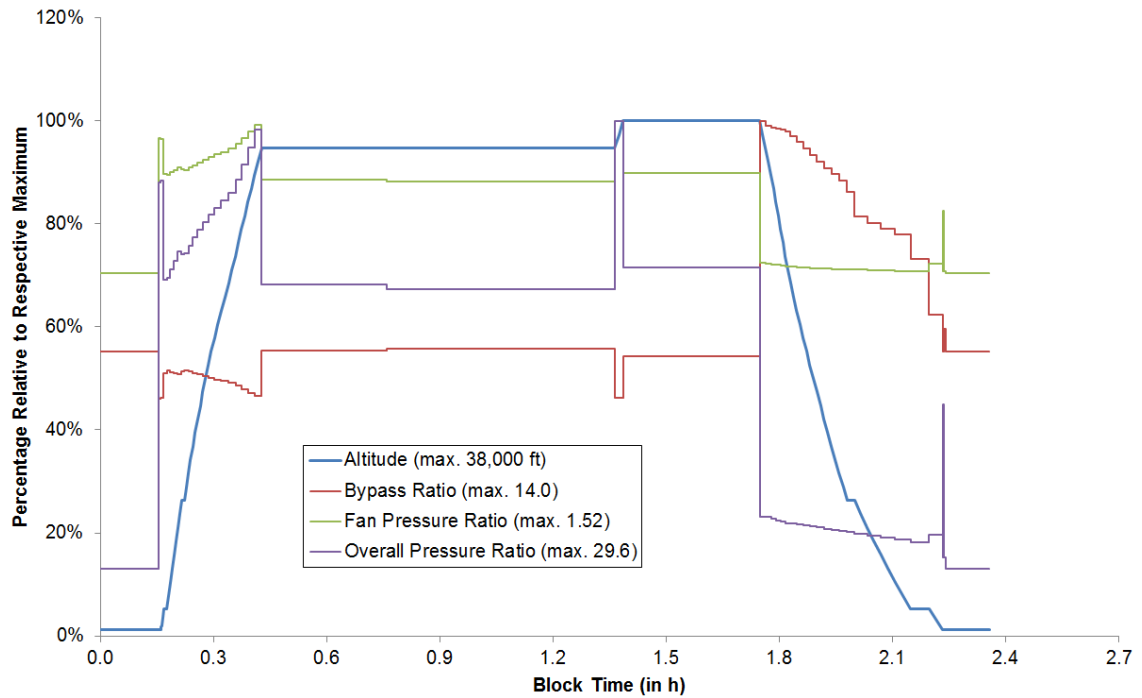


Figure 3.28: Two-Shaft Turbofan Mission Bypass Ratio and Pressure Ratios (Cruise Speed: Mach 0.78).

highlighted in yellow in Table 3.11. For example, according to the design data in Table 3.11, System Option 2's thrust should be higher than System Option 1's, which does not agree with the mission values where the three-shaft turbofan's maximum thrust is lower. This deviation is caused by variations in the operational performance limits, depending on whether the maximum growth thrust, which forms the basis of the derated thrust, is limited by the rotational speed or the turbine entry temperature in that instance.

Table 3.11 also shows that the maximum fuel flow rate of the three-shaft turbofan is 7% lower than System Option 1's, which deviates from the total fuel consumption reduction of 3%. In this case, a slight difference is not surprising because the fuel flow rate varies significantly throughout the mission, as Fig. 3.26 shows. The fluctuation of the bypass ratio, FPR and OPR in Table 3.11 can also be attributed to the varying operational environments and thrust levels.

As explained in Section 2.1.2 on page 29, the three-shaft turbofan has the advantage that the smaller rotors in the HP system have the freedom to rotate faster than the larger blades in the IP system, while the equivalent blades in the two-shaft turbofan are restricted to much lower speeds. This is clearly visible in Table 3.11, where System Option 2's HP

Table 3.11: Performance Data of System Options 1–3.

Performance Parameter	Max. Mission Performance ^a (Figs. 3.26–3.28, B.1–B.6)			Design Performance ^b (Tables C.1, C.3, C.5)		
	SO 1	SO 2 ^c	SO 3 ^c	SO 1	SO 2 ^d	SO 3 ^d
Max. Altitude	38,000 ft	0 %	0 %	38,000 ft	0 %	0 %
Cruise Speed	859 km/h	0 %	0 %	Mach 0.78	0 %	0 %
Total Thrust	195.2 kN	– 2 %	– 3 %	255.0 kN	+ 3 %	– 8 %
Total Fuel Flow	2.24 kg/s	– 7 %	– 4 %	4,563 kg	– 3 %	– 4 %
Turbine Entry Temp.	1655 K	+ 1 %	+ 7 %	1820 K	+ 3 %	+ 5 %
HP/IP Rot. Speed	14,600 rpm	+22 % / –14 %	+20 %	15,300 rpm	+24 % / –12 %	+22 %
LP Rot. Speed	3,400 rpm	– 3 %	+94 %	4,400 rpm	– 5 %	+86 %
Bypass Ratio	14.0	+ 9 %	+31 %	6.75	+11 %	+15 %
Fan Pressure Ratio	1.52	– 4 %	0 %	1.80	– 1 %	– 1 %
Overall Pressure Ratio	29.6	+ 4 %	+ 6 %	32.2	+11 %	+ 4 %

^aat $\Delta T = 0$ K, excludes the thrust growth factor of 1.25 (see page 41 for details)

^bat $\Delta T = 15$ K, includes the thrust growth factor

^cchange relative to SO 1's mission performance value

^dchange relative to SO 1's design performance value

■ > 50 % relative difference between respective mission and design percentages

system rotates more than 20 % quicker than System Option 1's, while the IP system rotates almost four times as fast as the two-shaft turbofan's LP system. However, as System Option 2 has a lower fan pressure ratio and therefore a greater fan diameter than System Option 1, Table 3.11 shows that System Option 2's LP system has a slightly lower rotational speed than the two-shaft turbofan.

Although the geared turbofan does not have an IP system, the gearbox allows the LP system to rotate at almost twice the speed of System Option 1's. This enables the geared turbofan's three LPC stages, illustrated in Fig. 2.3a on page 31, to compress the air almost twice as much as the two-shaft turbofan's three LPC stages displayed in Fig. 2.1a on page 29. The higher HP inlet pressure also means that System Option 3's HPC blades do not have to be as large, which therefore allows them to rotate 20 % faster than System Option 1's.

System Options 4–5: Turboprop and Open Rotor

As with the turbofans, only the turboprop is covered in detail in this section, because Figs. B.7 to B.12 on pages 150–153 indicate that the performance of the open rotor is similar to that of the turboprop. The reason for displaying the open rotor’s performance with two different cruise speeds of Mach 0.70 in Figs. B.7–B.9 and Mach 0.76 in Figs. B.10–B.12 is because the next section shows that the open rotor is the system option with the biggest difference in optimum cruise speed, depending on whether the value of time is included or not.

The most apparent difference between Figs. 3.26 and 3.29 is that, unlike the two-shaft turbofan, the turboprop remains at 36,000 ft throughout its cruise. As the turboprop cruises at Mach 0.70 instead of the turbofan’s Mach 0.78, it also performs its climb and descent at a maximum equivalent airspeed of 269 kn instead of 300 kn. This explains why the turboprop’s acceleration and deceleration phase at 10,000 ft is shorter than the two-shaft turbofan’s. The reduced speed is also the reason for the turboprop’s slightly higher block time of 2 hours and 37 minutes in contrast to the turbofan’s 2 hours and 22 minutes for the 1,546-km mission. As the slower open rotor aircraft cruises at the same speed as the turboprop, Fig. B.7 displays that it has a similar block time to the turboprop. The faster open rotor with a cruise speed of Mach 0.76 almost has the same block time as the two-shaft turbofan, however.

Although the turboprop only has to accelerate to Mach 0.70, Fig. 3.29 illustrates that the ascent takes 25 minutes in comparison to System Option 1’s 16-minute climb. Figure 3.29 shows that this is caused by the fact that the turboprop’s maximum thrust is lower which, due to the slower jet velocity produced by the propeller, also drops off more quickly with speed than System Option 1’s, as predicted in the literature [11]. However, Figs. 3.29 and 3.30 indicate that, after takeoff, the turboprop’s thrust and fuel flow rate initially do not decrease as rapidly as after the second acceleration phase, because the engine continues to operate at its maximum derate power by gradually increasing the turbine entry temperature to its limit. Due to the open rotor’s higher thrust rating and no maximum power derate, the altitude and thrust lines in Figs. B.7 and B.10 look more similar to System Option 1’s in Fig. 3.26.

As the open rotor cruising at Mach 0.76 has to accelerate to a higher equivalent airspeed, Fig. B.10 indicates that the fuel flow rate increases more during the second accel-

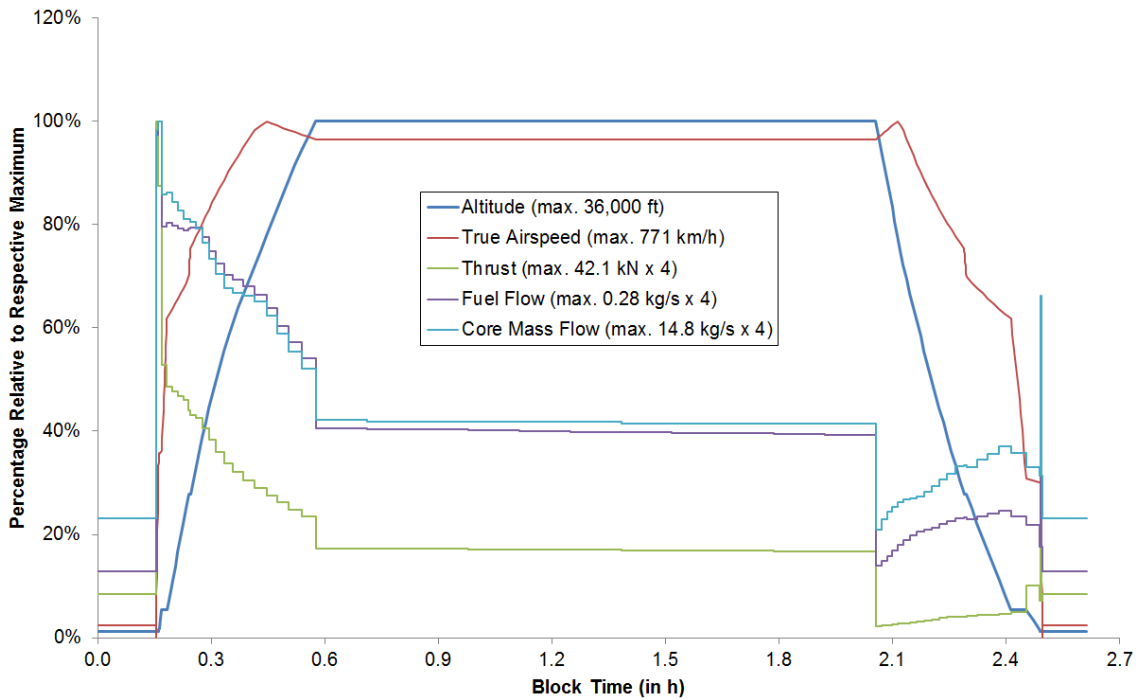


Figure 3.29: Turboprop Mission True Airspeed, Thrust and Fuel and Core Mass Flow Rates (Cruise Speed: Mach 0.70).

eration phase than for the turboprop in Fig. 3.29 and the slower open rotor in Fig. B.7. In all three figures, the fuel flow rate would also rise during the first acceleration phase to 250 kn, if it were not masked by the takeoff thrust setting. Similarly, unlike with the turbofans, the approach thrust does not lead to a visible increase in the fuel flow rate because it is overshadowed by the higher fuel consumption rates for the reverse thrust and the second deceleration phase due to the higher speed. As for the turbofans, however, the core mass flow rate shows close agreement with the fuel flow rate.

In Figs. 3.30, B.8 and B.11 there is a correlation between the turbine entry temperature and the rotational speeds of the shafts. This is caused by the requirement to reduce the rotational speed of the LP system as the relative airflow velocity over the propeller tip reaches Mach 0.95, as discussed on page 32. Figures B.8 and B.11 illustrate that this is more pronounced for the open rotor, particularly System Option 5.2 with the higher cruise speed, because of the open rotor's higher maximum rotational tip speed in comparison to the turboprop. When not restricted by the airflow velocity, Figs. 3.30, B.8 and B.11 indicate that the rotational speed of the LP system is at 100 %, i.e. the specified maximum propeller tip speed, except when taxiing. The interdependency between the TET and the

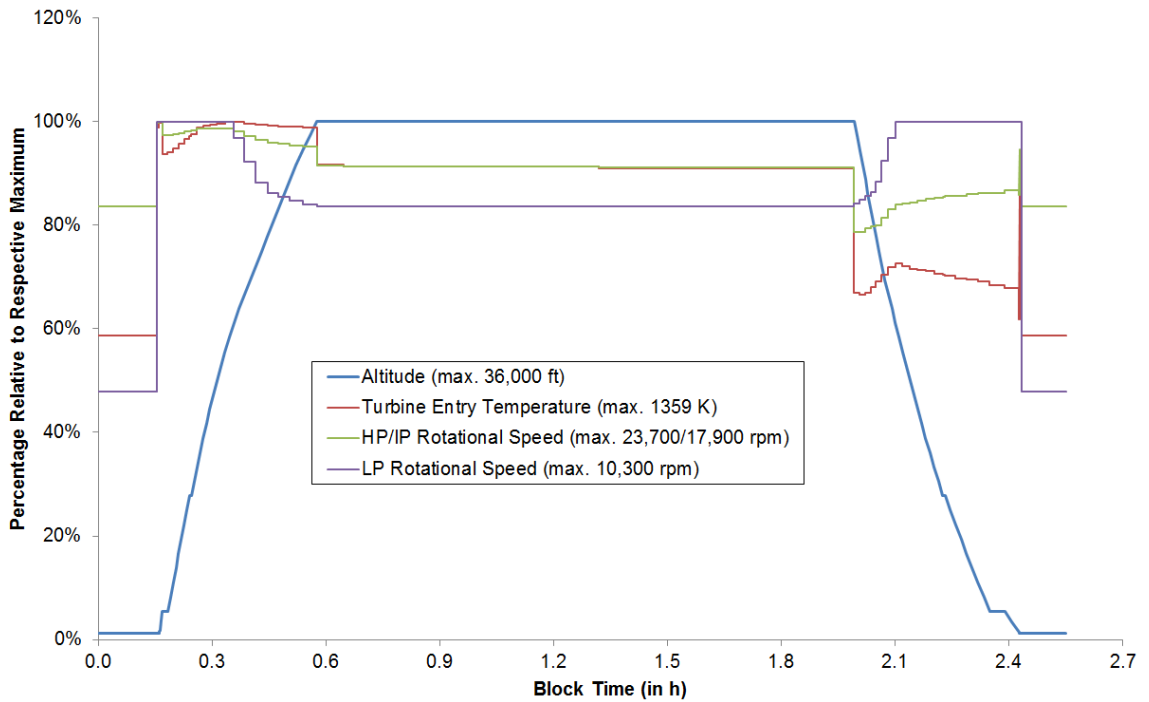


Figure 3.30: Turboprop Mission Turbine Entry Temperature and Rotational Speeds (Cruise Speed: Mach 0.70).

rotational speeds of the HP/IP and LP systems is especially visible during the descent, because an increase in the propeller speed leads to a greater power consumption, which has to be generated by the engine. This is reflected in a slightly steeper increase in fuel flow rate in the initial phase of the descent in comparison to the two-shaft turboprop in Fig. 3.26. There is no distinct increase in turbine entry temperature and HP/IP rotational speed during the approach for the same reason as for the fuel flow rate.

During the ascent, the propeller efficiency in Figs. 3.31, B.9 and B.12 follows a similar pattern as the rotational speed of the LP system. Then, however, the efficiency first increases with the reduction from climb to cruise thrust, before it drops and oscillates slightly as the thrust is throttled back to idle during the descent. This complex behaviour is caused by the fact the propeller efficiency is defined as the thrust generated multiplied by the forward speed and divided by the power input, making it a function of the lift, drag, blade pitch angle, rotational speed and forward velocity [86]. Figures 3.31 and B.9 also illustrate that System Option 5.1's propeller efficiency is only around 66 % during the cruise in contrast to the turboprop's 74 %, even though both propeller systems are operating at the maximum permissible relative tip airflow velocity of Mach 0.95. The

reason is that the open rotor aircraft has a total propeller surface area that is 25 % greater than System Option 4's, which is needed to meet the third segment climb requirement, but only creates additional drag during cruise. Figure B.11 indicates that System Option 5.2's higher cruise velocity leads to a further reduction in the propeller's rotational speed. This results in an increased blade pitch angle, and hence a lift vector with a greater torque component, which explains why System Option 5.2 has an even lower propeller efficiency of 57 %. Considering that the literature quotes a maximum turboprop propeller efficiency of 80–85 % [82], which agrees closely with Fig. 3.31's maximum value of 78.8 %, shows that the turboprop propeller has been modelled correctly in this study.

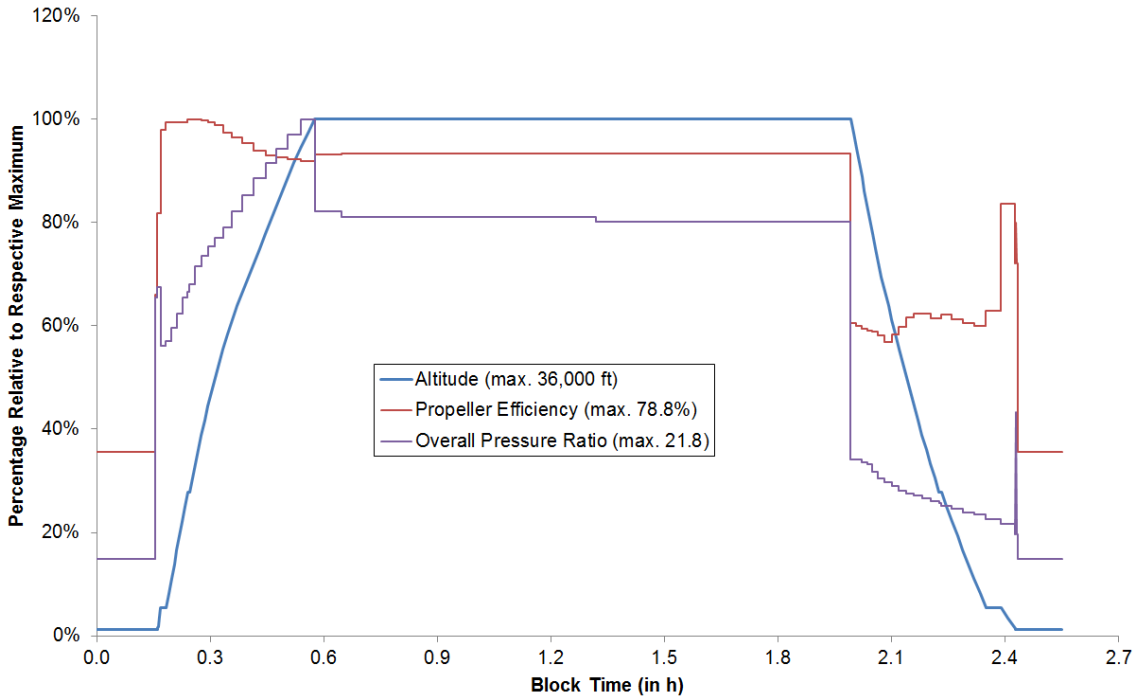


Figure 3.31: Turboprop Mission Propeller Efficiency and Overall Pressure Ratio (Cruise Speed: Mach 0.70).

Table 3.12 highlights that the turboprop aircraft has a 9 % lower design thrust than the two-shaft turbofan because Tables C.1 and C.7 in Appendix C show that System Option 4 has a 4 % lower maximum takeoff weight. As Tables C.1 and C.7 also state that the takeoff distance sets the thrust requirement for both system options, another important factor is the wing incidence angle, which, due to the lower cruise speed, is 4.8° for the turboprop but only 4.0° for the two-shaft turbofan. This means that the turboprop has to rotate less to take off and clear the obstacle height. The discrepancy between the turboprop's

maximum mission thrust and its design thrust in Table 3.12 is caused by the fact that the maximum thrust is reached during the takeoff roll, which is calculated at a slightly higher speed for the turboprop and the open rotor than for the turbofans, as Eqs. 3.6 and 3.7 on page 57 show. In addition, the turboprop has a greater thrust lapse rate than the turbofans, as was mentioned previously.

Table 3.12: Performance Data of System Options 4–5.

Performance Parameter	Max. Mission Performance ^a (Figs. 3.26–3.31, B.7–B.12)				Design Performance ^b (Tables C.1, C.7, C.9)			
	SO 1	SO 4 ^{c,d}	SO 5.1 ^c	SO 5.2 ^c	SO 1	SO 4 ^{d,e}	SO 5.1 ^e	SO 5.2 ^e
Max. Altitude	38,000 ft	– 5 %	– 5 %	– 5 %	38,000 ft	– 5 %	– 5 %	0 %
Cruise Speed	859 km/h	– 10 %	– 10 %	– 3 %	Mach 0.78	– 10 %	– 10 %	– 3 %
Total Thrust	195.2 kN	– 14 %	+ 12 %	+ 12 %	255.0 kN	– 9 %	+ 35 %	+ 39 %
Total Fuel Flow	2.24 kg/s	– 50 %	– 34 %	– 29 %	4,563 kg	– 14 %	– 15 %	– 7 %
Turbine Entry Temp.	1655 K	– 18 %	+ 4 %	+ 4 %	1820 K	– 19 %	+ 4 %	+ 4 %
HP/IP Rot. Speed	14,600 rpm	+ 62 % / + 23 %	+ 54 % / – 2 %	+ 51 % / – 4 %	15,300 rpm	+ 63 % / + 24 %	+ 53 % / – 3 %	+ 50 % / – 5 %
LP Rot. Speed	3,400 rpm	+203 %	+124 %	+118 %	4,400 rpm	+134 %	+ 73 %	+ 69 %
Overall Pressure Ratio	29.6	– 26 %	+ 49 %	+ 48 %	32.2	– 34 %	+ 15 %	+ 15 %

^aat $\Delta T = 0$ K, excludes the thrust growth factor of 1.25 (see page 41 for details)
^bat $\Delta T = 15$ K, includes the thrust growth factor
^cchange relative to SO 1's mission performance value
^dincludes the max. power derate factor of 0.85 (see Section 3.1.3 on page 56 for details)
^echange relative to SO 1's design performance value
■ > 50 % relative difference between respective mission and design percentages

Unlike the turboprop, Table C.9 indicates that System Options 5.1's and 5.2's thrust is set by the third segment climb with only one engine in operation. As Figs. B.7 and B.10 show that the open rotor has a thrust lapse rate that lies between that of System Options 1 and 4, Table 3.12 displays that System Options 5.1 and 5.2 consequently have a 35 % and 39 % higher design thrust, respectively, than the two-shaft turbofan.

The maximum fuel flow rates of System Options 4, 5.1 and 5.2 given in Table 3.12 are significantly lower than System Option 1's. The total fuel consumptions do not decrease

by the same percentage, however, because Figs. 3.29, B.7 and B.10 highlight that the fuel flow rate during the cruise is approximately 40 %, 30 % and 35 % of the maximum, respectively, while for the two-shaft turbofan it is only 25 %.

The turboprop's and open rotor's LP rotational speeds differ from the two-shaft turbofan's due to the gearbox, the reduced core size and the constant speed propellers that only rotate slower during taxiing and when the relative airflow velocity reaches Mach 0.95. The open rotor's maximum mission OPR also deviates significantly from the design value, because Figs. B.7 and B.10 illustrate that System Option 5.1's and 5.2's core mass flow rate at the top-of-climb is respectively 57 % and 63 % of the takeoff value in comparison to the two-shaft turbofan's 41 % shown in Fig. 3.26. The difference is caused by the core's nozzle area that limits the core mass flow rate so that none of the flow velocities exceed the speed of sound, as specified on page 48.

3.2.3 Optimum Cruise Speed

The cost charts presented in the following sub-sections are based on the cost formulas in Section 3.1.8 on page 75. Due to the similarity between the cost diagrams of the five system options, the first sub-section only shows how the costs of the two-shaft turbofan and the turboprop are affected by the cruise speed, while the figures of the other three system options are found in Appendix D on pages 167–168. The last two sub-sections then highlight how each system option performs relative to the others, depending on whether the value of time is included or not.

It is important to note that all charts include a relative cost of time, except where indicated, that is measured relative to the block time required when cruising at Mach 0.82, the highest cruise velocity investigated in this study. This means that a cruise speed of Mach 0.82 has a cost of time of zero, which increases as the cruise speed drops. The productivity and market share costs at the various cruise speeds are also measured relative to the cost baseline at a cruise speed of Mach 0.82. While the market share cost is the direct operating cost multiplied by the lost market share percentage, the productivity cost is the difference between the DOC at the actual cruise speed and the DOC if the same aircraft design were flown at a cruise speed of Mach 0.82. The productivity cost is therefore dependent on the number of aircraft in the fleet as well as the annual flight hours and flight cycles per aircraft, which are affected by the cruise speed as shown in Fig. 3.22 on

page 74.

System Options

Figures 3.32 and D.1–D.3 all illustrate two conflicting cost wedges: the first one increases with cruise speed and consists of the engine, airframe, landing, navigation, crew, ground, fuel and CO₂ costs, while the second one reduces with speed, including the productivity, market share and time costs.

The market share cost is not significant in any of the five diagrams, because Fig. 1.9 on page 21 displays that the market share only starts to decrease rapidly below a cruise speed of 400 km/h (\approx Mach 0.38). Similarly, the equipment and flight costs (i.e. the engine, airframe, landing, navigation, crew and ground costs) only increase gradually with velocity. The mean fuel and CO₂ costs, however, increase exponentially with speed due to the onset of wave drag and consequently rise more quickly at some point than the linearly reducing cost of time. The velocity at which this occurs is the optimum cruise speed if the value of time is included and varies as follows for the five system options, based on Table 3.13: while it is Mach 0.80 for the three turbofans, it is Mach 0.76 for the open rotor and only Mach 0.72 for the turboprop. If the value of time is ignored, however, then the minimum operating cost is at a lower speed, below which the asymptotically decreasing fuel cost saving is less than the productivity cost rise. For the three turbofan options this is Mach 0.76, while for open rotor and the turboprop it is Mach 0.70.

Table 3.13: Direct Operating Cost Range (based on Tables C.2, C.4, C.6, C.8 and C.10).

System Option	Optimum Cruise Speed (in Mach)		Mean DOC incl. VoT (in ¢/RPK, 2012)			Mean DOC excl. VoT (in ¢/RPK, 2012)		
	incl. VoT	excl. VoT	Rank ^a	Min.	Max. ^b	Rank ^a	Min.	Max. ^b
1	0.80	0.76	3	10.27	+2.5 %	4	9.98	+3.5 %
2	0.80	0.76	2	10.25	+2.9 %	5	10.00	+4.5 %
3	0.80	0.76	1	10.04	+2.8 %	2	9.77	+3.4 %
4	0.72	0.70	5	10.38	+3.5 %	1	9.62	+4.9 %
5	0.76	0.70	4	10.28	+5.7 %	3	9.85	+3.3 %

^abased on minimum DOC

^bchange relative to respective minimum DOC

■ System Option with lowest DOC

■ System Option with highest DOC

Table 3.13 displays that, in comparison to the two-shaft turbofan, System Options 2 and 3 have slightly different cost values and that the geared turbofan has the lowest direct operating cost of all system options if the value of time is included. Nevertheless, Figs. D.1 and D.2 look very similar to Fig. 3.32a because System Options 2 and 3 have the same optimum cruise speeds as the two-shaft turbofan. Despite the wide speed ranges investigated, Table 3.13 indicates that the biggest change in DOC (including the value of time) for the three turbofan options is only 2.9 % relative to the minimum, which increases to 4.5 % if the value of time is excluded.

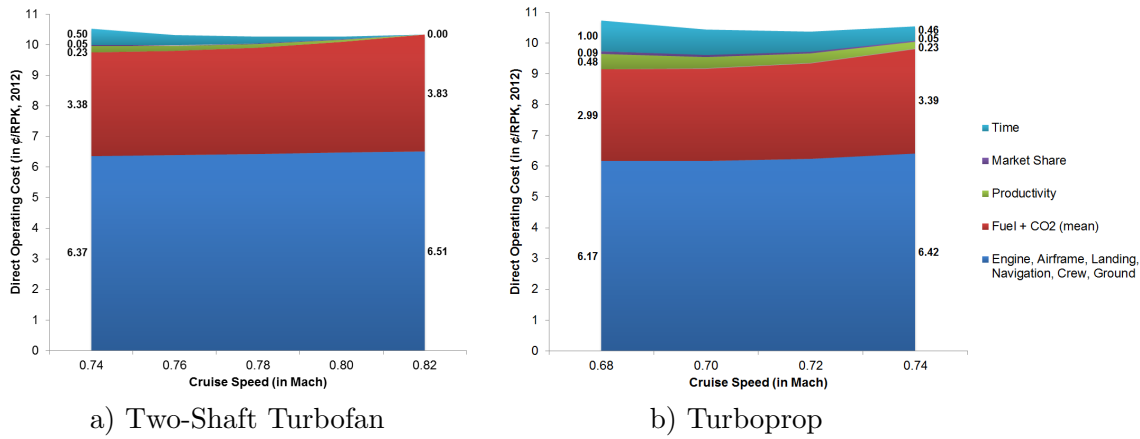


Figure 3.32: Direct Operating Cost Breakdown Vs. Cruise Speed.

The turboprop's and open rotor's cost wedges in Figs. 3.32b and D.3 have different proportions to those of the three turbofan system options, due to the lower optimum cruise speeds and the increased fuel efficiency. Consequently, the equipment, flight and mean fuel and CO₂ costs are lower, but the market share, productivity and time costs are more significant. Table 3.13 shows that the open rotor has the largest difference between the lowest and highest DOC if the value of time is included, because System Option 5 has the widest optimum cruise speed range. Conversely, the turboprop has the smallest range because Table C.7 illustrates that its thrust requirement is controlled by the initial cruise altitude and speed, while the open rotor's thrust remains constant as Table C.9 displays that it is set by the third segment climb. Irrespective of that, the turboprop has the lowest direct operating cost if the value of time is excluded.

Including the Value of Time

As implied in the name and defined in Eq. 1.3 on page 21, MSD is the mean of the squares of the DOC values. In order to make comparisons with the mean DOC values quoted in the previous sub-section easier, Fig. 3.33 presents the square root of the MSD, but including the absolute instead of the relative cost of time, based on Eq. 3.19 on page 79.

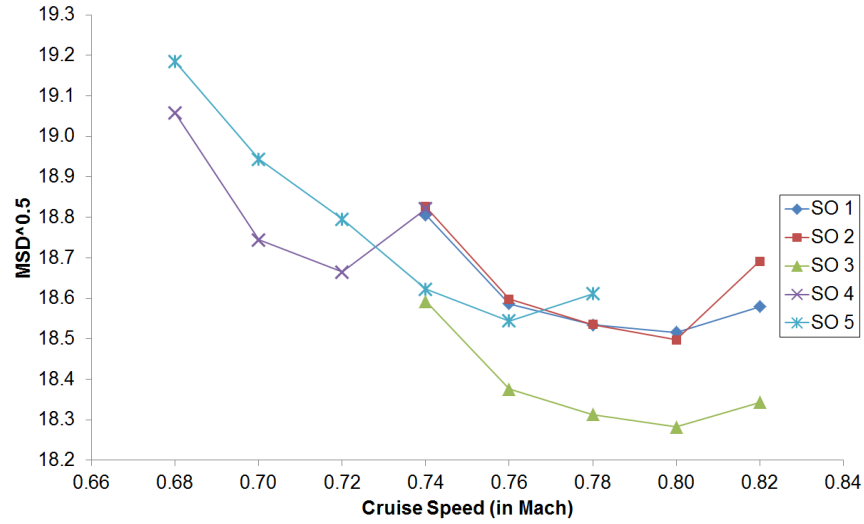


Figure 3.33: System Options MSD of Direct Operating Cost (incl. Value of Time) Vs. Cruise Speed.

If the value of time is included, Fig. 3.33 confirms that the geared turbofan has the lowest direct operating cost of the five system options at a cruise speed of Mach 0.80 and that System Option 2 has an almost identical operating cost to System Option 1, despite the 10 % engine acquisition cost penalty imposed on the three-shaft turbofan. Figure 3.33 also highlights the turboprop's narrow optimum cruise speed range in comparison to the three turbofans and the open rotor.

Figure 3.34 compares the optimum system option designs, based on the minimum DOC (including the relative value of time) at Mach 0.80 for System Options 1–3, Mach 0.72 for System Option 4 and Mach 0.76 for System Option 5 to the actual DOC data of U.S. passenger airlines in the Year 2009 taken from Fig. 1.3 on page 10 [28, 29]. The actual engine and airframe costs from 2009 have been blended together in Fig. 3.34 because the data does not differentiate between the two. As the U.S. passenger airlines data also does not separate the productivity cost from the rest and does not include market share and time costs, none of these are shown in Fig. 3.34. Although the actual cost data is an

average for all aircraft sizes and ages operated by U.S. passenger airlines in 2009, the comparison between the predicted and the actual DOC data nevertheless reveals that the costs estimates for 2030 are realistic, considering that Table 3.16 on page 108 shows that the aircraft acquisition costs are forecasted to rise to balance the high fuel and CO₂ cost estimates for 2030. The actual fuel cost in 2009 is significantly less than forecasted for 2030, because in addition to supplementary CO₂ costs, the mean predicted oil price for 2030 (≈ 135 \$/barrel in 2012 prices) is more than twice as high as the actual price in 2009 (≈ 63 \$/barrel in 2012 prices [28, 29]). This price increase between 2009 and 2030 does not translate into a similar fuel and CO₂ cost rise in Fig. 3.34 due to the significantly improved fuel efficiency highlighted in Table 3.15 on page 108. As the landing and navigation charges are dependent on the Operating Weight Empty (OWE) which, according to Table 3.16, is predicted to reduce, Fig. 3.34 indicates that these are the only costs that are expected to drop.

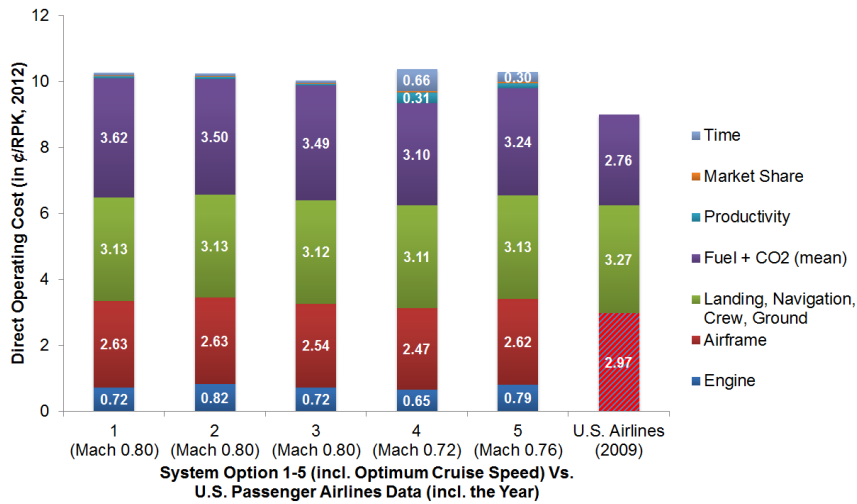


Figure 3.34: Optimum System Options (incl. Value of Time) Vs. Actual U.S. Passenger Airlines [28, 29] Direct Operating Cost Breakdown.

Focusing on the five system options, Fig. 3.34 confirms that the geared turbofan has the lowest operating cost if the value of time is included. Nevertheless, Table 3.13 shows that the turboprop, which has the highest operating cost, is only 3.4 % more expensive. Even though System Option 2 has the most costly engine, Fig. 3.34 illustrates that this is over-compensated by the reduced fuel consumption, making it slightly cheaper to operate than the two-shaft turbofan. However, System Option 3 outperforms both in terms of cost efficiency because the reduced engine weight and fuel consumption also make the

airframe lighter and therefore cheaper. Although the turboprop has the lowest engine cost due to the reduced turbine entry temperature and thrust requirement, the lightest and cheapest airframe and the highest fuel efficiency, the low cruise speed imposes a significant productivity and time cost, making it the most expensive option. Despite not having such a large time and productivity cost, System Option 5's high thrust and turbine entry temperature make the engine the second most expensive to operate. The high engine mass also does not help in reducing the airframe weight and hence its cost. Although the open rotor is more fuel-efficient than the geared turbofan, it has a higher fuel consumption than the turboprop due to the increased cruise speed.

Excluding the Value of Time

As the cost of time drops linearly with an increase in cruise speed, Fig. 3.35 is a tilted version of Fig. 3.33 in which the turboprop is the cheapest system option after being the most expensive in Fig. 3.33. However, as indicated in Table 3.13 on page 101, the geared turbofan only slips down one rank to second, ahead of the open rotor and the two- and three-shaft turbofan.

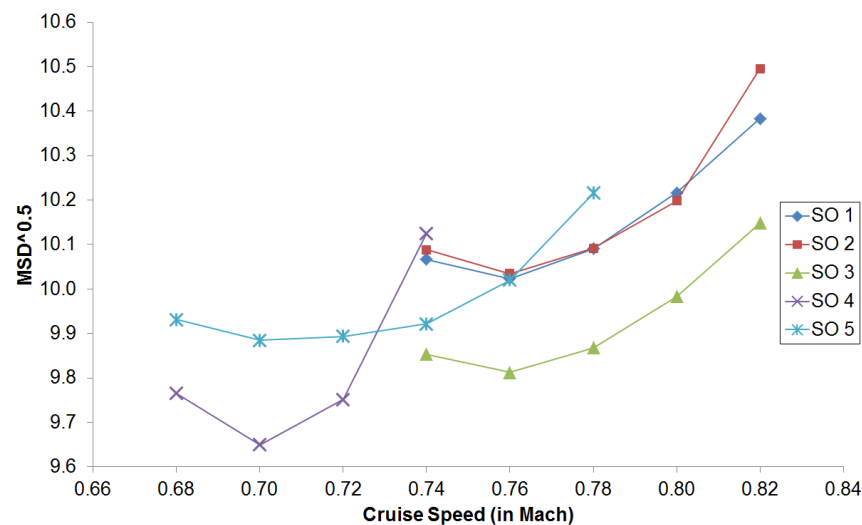


Figure 3.35: System Options MSD of Direct Operating Cost (excl. Value of Time) Vs. Cruise Speed.

Figure 3.36 looks similar to Fig. 3.34, except that the cost of time is not included and that most of the costs have decreased, except for a marginal rise in the productivity and market share costs due to the reduced cruise speeds. While the turboprop's cruise

velocity has only dropped by Mach 0.02, the turbofans' have decreased by Mach 0.04 and the open rotor's by Mach 0.06 which explains their more pronounced fuel cost saving. All system options have similar reductions in engine and airframe costs, however, due to the lower airframe weight and thrust requirement. As all costs, except for fuel and CO₂, have changed by similar amounts, it is not surprising that the turboprop is now the cheapest to operate without the cost of time. Similarly, the geared turbofan's lower engine and airframe weight and cost and its productivity cost advantage outweigh the open rotor's superior fuel efficiency. This shows that the most *fuel-efficient* option, the open rotor, is not automatically the most *cost-efficient* solution because of the relatively high engine and airframe costs.

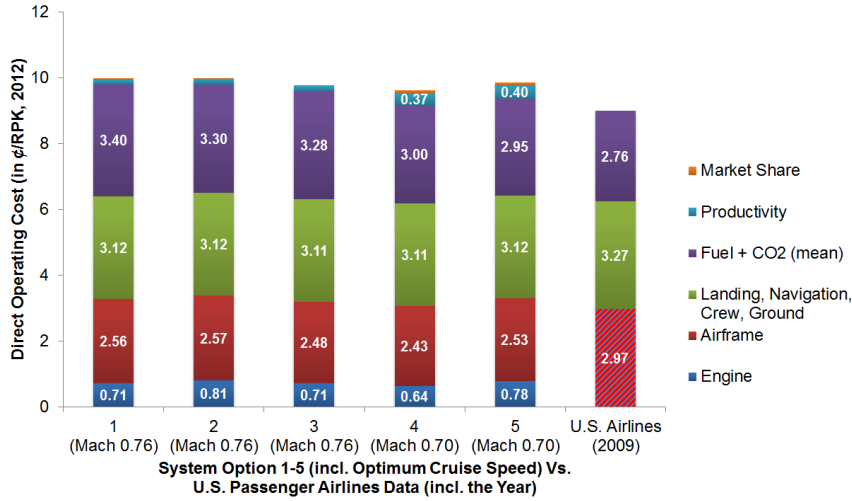


Figure 3.36: Optimum System Options (excl. Value of Time) Vs. Actual U.S. Passenger Airlines [28, 29] Direct Operating Cost Breakdown.

Table 3.14 shows that the $\sqrt{\text{MSD}}$ and mean DOC values are almost identical, which explains why both have the same optimum cruise speeds. The minor difference in cost is caused by the fact that, despite the uniform uncertainty distributions, $\sqrt{\text{MSD}}$ is skewed by the higher fuel and carbon cost values due to the squaring, as Eqs. 3.22 and 3.23 demonstrate for imagined values of 1.0, 1.5 and 2.0:

$$\sqrt{\text{MSD}} = \sqrt{\frac{1}{M} \sum_{j=1}^M y_j^2} = \sqrt{\frac{1}{3} \times (1.0^2 + 1.5^2 + 2.0^2)} = 1.55 \quad (3.22)$$

$$\text{Mean DOC} = \frac{1}{M} \sum_{j=1}^M y_j = \frac{1}{3} \times (1.0 + 1.5 + 2.0) = 1.50 \quad (3.23)$$

Table 3.14: Comparison of $\sqrt{\text{MSD}}$ and Mean DOC (based on Tables C.2, C.4, C.6, C.8 and C.10).

System Option	$\sqrt{\text{MSD}}$ (excl. VoT)		Mean DOC (excl. VoT)	
	Cruise Speed (in Mach)	Min. Cost (in ¢/RPK, 2012)	Cruise Speed (in Mach)	Min. Cost (in ¢/RPK, 2012)
1	0.76	10.02	0.76	9.98
2	0.76	10.03	0.76	10.00
3	0.76	9.81	0.76	9.77
4	0.70	9.65	0.70	9.62
5	0.70	9.88	0.70	9.85

This raises the question whether it was worthwhile determining the MSD when using a uniform uncertainty distribution. The author argues that it was, considering that calculating the MSD did not require significant computing power and provided a clear link between the fuel and carbon price ranges, specified on page 11, and the model, as well as a baseline against which the mean DOC could be compared.

3.2.4 Verification

Table 3.15 proves that the optimum cruise speed and fuel consumption values presented in the previous sub-sections agree well with performance data in the public domain. It is particularly interesting to note that neither the cruise speeds of the three turbofan options nor of the turboprop deviate significantly from the Airbus A320's and A400M's current velocity, respectively, regardless of whether the value of time is included or not. The open rotor's wider speed range is also confirmed by the references given in Table 3.15.

Table 3.15: Verification of Cruise Speed and Fuel Consumption Results.

System Option	Cruise Speed (in Mach)		Fuel Consumption	
	System Study ^a	Literature	System Study ^{a,b}	Literature ^b
Current Airbus A320	0.78	0.78 [78]	3.58 kg/km ^c	3.68 kg/km ^d [119]
1	0.76/0.80	0.78 ^e [78]	−19.4 %/−14.2 %	−15 % [62]
2	0.76/0.80		−21.8 %/−16.9 %	
3	0.76/0.80		−22.2 %/−17.4 %	
4	0.70/0.72	0.68–0.72 ^f [85]	−28.9 %/−26.4 %	
5	0.70/0.76	0.72–0.75 [24, 120]	−30.1 %/−23.1 %	−30 %/−25 % [62]

^abased on Tables C.1, C.3, C.5, C.7 and C.9

^bpercentages relative to the current Airbus A320

^c5,537 kg fuel for the System Study's 1,546-km mission

^d16,500 kg fuel for a max. range mission of 4,482 km (2,420 nm) at a MTOW of 77,000 kg

^ebased on the Airbus A320

^fbased on the Airbus A400M

According to Morrison [17], a new generation of aircraft will have an increased wing span and an increased capital cost in order to further reduce fuel consumption, as was the case in the past [18]. Both forecasts are verified by Table 3.16, where all system options have a greater wing span and a higher acquisition cost than the current A320. Furthermore, Tables A.1–A.10 in Appendix A show that all system options, except for the turboprop, would have an even lower operating cost if their wing spans were allowed to exceed the limit of 36 m.

Table 3.16: Verification of Aircraft Wing Span, Operating Weight Empty and Acquisition Cost Results.

System Option	Wing Span (in m) ^a	Operating Weight Empty (in kg) ^b	Aircraft Acquisition Cost (in million \$, 2012) ^b
Current Airbus A320	34.1 [78]	43,000 [78]	69.6 [29, 78]
1	36.0	−18.1 %	+11.2 %
2	36.0	−18.0 %	+15.2 %
3	35.8	−21.2 %	+ 8.6 %
4	35.3	−24.3 %	+ 3.7 %
5.1	35.2	−20.4 %	+11.2 %
5.2	35.3	−16.9 %	+15.1 %

^abased on Tables C.1, C.3, C.5, C.7 and C.9

^bpercentages relative to the current Airbus A320

Although Concorde was primarily retired in 2003 because of the increasing maintenance burden and the reduced passenger numbers after the Concorde crash in 2000 and the terrorist attacks of 2001, even in its hay-day the 14 Concorde aircraft only covered a niche-market [121, 122]. This was partly because the sonic boom prevented Concorde from flying supersonic over land, but primarily because it consumed six times as much fuel per passenger as a Boeing 787 today [121]. The high fuel consumption also restricted Concorde's maximum range, which meant that a scheduled non-stop service over the North Atlantic was the only viable business case [121]. Concorde's retirement followed shortly after Boeing's decision in 2002 to cancel the Sonic Cruiser in favour of the 10% more fuel-efficient Boeing 787 despite the Sonic Cruiser's 15% higher cruise speed of Mach 0.98 [123, 124]. This highlights that the trade-off between the cost of fuel and the value of time has shifted towards fuel economy since the rise of oil prices in the 1970s and consequently all attempts to build a new supersonic or 'near-supersonic' passenger aircraft have failed and it is not likely to happen in the future [121].

The results presented in this study concur with the historical development of increasing fuel efficiency at the cost of a cruise speed well below Mach 1 and greater capital investment in weight- and fuel-saving technologies like the geared turbofan and composite airframes. This development is already taking place today, as Pratt & Whitney's geared turbofan is being installed on several single-aisle aircraft and Rolls-Royce is pursuing a similar development [81, 125].

Morrison [17] predicts that rising fuel prices will lead to a further reduction in cruise speed, but this can only be verified by the results if the value of time is excluded. If the fuel and carbon prices were to increase above the range assumed in this study, however, then the higher fuel costs will have a greater leverage on the cruise speed than the value of time. Consequently, it would be more likely that the turboprop would be the cheapest aircraft to operate, regardless of whether the value of time is included or not. This would agree with Rolls-Royce's statement [77] that "there is very sound argument to be made for the majority of the 150-seat market, which flies mostly for less than 1.5 hours [being turboprop-powered]".

Chapter 4

Component Study

To gain a better understanding of the trade-offs involved in blisk design, Rolls-Royce (R-R) needed a scalable cost model for Linear Friction Welded (LFW) blisks to be able to quantify the impact on the blisk’s unit cost caused by changing design variables, including the blisk’s dimensions, the number of blades and special features such as holes and seals.

At the same time, a factory cost model was required to be able to predict the cost rate of a future LFW blisk manufacturing facility, including all the manufacturing cells within it. Such a detailed cost breakdown was needed in order to support the optimization of the method of manufacture and the factory layout in terms of cost, quality and lead time.

While the *Factory Cost Model* is covered in the next section, the *Scalable Blisk Cost Model* is described in more detail in Section 4.2 on page 114. Due to confidentiality, the data presented in both the text and the figures had to be simplified, normalised or removed. All models were set up in Vanguard Studio, a software package that, unlike a spreadsheet, generates hierarchical trees which forces the model builder to decompose a problem into a logical sequence of steps [5].

4.1 Factory Cost Model

4.1.1 Model Schematics

Figure 4.1 illustrates how the Factory Cost Model replicates the structure of a real production facility by containing various manufacturing cell cost models. Machines are allocated to these cell models as indicated by the ‘Fixed Costs’ branch in Fig. 4.2. Each part type can then ‘flow’ through the factory according to the sequence of manufacturing operations,

also known as Method of Manufacture (MoM). The ‘Variable Costs’ branch in Fig. 4.2 shows that each manufacturing operation has to be assigned to a specific machine within a specific manufacturing cell. Finally, the cell model outputs are added up in the Factory Cost Model, together with the factory overheads and the external material costs, as illustrated in Fig. 4.1. In order to handle the large amount of generic input data listed in Fig. 4.2 efficiently, the Factory Cost Model is based on code written in Vanguard Studio’s inbuilt scripting language, DScript, that creates the cell models and all hierarchical trees automatically.

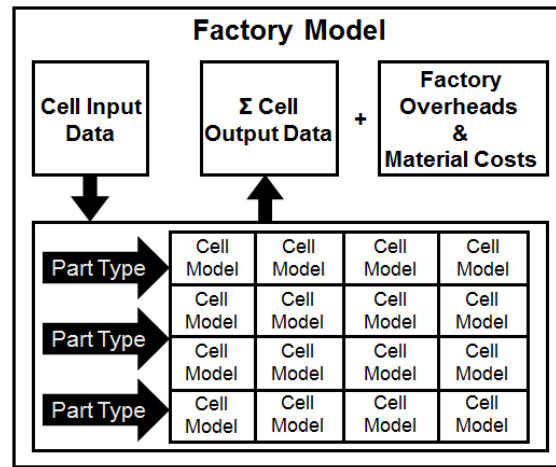


Figure 4.1: Factory Cost Model Structure.

Figure 4.3 demonstrates how the Factory Cost Model was broken down into five levels that comply with the general rule that activities in an Activity-Based Costing (ABC) model should be separated into four categories: facility-sustaining, product-sustaining, batch-level and unit-level activities [66, 68, 126]. The Factory Cost Model’s tree structure does not include a batch level, however, because the bulkiness of LFW blisks and their low production volumes make automatic batch setup and handling ineffective. Consequently, batch size does not have a significant effect on the machine setup times and costs of LFW blisks.

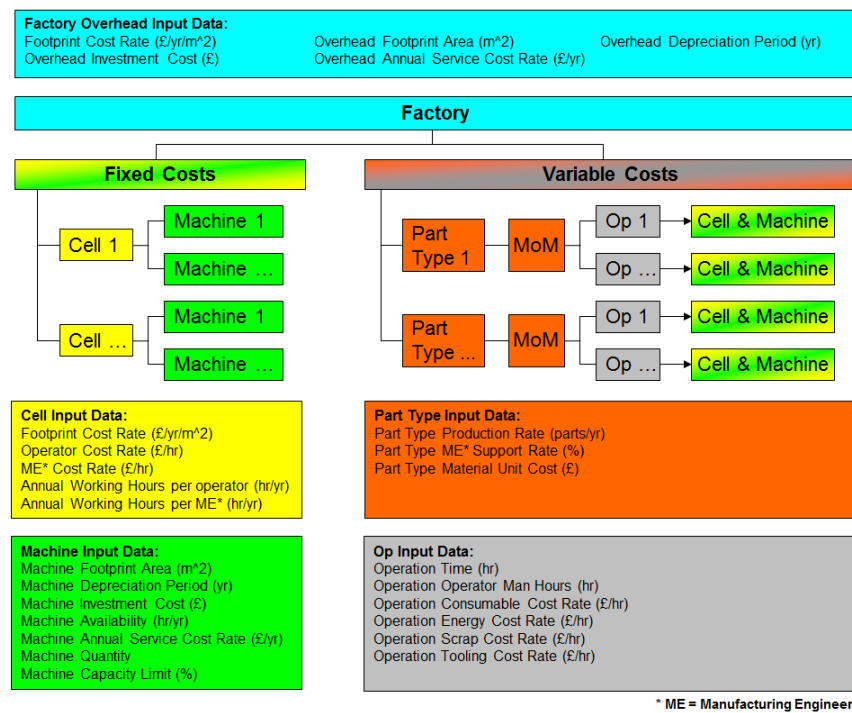


Figure 4.2: Factory Cost Model Inputs.

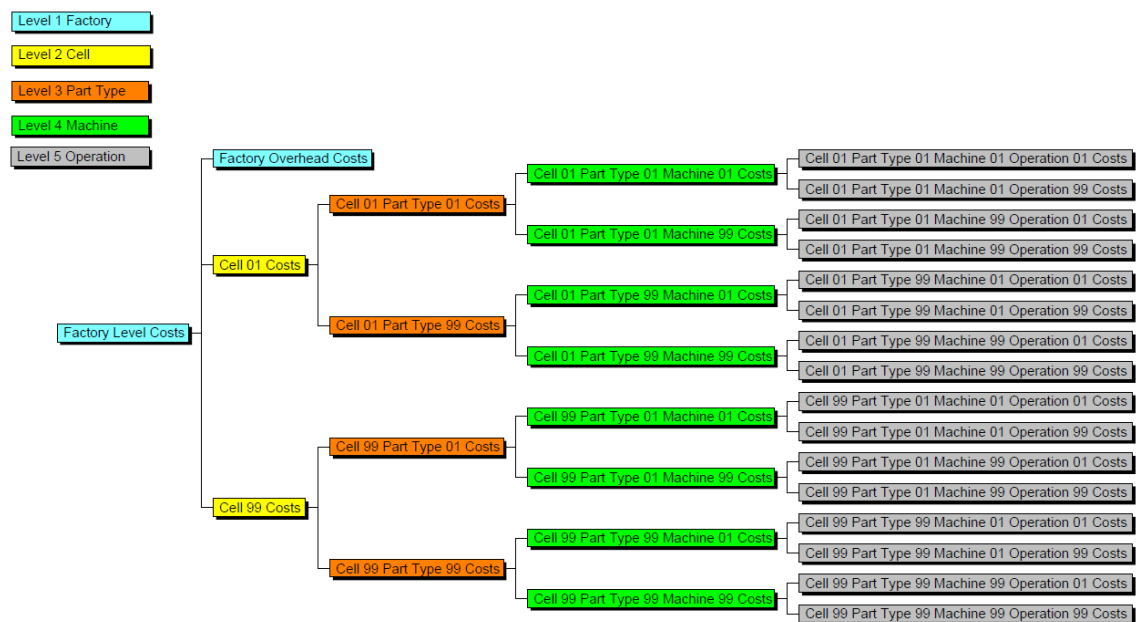


Figure 4.3: Factory Cost Model Hierarchy.

4.2 Scalable Blisk Cost Model

Figure 4.4 represents the interaction between the activity-based Factory Cost Model and the parametric Scalable Blisk Cost Model. The main purpose of the Scalable Blisk Cost Model is to estimate the operation times required to manufacture a future blisk, based on design parameters that drive the operation times and hence cost. These times are then passed to the Factory Cost Model together with the planned production volume, in order to calculate the machine cost rates and the other outputs specified in Fig. 4.4. The machine cost rates can then be fed back into the scalable model in order to generate uncertainty distributions of the blisk unit cost. The details of how the operation times and the uncertainty distributions are generated are discussed in the following sub-sections.

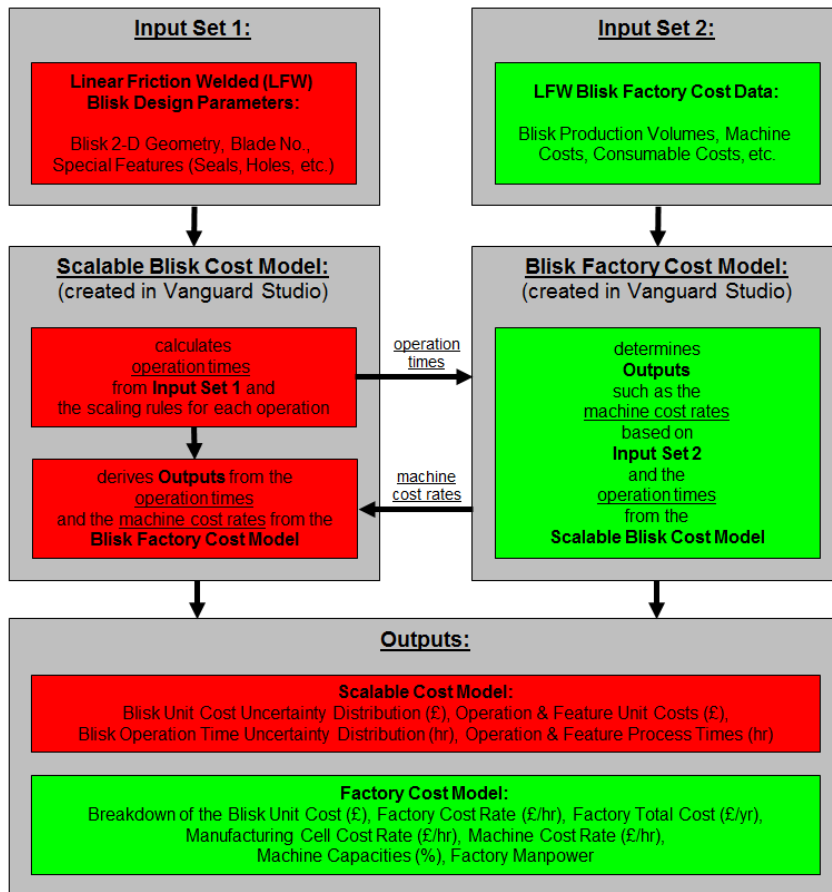


Figure 4.4: Scalable Blisk and Factory Cost Model Interaction.

4.2.1 Blisk Design Variability

Each LFW blisk has a highly unique design with several hundred features and many thousand measured points. Consequently, the method of manufacture and the duration of its operations vary significantly. The unit cost of a LFW blisk with hollow blades and a disc with many complex features can cost several times more in a full-production environment than a simpler LFW blisk with solid blades.

The Scalable Blisk Cost Model therefore had to be able to automatically modify the MoM and the operation times based on the design inputs. An additional challenge arose as the author only had access to sparse and inaccurate data of five pre-production blisk designs.

4.2.2 Model Structure

The disguised MoM in Fig. 4.5 reflects the uniqueness of each blisk design, considering that only 28 operations are common to each blisk, while the remaining 37 operations only apply under certain conditions. Only 53 of the total 65 operations and sub-operations are unique, however, because several operations in the method appear more than once. Rather than modelling the complex machining and inspection operations in their entirety, they were broken down into the 14 sub-operations shown in the top right table in Fig. 4.5, including rough turning, finish turning, hole machining and tight tolerance inspection for example.

For the 15 processes identified as R1 to R15 in Fig. 4.5, linear regression analysis was used to determine an approximate relationship between the varying operation times and the design parameters, because simple and intuitive scaling rules, such as the material volume removed multiplied by the material removal rate, could not capture the complexity of these operations. While the regression analysis methodology is described in more detail in the next sub-section, the Gaussian uncertainty distribution that was applied to these 15 scaling rules is covered on page 120.

While regression or intuitive linear relationships were used to derive the scaling rules for operations L1 to L13, C1 to C25 have constant times. As the manufacturing engineers estimated the error bounds of the scaling rules for L1 to L13 and C1 to C25, the predicted operation times have triangular uncertainty distributions, which are also further discussed on page 120.

OP No.	Manufacturing Operation	Applies When	OP No.	Manufacturing Operation	Applies When	Manufacturing Operation	OP No.	Manufacturing Sub-Operation	Applies When
10	MISCELLANEOUS (C1)	always	320	INSPECTION (L5)	optional	MACHINING (S1)	620	MACHINING (R12)	optional
20	OUTSOURCED (L1)	always	330	INSPECTION (C9)	always		630	MACHINING (R13)	optional
30	MISCELLANEOUS (L2)	always	340	SURFACE TREATMENT (C10)	always		640	MACHINING (R14)	always
40	SURFACE TREATMENT (C2)	always	350	INSPECTION (C11)	always		650	MACHINING (R15)	always
50	INSPECTION (R1)	always	360	SURFACE TREATMENT (C12)	optional		660	MACHINING (L6)	optional
60	OUTSOURCED (C3)	always	370	INSPECTION (C13)	optional		670	MACHINING (L7)	optional
70	SURFACE TREATMENT (C4)	always	380	OUTSOURCED (R6)	optional		680	MACHINING (L8)	optional
80	SURFACE TREATMENT (C5)	always	390	SURFACE TREATMENT (C14)	optional		690	MACHINING (L9)	optional
90	MACHINING (S1)	see sub-operations	400	SURFACE TREATMENT (C15)	always		700	MACHINING (L10)	optional
100	SURFACE TREATMENT (C5)	optional	410	SURFACE TREATMENT (C5)	optional		710	MACHINING (L11)	optional
110	SURFACE TREATMENT (C5)	optional	420	MACHINING (S1)	see sub-operations		720	MACHINING (L12)	optional
120	MACHINING (S1)	see sub-operations	430	MACHINING (S1)	see sub-operations		730	MACHINING (L13)	optional
130	MACHINING (S1)	see sub-operations	440	SURFACE TREATMENT (C5)	always	INSPECTION (S2)	740	INSPECTION (C24)	optional
140	SURFACE TREATMENT (C6)	always	450	MACHINING (R7)	always		750	INSPECTION (C25)	optional
150	MACHINING (R2)	always	460	SURFACE TREATMENT (C16)	optional				
160	INSPECTION (R3)	always	470	SURFACE TREATMENT (R8)	optional				
170	SURFACE TREATMENT (C2)	optional	480	INSPECTION (C17)	optional				
180	OUTSOURCED (L3)	optional	490	INSPECTION (C18)	optional				
190	MACHINING (S1)	see sub-operations	500	INSPECTION (C19)	optional				
200	SURFACE TREATMENT (C5)	always	510	INSPECTION (C19)	optional				
210	SURFACE TREATMENT (C5)	always	520	MACHINING (C20)	optional				
220	MACHINING (S1)	see sub-operations	530	SURFACE TREATMENT (C21)	optional				
230	MACHINING (S1)	see sub-operations	540	INSPECTION (C11)	optional				
240	SURFACE TREATMENT (C5)	always	550	INSPECTION (C7)	always				
250	MACHINING (L4)	optional	560	INSPECTION (R9)	optional				
260	MACHINING (S1)	see sub-operations	570	INSPECTION (R10)	optional				
270	SURFACE TREATMENT (C5)	optional	580	INSPECTION (S2)	see sub-operations				
280	SURFACE TREATMENT (R4)	always	590	SURFACE TREATMENT (C22)	always				
290	INSPECTION (C7)	optional	600	INSPECTION (R11)	always				
300	INSPECTION (R5)	always	610	MISCELLANEOUS (C23)	optional				
310	SURFACE TREATMENT (C8)	always							

LEGEND	
	regressed scaling rule with a Gaussian uncertainty distribution (R1 to R15)
	linear or regressed scaling rule with a triangular uncertainty distribution (L1 to L13)
	constant operation time with a triangular uncertainty distribution (C1 to C25)
	manufacturing operation broken down into sub-operations (S1 & S2)
	standard operation
	extra operation

Figure 4.5: Scaling Rules for the Generic LFW Method of Manufacture.

When the Scalable Blisk Cost Model is run, the input windows illustrated in Fig. 4.6a–d are successively presented to the user. The blade, disc and blisk input screens list both the design parameters required to drive the scaling rules and the conditions that determine which optional operations apply. Instead of specifying the values of the parameters listed in Fig. 4.6b–d every time the model is run, the values of an unlimited number of blisks can be stored in a table within the model. By typing the name of the blisk into Fig. 4.6a, the relevant data can then be loaded when required.

a) Optional Loading of Blisk Data

Please enter a name for the blisk:

OK Cancel

b) Blisk Blade Parameters

Inputs 1 of 3: Blade Parameters

Number of Blades:

Blade Root Chord Length (in mm):

Blade Tip Chord Length (in mm):

Blade Leading Edge Height (in mm):

Blade Trailing Edge Height (in mm):

Blade Surface Area excluding the blade foot area (in cm squared):

Are the following two Stagger Angle Rates available? ☒ Yes ☐ No

Blade Average Stagger Angle Rate, if available (in deg/mm):

Blade Root Stagger Angle Rate, if available (in deg/mm):

OK Cancel

c) Blisk Disc Parameters

Inputs 2 of 3: Disc Parameters

Disc Rim Diameter (in mm):

Disc Perimeter excluding the annulus perimeter (in m):

Disc Surface Area excluding the annulus area (in m squared):

Disc Surface Area excluding the blade foot area (in m squared):

OK Cancel

d) Blisk Parameters

Inputs 3 of 3: Blisk Parameters

Is a significant amount of Rough Turning required? ☐ Yes ☒ No

Is blisk a Military or Civil project? ☐ Military ☒ Civil

Is blisk Bolted or Welded onto other rotors? ☐ Bolted ☒ Welded

Is blisk project in partnership with GE or P&W? ☐ Yes ☒ No

Is blisk Laser Shock Peened? ☐ Yes ☒ No

Is blisk Balanced? ☒ Yes ☐ No

Is blisk Balance Corrected? ☒ Yes ☐ No

Are Shank Nuts fitted onto blisk? ☐ Yes ☒ No

Blisk Complexity:

Number of Non-Angled Holes (<=10mm diameter):

Number of Non-Angled Holes (>10mm diameter):

Number of Angled Holes:

Number of Balance Hooks with scallops:

Number of Scallops with holes:

Number of Seals:

Number of Slots:

Number of Spline Teeth:

Tight Tolerance Surface Area (in cm squared):

OK Cancel

e) Extrapolation Warning

WARNING: You are extrapolating!

The estimated ADAPTIVE MILLING TIME and BLADE FOOT CMM TIME are 7% below the dataset range the model is based on.

If possible, please increase the BLADE NUMBER by least 4, the BLADE ROOT STAGGER ANGLE RATE by at least 0.022 deg/mm or the BLADE ROOT CHORD LENGTH by at least 7 mm (or a combination of the three).

OK Cancel

Figure 4.6: Scalable Blisk Cost Model User Interface. a) Optional Loading of Blisk Data, b) Blisk Blade Parameters, c) Blisk Disc Parameters, d) Blisk Parameters, and e) Extrapolation Warning

A common pitfall with regression that can lead to an incorrect cost forecast is to predict outside the existing data range or to apply it to a new technology that is radically different from those the relationship is based on [1, 67]. If the user therefore chooses design parameter settings that lead to an extrapolation beyond the dataset that define the scaling rules, then one or more warning messages will appear, such as the example in Fig. 4.6e.

Many of the design parameters, including the blade surface area and the disc perimeter, can only be obtained from Computer-Aided Design (CAD) models. As these are usually

not available at the preliminary design stage, the user has the option of using a Microsoft Excel interface that approximates the blade surface area and the disc perimeter using a simplistic cross-sectional blisk model defined by 24 grid points, the number of blades and the blade root stagger angle, i.e. the angle between the chord line at the blade root and the blisk's axis of rotation. As special features, such as the number of holes and seals, might also be unknown during the conceptual design phase, the user could apply uncertainty distributions to those inputs in addition to the ones that already exist for the scaling rules.

Due to time constraints and limited access to data, the Scalable Blisk Cost Model does not account for the disc and blade manufacturing costs. It is critical that these costs are eventually included in the model considering that they account for approximately half of the total unit costs of a solid-bladed blisk and significantly more of a blisk with hollow blades.

4.2.3 Regression Analysis

The blisk design variables that affect the operation times, and hence the unit cost, were identified by questioning R-R manufacturing engineers. A trial and error approach was then used to find the combination of design parameters that best explained the variability in the operation times. In order to predict the inspection operation time of a future blisk using the scaling rule shown in Fig. 4.7 for example, the Blade Parameter 1 and Blade Parameter 2 values of that blisk simply have to be inserted into the regression line equation shown in Fig. 4.7.

While the coefficient of determination, R^2 , measures how well the regression line describes the variability in the data, the p-value is the probability that the variability is better explained by chance rather than by the regression model. In order to be a good fit, the R^2 value should be close to 100 % and the p-value below 5 % [127]. One of the best fits found is displayed in Fig. 4.7, which has a R^2 value of 99.2 % and a p-value of 0.03 %. Here, the data points of the five blisks lie very close to the regression line. The fitted line in Fig. 4.8, on the other hand, only has a R^2 value of 62.1 % and a p-value of 11.3 % because the five data points are scattered far from the regression line. This is the most inaccurate scaling rule in the model, not only because it is a bad fit but also because it accounts for a significant proportion of the total manufacturing operation time of a blisk.

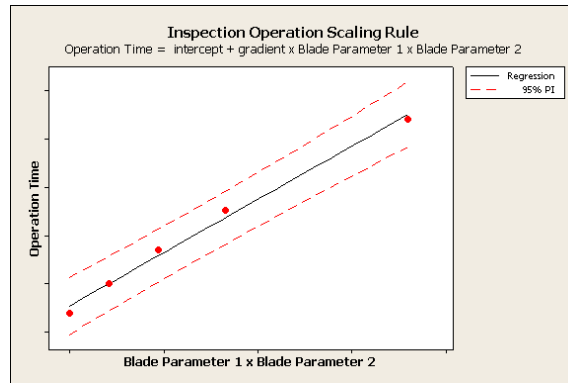


Figure 4.7: A Scaling Rule With a Good Fit.

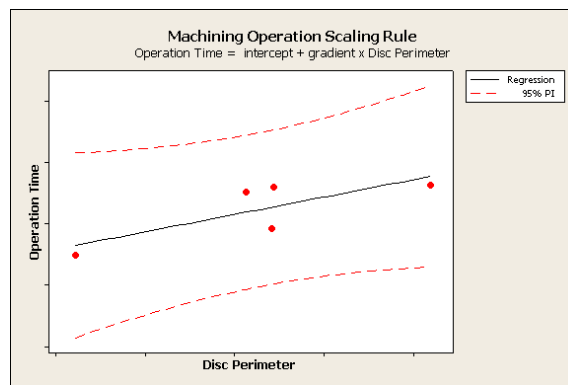


Figure 4.8: A Scaling Rule With a Bad Fit.

4.2.4 Uncertainty

Background

Although more complicated to implement, estimate ranges have the following advantages in comparison to single point predictions:

- They are more realistic because mathematical theory states that the summation of ‘most likely’ point estimates tends to underestimate costs by a large margin [128].
- The sensitivity of product costs to manufacturing process variability and other uncertainties can be determined [129].
- Single point estimates ignore the fact that cost drivers are often correlated which increases the cost uncertainty [128].

Knowing the probability distribution of cost can help to mitigate the risk of a project if the variability is addressed through avoidance, adjustment and contingency [1]. By not

only comparing and optimizing product designs in terms of their expected cost but also their cost uncertainty, robust designs can be formed [1].

Monte Carlo Simulation is a simple and widely used method for cascading uncertainty through a computer model. In cost models, one application of Monte Carlo Simulation is to determine the impact of design parameter variability on the product's cost uncertainty. The Monte Carlo Simulation Add-In for Vanguard Studio [130] can model various input uncertainty distributions to generate the Gaussian-type Probability Density Function (PDF) and the S-shaped Cumulative Distribution Function (CDF) shown in both Figs. 4.10 and 4.11 on page 124. While the PDF shows the relative likelihood of meeting a specific cost target, the CDF accrues the probabilities of all costs less or equal to the target value. Being able to predict costs at the 50 %, 70 % or 85 % confidence level is much more valuable to decision makers than 'most likely' estimates [128]. Vanguard Studio's Monte Carlo simulation package therefore enables cost model builders to meet the requirement of providing a cost prediction together with its associated probability of occurrence [1].

Triangular Uncertainty Distribution

In addition to the expected blisk operation times, their uncertainty ranges were collected because the predictability of the operation times varied significantly, depending on the maturity of each process. Accounting for the uncertainty also ensured that the manufacturing engineers agreed to formally sign off the scaling rules created. The scaling rules with triangular uncertainty distributions are simply described by a maximum, a most likely and a minimum operation time that define the shape of the triangle displayed in Fig. 4.9.

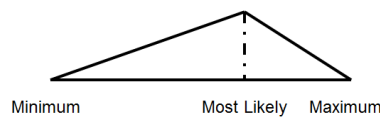


Figure 4.9: Triangular Uncertainty Distribution.

Prediction Interval

The scaling rules for operations R1 to R15 in Fig. 4.5 on page 116 have Gaussian uncertainty distributions which are based on the prediction intervals derived from the regression analysis described on page 118. The prediction interval represents the range in which a

single new prediction is likely to fall, usually with 95 % confidence [131]. This analytical method is statistically more accurate than the subjective triangular distribution because, according to Montgomery and Runger [61], it is a reasonable assumption that even for a small sample size the underlying distribution is normal, i.e. Gaussian. The prediction interval also takes the fit of the regression line into account as well as the number of data points [1]. Unlike the triangular distributions provided by the manufacturing engineers, the prediction intervals cannot take the uncertainty in the underlying data into account, however. Nonetheless, the scaling rules for R1 to R15 are based on the prediction intervals because they produced greater and therefore more conservative uncertainty ranges than the triangular distributions.

The dashed lines in Figs. 4.7 and 4.8 on page 119 indicate the outer boundaries of the 95 % confidence Prediction Interval (PI). They illustrate how significant the impact of the goodness of the regression line fit is on the prediction interval. While the limits of the prediction interval in Fig. 4.7 only deviate from the mean by 5 to 10 %, it is around 100 to 200 % in Fig. 4.8. The lower prediction interval limit in Fig. 4.8 was not capped at zero, even though it extends into negative operation time, in order not to falsify the unit cost distribution.

The prediction interval is based on the t-distribution, which is identical to the normal distribution when the number of data samples, k , is infinite [61]. If only a finite number of data points is available, however, the tails of the t-distribution become larger, which increases the prediction interval [61].

Eq. 4.1, adapted from Montgomery and Runger [61], shows how the prediction interval limits, Y , of the dependent variable, y , are calculated based on the value of the independent variable, x .

$$Y = \hat{y} \pm t_{\alpha/2, \nu} \sqrt{\hat{\sigma}^2 \left[1 + \frac{1}{n} + \frac{(x - \bar{x})^2}{S_{xx}} \right]} \quad \text{where} \quad \begin{aligned} \hat{y} &= \hat{\beta}_0 + \hat{\beta}_1 x \\ \nu &= n - 2 \\ \hat{\sigma}^2 &= \frac{\sum_{i=1}^n (y_i - \hat{y}_i)^2}{\nu} \\ S_{xx} &= \sum_{i=1}^n (x_i - \bar{x})^2 \end{aligned} \quad (4.1)$$

here:

- \hat{y} is the value of the regression model's dependent variable
- $t_{\alpha/2, \nu}$ is the percentage point in the t-distribution's statistical table [61], based on a confidence limit of α and ν degrees of freedom
- $\hat{\sigma}$ is the standard deviation of the data points with respect to the regression model
- \bar{x} is the mean value of the independent variable of the n data points
- S_{xx} is the sum of squares of the independent variable x of the n data points
- $\hat{\beta}_0$ is the intercept of the regression line
- $\hat{\beta}_1$ is the slope of the regression line
- y_i is the value of the dependent variable of the i^{th} data point and \hat{y}_i is its regressed value
- x_i is the value of the independent variable of the i^{th} data point

The prediction interval limits of R1 to R15 were converted into Gaussian uncertainty distributions, with mean, \hat{y} , and standard deviation, σ , by inserting Eq. 4.1 into the formula for the standard normal random variable, Z , given in Eq. 4.2, also adapted from Montgomery and Runger [61]. For a 95 % confidence prediction interval limit, α has to equal 5 %. The cumulative probability at $t_{\alpha/2, \nu}$ therefore has to be 97.5 %, at which Z equals 1.96 in the Cumulative Standard Normal Distribution statistical table [61].

$$Z = \frac{Y - \hat{y}}{\sigma} \Rightarrow \sigma = \frac{Y - \hat{y}}{Z} = \frac{t_{\alpha/2, \nu} \sqrt{\hat{\sigma}^2 \left[1 + \frac{1}{n} + \frac{(x - \bar{x})^2}{S_{xx}} \right]}}{1.96} \quad (4.2)$$

4.3 Results and Discussion

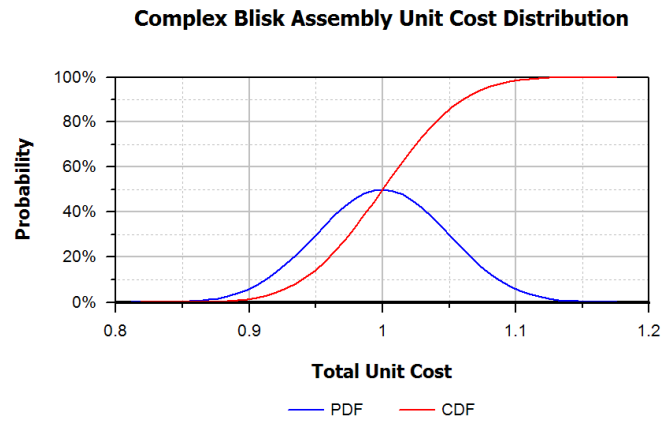
The scaling rules created can predict the total operation times of the five blisk designs within 4%, using the expected values of the triangular distributions and the mean of the prediction intervals. This level of accuracy is not surprising, however, considering that the scaling rules are based on these operation times. Hence, this value only reflects the lack of fit of the regression lines. In order to validate the scaling rules, the operation times of a new blisk design were forecasted and the prediction was within 2.7% of the expectation of the manufacturing engineers.

4.3.1 Unit Cost Prediction

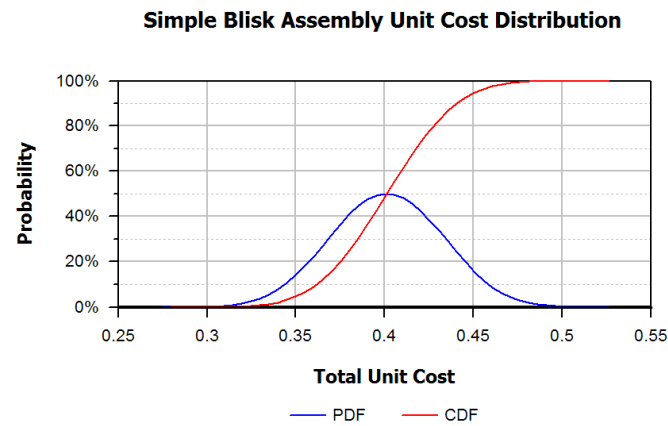
Figures 4.10 and 4.11 display the Scalable Blisk Cost Model's unit cost uncertainty distribution of a complex blisk with many features and a simple blisk with fewer features, respectively. Both figures, normalised with respect to the complex blisk's mean unit cost, also show a table that summarises statistical information related to the corresponding PDF and CDF graphs. As page 20 states that the standard error is inversely proportional to the square root of the sample number [61], 100,000 samples were generated for each cost distribution so that the standard error is less than 0.3% relative to the mean. Despite the large uncertainty distribution of some of the scaling rules, including the one shown in Fig. 4.8 on page 119, their impact is not significant considering that the 5th and 95th percentiles are within 8% and 13% of the complex and the simple blisk's average unit cost, respectively.

Complex Blisk Assembly Unit Cost Distribution Summary

Measure	Blisk Assembly Unit Cost
Observations	100,000
Mean	1
Standard Deviation	0.05
Posterior STD	1.5e-4
Variance	2.2e-3
Minimum	0.81
5th Percentile	0.92
Median	1
95th Percentile	1.08
Maximum	1.18

**Figure 4.10: Unit Cost Uncertainty Distribution of the Complex Blisk.****Simple Blisk Assembly Unit Cost Distribution Summary**

Measure	Blisk Assembly Unit Cost
Observations	100,000
Mean	0.4
Standard Deviation	0.03
Posterior STD	9.7e-5
Variance	9.3e-4
Minimum	0.27
5th Percentile	0.35
Median	0.4
95th Percentile	0.45
Maximum	0.53

**Figure 4.11: Unit Cost Uncertainty Distribution of the Simple Blisk.**

Figures 4.12 and 4.13 provide information at feature level based on the 14 sub-operations listed in Fig. 4.5 on page 116. Although the Scalable Blisk Cost Model cannot show all the bar charts simultaneously, the purpose of Figs. 4.12 and 4.13 is to highlight how much insight an activity-based-parametric hybrid cost model can provide about how the resource consumption varies, depending on the design.

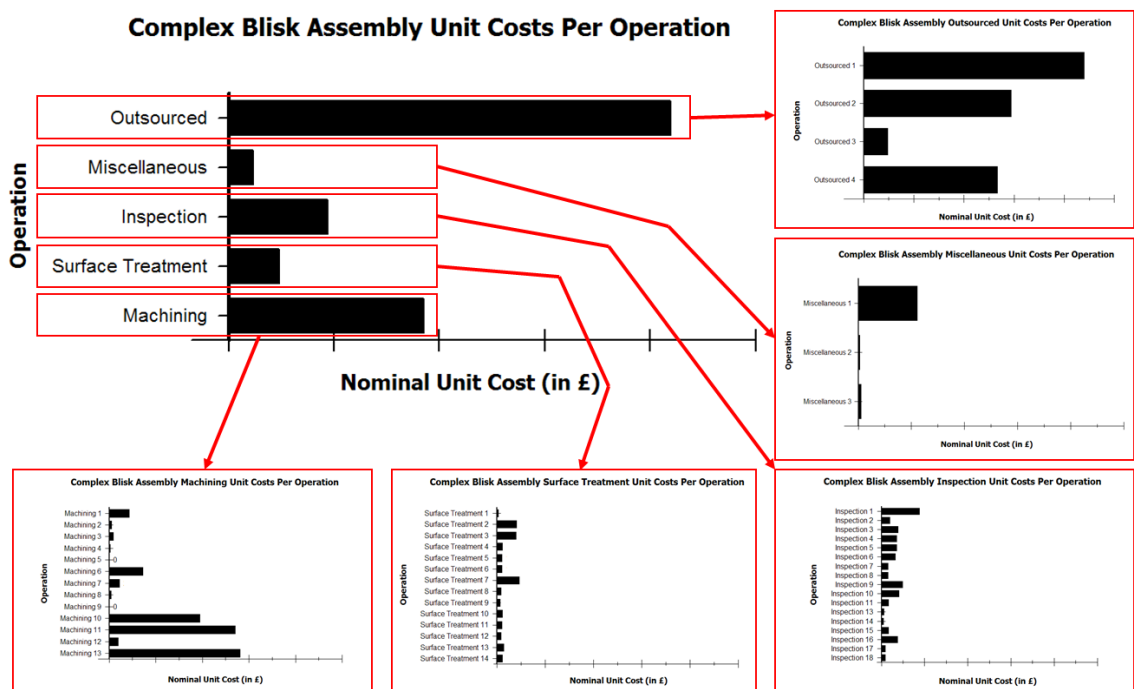


Figure 4.12: Operation and Feature Unit Costs of the Complex Blisk.

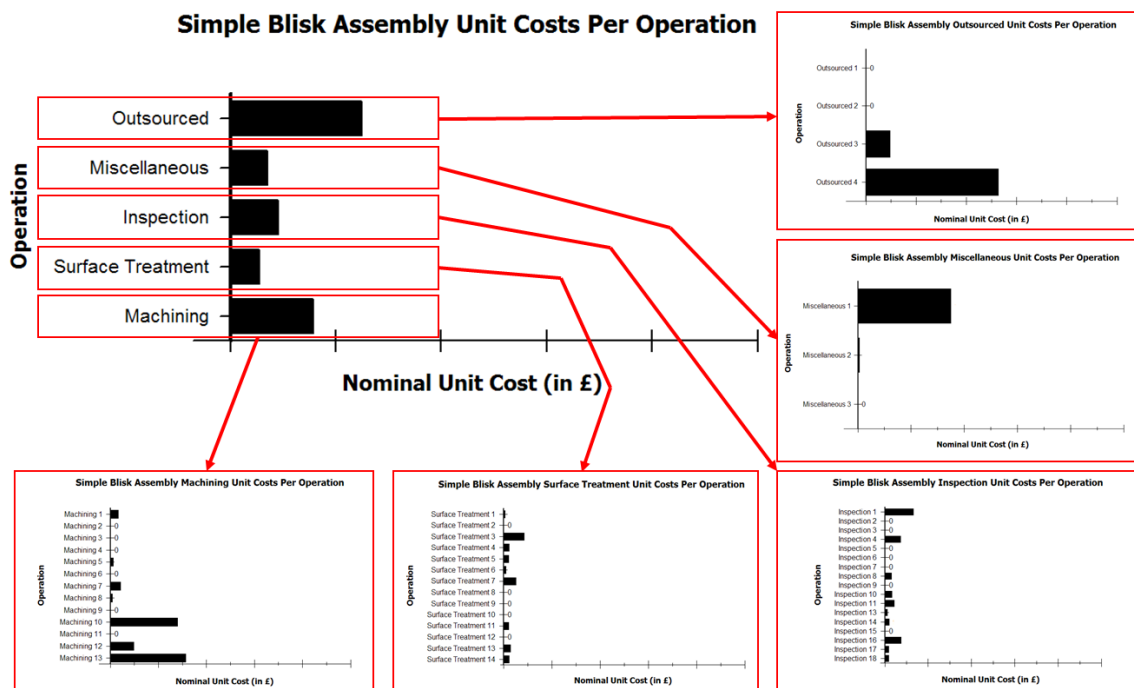


Figure 4.13: Operation and Feature Unit Costs of the Simple Blisk.

4.3.2 Blisk Design Space

In order to explore how the blisk design parameters affect unit cost, a sensitivity study was carried out. This was done by generating a Design of Experiments (DoE) in Design-Expert, a commercial DoE program. In these computational experiments the number of blades, the root and the average blade stagger angle rates (i.e. the rate at which the blade twists at its root and over its entire length, respectively), the disc rim diameter and the disc surface area were varied independently over the ranges recorded for the five blisks. The blisk design data indicated that the number of blades and the blade surface area had a correlation¹ of -0.92 , meaning that the blades got smaller as the number of blades increased. Throughout the DoE study, the number of blades therefore controlled the blade height and chord length accordingly. The remaining design parameters, such as the number of holes and seals, were first set at the complex blisk's and then the simple blisk's values, in order to plot a Pareto Chart and a response surface for both types as shown in Figs. 4.14 and 4.15, respectively.

The advantage of using Design-Expert instead of conducting experiments randomly is that the software minimizes the number of experiments required while also minimizing statistical error. For this study that meant that Design-Expert only needed 61 'design-optimally' distributed points in order to generate a third order surrogate model for the complex blisk. As the Pareto Chart in Fig. 4.14 indicates that the number of blades and the average blade stagger angle rate are the biggest cost drivers, the unit cost response surface of the complex blisk was plotted against those two parameters, while the remaining three cost drivers were set at their mean. Although the DoE is capable of detecting third order effects, the response surface is only second order because the Pareto Chart shows that only first order effects (like the blade number) and second order interaction effects (between the disc rim diameter and the disc surface area for example) are above the 5% significance threshold labelled 't-value Limit'. No insignificant effects are shown in the Pareto Chart because Design-Expert removes these automatically. Since the Scalable Blisk Cost Model has no discontinuities, the response surface has a R^2 value of 99.6% for the 61 design-optimally distributed points. Considering that unit cost increases as the

¹The correlation is a measure of the linear relationship between two random variables [61]. It ranges from -1 to $+1$, where -1 and $+1$ indicate that, when plotted against each other, the points of the random variables fall exactly along a negative (-1) or a positive slope ($+1$). If the correlation is 0, however, there is no relationship.

number of blades is reduced means that the cost saving from the lower blade count does not compensate for the cost increase from the larger blades.

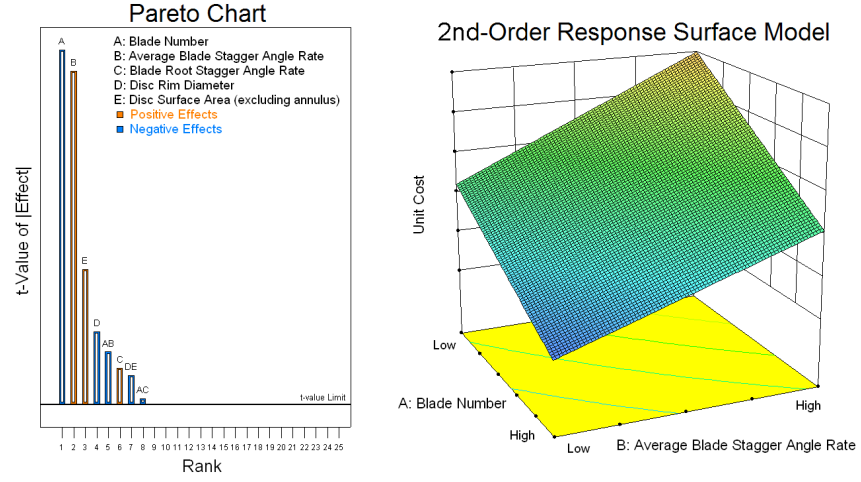


Figure 4.14: Unit Cost Sensitivity of the Complex BliSk.

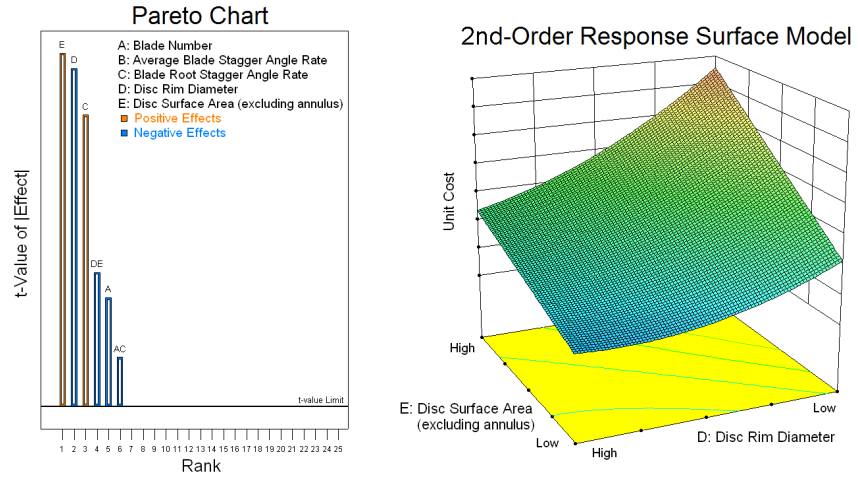


Figure 4.15: Unit Cost Sensitivity of the Simple BliSk.

Unlike its counterpart, the Pareto Chart in Fig. 4.15 shows that the biggest cost drivers of the simple bliSk are the disc surface area and the disc rim diameter, while the average blade stagger angle rate has no impact at all. These large changes can be explained by the fact that the simple bliSk uses fewer and different scaling rules that do not depend on the average blade stagger angle rate. As the response surface therefore only had to model the variation of four design parameters, 40 instead of 61 design-optimally distributed points were needed in order to detect third order effects. Similar to Fig. 4.14, the Pareto Chart in Fig. 4.15 shows that only first and second order effects are significant. Just like before,

a second order response surface was therefore plotted against the two biggest cost drivers, while the other two parameters were set at their mean. Although it makes sense that unit cost increases with disc surface area, it might seem counterintuitive that cost decreases with an increasing disc rim diameter. The explanation is that for a given disc surface area, a smaller rim diameter will increase the cross-sectional perimeter of the disc. As a blisk with a large perimeter tends to have more expensive features, a smaller rim diameter leads to a higher unit cost unless the disc surface area reduces proportionately.

Chapter 5

Conclusion and Recommendations

5.1 System Study

5.1.1 Contribution and Limitations

As outlined in Section 1.2.1 on page 4, the originality of this study lies in the holistic approach of combining system design engineering and performance simulation with economic forecasting, operational research, robust design and multi-disciplinary optimization. This enabled five different engine and airframe system options, including the two- and three-shaft turbofan, the geared turbofan, the turboprop and the open rotor aircraft designs to be optimized in MATLAB in terms of direct operating cost for a standard mission, so that a fair quantitative comparison could be made in light of uncertain fuel and CO₂ prices in 2030.

The design parameters optimized include the engine's turbine entry temperature, its overall pressure ratio and the airframe's wing span and mean chord length. In addition, the three turbofan options' fan pressure ratio was varied, as well as the turboprop's and the open rotor's propeller diameter and rotational tip speed. Although the effect of the cruise speed on the system performance was also investigated, the designs were only optimized for one cruise velocity.

The cruise speed not only affects the fuel consumption, but also the productivity of the aircraft fleet, the opportunity cost resulting from the Value of Time (VoT) of the passengers, and the market share of the aircraft in comparison to other modes of transport. All these aspects are therefore taken into account by the model, but not different aircraft sizes, flight profiles and annual passenger numbers (i.e. demand).

The passenger VoT has a large effect on the trade-off between the cost of fuel and the total cost of time of the aircraft, crew and passengers: while the geared turbofan cruising at Mach 0.80 is the optimum design when the passenger VoT is taken into account, it is the turboprop at Mach 0.70 when the value of time is excluded for a monopolistic scenario in which the passenger does not have the opportunity to select a faster mode of transport. This shows that the most *fuel-efficient* option, the open rotor, is not automatically the most *cost-efficient* solution because of the relatively high engine and airframe costs. The results also give an insight into the local design and cost space surrounding the optimum design point of each system option and show how the various performance parameters vary throughout the standard mission. These include the altitude, flight speed and the engine thrust, fuel and core mass flow rates, turbine entry temperature, rotational speeds, pressure ratios, the turbofans' bypass ratio and the turboprop's and open rotor's propeller efficiency.

Although all results agree well with public data, the engine design and performance is slightly stochastic due to hard design constraints, including a minimum blade height of 13 mm, and only permitting subsonic flow velocities within the engine. It is also only by chance that the simplistic direct operating cost formulas capture the complexity of the open rotor, as the open rotor's relatively high takeoff thrust requirement is one of the parameters that affects the predicted engine cost.

5.1.2 Future Work

Improvements

- Make the engine design and performance models (Modules 1 and 3) more stable and remove their stochastic nature by replacing the hard constraints, like the minimum blade height, with efficiency penalties. Also uncouple the rotational speeds of the HP and IP systems.
- Rerun the engine and airframe design models (Modules 1 and 2) until the thrust requirement in Module 5 has converged.
- Investigate whether the run-time can be shortened by simplifying the mission profile in Module 6.
- Examine the effect of optimized scheduling on the fleet simulation (Module 7) and

verify the modal shift model using actual data.

- Improve the various operating cost element formulas in Module 8 as they are very simplistic and the baseline values are out of date. This poses a significant challenge, however, as cost estimating is affected by many non-engineering factors [52, 54]. The use of simple cost estimating relationships and ‘fudge’ factors is therefore a common method of accounting for these variabilities and is not necessarily more inaccurate than more complex formulas [52].
- Refine the optimization process by allowing smaller step lengths in Module 9.

Further Studies

- Optimize the system options for each cruise speed.
- Explore how the propeller blade count and the maximum relative airflow velocity at the propeller blade tip affect the turboprop and the open rotor engine performance.
- Future studies could also compare a high-wing mounted open rotor and a turboprop engine with a centrifugal compressor against the other system options.
- Investigate how the optimum design is affected by other fuel prices and mission scenarios (including different and more realistic takeoff, climb and descent thrust settings and propeller rotational speed regimes, wind conditions, flight delays, etc.), aircraft sizes and lifespans and values of time.
- Integrate the Component Study into the System Study and conduct trade-off studies on other advanced gas turbine systems and components, including not only blisks but also the more-electric aircraft, variable fan blades, or a mixed instead of a separate core and bypass nozzle for example.
- Conduct a sensitivity study to analyse which design parameters have the biggest impact on the operating cost.
- Apply further uncertainty distributions to reflect the unpredictability of aircraft weight and acquisition cost, as well as other operating cost elements.

- Use other robustness metrics to investigate how that affects the optimum design solutions and create a Pareto Front that shows the trade-off between the mean and the variance of the operating cost, as described on page 12.
- As the effect of the modal shift on the operating cost can only be simulated by dividing the costs by the relative market share of the aircraft, the calculation of the NPV of profits might produce more accurate results despite the large amount of uncertain data required, as stated on page 14. This would also allow different economic growth scenarios and their effect on the flight demand and fuel price to be modelled.

5.2 Component Study

5.2.1 Factory Cost Model

The Factory Cost Model can aid manufacturing engineers optimize their methods of manufacture by indicating how cost can be minimized while meeting the required throughput and quality. Manufacturing costs can be reduced, for example, by trading inspection costs between machining operations against potential scrap costs resulting from removing these inspections [132]. If the model is loaded onto a global server, the latest methods of manufacture, operation times and cost estimates can also be viewed and updated by the rest of the organisation through Vanguard Studio's standard web browser, facilitating design automation and the integration of cost into design optimization frameworks [5].

While the Factory Cost Model was being built, R-R created a factory simulation for the future LFW blisk factory in WITNESS, a commercial simulation package. Unlike the Factory Cost Model, a factory simulation can model the stochastic nature of manufacturing that arises due to the dynamic effect of time [66]. As an event in a simulation occurs at the same level as an activity in an ABC model, the factory simulation should be linked to the Factory Cost Model to enable ABC to move beyond the static framework [66, 129]. Finally, the creation of the Factory Cost Model's manufacturing cell files should be fully automated and the Factory Cost Model adjusted so that uncertainty ranges can be applied to the inputs. This would enable the uncertainty in the operation times, calculated by the Scalable Blisk Cost Model or the WITNESS factory simulation for example, to be taken into account.

5.2.2 Scalable Blisk Cost Model

Using the Scalable Blisk Cost Model in conjunction with the Factory Cost Model offers a step towards implementing Toyota's Set-Based Concurrent Engineering (SBCE) principles, where design engineering and manufacturing engineering define a large set of feasible design solutions from their respective areas of expertise and, through an interactive process, gradually converge on a final design [133]. Unlike traditional design practice, SBCE does not fix the final design early in the design process, resulting in a reduced risk of both time-consuming rework and sub-optimal product performance [133]. As it is difficult to explain why a particular combination of design parameters produced the best fit for the regressed scaling rules, it is not advisable to use the Scalable Blisk Cost Model in optimization routines without further validation. A sensitivity study such as the one in Section 4.3.2 on page 126 can be beneficial, however, because it highlights the biggest cost drivers and how they affect cost. Such a study also allows the engineers to assess whether the cost model is realistic.

Since Vanguard Studio can handle cumulative uncertainty distributions, ideally, the user should have the option of attributing uncertainty ranges to the inputs of the Scalable Blisk Cost Model in addition to the uncertainty distributions that already exist for the scaling rules. In view of the fact that the LFW blisk operation times are likely to change as the processes mature and, with time, further blisk designs will be created, the scaling rules should be updated and validated at regular intervals. These updates could also help improve the scaling rule shown in Fig. 4.8 on page 119.

Appendix A

Design Optimization Data

Table A.1: Two-Shaft Turbofan Design Space (Cruise Speed: Mach 0.78).

Design Variables										Design Parameters					
Engine					Airframe					Engine					
Turbine Entry Temp. (K)	Overall Pressure Ratio	Fan Pressure Ratio	Wing Span Factor	Wing Mean Chord Length Factor	Airframe					Engine					
					Max. Static Thrust (kN) ^a	Crit. Thrust Requirement ^b	Fan Dia. (m)	Bypass Ratio ^c	Min. Blade Height (mm)	Engine Mass (kg)	Wing Span (m)	Wing Mean Chord Length (m)	Max. Take-off Weight (kg)	Initial Cruise Altitude (ft)	Final Cruise Altitude (ft)
1,820	32.2	1.80	0.34	0.05	127.5	1	1.79	6.75	13.1	1,868	36.0	3.31	70,232	32,000	38,000
1,840	32.2	1.80	0.34	0.05	+ 2.8 %	1	+ 1.4 %	+ 2.7 %	13.2	+ 2.3 %	36.0	3.31	+ 0.2 %	32,000	38,000
1,800	32.2	1.80	0.34	0.05	+ 4.4 %	1	+ 2.2 %	− 2.7 %	12.5	+14.6 %	36.1	3.34	+ 1.2 %	32,000	38,000
1,820	33.4	1.80	0.34	0.05	− 1.0 %	1	− 0.4 %	− 0.3 %	12.7	− 1.6 %	36.0	3.30	− 0.1 %	32,000	38,000
1820	31.0	1.80	0.34	0.05	+ 1.7 %	1	+ 0.8 %	+ 0.3 %	13.6	+ 3.9 %	36.0	3.31	+ 0.3 %	32,000	38,000
1,820	32.2	1.83	0.34	0.05	+13.2 %	1	+ 5.5 %	− 3.6 %	14.0	+27.6 %	36.2	3.36	+ 2.4 %	32,000	38,000
1,820	32.2	1.78	0.34	0.05	+ 3.8 %	1	+ 2.8 %	+ 4.0 %	12.5	+ 5.0 %	36.0	3.32	+ 0.5 %	32,000	38,000
1820	32.2	1.80	0.38	0.05	− 0.7 %	1	− 0.3 %	− 0.0 %	13.1	− 1.0 %	37.5	3.21	+ 0.4 %	32,000	38,000
1,820	32.2	1.80	0.30	0.05	+ 2.3 %	5	+ 1.2 %	+ 0.0 %	13.2	+ 3.4 %	34.5	3.41	− 0.1 %	32,000	38,000
1,820	32.2	1.80	0.34	0.09	− 2.1 %	5	− 1.1 %	− 0.0 %	13.0	− 3.1 %	36.0	3.47	+ 0.0 %	32,000	38,000
1,820	32.2	1.80	0.34	0.01	+ 6.0 %	1	+ 3.0 %	+ 0.1 %	13.4	+ 8.9 %	36.0	3.15	+ 0.5 %	32,000	36,000

^aat $\Delta T = 15$ K, includes the thrust growth factor of 1.25 (see page 41)

^b1 = takeoff field length, 2 = balanced field length, 3 = 1st segment climb, 4 = 2nd segment climb, 5 = 3rd segment climb, 6 = initial cruise altitude, 7 = final cruise altitude

^cat max. static thrust

□ design variable changed relative to optimum design □ diminishment relative to optimum design □ constraint violated

Table A.2: Two-Shaft Turbofan Design Cost Space (Cruise Speed: Mach 0.78).

Design Variables				Direct Operating Cost (¢/RPK in 2012 prices)								
Engine		Airframe		Engine	Airframe			Total				
Turbine Entry Temp. (K)	Overall Pressure Ratio	Fan Pressure Ratio	Wing Span Factor	Wing Mean Chord Length Factor	Depreciation + Interest + Insurance + Maintenance	Landing + Navigation	Fuel + CO ₂ (mean)	Crew + Ground Handling	Time	Excl. Time (mean)	Incl. Time (mean)	
1,820	32.2	1.80	0.34	0.05	0.743	2.704	0.678	3.454	2.470	8.459	10.050	18.509
<div>1,840</div>	32.2	1.80	0.34	0.05	<div>+ 2.9 %</div>	<div>+ 0.4 %</div>	<div>+ 0.2 %</div>	<div>+ 0.2 %</div>	0.0 %	<div>+ 0.0 %</div>	<div>+ 0.4 %</div>	<div>+ 0.2 %</div>
<div>1,800</div>	32.2	1.80	0.34	0.05	<div>+ 2.0 %</div>	<div>+ 2.0 %</div>	<div>+ 0.9 %</div>	<div>+ 5.7 %</div>	0.0 %	<div>+ 0.1 %</div>	<div>+ 2.7 %</div>	<div>+ 1.5 %</div>
1,820	<div>33.4</div>	1.80	0.34	0.05	<div>− 0.6 %</div>	<div>− 0.2 %</div>	<div>− 0.1 %</div>	<div>− 1.2 %</div>	0.0 %	<div>− 0.0 %</div>	<div>− 0.5 %</div>	<div>− 0.3 %</div>
1,820	<div>31.0</div>	1.80	0.34	0.05	<div>+ 1.2 %</div>	<div>+ 0.5 %</div>	<div>+ 0.3 %</div>	<div>+ 1.6 %</div>	0.0 %	<div>+ 0.0 %</div>	<div>+ 0.8 %</div>	<div>+ 0.4 %</div>
1,820	32.2	<div>1.83</div>	0.34	0.05	<div>+ 8.9 %</div>	<div>+ 3.9 %</div>	<div>+ 1.8 %</div>	<div>+ 4.1 %</div>	0.0 %	<div>+ 0.1 %</div>	<div>+ 3.2 %</div>	<div>+ 1.8 %</div>
1,820	32.2	<div>1.78</div>	0.34	0.05	<div>+ 2.5 %</div>	<div>+ 0.8 %</div>	<div>+ 0.4 %</div>	<div>+ 0.8 %</div>	0.0 %	<div>+ 0.0 %</div>	<div>+ 0.7 %</div>	<div>+ 0.4 %</div>
1,820	32.2	1.80	<div>0.38</div>	0.05	<div>− 0.4 %</div>	<div>+ 0.6 %</div>	<div>+ 0.3 %</div>	<div>− 0.9 %</div>	0.0 %	<div>+ 0.1 %</div>	<div>− 0.2 %</div>	<div>− 0.0 %</div>
1,820	32.2	1.80	<div>0.30</div>	0.05	<div>+ 1.6 %</div>	<div>− 0.2 %</div>	<div>− 0.1 %</div>	<div>+ 1.4 %</div>	0.0 %	<div>− 0.1 %</div>	<div>+ 0.5 %</div>	<div>+ 0.2 %</div>
1,820	32.2	1.80	0.34	<div>0.09</div>	<div>− 1.4 %</div>	<div>+ 0.0 %</div>	<div>+ 0.0 %</div>	<div>+ 0.5 %</div>	0.0 %	<div>+ 0.0 %</div>	<div>+ 0.1 %</div>	<div>+ 0.0 %</div>
1,820	32.2	1.80	0.34	<div>0.01</div>	<div>+ 4.0 %</div>	<div>+ 0.8 %</div>	<div>+ 0.4 %</div>	<div>+ 0.5 %</div>	0.0 %	<div>− 0.2 %</div>	<div>+ 0.7 %</div>	<div>+ 0.3 %</div>
<div><div></div> design variable changed relative to optimum design</div>												
<div><div></div> improvement relative to optimum design</div>												
<div><div></div> diminishment relative to optimum design</div>												

Table A.3: Three-Shaft Turbofan Design Space (Cruise Speed: Mach 0.78).

Design Variables					Design Parameters											
Engine			Airframe		Engine					Airframe						
Turbine Entry Temp. (K)	Overall Pressure Ratio	Fan Pressure Ratio	Wing Span Factor	Wing Mean Chord Length Factor	Max. Static Thrust (kN) ^a	Crit. Thrust Requirement ^b	Fan Dia. (m)	Bypass Ratio ^c	Min. Blade Height (mm)	Engine Mass (kg)	Wing Span (m)	Wing Mean Chord Length (m)	Max. Take-off Weight (kg)	Initial Cruise Altitude (ft)	Final Cruise Altitude (ft)	Mission Fuel (kg)
1,880	35.8	1.78	0.34	0.05	131.4	5	1.83	7.46	15.4	1,871	36.0	3.31	70,280	32,000	38,000	4,433
1,900	35.8	1.78	0.34	0.05	+ 3.3 %	5	+ 1.7 %	+ 2.5 %	15.1	+ 2.6 %	36.0	3.31	+ 0.2 %	32,000	38,000	+ 0.9 %
1,860	35.8	1.78	0.34	0.05	+ 0.8 %	5	+ 0.4 %	− 2.5 %	15.6	+ 2.4 %	36.0	3.31	+ 0.2 %	32,000	38,000	+ 0.6 %
1,880	37.0	1.78	0.34	0.05	+ 2.9 %	5	+ 1.5 %	− 0.2 %	14.9	+ 2.3 %	36.0	3.31	+ 0.2 %	32,000	38,000	− 0.2 %
1,880	34.6	1.78	0.34	0.05	+ 1.1 %	5	+ 0.5 %	+ 0.2 %	15.9	+ 2.2 %	36.0	3.31	+ 0.2 %	32,000	38,000	+ 0.8 %
1,880	35.8	1.80	0.34	0.05	+ 0.4 %	1	− 0.7 %	− 3.8 %	15.6	+ 0.2 %	36.0	3.31	+ 0.0 %	32,000	38,000	+ 0.6 %
1,880	35.8	1.75	0.34	0.05	+ 4.3 %	5	+ 3.1 %	+ 4.1 %	15.2	+ 5.7 %	36.0	3.32	+ 0.5 %	32,000	38,000	+ 0.9 %
1,880	35.8	1.78	0.38	0.05	− 0.9 %	1	− 0.5 %	− 0.0 %	15.4	− 1.4 %	37.5	3.22	+ 0.3 %	32,000	38,000	− 1.0 %
1,880	35.8	1.78	0.30	0.05	+ 3.0 %	5	+ 1.5 %	+ 0.0 %	15.7	+ 4.7 %	34.5	3.42	− 0.0 %	32,000	38,000	+ 1.5 %
1,880	35.8	1.78	0.34	0.09	− 1.4 %	5	− 0.7 %	− 0.0 %	15.3	− 2.1 %	36.0	3.47	+ 0.1 %	32,000	38,000	+ 0.5 %
1,880	35.8	1.78	0.34	0.01	+ 6.1 %	1	+ 3.0 %	+ 0.1 %	15.9	+ 9.5 %	36.0	3.16	+ 0.4 %	30,000	38,000	+ 0.7 %
^a at ΔT = 15 K, includes the thrust growth factor of 1.25 (see page 41)																
^b 1 = takeoff field length, 2 = balanced field length, 3 = 1 st segment climb, 4 = 2 nd segment climb, 5 = 3 rd segment climb,																
6 = initial cruise altitude, 7 = final cruise altitude																
^c at max. static thrust																
<div><div> design variable changed relative to optimum design</div><div> improvement relative to optimum design</div><div> diminishment relative to optimum design</div><div> constraint violated</div></div>																

^aat $\Delta T = 15$ K, includes the thrust growth factor of 1.25 (see page 41)^b1 = takeoff field length, 2 = balanced field length, 3 = 1st segment climb, 4 = 2nd segment climb, 5 = 3rd segment climb,

6 = initial cruise altitude, 7 = final cruise altitude

^cat max. static thrust design variable changed relative to optimum design improvement relative to optimum design diminishment relative to optimum design constraint violated

Table A.4: Three-Shaft Turbofan Design Cost Space (Cruise Speed: Mach 0.78).

Design Variables				Direct Operating Cost (¢/RPK in 2012 prices)								
Engine		Airframe		Engine	Airframe			Total				
Turbine Entry Temp. (K)	Overall Pressure Ratio	Fan Pressure Ratio	Wing Span Factor	Wing Mean Chord Length Factor	Depreciation + Interest + Insurance + Maintenance	Landing + Navigation	Fuel + CO ₂ (mean)	Crew + Ground Handling	Time	Excl. Time (mean)	Incl. Time (mean)	
1,880	35.8	1.78	0.34	0.05	0.842	2.707	0.679	3.356	2.470	8.458	10.053	18.511
1,900	35.8	1.78	0.34	0.05	+ 3.2 %	+ 0.4 %	+ 0.2 %	+ 0.9 %	0.0 %	+ 0.0 %	+ 0.7 %	+ 0.4 %
1,860	35.8	1.78	0.34	0.05	− 0.5 %	+ 0.3 %	+ 0.2 %	+ 0.6 %	0.0 %	+ 0.0 %	+ 0.3 %	+ 0.1 %
1,880	37.0	1.78	0.34	0.05	+ 1.9 %	+ 0.4 %	+ 0.2 %	− 0.2 %	0.0 %	+ 0.0 %	+ 0.2 %	+ 0.1 %
1,880	34.6	1.78	0.34	0.05	+ 0.7 %	+ 0.3 %	+ 0.1 %	+ 0.8 %	0.0 %	− 0.0 %	+ 0.4 %	+ 0.2 %
1,880	35.8	1.80	0.34	0.05	+ 0.3 %	+ 0.0 %	+ 0.0 %	+ 0.6 %	0.0 %	+ 0.0 %	+ 0.2 %	+ 0.1 %
1,880	35.8	1.75	0.34	0.05	+ 2.8 %	+ 0.9 %	+ 0.4 %	+ 0.9 %	0.0 %	+ 0.0 %	+ 0.8 %	+ 0.4 %
1,880	35.8	1.78	0.38	0.05	− 0.6 %	+ 0.5 %	+ 0.2 %	− 1.0 %	0.0 %	+ 0.1 %	− 0.2 %	− 0.1 %
1,880	35.8	1.78	0.30	0.05	+ 2.0 %	− 0.0 %	− 0.0 %	+ 1.5 %	0.0 %	− 0.1 %	+ 0.7 %	+ 0.3 %
1,880	35.8	1.78	0.34	0.09	− 0.9 %	+ 0.2 %	+ 0.1 %	+ 0.5 %	0.0 %	+ 0.0 %	+ 0.1 %	+ 0.1 %
1,880	35.8	1.78	0.34	0.01	+ 4.0 %	+ 0.9 %	+ 0.4 %	+ 0.7 %	0.0 %	− 0.2 %	+ 0.8 %	+ 0.4 %
<div><div><div></div><div>design variable changed relative to optimum design</div></div><div><div></div><div>improvement relative to optimum design</div></div><div><div></div><div>diminishment relative to optimum design</div></div></div>												

Table A.5: Geared Turbofan Design Space (Cruise Speed: Mach 0.78).

Design Variables										Design Parameters					
Engine					Airframe					Engine					
Turbine Entry Temp. (K)	Overall Pressure Ratio	Fan Pressure Ratio	Wing Span Factor	Wing Mean Chord Length Factor	Max. Static Thrust (kN) ^a	Crit. Thrust Requirement ^b	Fan Dia. (m)	Bypass Ratio ^c	Min. Blade Height (mm)	Engine Mass (kg)	Wing Span (m)	Wing Mean Chord Length (m)	Airframe		
													Max. Take-off Weight (kg)	Initial Cruise Altitude (ft)	Final Cruise Altitude (ft)
1,920	33.4	1.78	0.34	0.05	117.8	1	1.74	7.78	13.0	1,449	35.8	3.26	68,870	32,000	38,000
1,940	33.4	1.78	0.34	0.05	+ 2.5 %	1	+ 1.2 %	+ 1.4 %	13.2	+ 9.6 %	35.9	3.27	+ 0.6 %	32,000	38,000
1,900	33.4	1.78	0.34	0.05	+ 0.6 %	1	+ 0.3 %	− 2.1 %	13.4	+ 2.7 %	35.9	3.26	+ 0.2 %	32,000	38,000
1,920	34.6	1.78	0.34	0.05	+ 0.4 %	1	+ 0.2 %	− 0.1 %	12.6	+ 1.5 %	35.8	3.26	+ 0.1 %	32,000	38,000
1,920	32.2	1.78	0.34	0.05	+ 0.8 %	1	+ 0.4 %	+ 0.1 %	13.5	+ 1.8 %	35.9	3.26	+ 0.1 %	32,000	38,000
1,920	33.4	1.80	0.34	0.05	+ 0.3 %	1	− 0.8 %	− 3.7 %	13.4	+ 0.6 %	35.8	3.26	+ 0.0 %	32,000	38,000
1,920	33.4	1.75	0.34	0.05	+ 1.2 %	5	+ 1.5 %	+ 4.2 %	12.7	+ 4.0 %	35.9	3.27	+ 0.3 %	32,000	38,000
1,920	33.4	1.78	0.38	0.05	− 0.7 %	1	− 0.3 %	− 0.0 %	13.0	− 1.0 %	37.3	3.17	+ 0.4 %	32,000	38,000
1,920	33.4	1.78	0.30	0.05	+ 2.9 %	5	+ 1.4 %	+ 0.1 %	13.5	+ 4.9 %	34.4	3.37	− 0.1 %	32,000	38,000
1,920	33.4	1.78	0.34	0.09	− 1.5 %	5	− 0.8 %	− 0.0 %	12.9	− 2.2 %	35.9	3.43	+ 0.1 %	32,000	38,000
1,920	33.4	1.78	0.34	0.01	+ 6.4 %	1	+ 3.2 %	+ 0.1 %	13.7	+ 10.1 %	35.9	3.11	+ 0.4 %	32,000	36,000

^aat $\Delta T = 15$ K, includes the thrust growth factor of 1.25 (see page 41)^b1 = takeoff field length, 2 = balanced field length, 3 = 1st segment climb, 4 = 2nd segment climb, 5 = 3rd segment climb, 6 = initial cruise altitude, 7 = final cruise altitude^cat max. static thrust□ design variable changed relative to optimum design■ improvement relative to optimum design■ diminishment relative to optimum design■ constraint violated

Table A.6: Geared Turbofan Design Cost Space (Cruise Speed: Mach 0.78).

Design Variables				Direct Operating Cost (¢/RPK in 2012 prices)							
Engine		Airframe		Engine	Airframe			Total			
Turbine Entry Temp. (K)	Overall Pressure Ratio	Fan Pressure Ratio	Wing Span Factor	Wing Mean Chord Length Factor	Depreciation + Interest + Insurance + Maintenance	Landing + Navigation	Fuel + CO ₂ (mean)	Crew + Ground Handling	Time	Excl. Time (mean)	Incl. Time (mean)
1,920	33.4	1.78	0.34	0.05	0.743	2.618	0.668	3.330	2.470	8.459	18.288
<div>1,940</div>	33.4	1.78	0.34	0.05	+ 2.6 %	+ 1.1 %	+ 0.5 %	+ 0.2 %	0.0 %	+ 0.0 %	+ 0.3 %
<div>1,900</div>	33.4	1.78	0.34	0.05	− 0.6 %	+ 0.3 %	+ 0.1 %	+ 0.4 %	0.0 %	+ 0.0 %	+ 0.1 %
<div>1,920</div>	<div>34.6</div>	1.78	0.34	0.05	+ 0.2 %	+ 0.2 %	+ 0.1 %	− 0.9 %	0.0 %	− 0.0 %	− 0.1 %
<div>1,920</div>	<div>32.2</div>	1.78	0.34	0.05	+ 0.5 %	+ 0.2 %	+ 0.1 %	+ 1.3 %	0.0 %	+ 0.0 %	+ 0.3 %
<div>1,920</div>	33.4	<div>1.80</div>	0.34	0.05	+ 0.2 %	+ 0.1 %	+ 0.0 %	+ 0.6 %	0.0 %	+ 0.0 %	+ 0.1 %
<div>1,920</div>	33.4	<div>1.75</div>	0.34	0.05	+ 0.7 %	+ 0.5 %	+ 0.2 %	− 0.3 %	0.0 %	+ 0.0 %	+ 0.1 %
<div>1,920</div>	33.4	1.78	<div>0.38</div>	0.05	− 0.4 %	+ 0.6 %	+ 0.3 %	− 0.9 %	0.0 %	+ 0.1 %	− 0.0 %
<div>1,920</div>	33.4	1.78	<div>0.30</div>	0.05	+ 1.8 %	− 0.1 %	− 0.1 %	+ 1.4 %	0.0 %	− 0.1 %	+ 0.2 %
<div>1,920</div>	33.4	1.78	0.34	<div>0.09</div>	− 0.9 %	+ 0.2 %	+ 0.1 %	+ 0.6 %	0.0 %	− 0.0 %	+ 0.1 %
<div>1,920</div>	33.4	1.78	0.34	<div>0.01</div>	+ 4.0 %	+ 0.7 %	+ 0.3 %	+ 0.3 %	0.0 %	− 0.1 %	+ 0.3 %
<div><div></div> design variable changed relative to optimum design</div>											
<div><div></div> improvement relative to optimum design</div>											
<div><div></div> diminishment relative to optimum design</div>											

Table A.7: Turboprop Design Space (Cruise Speed: Mach 0.70).

Design Variables					Design Parameters											
Engine			Airframe		Engine			Airframe								
Turbine Entry Temp. (K)	Overall Pressure Ratio	Prop. Dia. (m)	Max. Prop. Tip Speed (m/s)	Wing Span Factor	Wing Mean Chord Length Factor	Max. Static Thrust (kN) ^a	Crit. Thrust Requirement ^b	Max. LPT Power (MW) ^a	Min. Blade Height (mm)	Engine Mass (kg)	Wing Span (m)	Wing Mean Chord Length (m)	Max. Takeoff Weight (kg)	Initial Cruise Altitude (ft)	Final Cruise Altitude (ft)	Mission Fuel (kg)
1,480	21.2	4.12	227.2	0.20	0.05	58.3	1	5.30	13.1	809	35.3	3.24	67,541	30,000	36,000	3,936
1,500	21.2	4.12	227.2	0.20	0.05	+ 4.1 %	6	+ 9.7 %	13.5	+ 5.3 %	35.3	3.25	+ 0.4 %	32,000	38,000	+ 1.4 %
1,460	21.2	4.12	227.2	0.20	0.05	+ 2.4 %	1	+ 5.4 %	12.7	+ 5.7 %	35.3	3.26	+ 0.4 %	30,000	36,000	+ 1.0 %
1,480	22.4	4.12	227.2	0.20	0.05	+ 0.1 %	1	+ 0.3 %	11.8	- 0.3 %	35.3	3.24	- 0.0 %	30,000	36,000	- 1.4 %
1,480	20.0	4.12	227.2	0.20	0.05	+ 4.3 %	6	+ 10.1 %	13.1	+ 5.3 %	35.3	3.25	+ 0.4 %	32,000	38,000	+ 3.4 %
1,480	21.2	4.20	227.2	0.20	0.05	+ 5.3 %	6	+ 7.1 %	13.2	+ 9.1 %	35.6	3.24	+ 0.8 %	32,000	36,000	+ 1.4 %
1,480	21.2	4.04	227.2	0.20	0.05	- 1.0 %	1	+ 2.7 %	13.2	- 1.6 %	35.0	3.26	- 0.2 %	30,000	36,000	+ 0.7 %
1,480	21.2	4.12	235.2	0.20	0.05	+ 19.2 %	6	+ 40.7 %	15.2	+ 38.0 %	35.3	3.33	+ 2.8 %	32,000	38,000	+ 9.0 %
1,480	21.2	4.12	219.2	0.20	0.05	+ 2.5 %	6	+ 12.9 %	13.6	+ 10.8 %	35.3	3.27	+ 0.8 %	32,000	38,000	+ 2.2 %
1,480	21.2	4.12	227.2	0.24	0.05	+ 2.6 %	6	+ 6.1 %	13.1	+ 5.4 %	36.5	3.18	+ 0.7 %	32,000	38,000	+ 0.2 %
1,480	21.2	4.12	227.2	0.16	0.05	+ 0.4 %	1	+ 1.0 %	13.2	+ 0.8 %	34.1	3.33	- 0.2 %	30,000	36,000	+ 11.3 %
1,480	21.2	4.12	227.2	0.20	0.09	+ 12.6 %	1	+ 31.7 %	14.7	+ 28.8 %	35.3	3.47	+ 2.4 %	32,000	38,000	+ 7.4 %
1,480	21.2	4.12	227.2	0.20	0.01	+ 3.9 %	1	+ 9.0 %	13.3	+ 6.8 %	35.3	3.09	+ 0.3 %	30,000	36,000	+ 1.1 %

^aat ΔT = 15 K, includes the thrust growth factor of 1.25 and the max. power derate factor of 0.85 (see pages 41 and 56)

^b1 = takeoff field length, 2 = balanced field length, 3 = 1st segment climb, 4 = 2nd segment climb, 5 = 3rd segment climb, 6 = initial cruise altitude, 7 = final cruise altitude

□ design variable changed relative to optimum design
■ improvement relative to optimum design ■ diminishment relative to optimum design ■ constraint violated

^aat $\Delta T = 15$ K, includes the thrust growth factor of 1.25 and the max. power derate factor of 0.85 (see pages 41 and 56)^b1 = takeoff field length, 2 = balanced field length, 3 = 1st segment climb, 4 = 2nd segment climb, 5 = 3rd segment climb, 6 = initial cruise altitude, 7 = final cruise altitude

□ design variable changed relative to optimum design

■ improvement relative to optimum design

■ diminishment relative to optimum design

■ constraint violated

Table A.8: Turboprop Design Cost Space (Cruise Speed: Mach 0.70).

Design Variables					Direct Operating Cost (¢/RPK in 2012 prices)								
Engine			Airframe		Engine	Airframe			Total				
Turbine Entry Temp. (K)	Overall Pressure Ratio	Prop. Dia. (m)	Max. Prop. Tip Speed (m/s)	Wing Span Factor	Wing Mean Chord Length Factor	Depreciation + Interest + Insurance + Maintenance	Depreciation + Interest + Insurance + Maintenance	Landing + Navigation	Fuel + CO ₂ (mean)	Crew + Ground Handling	Time	Excl. Time (mean)	Incl. Time (mean)
1,480	21.2	4.12	227.2	0.20	0.05	0.716	2.729	0.655	2.966	2.552	9.107	9.618	18.725
1,500	21.2	4.12	227.2	0.20	0.05	+ 4.5 %	+ 0.7 %	+ 0.3 %	+ 1.4 %	0.0 %	− 0.1 %	+ 1.0 %	+ 0.4 %
1,460	21.2	4.12	227.2	0.20	0.05	− 0.9 %	+ 0.7 %	+ 0.3 %	+ 1.0 %	0.0 %	− 0.1 %	+ 0.5 %	+ 0.2 %
1,480	22.4	4.12	227.2	0.20	0.05	+ 0.1 %	− 0.0 %	− 0.0 %	− 1.4 %	0.0 %	− 0.0 %	− 0.4 %	− 0.2 %
1,480	20.0	4.12	227.2	0.20	0.05	+ 2.4 %	+ 0.7 %	+ 0.3 %	+ 3.4 %	0.0 %	− 0.1 %	+ 1.4 %	+ 0.7 %
1,480	21.2	4.20	227.2	0.20	0.05	+ 2.9 %	+ 1.3 %	+ 0.6 %	+ 1.4 %	0.0 %	− 0.1 %	+ 1.0 %	+ 0.5 %
1,480	21.2	4.04	227.2	0.20	0.05	− 0.6 %	− 0.3 %	− 0.1 %	+ 0.7 %	0.0 %	− 0.0 %	+ 0.1 %	+ 0.0 %
1,480	21.2	4.12	235.2	0.20	0.05	+10.6 %	+ 4.8 %	+ 2.2 %	+ 9.0 %	0.0 %	− 0.3 %	+ 5.1 %	+ 2.5 %
1,480	21.2	4.12	219.2	0.20	0.05	+ 1.4 %	+ 1.4 %	+ 0.6 %	+ 2.2 %	0.0 %	− 0.1 %	+ 1.2 %	+ 0.6 %
1,480	21.2	4.12	227.2	0.24	0.05	+ 1.4 %	+ 1.2 %	+ 0.5 %	+ 0.2 %	0.0 %	+ 0.0 %	+ 0.5 %	+ 0.3 %
1,480	21.2	4.12	227.2	0.16	0.05	+ 0.2 %	− 0.4 %	− 0.2 %	+11.3 %	0.0 %	+ 0.4 %	+ 3.4 %	+ 1.9 %
1,480	21.2	4.12	227.2	0.20	0.09	+ 7.0 %	+ 4.0 %	+ 1.8 %	+ 7.4 %	0.0 %	− 0.2 %	+ 4.1 %	+ 2.0 %
1,480	21.2	4.12	227.2	0.20	0.01	+ 2.1 %	+ 0.6 %	+ 0.3 %	+ 1.1 %	0.0 %	− 0.2 %	+ 0.7 %	+ 0.2 %

design variable changed relative to optimum design

improvement relative to optimum design

diminishment relative to optimum design

Table A.9: Open Rotor Design Space (Cruise Speed: Mach 0.70).

Design Variables						Design Parameters										
Engine			Airframe			Engine				Airframe						
Turbine Entry Temp. (K)	Overall Pressure Ratio	Prop. Dia. (m)	Max. Prop. Tip Speed (m/s)	Wing Span Factor	Wing Mean Chord Length Factor	Max. Static Thrust (kN) ^a	Crit. Thrust Requirement ^b	Max. LPT Power (MW) ^a	Min. Blade Height (mm)	Engine Mass (kg)	Wing Span (m)	Wing Mean Chord Length (m)	Max. Take-off Weight (kg)	Initial Cruise Altitude (ft)	Final Cruise Altitude (ft)	Mission Fuel (kg)
1,900	37.0	4.36	283.2	0.32	0.01	172.3	5	21.62	13.3	2,042	35.2	3.17	69,241	30,000	36,000	3,870
<div>1,920</div>	37.0	4.36	283.2	0.32	0.01	+ 0.6 %	5	+ 1.3 %	12.5	− 0.6 %	35.1	3.17	− 0.1 %	30,000	36,000	+ 0.1 %
<div>1,880</div>	37.0	4.36	283.2	0.32	0.01	− 0.4 %	5	− 1.0 %	12.8	+ 0.8 %	35.2	3.17	+ 0.1 %	30,000	36,000	+ 0.2 %
1,900	<div>38.2</div>	4.36	283.2	0.32	0.01	+ 0.1 %	5	+ 0.1 %	12.4	− 0.1 %	35.2	3.17	− 0.0 %	30,000	36,000	− 0.5 %
1,900	<div>35.8</div>	4.36	283.2	0.32	0.01	+ 0.3 %	5	+ 0.6 %	13.2	+ 0.8 %	35.2	3.17	+ 0.1 %	30,000	36,000	+ 1.0 %
1,900	37.0	<div>4.44</div>	283.2	0.32	0.01	+ 0.7 %	5	− 1.9 %	12.4	+ 0.2 %	35.2	3.17	+ 0.0 %	30,000	36,000	− 0.3 %
1,900	<div>37.0</div>	<div>4.28</div>	283.2	0.32	0.01	− 0.7 %	5	+ 2.0 %	13.4	− 0.6 %	35.1	3.17	− 0.1 %	30,000	36,000	+ 0.5 %
1,900	37.0	4.36	<div>291.2</div>	0.32	0.01	+ 0.9 %	5	− 0.8 %	12.5	− 1.4 %	35.1	3.17	− 0.1 %	30,000	36,000	+ 0.1 %
1,900	37.0	4.36	<div>275.2</div>	0.32	0.01	− 0.8 %	5	+ 1.1 %	13.3	+ 1.0 %	35.2	3.17	+ 0.1 %	30,000	36,000	+ 0.0 %
1,900	37.0	4.36	283.2	<div>0.36</div>	0.01	− 2.5 %	5	− 4.7 %	12.0	− 4.2 %	36.6	3.05	− 0.0 %	30,000	36,000	− 2.4 %
1,900	37.0	4.36	283.2	<div>0.28</div>	0.01	+ 2.9 %	5	+ 5.5 %	13.6	+ 5.0 %	33.7	3.30	+ 0.1 %	30,000	36,000	+ 3.2 %
1,900	37.0	4.36	283.2	0.32	<div>0.05</div>	− 0.6 %	5	− 1.2 %	12.5	− 1.7 %	35.2	3.33	+ 0.1 %	30,000	36,000	+ 0.4 %
^a at ΔT = 15 K, includes the thrust growth factor of 1.25 (see page 41)																
^b 1 = takeoff field length, 2 = balanced field length, 3 = 1 st segment climb, 4 = 2 nd segment climb, 5 = 3 rd segment climb, 6 = initial cruise altitude, 7 = final cruise altitude																
□ design variable changed relative to optimum design																
■ improvement relative to optimum design ■ diminishment relative to optimum design ■ constraint violated																

^aat $\Delta T = 15$ K, includes the thrust growth factor of 1.25 (see page 41)^b1 = takeoff field length, 2 = balanced field length, 3 = 1st segment climb, 4 = 2nd segment climb, 5 = 3rd segment climb, 6 = initial cruise altitude, 7 = final cruise altitude design variable changed relative to optimum design improvement relative to optimum design diminishment relative to optimum design constraint violated

Table A.10: Open Rotor Design Cost Space (Cruise Speed: Mach 0.70).

Design Variables				Direct Operating Cost (¢/RPK in 2012 prices)									
Engine			Airframe		Engine			Airframe			Total		
Turbine Entry Temp. (K)	Overall Pressure Ratio	Prop. Dia. (m)	Max. Prop. Tip Speed (m/s)	Wing Span Factor	Wing Mean Chord Length Factor	Depreciation + Interest + Insurance + Maintenance	Depreciation + Interest + Insurance + Maintenance	Landing + Navigation	Fuel + CO ₂ (mean)	Crew + Ground Handling	Time	Excl. Time (mean)	Incl. Time (mean)
1,900	37.0	4.36	283.2	0.32	0.01	0.874	2.844	0.668	2.916	2.552	9.071	9.854	18.925
1,920	37.0	4.36	283.2	0.32	0.01	+ 1.3 %	− 0.1 %	− 0.0 %	+ 0.1 %	0.0 %	− 0.0 %	+ 0.1 %	+ 0.1 %
1,880	37.0	4.36	283.2	0.32	0.01	− 1.2 %	+ 0.1 %	+ 0.1 %	+ 0.2 %	0.0 %	+ 0.0 %	− 0.0 %	− 0.0 %
1,900	38.2	4.36	283.2	0.32	0.01	+ 0.0 %	− 0.0 %	− 0.0 %	− 0.5 %	0.0 %	+ 0.0 %	− 0.2 %	− 0.1 %
1,900	35.8	4.36	283.2	0.32	0.01	+ 0.2 %	+ 0.1 %	+ 0.1 %	+ 1.0 %	0.0 %	+ 0.0 %	+ 0.4 %	+ 0.2 %
1,900	37.0	4.44	283.2	0.32	0.01	+ 0.5 %	+ 0.0 %	+ 0.0 %	− 0.3 %	0.0 %	− 0.1 %	− 0.0 %	− 0.0 %
1,900	37.0	4.28	283.2	0.32	0.01	− 0.5 %	− 0.1 %	− 0.1 %	+ 0.5 %	0.0 %	− 0.0 %	+ 0.1 %	+ 0.0 %
1,900	37.0	4.36	291.2	0.32	0.01	+ 0.6 %	− 0.2 %	− 0.1 %	+ 0.1 %	0.0 %	− 0.0 %	+ 0.0 %	+ 0.0 %
1,900	37.0	4.36	275.2	0.32	0.01	− 0.6 %	+ 0.2 %	+ 0.1 %	+ 0.0 %	0.0 %	+ 0.0 %	+ 0.0 %	+ 0.0 %
1,900	37.0	4.36	283.2	0.36	0.01	− 1.7 %	− 0.1 %	− 0.0 %	− 2.4 %	0.0 %	+ 0.2 %	− 0.9 %	− 0.4 %
1,900	37.0	4.36	283.2	0.28	0.01	+ 1.9 %	+ 0.2 %	+ 0.1 %	+ 3.2 %	0.0 %	− 0.3 %	+ 1.2 %	+ 0.5 %
1,900	37.0	4.36	283.2	0.32	0.05	− 0.4 %	+ 0.1 %	+ 0.0 %	+ 0.4 %	0.0 %	+ 0.3 %	+ 0.1 %	+ 0.2 %
<div><div> design variable changed relative to optimum design</div><div> improvement relative to optimum design</div><div> diminishment relative to optimum design</div></div>													

Appendix B

Performance Diagrams

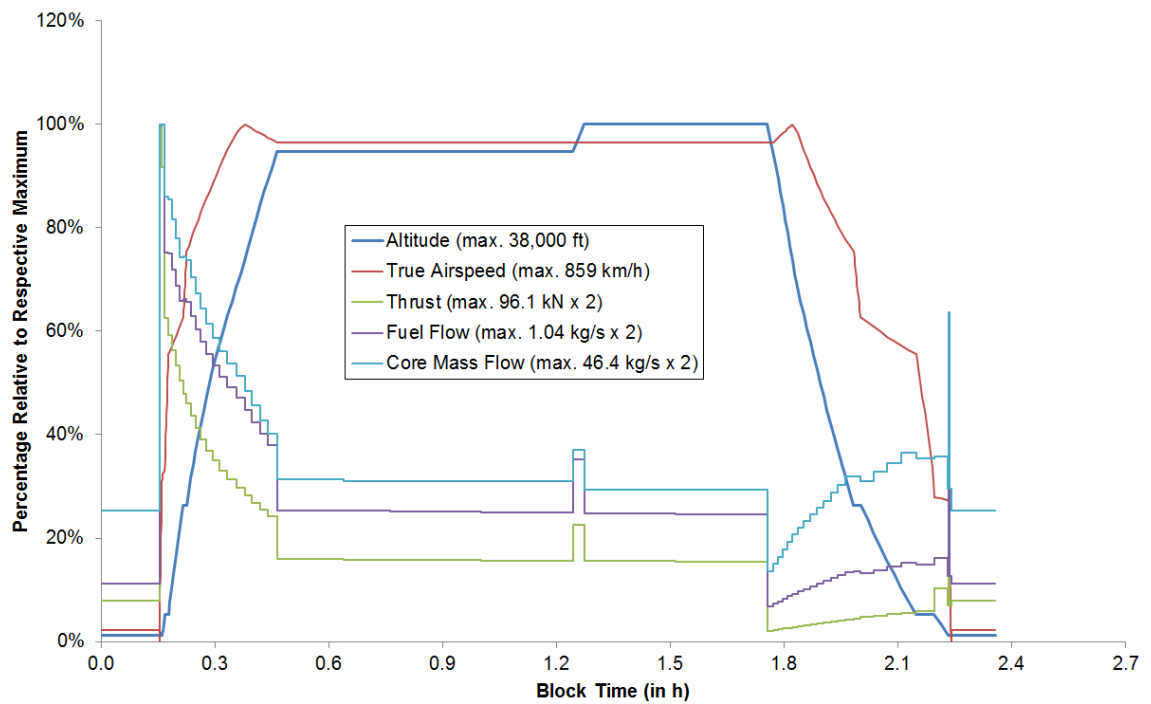


Figure B.1: Three-Shaft Turbofan Mission True Airspeed, Thrust and Fuel and Core Mass Flow Rates (Cruise Speed: Mach 0.78).

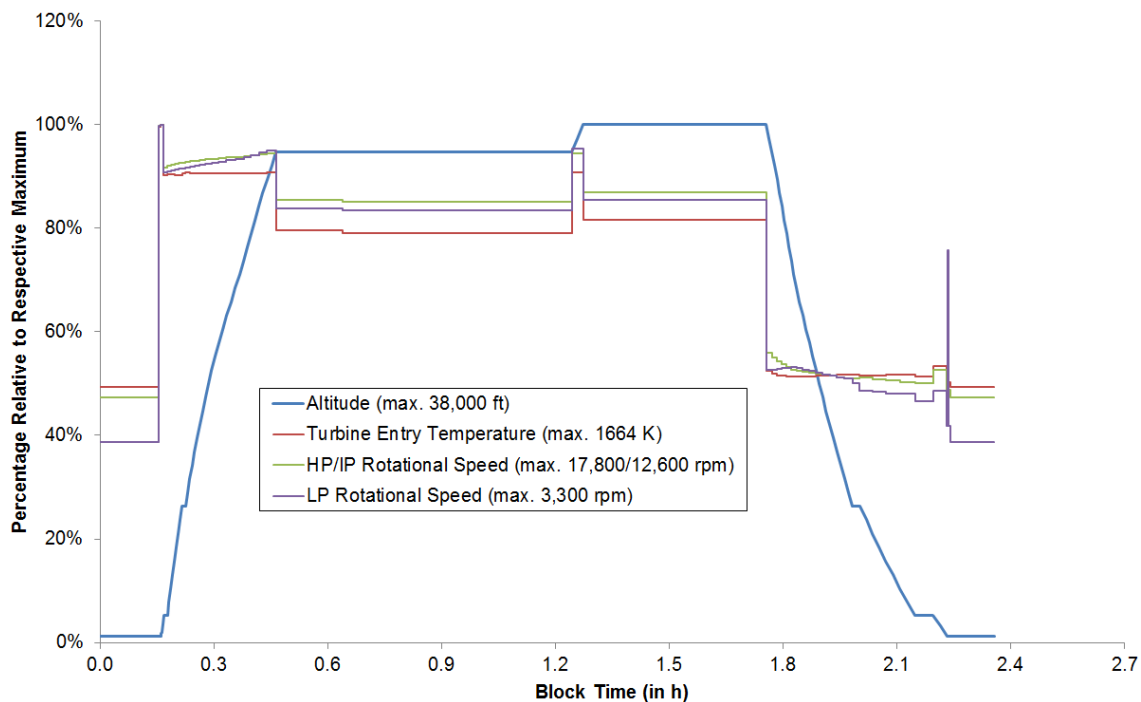


Figure B.2: Three-Shaft Turbofan Mission Turbine Entry Temperature and Rotational Speeds (Cruise Speed: Mach 0.78).

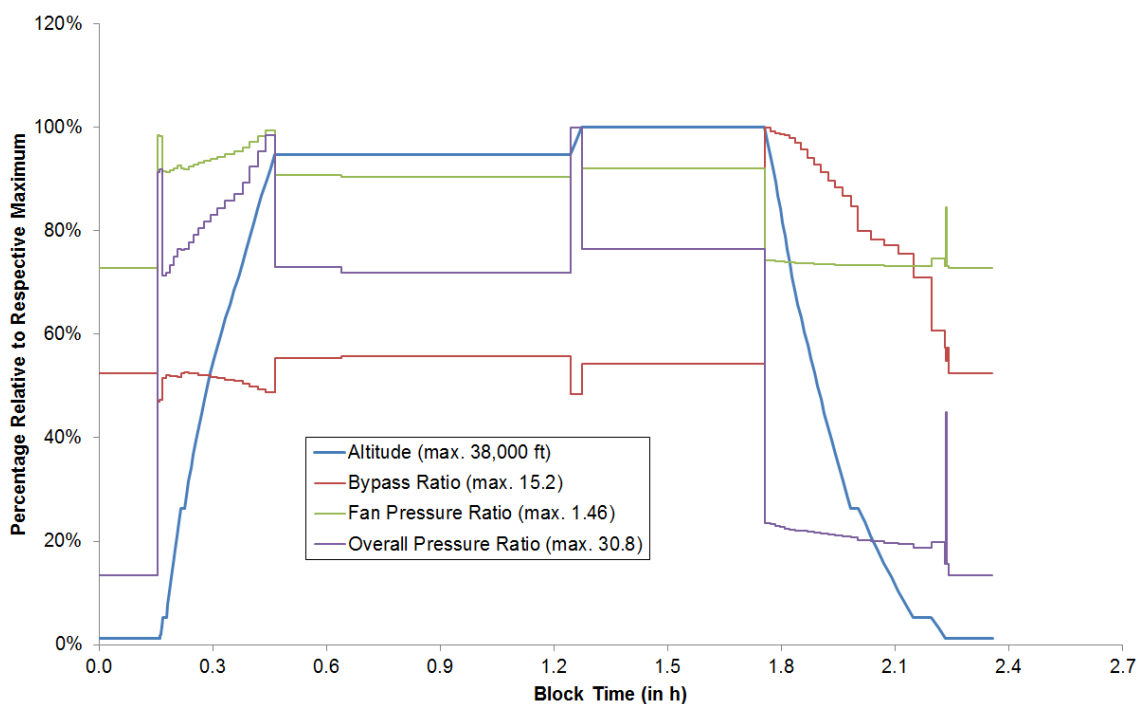


Figure B.3: Three-Shaft Turbofan Mission Bypass Ratio and Pressure Ratios (Cruise Speed: Mach 0.78).

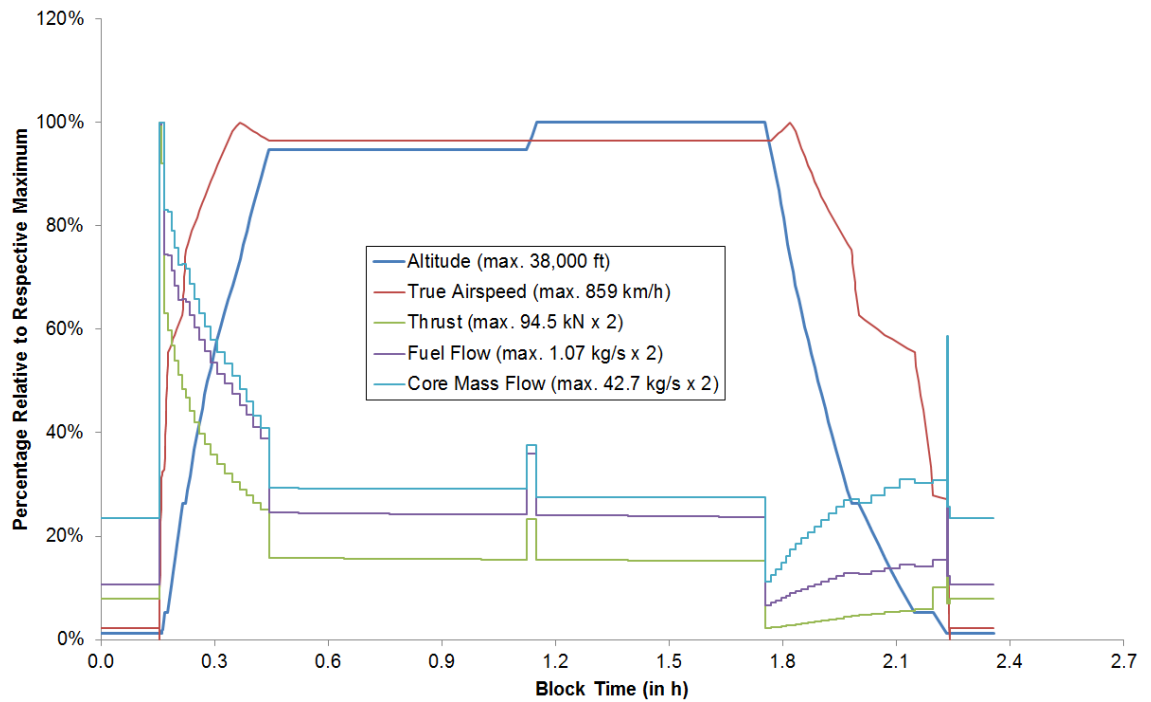


Figure B.4: Geared Turbofan Mission True Airspeed, Thrust and Fuel and Core Mass Flow Rates (Cruise Speed: Mach 0.78).

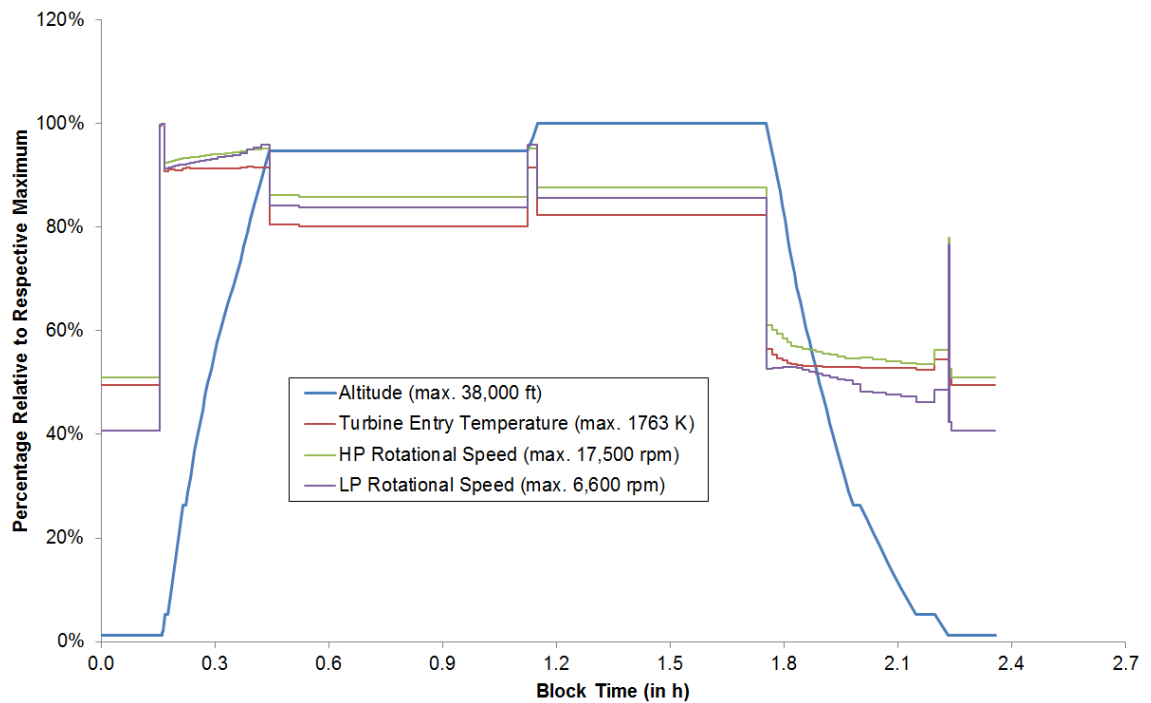


Figure B.5: Geared Turbofan Mission Turbine Entry Temperature and Rotational Speeds (Cruise Speed: Mach 0.78).

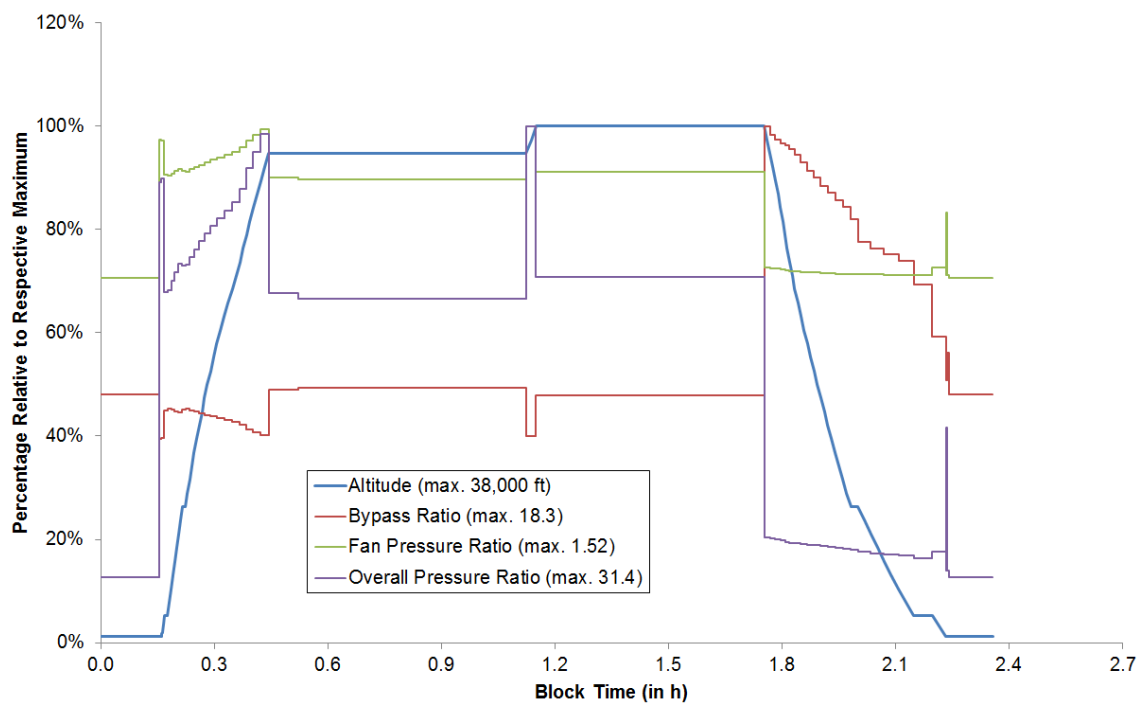


Figure B.6: Geared Turbofan Mission Bypass Ratio and Pressure Ratios (Cruise Speed: Mach 0.78).

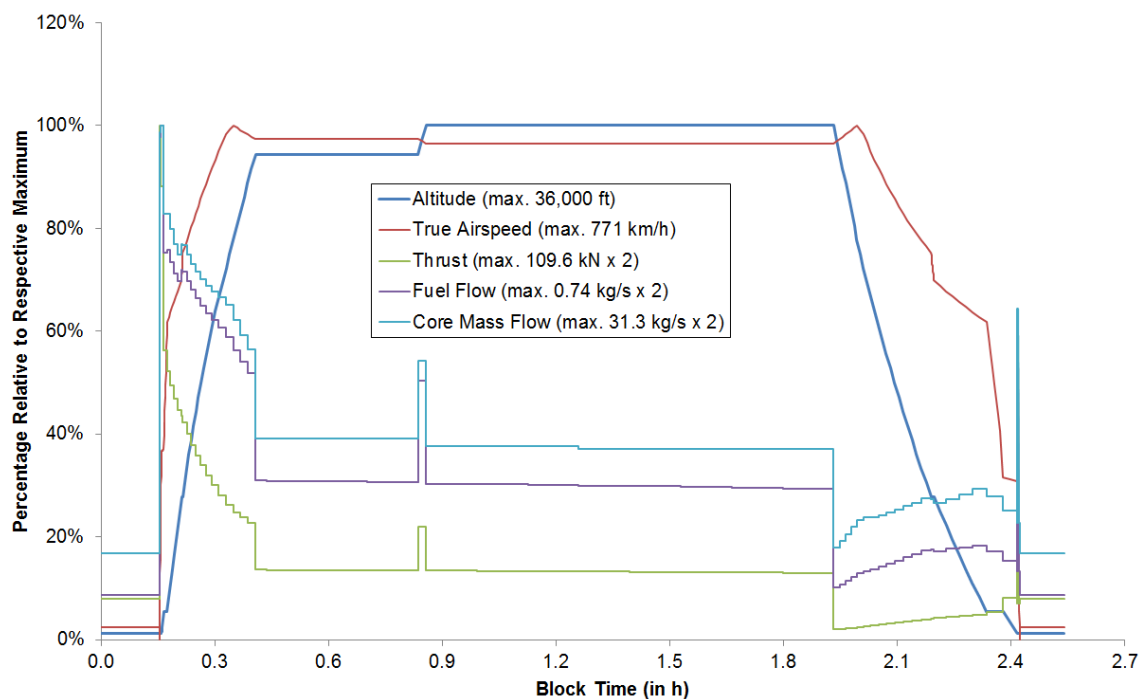


Figure B.7: Open Rotor Mission True Airspeed, Thrust and Fuel and Core Mass Flow Rates (Cruise Speed: Mach 0.70).

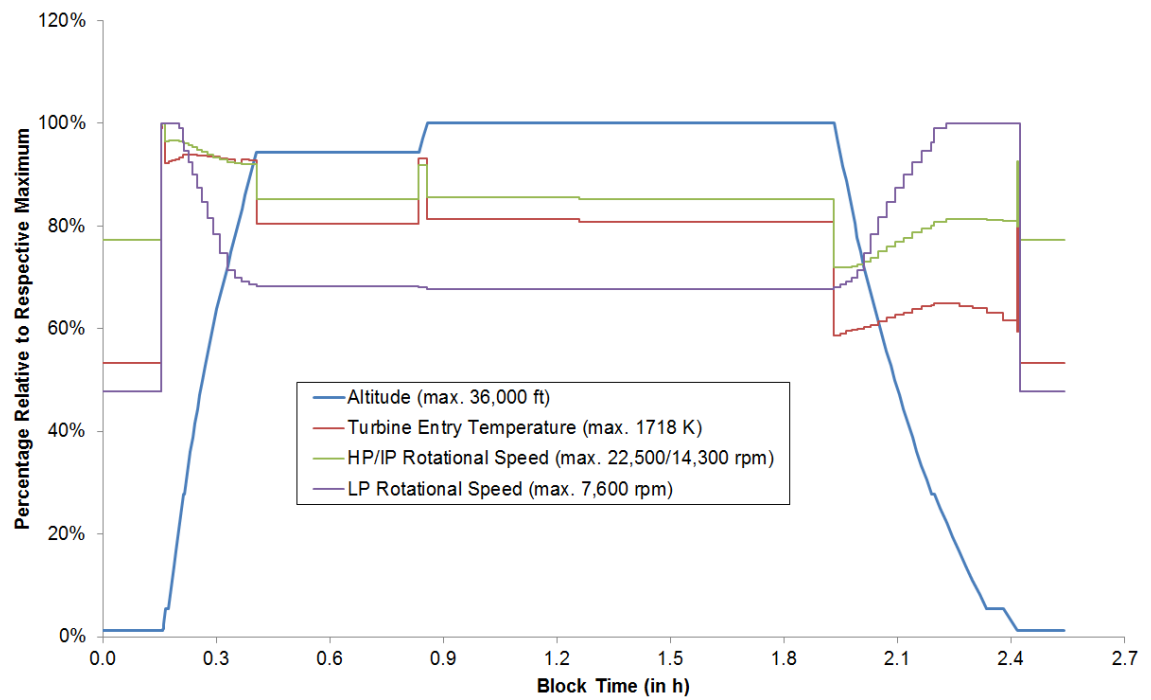


Figure B.8: Open Rotor Mission Turbine Entry Temperature and Rotational Speeds (Cruise Speed: Mach 0.70).

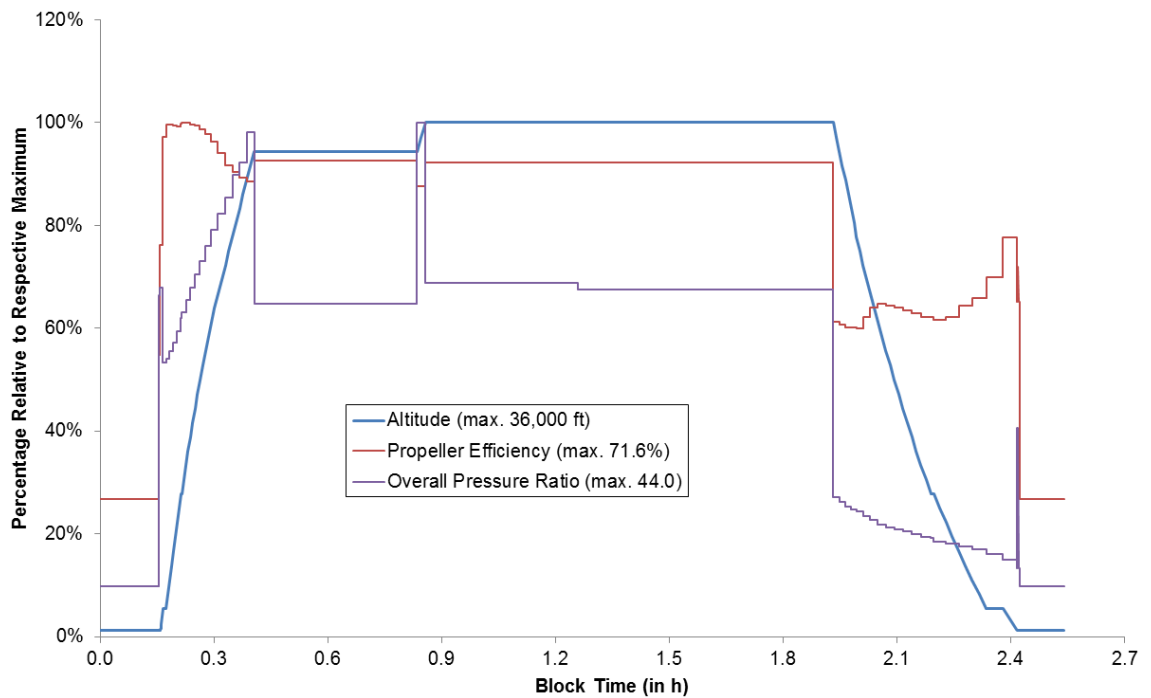


Figure B.9: Open Rotor Mission Propeller Efficiency and Overall Pressure Ratio (Cruise Speed: Mach 0.70).

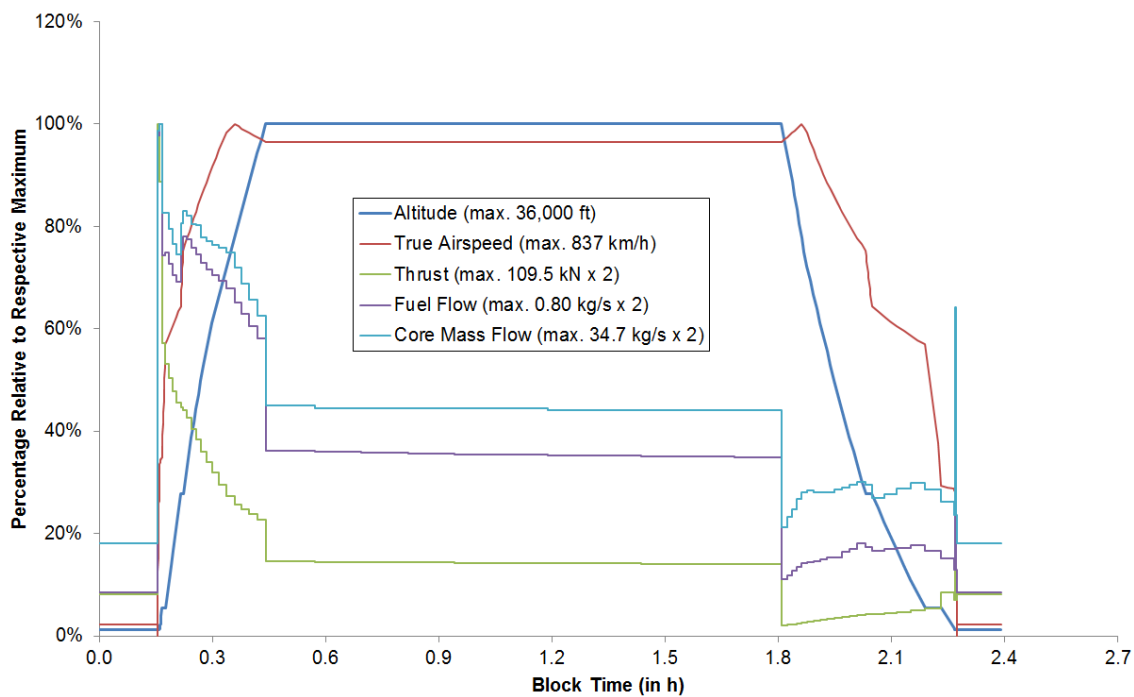


Figure B.10: Open Rotor Mission True Airspeed, Thrust and Fuel and Core Mass Flow Rates (Cruise Speed: Mach 0.76).

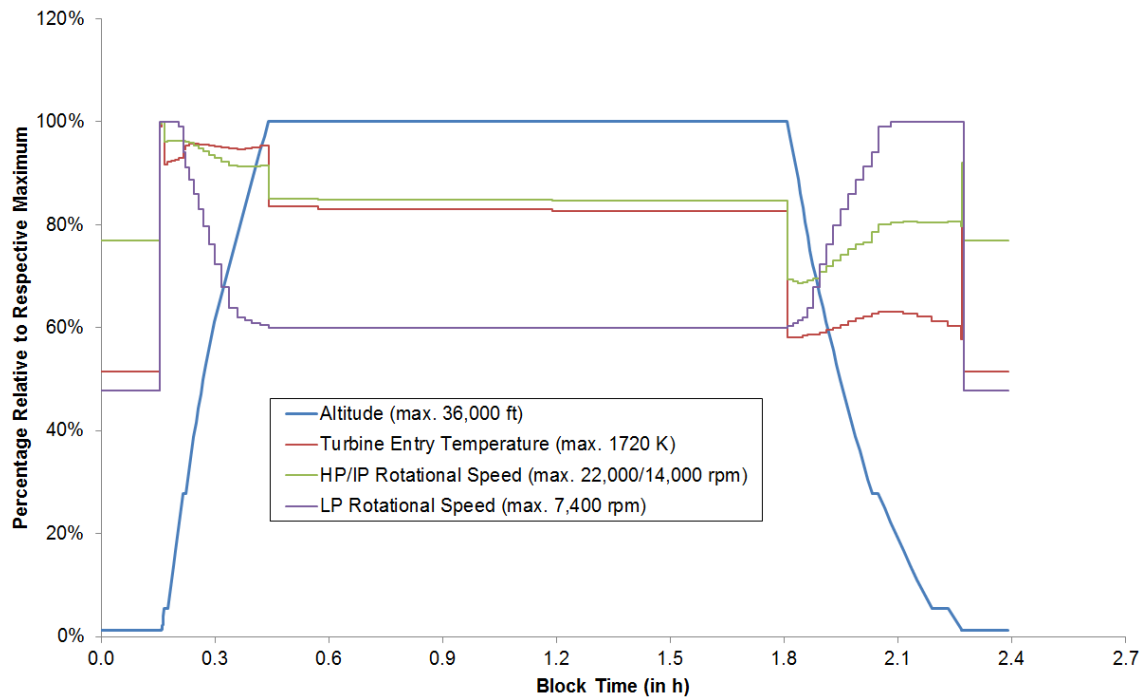


Figure B.11: Open Rotor Mission Turbine Entry Temperature and Rotational Speeds (Cruise Speed: Mach 0.76).

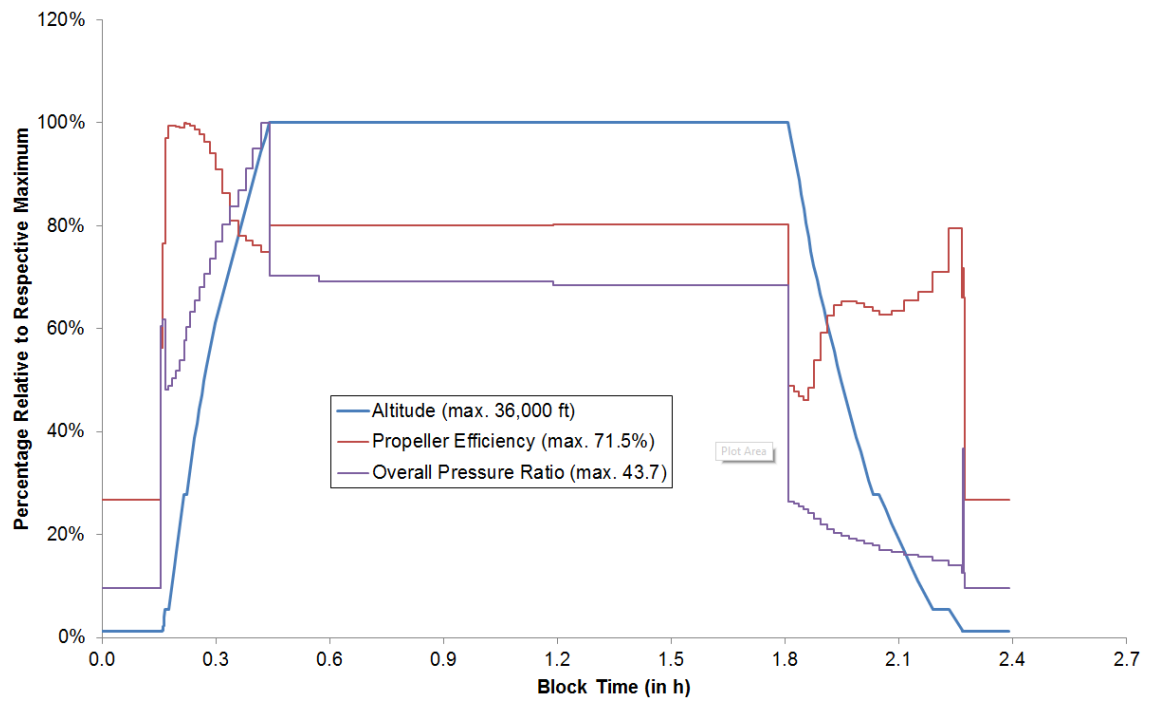


Figure B.12: Open Rotor Mission Propeller Efficiency and Overall Pressure Ratio (Cruise Speed: Mach 0.76).

Appendix C

Cruise Speed Optimization Data

Table C.1: Two-Shaft Turbofan Cruise Speed Space (TET = 1,820 K, OPR = 32.2, FPR = 1.80, Wing Span Factor = 0.34, Wing Mean Chord Length Factor = 0.05).

Design Parameters															
Cruise Speed (Mach)	Engine					Airframe									
	Max. Static Thrust (kN) ^a	Crit. Thrust Requirement ^b	Fan Dia. (m)	Bypass Ratio ^c	Min. Blade Height (mm)	HP Rot. Speed (rpm) ^c	LP Rot. Speed (rpm) ^c	Engine Mass (kg)	Wing Span (m)	Wing Mean Chord Length (m)	Wing 1/4-Chord Sweep (°)	Max. Take-off Weight (kg)	Initial Cruise Altitude (ft)	Final Cruise Altitude (ft)	Mission Fuel (kg)
<div><div>0.74</div><div>− 0.2 %</div></div>	5	− 0.1 %	− 0.0 %	13.1	+ 0.1 %	+ 0.1 %	− 0.2 %	35.9	3.28	17.2	− 1.2 %	34,000	38,000	− 2.7 %	
<div><div>0.76</div><div>− 0.4 %</div></div>	5	− 0.2 %	− 0.0 %	13.1	+ 0.2 %	+ 0.2 %	− 0.6 %	35.9	3.29	21.5	− 0.6 %	34,000	38,000	− 2.2 %	
0.78	127.5	1	1.79	6.75	13.1	15,321	4,356	1,868	36.0	3.31	24.9	70,232	32,000	38,000	4,563
<div><div>0.80</div><div>+ 2.2 %</div></div>	1	+ 1.1 %	+ 0.0 %	13.2	− 1.0 %	− 1.1 %	+ 3.2 %	36.1	3.33	27.7	+ 0.9 %	30,000	36,000	+ 4.1 %	
<div><div>0.82</div><div>+ 2.3 %</div></div>	2	+ 1.1 %	+ 0.0 %	13.2	− 1.1 %	− 1.1 %	+ 3.3 %	36.1	3.34	30.2	+ 1.5 %	30,000	36,000	+10.0 %	

^aat ΔT = 15 K, includes the thrust growth factor of 1.25 (see page 41)

^b1 = takeoff field length, 2 = balanced field length, 3 = 1st segment climb, 4 = 2nd segment climb, 5 = 3rd segment climb,

6 = initial cruise altitude, 7 = final cruise altitude

^cat max. static thrust

□

 cruise speed changed relative to design point

■

 improvement relative to design point

■

 diminishment relative to design point

■

 constraint violated

^aat $\Delta T = 15$ K, includes the thrust growth factor of 1.25 (see page 41)

^b1 = takeoff field length, 2 = balanced field length, 3 = 1st segment climb, 4 = 2nd segment climb, 5 = 3rd segment climb,

6 = initial cruise altitude, 7 = final cruise altitude

^cat max. static thrust

□ cruise speed changed relative to design point

■ improvement relative to design point

■ diminishment relative to design point

■ constraint violated

Table C.2: Two-Shift Turbofan Cruise Speed Cost Space (TET = 1,820 K, OPR = 32.2, FPR = 1.80, Wing Span Factor = 0.34, Wing Mean Chord Length Factor = 0.05).

Direct Operating Cost (¢/RPK in 2012 prices)												
Cruise Speed (Mach)	Engine				Airframe				Total		$\sqrt{\text{MSD}}$	
	Depreciation + Interest + Insurance + Maintenance	Depreciation + Interest + Insurance + Maintenance	Landing + Navigation	Fuel + CO ₂ (mean)	Crew + Ground Handling	Productivity ^a	Market Share ^a	Time ^a	Excl. Time (mean) ^b	Incl. Time (mean) ^b	Excl. Time (mean) ^c	Incl. Time (mean) ^c
0.74	− 0.4 %	− 1.9 %	− 0.9 %	− 2.7 %	0.0 %	0.227	0.049	0.497	− 0.2 %	+ 2.4 %	− 0.2 %	+ 1.5 %
0.76	− 0.4 %	− 1.0 %	− 0.5 %	− 2.2 %	0.0 %	0.154	0.035	0.334	− 0.7 %	+ 0.4 %	− 0.7 %	+ 0.3 %
0.78	0.712	2.589	0.683	3.476	2.443	0.123	0.023	0.226	10.050	10.276	10.091	18.535
0.80	+ 1.6 %	+ 1.4 %	+ 0.7 %	+ 4.1 %	0.0 %	0.062	0.011	0.093	+ 1.2 %	− 0.1 %	+ 1.2 %	− 0.1 %
0.82	+ 1.8 %	+ 2.4 %	+ 1.1 %	+10.0 %	0.0 %	0.000	0.000	0.000	+ 2.8 %	+ 0.6 %	+ 2.9 %	+ 0.2 %
^a cost change relative to Mach 0.82												
^b incl. relative productivity, market share and time cost												
^c incl. absolute productivity, market share and time cost												
 cruise speed changed relative to design point improvement relative to design point diminishment relative to design point												

^acost change relative to Mach 0.82

^bincl. relative productivity, market share and time cost

^cincl. absolute productivity, market share and time cost

 cruise speed changed relative to design point

 improvement relative to design point

 diminishment relative to design point


Table C.3: Three-Shaft Turbofan Cruise Speed Space (TET = 1,880 K, OPR = 35.8, FPR = 1.78, Wing Span Factor = 0.34, Wing Mean Chord Length Factor = 0.05).

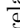
Design Parameters																
Engine										Airframe						
Cruise Speed (Mach)	Max. Static Thrust (kN) ^a	Crit. Thrust Requirement ^b	Fan Dia. (m)	Bypass Ratio ^c	Min. Blade Height (mm)	HP Rot. Speed (rpm) ^c	IP Rot. Speed (rpm) ^c	LP Rot. Speed (rpm) ^c	Engine Mass (kg)	Wing Span (m)	Wing Mean Chord Length (m)	Wing 1/4-Chord Sweep (°)	Max. Take-off Weight (kg)	Initial Cruise Altitude (ft)	Final Cruise Altitude (ft)	Mission Fuel (kg)
0.74	+ 0.7 %	5	+ 0.3 %	+ 0.0 %	15.5	− 0.3 %	− 0.3 %	− 0.3 %	+ 1.1 %	35.9	3.28	17.2	− 1.1 %	34,000	40,000	− 2.6 %
0.76	+ 0.3 %	5	+ 0.2 %	+ 0.0 %	15.5	− 0.2 %	− 0.2 %	− 0.2 %	+ 0.5 %	36.0	3.30	21.5	− 0.5 %	34,000	38,000	− 2.3 %
0.78	131.4	5	1.83	7.46	15.4	18,957	13,445	4,246	1,871	36.0	3.31	24.9	70,280	32,000	38,000	4,433
0.80	+ 1.9 %	1	+ 0.9 %	+ 0.0 %	15.6	− 0.9 %	− 0.9 %	− 0.9 %	+ 2.9 %	36.1	3.33	27.7	+ 0.8 %	30,000	36,000	+ 3.8 %
0.82	+ 8.5 %	6	+ 4.2 %	+ 0.1 %	16.0	− 4.2 %	− 4.0 %	− 4.0 %	+13.4 %	36.2	3.36	30.2	+ 2.4 %	32,000	38,000	+11.5 %


^aat ΔT = 15 K, includes the thrust growth factor of 1.25 (see page 41)


^b1 = takeoff field length, 2 = balanced field length, 3 = 1st segment climb, 4 = 2nd segment climb, 5 = 3rd segment climb, 6 = initial cruise altitude, 7 = final cruise altitude

^cat max. static thrust

 cruise speed changed relative to design point

 improvement relative to design point

 diminishment relative to design point

 constraint violated

^aat $\Delta T = 15$ K, includes the thrust growth factor of 1.25 (see page 41)

^b1 = takeoff field length, 2 = balanced field length, 3 = 1st segment climb, 4 = 2nd segment climb, 5 = 3rd segment climb,

6 = initial cruise altitude, 7 = final cruise altitude

^cat max. static thrust

□ cruise speed changed relative to design point

■ improvement relative to design point

■ diminishment relative to design point

■ constraint violated

Table C.4: Three-Shift Turbofan Cruise Speed Cost Space (TET = 1,880K, OPR = 35.8, FPR = 1.78, Wing Span Factor = 0.34, Wing Mean Chord Length Factor = 0.05).

Direct Operating Cost (¢/RPK in 2012 prices)												
Cruise Speed (Mach)	Engine			Airframe				Total			$\sqrt{\text{MSD}}$	
	Depreciation + Interest + Insurance + Maintenance	Depreciation + Interest + Insurance + Maintenance	Landing + Navigation	Fuel + CO ₂ (mean)	Crew + Ground Handling	Productivity ^a	Market Share ^a	Time ^a	Excl. Time (mean) ^b	Incl. Time (mean) ^b	Excl. Time (mean) ^c	Incl. Time (mean) ^c
0.74	+ 0.2 %	− 1.8 %	− 0.8 %	− 2.6 %	0.0 %	0.237	0.049	0.497	− 0.0 %	+ 2.6 %	− 0.0 %	+ 1.6 %
0.76	+ 0.1 %	− 0.9 %	− 0.4 %	− 2.3 %	0.0 %	0.162	0.035	0.334	− 0.6 %	+ 0.5 %	− 0.6 %	+ 0.3 %
0.78	0.806	2.592	0.683	3.377	2.443	0.128	0.023	0.226	10.053	10.279	10.092	18.535
0.80	+ 1.4 %	+ 1.4 %	+ 0.6 %	+ 3.8 %	0.0 %	0.065	0.011	0.092	+ 1.0 %	− 0.3 %	+ 1.1 %	− 0.2 %
0.82	+ 5.8 %	+ 3.9 %	+ 1.8 %	+11.5 %	0.0 %	0.000	0.000	0.000	+ 3.9 %	+ 1.7 %	+ 4.0 %	+ 0.8 %
^a cost change relative to Mach 0.82												
^b incl. relative productivity, market share and time cost												
^c incl. absolute productivity, market share and time cost												
 cruise speed changed relative to design point improvement relative to design point diminishment relative to design point												

^acost change relative to Mach 0.82

^bincl. relative productivity, market share and time cost

^cincl. absolute productivity, market share and time cost

 cruise speed changed relative to design point

 improvement relative to design point

 diminishment relative to design point

Table C.5: Geared Turbofan Cruise Speed Space (TET = 1,920 K, OPR = 33.4, FPR = 1.78, Wing Span Factor = 0.34, Wing Mean Chord Length Factor = 0.05).

Design Parameters																
Engine										Airframe						
Cruise Speed (Mach)	Max. Static Thrust (kN) ^a	Crit. Thrust Requirement ^b	Fan Dia. (m)	Bypass Ratio ^c	Min. Blade Height (mm)	HP Rot. Speed (rpm) ^c	LP Rot. Speed (rpm) ^c	Fan Gear Ratio	Engine Mass (kg)	Wing Span (m)	Wing Mean Chord Length (m)	Wing 1/4-Chord Sweep (°)	Max. Take-off Weight (kg)	Initial Cruise Altitude (ft)	Final Cruise Altitude (ft)	Mission Fuel (kg)
<div>0.74</div>	+ 0.5 %	5	+ 0.3 %	+ 0.0 %	13.1	− 0.3 %	− 0.3 %	+ 0.0 %	+ 0.8 %	35.8	3.23	17.2	− 1.1 %	34,000	40,000	− 2.6 %
<div>0.76</div>	+ 0.2 %	5	+ 0.1 %	+ 0.0 %	13.0	− 0.1 %	− 0.1 %	+ 0.0 %	+ 0.3 %	35.8	3.25	21.5	− 0.6 %	34,000	38,000	− 2.1 %
0.78	117.8	1	1.74	7.78	13.0	18,616	8,241	1.84	1,449	35.8	3.26	24.9	68,870	32,000	38,000	4,399
<div>0.80</div>	+ 2.2 %	1	+ 1.1 %	+ 0.0 %	13.4	− 1.0 %	− 1.1 %	+ 0.0 %	+ 3.8 %	35.9	3.28	27.7	+ 0.9 %	30,000	36,000	+ 4.0 %
<div>0.82</div>	+ 2.5 %	2	+ 1.2 %	+ 0.0 %	13.4	− 1.2 %	− 1.2 %	+ 0.0 %	+ 4.2 %	36.0	3.29	30.2	+ 1.5 %	30,000	36,000	+ 10.0 %

^aat ΔT = 15 K, includes the thrust growth factor of 1.25 (see page 41)

^b1 = takeoff field length, 2 = balanced field length, 3 = 1st segment climb, 4 = 2nd segment climb, 5 = 3rd segment climb,

6 = initial cruise altitude, 7 = final cruise altitude

^cat max. static thrust

cruise speed changed relative to design point

improvement relative to design point

diminishment relative to design point

constraint violated

^aat $\Delta T = 15$ K, includes the thrust growth factor of 1.25 (see page 41)

^b1 = takeoff field length, 2 = balanced field length, 3 = 1st segment climb, 4 = 2nd segment climb, 5 = 3rd segment climb,

6 = initial cruise altitude, 7 = final cruise altitude

^cat max. static thrust

□ cruise speed changed relative to design point

■ improvement relative to design point

■ diminishment relative to design point

■ constraint violated

Table C.6: Geared Turbofan Cruise Speed Cost Space (TET = 1,920 K, OPR = 33.4, FPR = 1.78, Wing Span Factor = 0.34, Wing Mean Chord Length Factor = 0.05).

Direct Operating Cost (¢/RPK in 2012 prices)													
Cruise Speed (Mach)	Engine				Airframe				Total		$\sqrt{\text{MSD}}$		
	Depreciation + Interest + Insurance + Maintenance	Depreciation + Interest + Insurance + Maintenance	Landing + Navigation	Fuel + CO ₂ (mean)	Crew + Ground Handling	Productivity ^a	Market Share ^a	Time ^a	Excl. Time (mean) ^b	Incl. Time (mean) ^b	Excl. Time (mean) ^c	Incl. Time (mean) ^c	
0.74	+ 0.1 %	− 1.9 %	− 0.9 %	− 2.6 %	0.0 %	0.224	0.048	0.498	− 0.1 %	+ 2.6 %	− 0.1 %	+ 1.5 %	
0.76	− 0.0 %	− 0.9 %	− 0.4 %	− 2.1 %	0.0 %	0.152	0.035	0.336	− 0.6 %	+ 0.5 %	− 0.6 %	+ 0.3 %	
0.78	0.711	2.507	0.672	3.352	2.443	0.121	0.023	0.228	9.829	10.057	9.868	18.313	
0.80	+ 1.5 %	+ 1.4 %	+ 0.7 %	+ 4.0 %	0.0 %	0.061	0.011	0.093	+ 1.1 %	− 0.2 %	+ 1.2 %	− 0.2 %	
0.82	+ 1.8 %	+ 2.4 %	+ 1.1 %	+10.0 %	0.0 %	0.000	0.000	0.000	+ 2.8 %	+ 0.5 %	+ 2.8 %	+ 0.2 %	
^a cost change relative to Mach 0.82													
^b incl. relative productivity, market share and time cost													
^c incl. absolute productivity, market share and time cost													
 cruise speed changed relative to design point improvement relative to design point diminishment relative to design point													

^acost change relative to Mach 0.82

^bincl. relative productivity, market share and time cost

^cincl. absolute productivity, market share and time cost

 cruise speed changed relative to design point

 improvement relative to design point

 diminishment relative to design point

Table C.7: Turboprop Cruise Speed Space (TET = 1,480 K, OPR = 21.2, Prop. Diameter = 4.12 m, Max. Propeller Tip Speed = 227.2 m/s, Wing Span Factor = 0.20, Wing Mean Chord Length Factor = 0.05).

Design Parameters																
Engine										Airframe						
Cruise Speed (Mach)	Max. Static Thrust (kN) ^a	Crit. Thrust Requirement ^b	Max. LPT Power (MW) ^a	Min. Blade Height (mm)	HP Rot. Speed (rpm) ^c	IP Rot. Speed (rpm) ^c	LP Rot. Speed (rpm) ^c	Prop. Gear Ratio	Engine Mass (kg)	Wing Span (m)	Wing Mean Chord Length (m)	Wing 1/4-Chord Sweep (°)	Max. Take-off Weight (kg)	Initial Cruise Altitude (ft)	Final Cruise Altitude (ft)	Mission Fuel (kg)
<div>0.68</div>	<div>+ 2.3 %</div>	6	<div>+ 5.3 %</div>	13.1	<div>- 2.4 %</div>	<div>- 2.4 %</div>	<div>- 2.5 %</div>	<div>- 2.5 %</div>	<div>+ 3.7 %</div>	35.3	3.24	3.1	<div>- 0.2 %</div>	32,000	38,000	<div>- 0.3 %</div>
0.70	58.3	1	5.30	13.1	24,921	18,864	10,275	9.76	809	35.3	3.24	3.1	67,541	30,000	36,000	3,936
<div>0.72</div>	<div>+ 4.3 %</div>	6	<div>+10.0 %</div>	13.7	<div>- 4.8 %</div>	<div>- 4.4 %</div>	<div>- 4.5 %</div>	<div>- 4.5 %</div>	<div>+ 7.9 %</div>	35.3	3.28	11.2	<div>+ 1.2 %</div>	32,000	38,000	<div>+ 3.5 %</div>
<div>0.74</div>	<div>+16.2 %</div>	7	<div>+42.5 %</div>	15.3	<div>-16.0 %</div>	<div>-15.6 %</div>	<div>-15.9 %</div>	<div>-15.9 %</div>	<div>+39.9 %</div>	35.3	3.36	17.2	<div>+ 4.1 %</div>	34,000	40,000	<div>+12.9 %</div>

^aat ΔT = 15K, includes the thrust growth factor of 1.25 and the max. power derate factor of 0.85 (see pages 41 and 56)

^b1 = takeoff field length, 2 = balanced field length, 3 = 1st segment climb, 4 = 2nd segment climb, 5 = 3rd segment climb, 6 = initial cruise altitude, 7 = final cruise altitude

^cat max. static thrust

cruise speed changed relative to design point

improvement relative to design point

diminishment relative to design point

constraint violated

Table C.8: Turboprop Cruise Speed Cost Space (TET = 1,480 K, OPR = 21.2, Prop. Diameter = 4.12 m, Max. Propeller Tip Speed = 227.2 m/s, Wing Span Factor = 0.20, Wing Mean Chord Length Factor = 0.05).

Direct Operating Cost (¢/RPK in 2012 prices)												
Cruise Speed (Mach)	Engine					Airframe				Total		$\sqrt{\text{MSD}}$
	Depreciation + Interest + Insurance + Maintenance	Depreciation + Interest + Insurance + Maintenance	Landing + Navigation	Fuel + CO ₂ (mean)	Crew + Ground Handling	Productivity ^a	Market Share ^a	Time ^a	Excl. Time (mean) ^b	Incl. Time (mean) ^b	Excl. Time (mean) ^c	Incl. Time (mean) ^c
0.68	+ 0.9 %	− 0.3 %	− 0.2 %	− 0.3 %	0.0 %	0.484	0.093	1.003	+ 1.2 %	+ 2.8 %	+ 1.2 %	+ 1.7 %
0.70	0.637	2.427	0.662	2.999	2.443	0.374	0.075	0.824	9.618	10.442	9.650	18.745
0.72	+ 2.7 %	+ 1.9 %	+ 0.9 %	+ 3.5 %	0.0 %	0.313	0.061	0.659	+ 1.0 %	− 0.6 %	+ 1.0 %	− 0.4 %
0.74	+ 9.6 %	+ 7.0 %	+ 3.2 %	+ 12.9 %	0.0 %	0.231	0.049	0.456	+ 4.9 %	+ 1.0 %	+ 4.9 %	+ 0.4 %

^acost change relative to Mach 0.82
^bincl. relative productivity, market share and time cost
^cincl. absolute productivity, market share and time cost
 cruise speed changed relative to design point
 improvement relative to design point diminishment relative to design point

Table C.9: Open Rotor Cruise Speed Space (TET = 1,900 K, OPR = 37.0, Prop. Diameter = 4.36 m, Max. Propeller Tip Speed = 283.2 m/s, Wing Span Factor = 0.32, Wing Mean Chord Length Factor = 0.01).

Design Parameters																	
Engine										Airframe							
Cruise Speed (Mach)	Max. Static Thrust (kN) ^a	Crit. Thrust Requirement ^b	Max. LPT Power (MW) ^a	Min. Blade Height (mm)	HP Rot. Speed (rpm) ^c	IP Rot. Speed (rpm) ^c	LP Rot. Speed (rpm) ^c	Prop. 1 Gear Ratio	Prop. 2 Gear Ratio	Engine Mass (kg)	Wing Span (m)	Wing Mean Chord Length (m)	Wing 1/4-Chord Sweep (°)	Max. Take-off Weight (kg)	Initial Cruise Altitude (ft)	Final Cruise Altitude (ft)	Mission Fuel (kg)
<div><div>0.68</div><div>− 0.5 %</div></div>	<div><div>− 0.9 %</div><div>12.5</div></div>	5	<div><div>− 0.9 %</div><div>− 0.1 %</div></div>	<div><div>12.5</div><div>+ 0.5 %</div></div>	<div><div>+ 0.5 %</div><div>+ 0.5 %</div></div>	<div><div>+ 0.5 %</div><div>+ 0.5 %</div></div>	<div><div>+ 0.5 %</div><div>+ 0.5 %</div></div>	<div><div>+ 0.5 %</div><div>+ 0.5 %</div></div>	<div><div>− 4.5 %</div><div>+ 0.5 %</div></div>	<div><div>− 1.5 %</div><div>− 1.5 %</div></div>	35.1	3.16	3.0	<div><div>− 0.6 %</div><div>− 0.6 %</div></div>	30,000	36,000	<div><div>− 1.8 %</div><div>− 1.8 %</div></div>
0.70	172.3	5	21.62	13.3	23,417	14,916	7,596	6.12	11.24	2,042	35.2	3.17	3.0	69,241	30,000	36,000	3,870
<div><div>0.72</div><div>+ 0.3 %</div></div>	<div><div>+ 0.6 %</div><div>13.3</div></div>	5	<div><div>+ 0.6 %</div><div>− 0.3 %</div></div>	<div><div>13.3</div><div>− 0.3 %</div></div>	<div><div>− 0.3 %</div><div>− 0.3 %</div></div>	<div><div>− 0.3 %</div><div>− 0.3 %</div></div>	<div><div>− 0.3 %</div><div>− 0.3 %</div></div>	<div><div>− 0.3 %</div><div>− 0.3 %</div></div>	<div><div>+ 6.4 %</div><div>− 0.3 %</div></div>	<div><div>+ 0.6 %</div><div>+ 0.6 %</div></div>	35.2	3.18	11.2	<div><div>+ 0.6 %</div><div>+ 0.6 %</div></div>	32,000	38,000	<div><div>+ 2.0 %</div><div>+ 2.0 %</div></div>
<div><div>0.74</div><div>+ 0.9 %</div></div>	<div><div>+ 1.8 %</div><div>13.4</div></div>	5	<div><div>+ 1.8 %</div><div>− 0.9 %</div></div>	<div><div>13.4</div><div>− 0.9 %</div></div>	<div><div>− 0.9 %</div><div>− 0.9 %</div></div>	<div><div>− 0.9 %</div><div>− 0.9 %</div></div>	<div><div>− 0.8 %</div><div>− 0.8 %</div></div>	<div><div>+14.0 %</div><div>− 0.8 %</div></div>	<div><div>+14.0 %</div><div>+14.0 %</div></div>	<div><div>+ 1.6 %</div><div>+ 1.6 %</div></div>	35.3	3.20	17.2	<div><div>+ 1.3 %</div><div>+ 1.3 %</div></div>	32,000	38,000	<div><div>+ 5.4 %</div><div>+ 5.4 %</div></div>
<div><div>0.76</div><div>+ 2.5 %</div></div>	<div><div>+ 4.9 %</div><div>14.2</div></div>	5	<div><div>+ 4.9 %</div><div>− 2.3 %</div></div>	<div><div>14.2</div><div>− 2.3 %</div></div>	<div><div>− 2.3 %</div><div>− 2.3 %</div></div>	<div><div>− 2.3 %</div><div>− 2.3 %</div></div>	<div><div>− 2.3 %</div><div>− 2.3 %</div></div>	<div><div>+25.0 %</div><div>− 2.3 %</div></div>	<div><div>+25.0 %</div><div>+25.0 %</div></div>	<div><div>+ 3.9 %</div><div>+ 3.9 %</div></div>	35.3	3.22	21.5	<div><div>+ 2.1 %</div><div>+ 2.1 %</div></div>	32,000	38,000	<div><div>+10.0 %</div><div>+10.0 %</div></div>
<div><div>0.78</div><div>+ 2.7 %</div></div>	<div><div>+ 5.2 %</div><div>14.2</div></div>	5	<div><div>+ 5.2 %</div><div>− 2.4 %</div></div>	<div><div>14.2</div><div>− 2.4 %</div></div>	<div><div>− 2.4 %</div><div>− 2.5 %</div></div>	<div><div>− 2.4 %</div><div>− 2.4 %</div></div>	<div><div>− 2.4 %</div><div>− 2.4 %</div></div>	<div><div>+38.0 %</div><div>− 2.4 %</div></div>	<div><div>+38.0 %</div><div>+38.0 %</div></div>	<div><div>+ 4.3 %</div><div>+ 4.3 %</div></div>	35.4	3.24	24.9	<div><div>+ 2.7 %</div><div>+ 2.7 %</div></div>	30,000	36,000	<div><div>+17.1 %</div><div>+17.1 %</div></div>

^aat ΔT = 15 K, includes the thrust growth factor of 1.25 (see page 41)

^b1 = takeoff field length, 2 = balanced field length, 3 = 1st segment climb, 4 = 2nd segment climb, 5 = 3rd segment climb,

^cat max. static thrust

cruise speed changed relative to design point

improvement relative to design point

diminishment relative to design point

constraint violated

^aat $\Delta T = 15$ K, includes the thrust growth factor of 1.25 (see page 41)

^b1 = takeoff field length, 2 = balanced field length, 3 = 1st segment climb, 4 = 2nd segment climb, 5 = 3rd segment climb,

6 = initial cruise altitude, 7 = final cruise altitude

^cat max. static thrust

□ cruise speed changed relative to design point

■ improvement relative to design point

■ diminishment relative to design point

■ constraint violated

Table C.10: Open Rotor Cruise Speed Cost Space (TET = 1,900 K, OPR = 37.0, Prop. Diameter = 4.36 m, Max. Propeller Tip Speed = 283.2 m/s, Wing Span Factor = 0.32, Wing Mean Chord Length Factor = 0.01).

Direct Operating Cost (¢/RPK in 2012 prices)												
Cruise Speed (Mach)	Engine					Airframe				Total		$\sqrt{\text{MSD}}$
	Depreciation + Interest + Insurance + Maintenance	Depreciation + Interest + Insurance + Maintenance	Landing + Navigation	Fuel + CO ₂ (mean)	Crew + Ground Handling	Productivity ^a	Market Share ^a	Time ^a	Excl. Time (mean) ^b	Incl. Time (mean) ^b	Excl. Time (mean) ^c	Incl. Time (mean) ^c
0.68	− 0.5 %	− 1.0 %	− 0.5 %	− 1.8 %	0.0 %	0.517	0.095	0.964	+ 0.5 %	+ 2.1 %	+ 0.5 %	+ 1.3 %
0.70	0.777	2.530	0.675	2.948	2.443	0.403	0.077	0.788	9.854	10.642	9.885	18.944
0.72	+ 0.4 %	+ 1.0 %	+ 0.5 %	+ 2.0 %	0.0 %	0.334	0.062	0.646	+ 0.1 %	− 1.3 %	+ 0.1 %	− 0.8 %
0.74	+ 0.9 %	+ 2.1 %	+ 1.0 %	+ 5.4 %	0.0 %	0.241	0.048	0.459	+ 0.3 %	− 2.8 %	+ 0.4 %	− 1.7 %
0.76	+ 2.1 %	+ 3.5 %	+ 1.6 %	+10.0 %	0.0 %	0.165	0.035	0.296	+ 1.3 %	− 3.4 %	+ 1.4 %	− 2.1 %
0.78	+ 2.3 %	+ 4.5 %	+ 2.1 %	+17.1 %	0.0 %	0.129	0.023	0.179	+ 3.3 %	− 2.7 %	+ 3.4 %	− 1.8 %

^acost change relative to Mach 0.82

^bincl. relative productivity, market share and time cost

^cincl. absolute productivity, market share and time cost

□ cruise speed changed relative to design point

■ improvement relative to design point ■ diminishment relative to design point

Appendix D

Cost Diagrams

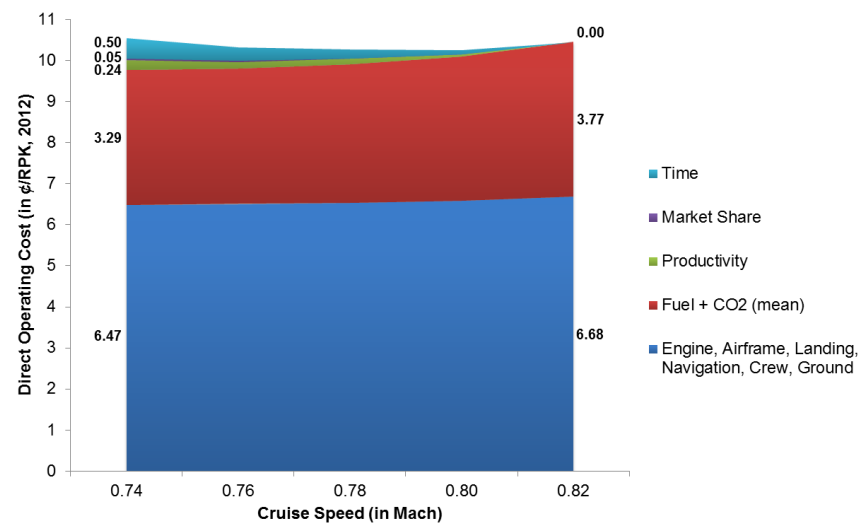


Figure D.1: Three-Shaft Turbofan Direct Operating Cost Breakdown Vs. Cruise Speed.

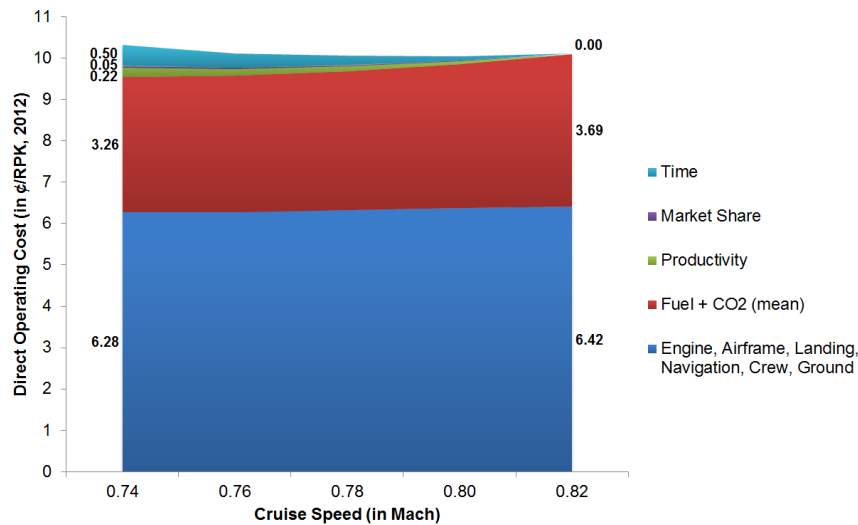


Figure D.2: Geared Turbofan Direct Operating Cost Breakdown Vs. Cruise Speed.

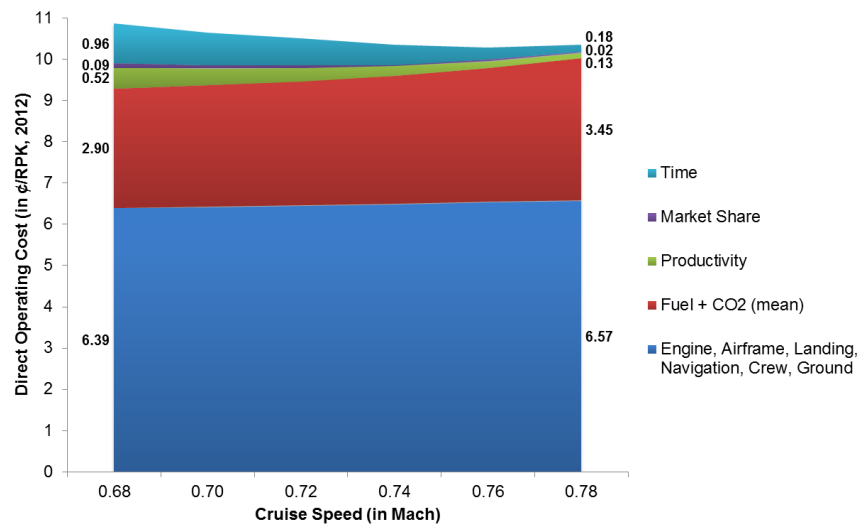


Figure D.3: Open Rotor Direct Operating Cost Breakdown Vs. Cruise Speed.

Bibliography

- [1] Curran, R., Raghunathan, S., Price, M., “Review of Aerospace Engineering Cost Modelling: the Genetic Causal Approach,” *Progress in Aerospace Sciences*, Vol. 40, No. 8, 2004, pp. 487–534.
- [2] Scanlan, J., Hill, T., Marsh, R., Bru, C., Dunkley, M., “Cost Modelling for Aircraft Design Optimization,” *Journal of Engineering Design*, Vol. 13, No. 3, 2002, pp. 261–269.
- [3] Collopy, P., Curran, R., “The Challenge of Modeling Cost: the Problem,” *1st International Conference on Innovation and Integration in Aerospace Sciences*, Belfast, United Kingdom, 2005.
- [4] Smith, A. E., Mason, A. K., “Cost Estimation Predictive Modeling: Regression Versus Neural Network,” *The Engineering Economist*, Vol. 42, No. 2, 1997, pp. 137–161.
- [5] Scanlan, J., Rao, A., Bru, C., Hale, P., Marsh, R., “DATUM Project: Cost Estimating Environment for Support of Aerospace Design Decision Making,” *Journal of Aircraft*, Vol. 43, No. 4, 2006, pp. 1022–1028.
- [6] Curran, R., Kundu, A. K., Wright, J. M., Crosby, S., Price, M., “Modelling of Aircraft Manufacturing Cost at the Concept Stage,” *International Journal of Advanced Manufacturing Technology*, Vol. 31, No. 3, 2006, pp. 407–420.
- [7] Locascio, A., “Manufacturing Cost Modelling for Product Design,” *The International Journal of Flexible Manufacturing Systems*, Vol. 12, No. 2, 2000, pp. 207–217.
- [8] Weustink, I. F., Ten Brinke, E., Streppel, A. H., Kals, H. J. J., “A Generic Framework for Cost Estimation and Cost Control in Product Design,” *Journal of Materials Processing Technology*, Vol. 103, No. 1, 2000, pp. 141–148.

- [9] Collopy, P. D., Eames, D. J. H., “Aerospace Manufacturing Cost Prediction from a Measure of Part Definition Information,” *SAE World Aviation Congress and Exposition*, Seattle, Washington, USA, 2001.
- [10] Kim, G. H., An, S. H., Kang, K. I., “Comparison of Construction Cost Estimating Models Based on Regression Analysis, Neural Networks, and Case-Based Reasoning,” *Building and Environment*, Vol. 39, No. 10, 2004, pp. 1235–1242.
- [11] Rolls-Royce, *The Jet Engine*, 6th ed., Rolls-Royce plc, London, United Kingdom, 2005.
- [12] Advisory Council for Aeronautics Research in Europe (ACARE), “Aeronautics and Air Transport: Beyond Vision 2020 (Towards 2050),” *ACARE*, 2010.
- [13] Keane, A. J., Nair, P. B., *Computational Approaches for Aerospace Design*, 1st ed., John Wiley & Sons, Chichester, United Kingdom, 2005.
- [14] House of Commons Transport Committee, “The Future of Aviation,” *House of Commons Transport Committee*, 2009.
- [15] Committee on Climate Change (CCC), “Meeting the UK Aviation Target — Options for Reducing Emissions to 2050,” *CCC*, 2009.
- [16] Mentzer, W. C., Nourse, H. E., “Some Economic Aspects of Transport Airplane Performance. Part I,” *Journal of the Aeronautical Sciences*, Vol. 7, No. 6, 1940, pp. 227–234.
- [17] Morrison, S. A., “An Economic Analysis of Aircraft Design,” *Journal of Transport Economics and Policy*, Vol. 18, No. 2, 1984, pp. 123–143.
- [18] Lee, J. J., Lukachko, S. P., Waitz, I. A., Schafer, A., “Historical and Future Trends in Aircraft Performance, Cost, and Emissions,” *Annual Review of Energy and the Environment*, Vol. 26, No. 1, 2001, pp. 167–200.
- [19] Antoine, N., Kroo, I., Willcox, K., Barter, G., “A Framework for Aircraft Conceptual Design and Environmental Performance Studies,” *10th AIAA/ISSMO Multidisciplinary Analysis and Optimization Conference*, Albany, New York, USA, 2004.

- [20] Bower, G. C., Kroo, I. M., “Multi-Objective Aircraft Optimization for Minimum Cost and Emissions over Specific Route Networks,” *26th International Congress of the Aeronautical Sciences (ICAS)*, Anchorage, Alaska, USA, 2008.
- [21] Kernstine, K., Boling, B., Bortner, L., Hendricks, E., Mavris, D., “Designing for a Green Future: a Unified Aircraft Design Methodology,” *Journal of Aircraft*, Vol. 47, No. 5, 2010, pp. 1789–1797.
- [22] Mavris, D. N., Mantis, G. C., Kirby, M. R., “Demonstration of a Probabilistic Technique for the Determination of Aircraft Economic Viability,” *SAE Transactions*, Vol. 106, No. 1, 1997, pp. 1704–1713.
- [23] Ryerson, M. S., Hansen, M., “The Potential of Turboprops for Reducing Aviation Fuel Consumption,” *Transportation Research Part D: Transport and Environment*, Vol. 15, No. 6, 2010, pp. 305–314.
- [24] Guynn, M. D., Berton, J. J., Hendricks, E. S., Tong, M. T., Haller, W. J., “Initial Assessment of Open Rotor Propulsion Applied to an Advanced Single-Aisle Aircraft,” *11th AIAA Aviation Technology, Integration, and Operations Conference (ATIO)*, Virginia Beach, Virginia, USA, 2011.
- [25] Peters, A., “Assessment of Propfan Propulsion Systems for Reduced Environmental Impact,” M.Sc. Thesis, Massachusetts Institute of Technology, Boston, Massachusetts, USA, 2010.
- [26] Hendricks, E. S., Tong, M. T., “Performance and Weight Estimates for an Advanced Open Rotor Engine,” *48th AIAA/ASME/SAE/ASEE Joint Propulsion Conference & Exhibit*, Atlanta, Georgia, USA, 2012.
- [27] Qian, L., Ben-Arieh, D., “Parametric Cost Estimation Based on Activity-Based Costing: a Case Study for Design and Development of Rotational Parts,” *International Journal of Production Economics*, Vol. 113, No. 2, 2008, pp. 805–818.
- [28] Airlines for America (A4A), “A4A Passenger Airlines Cost Index Tables,” A4A [online], 2009, <https://publications.airlines.org/CommerceProductDetail.aspx?Product=152> [revisited 22 May 2015].

- [29] Bureau of Labor Statistics, “CPI Inflation Calculator,” *United States Department of Labor* [online], 2014, http://www.bls.gov/data/inflation_calculator.htm [revisited 22 May 2015].
- [30] Airbus, “Global Market Forecast 2009–2028,” *Airbus S.A.S.*, 2009.
- [31] Bowler, T., “Falling Oil Prices: Who are the Winners and Losers?,” *BBC News* [online], 2015, <http://www.bbc.com/news/business-29643612> [revisited 22 May 2015].
- [32] Donovan, S., Petrenas, B., Leyland, G., Caldwell, S., Barker, A., “Price Forecasts for Transport Fuels and Other Delivered Energy Forms,” *Auckland Regional Council*, 2009.
- [33] BBC News, “Oil Hits \$ 100 Barrel,” *BBC News* [online], 2008, <http://news.bbc.co.uk/1/hi/business/7083015.stm> [revisited 22 May 2015].
- [34] Flightglobal, “Whatever Happened to Propfans,” *Flightglobal* [online], 2007, <http://www.flightglobal.com/news/articles/whatever-happened-to-propfans-214520/> [revisited 22 May 2015].
- [35] Flightglobal, “The Arrogant Decade,” *Flightglobal* [online], 1990, <http://www.flightglobal.com/pdfarchive/view/1990/1990%20-%200106.html?search=two-man%20cockpit> [revisited 22 May 2015].
- [36] The Economist, “Why are No-Frills Airlines so Cheap?,” *The Economist* [online], 2013, <http://www.economist.com/blogs/economist-explains/2013/10/economist-explains-13> [revisited 22 May 2015].
- [37] Vasigh, B., Fleming, K., Tacker, T., *Introduction to Air Transport Economics: from Theory to Applications*, 1st ed., Ashgate Publishing Limited, Farnham, United Kingdom, 2008.
- [38] U.S. Energy Information Administration (EIA), “International Energy Outlook 2013,” *EIA*, 2013.
- [39] Department of Energy & Climate Change (DECC), “DECC Fossil Fuel Price Projections,” *DECC*, 2013.

- [40] Kahn Ribeiro, S., Kobayashi, S., Beuthe, M., Gasca, J., Greene, D., “Transport and its Infrastructure,” *Fourth Assessment Report of the Intergovernmental Panel on Climate Change*, 2007.
- [41] Anastasi, L., Dickinson, H., Kass, G., Smith, K., Stein, C., “Aviation and the Environment,” *Parliamentary Office of Science and Technology (POST)*, 2003.
- [42] International Civil Aviation Organization (ICAO), “ICAO Environmental Report,” ICAO, 2010.
- [43] European Central Bank (ECB), “Euro Foreign Exchange Reference Rates,” *ECB* [online], 2015, <http://www.ecb.europa.eu/stats/exchange/eurofxref/html/index.en.html> [revisited 22 May 2015].
- [44] Scheelhaase, J. D., Grimme, W. G., “Emissions Trading for International Aviation — an Estimation of the Economic Impact on Selected European Airlines,” *Journal of Air Transport Management*, Vol. 13, No. 5, 2007, pp. 253–263.
- [45] Department for Transport (DfT), “The Future of Air Transport,” *DfT*, 2003.
- [46] Van Hasselt, M., Van der Zwan, F., Ghijs, S., Santema, S., “Developing a Strategic Framework for an Airline Dealing with the EU Emission Trading Scheme,” *9th AIAA Aviation Technology, Integration, and Operations Conference (ATIO)*, Hilton Head, South Carolina, USA, 2009.
- [47] The Guardian, “UK Calls for Cancelling of Carbon Permits to Revive EU Emissions Trading,” *The Guardian* [online], 2014, <http://www.theguardian.com/environment/2014/jul/16/uk-calls-for-cancelling-of-carbon-permits-to-revive-eu-emissions-trading> [revisited 22 May 2015].
- [48] Collopy, P. D., “Economic-Based Distributed Optimal Design,” *AIAA Space 2001 Conference and Exposition*, Albuquerque, New Mexico, USA, 2001.
- [49] Collopy, P. D., “Surplus Value in Propulsion System Design Optimization,” *33rd AIAA/ASME/SAE/ASEE Joint Propulsion Conference & Exhibit*, Seattle, Washington, USA, 1997.
- [50] Hazelrigg, G. A., “A Framework for Decision-Based Engineering Design,” *Journal of Mechanical Design*, Vol. 120, No. 4, 1998, pp. 653–658.

- [51] Won, H. T., “A System-of Systems Modeling Methodology for Strategic General Aviation Design Decision-Making,” Ph.D. Thesis, Georgia Institute of Technology, Atlanta, Georgia, USA, 2008.
- [52] Raymer, D. P., *Aircraft Design: a Conceptual Approach*, 4th ed., American Institute of Aeronautics and Astronautics Inc., Reston, Virginia, USA, 2006.
- [53] Doganis, R., *Flying Off Course: the Economics of International Airlines*, 3rd ed., Routledge, London, United Kingdom, 2002.
- [54] Jenkinson, L. R., Simpkin, P., Rhodes, D., *Civil Jet Aircraft Design*, 1st ed., Butterworth-Heinemann, Oxford, United Kingdom, 1999.
- [55] Cook, A., Tanner, G., “European Airline Delay Cost Reference Values,” *University of Westminster*, London, United Kingdom, 2011.
- [56] Institut du Transport Aérien (ITA), “Costs of Air Transport Delay in Europe,” *ITA*, 2000.
- [57] Brons, M., Pels, E., Nijkamp, P., Rietveld, P., “Price Elasticities of Demand for Passenger Air Travel: a Meta-Analysis,” *Journal of Air Transport Management*, Vol. 8, No. 3, 2002, pp. 165–175.
- [58] EUROCONTROL, “Standard Inputs for EUROCONTROL Cost Benefit Analyses Edition 4.0,” *EUROCONTROL*, 2009.
- [59] Åkerman, J., “Sustainable Air Transport — on Track in 2050,” *Transportation Research Part D: Transport and Environment*, Vol. 10, No. 2, 2005, pp. 111–126.
- [60] Airbus, “Airbus UK / University of Bath Specification for Aerospace Design Project 2007 — Low Fare Airline Optimised Aircraft,” *Airbus S.A.S.*, 2007.
- [61] Montgomery, D. C., Runger, G. C., *Applied Statistics and Probability for Engineers*, 3rd ed., John Wiley & Sons, Danvers, Massachusetts, USA, 2003.
- [62] Parker, R., “From Blue Skies to Green Skies: Engine Technology to Reduce the Climate-Change Impacts of Aviation,” *Technology Analysis & Strategic Management*, Vol. 21, No. 1, 2009, pp. 61–78.

- [63] Trimble, S., "Analysis: Noise Goals in Sight for Open-Rotor Researchers," *Flight-global* [online], 2014, <http://www.flightglobal.com/news/articles/analysis-noise-goals-in-sight-for-open-rotor-researchers-395804/> [revisited 22 May 2015].
- [64] Xu, J. J., "Combining Activity-Based Costing with Manufacturing Simulation," M.Sc. Thesis, Cranfield University, Cranfield, United Kingdom, 2006.
- [65] Cooper, R., Kaplan, R. S., "How Cost Accounting Systematically Distorts Product Costs," *Accounting and Management: Field Study Perspectives*, 1987, pp. 204–228.
- [66] Spedding, T. A., Sun, G. Q., "Application of Discrete Event Simulation to the Activity Based Costing of Manufacturing Systems," *International Journal of Production Economics*, Vol. 58, No. 3, 1999, pp. 289–301.
- [67] Younossi, O., Arena, M. V., Moore, R. M., Lorell, M., Mason, J., "Military Jet Engine Acquisition — Technology Basics and Cost-Estimating Methodology," *RAND Corporation*, 2003.
- [68] Cooper, R., Kaplan, R. S., "Profit Priorities from Activity-Based Costing," *Harvard Business Review*, Vol. 69, No. 3, 1991, pp. 130–135.
- [69] Curran, R., Price, M., Raghunathan, S., Benard, E., Crosby, S., "Integrating Aircraft Cost Modeling into Conceptual Design," *Concurrent Engineering*, Vol. 13, No. 4, 2005, pp. 321–330.
- [70] Birkler, J. L., Garfinkle, J. B., Marks, K. E., "Development and Production Cost Estimating Relationships for Aircraft Turbine Engines," *RAND Corporation*, 1982.
- [71] Dryden, J. A., Large, J. P., "A Critique of Spacecraft Cost Models," *RAND Corporation*, 1977.
- [72] Kwak, Y. H., Watson, R. J., "Conceptual Estimating Tool for Technology-Driven Projects: Exploring Parametric Estimating Technique," *Technovation*, Vol. 25, No. 12, 2005, pp. 1430–1436.
- [73] Finnie, G. R., Wittig, G. E., Desharnais, J. M., "A Comparison of Software Effort Estimation Techniques: Using Function Points with Neural Networks, Case-Based

- Reasoning and Regression Models,” *Journal of Systems and Software*, Vol. 39, No. 3, 1997, pp. 281–289.
- [74] Bearden, D. A., “Small-Satellite Costs,” *Crosslink*, Vol. 2, No. 1, 2001, pp. 32–44.
- [75] Muia, T., Salam, A., Bhuiyan, N. F., “A Comparative Study to Estimate Costs at Bombardier Aerospace Using Regression Analysis,” *IEEE International Conference on Industrial Engineering and Engineering Management*, Hong Kong, China, 2009.
- [76] Riegler, C., Bichlmaier, C., “The Geared Turbofan Technology — Opportunities, Challenges and Readiness Status,” *1st CEAS European Air and Space Conference*, Berlin, Germany, 2007.
- [77] Daly, K., “Rolls-Royce Promotes Turboprop Solution for New Civil Airlines,” *Flightglobal* [online], 2008, <http://www.flightglobal.com/news/articles/rolls-royce-promotes-turboprop-solution-for-new-civil-224987/> [revisited 22 May 2015].
- [78] Jackson, P. A., *Jane’s All the World’s Aircraft 2006–2007*, 97th ed., Jane’s Information Group, Coulsdon, United Kingdom, 2006.
- [79] Flightglobal, “Bristol Olympus,” *Flightglobal* [online], 1955, <http://www.flightglobal.com/pdfarchive/view/1955/1955%20-%201753.html> [revisited 22 May 2015].
- [80] Flightglobal, “R.B.211 Certificated,” *Flightglobal* [online], 1972, <http://www.flightglobal.com/pdfarchive/view/1972/1972%20-%200676.html> [revisited 22 May 2015].
- [81] Polek, G., “Pratt & Whitney Geared Turbofan Promises New Engine Dominance,” *AInonline* [online], 2013, <http://www.ainonline.com/aviation-news/air-transport/2013-06-13/pratt-whitney-geared-turbofan-promises-new-engine-dominance> [revisited 22 May 2015].
- [82] Flightglobal, “Development of the Turboprop,” *Flightglobal* [online], 1950, <http://www.flightglobal.com/pdfarchive/view/1950/1950%20-%202035.html> [revisited 22 May 2015].

- [83] Saravanamuttoo, H. I. H., “Modern Turboprop Engines,” *Progress in Aerospace Sciences*, Vol. 24, No. 3, 1987, pp. 225–248.
- [84] European Aviation Safety Agency (EASA), “E.033 Europrop International GmbH TP400-D6 Engine,” *EASA*, 2014.
- [85] Jackson, P. A., *Jane’s All the World’s Aircraft 2011–2012*, 102nd ed., Jane’s Information Group, Coulsdon, United Kingdom, 2011.
- [86] McCormick, B. W., *Aerodynamics, Aeronautics, and Flight Mechanics*, 2nd ed., John Wiley & Sons, Hoboken, New Jersey, USA, 1995.
- [87] Warwick, G., “Noise Tests Keep Promise Of Open-Rotor Engines Alive,” *Aviation Week*, 2010.
- [88] Schimming, P., “Counter Rotating Fans — an Aircraft Propulsion for the Future,” *Journal of Thermal Science*, Vol. 12, No. 2, 2003, pp. 97–103.
- [89] Bellocq, P., Sethi, V., Cerasi, L., Ahlefeldt, S., Tantot, N., “Advanced Open Rotor Performance Modelling for Multidisciplinary Optimization Assessments,” *ASME Turbo Expo 2010: Power for Land, Sea and Air*, Glasgow, United Kingdom, 2010.
- [90] European Commission, “valiDation of Radical Engine Architecture systeMs (DREAM),” *European Commission* [online], 2014, http://ec.europa.eu/research/transport/news/items/dream_ip_encouraging_results_en.htm [revisited 22 May 2015].
- [91] Steffens, K., “Advanced Compressor Technology – Key Success Factor for Competitiveness in Modern Aero Engines,” *15th International Symposium on Air Breathing Engines (ISABE)*, Bangalore, India, 2001.
- [92] Bussmann, M., Kraus, J., Bayer, E., “An Integrated Cost-Effective Approach to Blisk Manufacturing,” *17th International Symposium on Air Breathing Engines (ISABE)*, Munich, Germany, 2005.
- [93] Chan, Y. J., “Variability of Blade Vibration in Mistuned Bladed Discs,” Ph.D. Thesis, Imperial College London, London, United Kingdom, 2009.

- [94] Ford, S., Tao, L., Probert, D., “Preparing for Takeoff: Breakthrough Process Innovation at Rolls-Royce,” *17th Portland International Conference on Management of Engineering and Technology (PICMET)*, Cape Town, South Africa, 2008.
- [95] Zhan, H., Zhao, W., Wang, G., “Manufacturing Turbine Blisks,” *Aircraft Engineering and Aerospace Technology*, Vol. 72, No. 3, 2000, pp. 247–252.
- [96] Bussmann, M., Bayer, E., “Blisk Production of the Future — Technological and Logistical Aspects of Future-Oriented Construction and Manufacturing Processes of Integrally Bladed Rotors,” *19th International Symposium on Air Breathing Engines (ISABE)*, Montreal, Canada, 2009.
- [97] Kosing, O. E., Scharl, R., Schmuhl, H. J., “Design Improvements of the EJ200 HP Compressor — from Design Verification Engine to a Future All Blisk Version,” *ASME Turbo Expo 2001: Land, Sea, and Air*, New Orleans, Louisiana, USA, 2001.
- [98] Coppinger, R., “MTU Aero Engines Claims Blisk Repair First,” *Flightglobal*, 2008.
- [99] European Aviation Safety Agency (EASA), “E.069 International Aero Engines AG (IAE) V2500-A5 and V2500-D5 Series Engines,” *EASA*, 2013.
- [100] Wickerson, J., “Holistic Gas Turbine,” *Rolls-Royce plc*, 2008.
- [101] Howe, D., *Aircraft Conceptual Design Synthesis*, 1st ed., Professional Engineering Publishing Limited, London and Bury St. Edmunds, United Kingdom, 2000.
- [102] Mattingly, J. D., Heiser, W. H., Pratt, D. T., *Aircraft Engine Design*, 2nd ed., American Institute of Aeronautics and Astronautics Inc., Reston, Virginia, USA, 2002.
- [103] Lock, G. D., “Aircraft Propulsion,” *University of Bath*, 2006.
- [104] Clare, J., “Examples of More Electric Aircraft Research in the Aerospace Research Centre,” *The University of Nottingham*, 2010.
- [105] Saravanamuttoo, H. I. H., Rogers, G. F. C., Cohen, H., *Gas Turbine Theory*, 5th ed., Pearson Education Limited, Harlow, United Kingdom, 2001.

- [106] Jain, R., “Prediction of Transient Loads and Perforation of Engine Casing During Blade-Off Event of Fan Rotor Assembly,” *IMPLAST 2010 Conference*, Providence, Rhode Island, USA, 2010.
- [107] Darling, J. C., “Solid Mechanics,” *University of Bath*, 2004.
- [108] Airbus, “Global Market Forecast 2011–2030,” *Airbus S.A.S.*, 2011.
- [109] Cumpsty, N., *Jet Propulsion*, 2nd ed., Cambridge University Press, Cambridge, United Kingdom, 2003.
- [110] Austyn Mair, W., Birdsall, D. L., *Aircraft Performance*, 1st ed., Cambridge University Press, Cambridge, United Kingdom, 1992.
- [111] Zurich Airport, “Night-Time Curfew,” *Flughafen Zürich AG* [online], 2013, <http://www.zurich-airport.com/the-company/media/current-topics/night-flight-ban> [revisited 22 May 2015].
- [112] Boeing, “Commercial Airplanes,” *Boeing* [online], 2014, <http://www.boeing.com/commercial/> [revisited 22 May 2015].
- [113] Boeing Capital Corporation, “Current Aircraft Finance Market Outlook 2014–2018,” *Boeing*, 2013.
- [114] Huber, M., “Airbus A320,” *Business Jet Traveler*, 2012.
- [115] Prospects, “Airline Pilot – Salary and Conditions,” *AGCAS & Graduate Prospects Ltd* [online], 2015, http://www.prospects.ac.uk/airline_pilot_salary.htm [revisited 22 May 2015].
- [116] Prospects, “Air Cabin Crew – Salary and Conditions,” *AGCAS & Graduate Prospects Ltd* [online], 2014, http://www.prospects.ac.uk/air_cabin_crew_salary.htm [revisited 22 May 2015].
- [117] Airlines for America (A4A), “Average Spot Prices,” *A4A* [online], 2014, <http://airlines.org/data/average-spot-prices/> [revisited 22 May 2015].
- [118] Hooke, R., Jeeves, T. A., “Direct Search Solution of Numerical and Statistical Problems,” *Journal of the ACM (JACM)*, Vol. 8, No. 2, 1961, pp. 212–229.

- [119] Airbus, “A320 Airplane Characteristics for Airport Planning,” *Airbus S.A.S.*, 2011.
- [120] Parker, R., Lathoud, M., “Green Aero-Engines: Technology to Mitigate Aviation Impact on Environment,” *Proceedings of the Institution of Mechanical Engineers, Part C: Journal of Mechanical Engineering Science*, Vol. 224, No. 3, 2010, pp. 529–538.
- [121] Calder, S., “Concorde and Supersonic Travel: the Days When the Sun Rose in the West,” *The Independent* [online], 2013, <http://www.independent.co.uk/travel/news-and-advice/concorde-and-supersonic-travel-the-days-when-the-sun-rose-in-the-west-8888836.html> [revisited 22 May 2015].
- [122] BBC News, “Concorde Grounded for Good,” *BBC News* [online], 2003, <http://news.bbc.co.uk/1/hi/uk/2934257.stm> [revisited 22 May 2015].
- [123] Fagan, M., “Boeing Axes Sonic Cruiser as Airlines Lose Interest,” *The Telegraph* [online], 2002, <http://www.telegraph.co.uk/finance/2837367/Boeing-axes-Sonic-Cruiser-as-airlines-lose-interest.html> [revisited 22 May 2015].
- [124] Norris, G., “Sonic Cruiser is Dead — Long Live Super Efficient,” *Flightglobal* [online], 2003, <http://www.flightglobal.com/news/articles/sonic-cruiser-is-dead-long-live-super-efficient-159915/> [revisited 22 May 2015].
- [125] Krauskopf, L., “GE Exec Says Avoided Geared Design in Jet Engine Battle with Pratt,” *Thomson Reuters* [online], 2014, <http://www.reuters.com/article/2014/09/15/us-general-electric-united-tech-engine-idUSKBN0HA2H620140915> [revisited 22 May 2015].
- [126] Takakuwa, S., “The Use of Simulation in Activity-Based Costing for Flexible Manufacturing Systems,” *1997 Winter Simulation Conference*, Atlanta, Georgia, USA, 1997.
- [127] Design-Expert 8.0.4, “Stat-Ease Help,” *Stat-Ease Inc.*, 2010.
- [128] Book, S. A., “Estimating Probable System Cost,” *Crosslink*, Vol. 2, No. 1, 2001, pp. 12–21.

- [129] Von Beck, U., Nowak, J. W., “The Merger of Discrete Event Simulation with Activity Based Costing for Cost Estimation in Manufacturing Environments,” *2000 Winter Simulation Conference*, Orlando, Florida, USA, 2000.
- [130] Vanguard Studio, “Monte Carlo Simulation Add-In,” *Vanguard Software Corporation*, 2010.
- [131] Minitab, “Minitab 15 Help,” *Minitab Inc.*, 2007.
- [132] Marsh, R., Cheung, W. M., Lanham, J., Newnes, L., Mileham, A., “Modelling an Assembly Process Using a Close Coupled Generative Cost Model and a Discrete Event Simulation,” *4th International Conference on Digital Enterprise Technology*, Bath, United Kingdom, 2007.
- [133] Sobek, D. K., Ward, A. C., Liker, J. K., “Toyota’s Principles of Set-Based Concurrent Engineering,” *Sloan Management Review*, Vol. 40, No. 2, 1999, pp. 67–83.